Studies on the Solid State Chemistry of Perovskite-Type Oxides for Oxygen Separating Membranes

Von der Naturwissenschaftlichen Fakultät

der Gottfried Wilhelm Leibniz Universität Hannover

zur Erlangung des Grades eines

**Doktors der Naturwissenschaften
Dr. rer. nat.**

genehmigte Dissertation

von

Diplom-Chemiker Mirko Arnold

geboren am 03. Januar 1980 in Hannover

2008

Studies on the Solid State Chemistry of Perovskite-Type Oxides for Oxygen Separating Membranes

Von der Naturwissenschaftlichen Fakultät

der Gottfried Wilhelm Leibniz Universität Hannover

zur Erlangung des Grades eines

Doktors der Naturwissenschaften
Dr. rer. nat.

genehmigte Dissertation

von

Diplom-Chemiker Mirko Arnold

geboren am 03. Januar 1980 in Hannover

2008

Abstract

The presented thesis contains and condenses seven original research articles on the solid-state chemistry of the cubic perovskite-type oxides $(Ba_{0.5}Sr_{0.5})(Co_{0.8}Fe_{0.2})O_{3-\delta}$ (denoted as BSCF) and $(Ba_{0.5}Sr_{0.5})(Fe_{0.8}Zn_{0.2})O_{3-\delta}$ (denoted as BSFZ), which are used as oxygen separating membranes.

Throughout this work integrative investigations such as results derived from powder X-ray diffraction (XRD) and oxygen permeation experiments, are correlated with microscopic investigations derived from analytical electron microscopy (AEM). Results of the synthetic process towards BSCF and BSFZ powders via the commonly used sol-gel route are reflected in the first part of this thesis and are summarised in chapters 2 and 3. Parallels as well as fundamental differences have been found in the formation of BSCF and BSFZ. While the first part of the synthesis is similar for both materials, the successive steps are different because of the particular electronic spin-state behaviour of cobalt in BSCF. This generates a large difference in the calcination temperatures necessary to synthesise the final perovskites structures. In the case of BSCF, the temperature has to be set to T = 1173 K, while the BSFZ can already be obtained at T = 1023 K.

The local charge disproportion in sintered BSCF membranes was investigated by *in situ* electron energy-loss spectroscopy (EELS) on the ionization edges of cobalt, iron and oxygen using monochromised electrons, where the results are discussed in chapter 4. In order to investigate the electronic structure of BSCF, the cobalt-$L_{2,3}$, the iron-$L_{2,3}$, and the oxygen K-edge were examined. The overall B-site was shown to decreases from +2.7 at T = 298 K to +2.3 between T = 773 K and T = 1223 K, where the stronger effect was at the cobalt site.

A summary of the CO_2 stability of BSCF membranes under oxygen permeation conditions is presented in chapter 5. Pure CO_2 on the permeate side yielded an immediate cessation in the oxygen permeation at T = 1148 K. It has been found that both the microstructure as well as oxygen permeation are recovered in a pure helium atmosphere. This indicates a reversible reaction with CO_2, which has been found to penetrate the membrane only to a maximum depth of 50 μm. Furthermore, BSCF membranes are capable of sustaining CO_2 for 120 min if the O_2:CO_2 ratio does not fall significantly below 2:1 at T = 1148 K.

Chapter 6 deals with the microstructure's influence on the oxygen permeation behaviour. Liquid-phase sintering with different concentrations of BN as a sintering aid was applied to adjust the grain size distribution in both BSCF and BSFZ membranes. Oxygen permeation experiments have shown that, the lower the average grain size, the lower the oxygen permeation performance. TEM revealed that no amorphous layer or any other interfacial phase was present at the grain boundary.

Zusammenfassung

Die vorliegende Arbeit umfasst sieben Forschungsarbeiten zur Festkörperchemie der kubischen perowskitischen Oxide $(Ba_{0.5}Sr_{0.5})(Co_{0.8}Fe_{0.2})O_{3-\delta}$ (BSCF) und $(Ba_{0.5}Sr_{0.5})(Fe_{0.8}Zn_{0.2})O_{3-\delta}$ (BSFZ) für die Sauerstoffabtrennung aus Gasgemischen. Der methodische Ansatz dieser Arbeit besteht dabei in der Korrelation von integrativen mit mikroskopischen Untersuchungsmethoden.

In Kap. 2 und 3 sind die Ergebnisse zur Untersuchung des Sol-Gel Syntheseprozesses der perowskitischen Oxide BSCF and BSFZ zusammengefasst. Während die ersten Schritte der Syntheseprozesse sehr ähnlich verlaufen, zeigen sich Unterschiede im weiteren Verlauf der Reaktion, welche auf das unterschiedliche Elektronenspinverhalten des Cobalts zurückzuführen sind. Dieser Unterschied wirkt sich maßgeblich auf die notwendigen Calcinationstemperaturen für die vollständige Reaktion zum kubischen Perowskiten aus. Kann BSFZ bereits bei Calcinationstemperaturen von 1023 K synthetisiert werden, sind im Fall von BSCF Temperaturen von mindestens 1173 K notwendig.

Die Untersuchung der temperaturabhängigen lokalen Ladungsverteilung in gesinterten BSCF-Membranen wurde mittels monochromatisierter Elektronen-Energie-Verlust Spektroskopie (EELS) durchgeführt und wird in Kap. 4 besprochen. Anhand der Cobalt-$L_{2,3}$, der Eisen-$L_{2,3}$ und der Sauerstoff K-Kante wird gezeigt, dass die gemittelte kationische B-Seite eine Valenz von $+2.7$ bei 298 K und $+2.3$ zwischen 773 - 1223 K aufweist und dass die Reduktion vornehmlich an Cobalt stattfindet.

Kap. 5 analysiert die CO_2-Stabilität von BSCF-Membranen während Sauerstoffpermeationsexperimenten. Reines CO_2 bewirkt, dass die Sauerstoffpermeation bei einer Temperatur von 1148 K sofort zum Erliegen kommt. Sowohl Mikrostruktur als auch Sauerstoffpermeation können jedoch in reinen Heliumatmosphären wiederhergestellt werden. Dies deutet auf eine reversible Reaktion von BSCF mit CO_2 hin, die eine Penetrationstiefe in die Membran von 50 μm nicht überschreitet. Weiter zeigte sich, dass BSCF-Membranen eine CO_2-Toleranz vom mindestens 120 min bei 875 °C aufweisen, insofern ein Verhältnis $O_2:CO_2$ von 2:1 nicht unterschritten wird.

Kap. 6 beinhaltet den Einfluss der Mikrostruktur von BSCF und BSFZ Membranen auf die Sauerstoffpermeation. Flüssig-Phasen-Sintern mit unterschiedlichen Konzentrationen von Bornitrid (BN) als Sinteradditiv wurde angewendet, um die Korngrößenverteilung dieser Membranen einzustellen. Es zeigte sich, dass kleinere Körner den Sauerstofftransport behindern, während größere Körner den Sauerstofffluss begünstigen. Anhand von TEM-Untersuchungen wurde deutlich, dass die Korngrenzen keinerlei amorphe Filme oder andere Zwischenphasen enthalten.

In memory of my mother († 22nd / November / 1994)

and for my father

Preface

The presented thesis has been developed in the last 28 months during my work at the Institut für Physikalische Chemie und Elektrochemie of the Gottfried Wilhelm Leibniz Universität Hannover under the supervision of Prof. Dr. Jürgen Caro.
In this time, I have been a scientific co-worker benefiting from the project FE 928 1-1 of the Deutsche Forschungsgemeinschaft. This project was conducted by Dr. Armin Feldhoff and Prof. Dr. Haihui Wang.

Seven research articles are represented within this thesis. Five articles were written by myself, whereas in two others I am the second author. In the following, my contributions to these articles will be assigned. For all articles, I acknowledge helpful discussions as well as support to the manuscript preparation from my co-authors, particularly from Dr. Armin Feldhoff, Julia Martynczuk and Prof. Dr. Haihui Wang.
The first two articles comprehend the synthetic process and the stability of the perovskite-type oxide $(Ba_{0.5}Sr_{0.5})(Co_{0.8}Fe_{0.2})O_{3-\delta}$ (BSCF) and are presented in chapter 2. All experimental results and data interpretation were done by myself within the first article, *In situ Study of the Reaction Sequence in the Sol-Gel Synthesis of a $(Ba_{0.5}Sr_{0.5})(Co_{0.8}Fe_{0.2})O_{3-\delta}$ Perovskite by X-Ray Diffraction and Transmission Electron Microscopy*. The second article in this assembly, *Correlation of the formation and decomposition process of the BSCF perovskite at intermediate temperatures*, was also written by myself and I acknowledge the fruitful collaboration with Priv.-Doz. Dr. Thorsten Gesing on the X-ray refinements. He measured the presented X-ray diffraction patterns at the Institut für Mineralogie of the Gottfried Wilhelm Leibniz Universität Hannover, where the refinements and the elaborated results regarding the X-ray diffraction experiments in this article were done by him and me in equal shares. All other experiments and interpretation were carried out by myself.
In chapter 3, studies on the formation of the $(Ba_{0.5}Sr_{0.5})(Fe_{0.8}Zn_{0.2})O_{3-\delta}$ (BSFZ) perovskite-type oxide are summarized. Within this chapter, the first article *How $(Ba_{0.5}Sr_{0.5})(Fe_{0.8}Zn_{0.2})O_{3-\delta}$ and $(Ba_{0.5}Sr_{0.5})(Co_{0.8}Fe_{0.2})O_{3-\delta}$ Perovskites Form via an EDTA/Citric Acid Complexing Method* was written by my colleague Julia Martynczuk. I kindly acknowledge the cooperation with her on this publication. My contribution was to compare the initial stage of the reaction sequence of the BSFZ to that of BSCF in order to draw a more general conclusion of the formation process of perovskite-type oxides with similar stoichiometries. Additionally, I delivered support with the manuscript preparation.
Within the second article, *The sol-gel synthesis of perovskites by an EDTA/citrate*

complexing method involves nanoscale solid state reactions, sample preparation, experiments, and data interpretation regarding the transmission electron microscopy were conducted by Dr. Armin Feldhoff and me in similar shares. The Rietveld refinement of the BSFZ was conducted by Priv.-Doz. Dr. Thorsten Gesing and myself. Additionally, the investigation of the stuffed γ-tridymite-type structure as an intermediate reaction product and the related discussion in this article was done by me.

The article *Local Charge Disproportion in a High Performance Perovskite* in chapter 4, regarding the temperature dependent and site specific charge disproportion in BSCF, was elaborated together with Dr. Frans D. Tichelaar and Dr. Qiang Xu from the *National Centre for High Resolution Electron Microscopy* at the Technical University of Delft, the Netherlands. I acknowledge the excellent collaboration in acquiring the EELS data with their monochromised transmission electron microscope. Data processing and interpretation as well as manuscript preparation was fully conducted by myself.

The investigation of BSCF in poisoning CO_2 atmospheres and the preparation of the article, *Influence of CO_2 on the oxygen permeation performance and the microstructure of perovskite-type $(Ba_{0.5}Sr_{0.5})(Co_{0.8}Fe_{0.2})O_{3-\delta}$ membranes*, presented in chapter 5 was carried out entirely by myself at Prof. Dr. Haihui Wang's suggestion.

Membrane preparation, measurements of the oxygen permeation flux, and membrane characterisation by X-ray diffraction and transmission electron microscopy represented in the article, *Grain boundaries as barrier for oxygen transport in perovskite-type membranes*, in chapter 6 were conducted by Konstantin Efimov and me in equal shares.

I thank all other group members for accomplishing a nice working atmosphere.

All mechanical and electronical issues, which arose during my time in this institute did not turn into problems because of the great job done by the team of the mechanical workshop around Mr. Hartwin Bieder and done by Mr. Wolfgang Rogge, respectively.

As a matter of fact, writing down a doctoral thesis does also mean that nice people, who do not have anything to do with black powder or fast electrons, are also getting involved. For their patience, my largest thank goes to my father Stephan, Simone, Felix, Colin, Thomas, Jörg and my very good friends. Actually, they are my fundament.

Contents

1 Introduction

1.1 Mixed ionic and electronic conductors with perovskite structure for oxygen separation

1.1.1 General considerations

Dramatic increases in the worldwide energy consumption coupled with the environmental consequences of such increased consumption require more intelligent energy usage. Improvements of established industrial processes, as well the development of new techniques, are therefore necessary. Enhancements in the production of pure oxygen or oxygen-enriched air, which have applications in the partial oxidation of hydrocarbons, the synthesis of ammonia, the Claus-Process, and in the furnace production of iron (to name only a few), would have immediate beneficial consequences [1–7].

The most common methods for producing pure oxygen or oxygen-enriched air are either by using the liquefaction of ambient air (Linde-Process) or by using the pressure swing adsorption (PSA) [8]. These techniques are both energetically and capitally intensive. Alternatives methods, such as those using membrane technologies, are therefore desireable.

In view of prospective membrane processes, mixed ionic-electronic conducting (MIEC) oxide membranes, based on a perovskite structure, are under consideration for application in the industrial oxygen separating processes. Such membranes can provide infinite oxygen permselectivies[1] next to remarkable high oxygen fluxes, which meet the economic requirements [9]. Substitution of large scale cryogenic facilities by membrane technologies seems to be rather improbable. However, in the field of chemical processing, which includes the partial oxidation and oxidative dehydrogenation of lighter hydrocarbons, and the employment as cathode material in solid-oxide fuel cells (SOFCs), applications of perovskite membranes seem to be promising. One other new and technologically promising method, the Oxyfuel-process, might solve environmental problems with the exhaust emissions from coal burning power plants. During the Oxyfuel-process, coal is burned with a circulating mixture of fumes and pure oxygen. Product gases, such as water and carbon dioxide, can be easily precipitated from the exhaust mixture, thereby resulting in an exhaust free power plant. In the Oxycoal-AC-process, which is

---

[1]The term *permselectivity* refers to the ratio of two or more different species that move through a semipermeable membrane. Infinite *permselectivity* means that only one species can move through the membrane.

basically a modified Oxyfuel-process, the oxygen delivery is realised by a MIEC membrane. (see section 1.3.2 and [10,11]). Therefore, MIEC perovskite-type membranes have attracted much interest in the last two decades, and it is likely that MIEC perovskite-type membranes will find their way into the chemical process technology in the near future [1, 9, 12–14].

The number of reported MIECs based on the perovskite structure is difficult to survey, but in this large field, some materials have stood out and generated intense study due to their exceptionally high oxygen fluxes and/or because of their excellent phase stability. One of these famous materials is the $(Ba_{0.5}Sr_{0.5})(Co_{0.8}Fe_{0.2})O_{3-\delta}$ (denoted as BSCF) perovskite-type oxide, which exhibits one of the highest oxygen permeation fluxes reported so far for a perovskite membrane as well as an excellent phase stability over a wide temperature regime.[2] In the year 2000, the oxygen permeability as well as long-time phase stability of BSCF was first examined by Shao et al. [15] and subsequent research has demonstrated the importance of BSCF. Successful applications of BSCF in oxygen separation [15–18], in membrane reactors [13, 19–25], and as cathodes in SOFCs [14, 26–28] have been previously published. Despite the importance of BSCF in process applications, very little basic research into BSCF has been conducted. Hence, research into understanding of the formation process as well as of the long-time instability, which is strongly related to the local charge disproportion of the transition metal cations in these perovskites-type oxides, needs to be performed. Next to the long-time instability, the effect of CO_2 is an urgent issue that needs to be addressed since CO_2 is a co-product in the partial oxidation of lighter hydrocarbons, which is one major application of BSCF membranes.

Additionally, since BSCF membranes display ceramic properties and possess a polycrystalline microstructure, the impact of the grain size distribution on the oxygen permeation performance needs to be investigated since this directly relates to economical issues.[3]

To gain deeper knowledge about these topics, the presented thesis condenses the work from seven original research articles which focus on the solid state chemistry of BSCF.

In order to draw more universal conclusions, the $(Ba_{0.5}Sr_{0.5})(Fe_{0.8}Zn_{0.2})O_{3-\delta}$ (denoted as BSFZ) perovskite was also investigated with regards to the synthetic process as well as to the influence of grain size distributions on the oxygen permeation performance. BSFZ was recently synthesised [29, 30] to present an alternative to BSCF due to BSCF's poor long-time stability at intermediate temperatures. BSFZ is also under consideration for prospective industrial applications.

Chapters 2 and 3 present an extensive study on the synthetic processes for BSCF and BSFZ, and chapter 4 reports on the temperature dependent local charge disproportion in BSCF. In chapter 5 work into the CO_2 stability of BSCF membranes under oxygen permeation conditions is presented. Finally, chapter 6 summarizes the results of a study on the microstructure of BSCF and BSFZ membranes and its impact on the oxygen permeability.

---

[2]At this point, the term *phase stability* is in reference only to short times, i.e. several hours.

[3]It is expected that the microstructure has a huge impact on the oxygen permeability, which is directly connected to efficiency.

Topic / View	Synthetic process and phase stability	Local charge disproportion of B-site cations	Performance in CO_2-environments	Microstructure's effect on the oxygen permeability
integrative	- Identification of all intermediate phases (*In situ* XRD) - Structure refinement (*Rietveld, Le Bail*)	- Temperature dependent oxygen non-stoichiometry and determination of the average valence of B-site cations (*McIntosh et al.*)	- CO_2-dependent oxygen permeability (*Quantitative GC*) - Phase formation at exposed surfaces (*XRD*)	- Oxygen permeability (*Quantitative GC*) - Quantification of grain size distribution (*SEM*)
microscopic	- Examination of contact zones between partly reacted intermediate products (*HRTEM, EDXS, EELS*)	- Temperature dependent direct measurement of B-site cation valence using monochromised electrons (*HREELS, TU Delft*)	- Investigation of membrane decomposition after exposition in CO_2-atmospheres (*SEM, TEM, EDXS, EELS*)	- Study of grain boundary morphology (*HRTEM, EDXS, EELS*)

Figure 1.1: *Matrix of the methodical approach of the presented thesis.[5] (XRD $\equiv$ X-ray diffraction; TEM $\equiv$ transmission electron microscopy; EELS $\equiv$ electron energy-loss spectroscopy; SEM $\equiv$ scanning electron microscopy; EDXS $\equiv$ energy-dispersive X-ray spectroscopy.*

The main goal of the presented thesis is to correlate integrative observations (i.e. observations representing an average of the whole sample) with microscopic investigations for each topic. A matrix representing this methodical approach correlated with the above mentioned topics can be found in fig. 1.1.

1.1.2 Structure of perovskite-type oxides

Compounds with ABO_3 stoichiometry (A = rare earth, alkaline earth; B = transition metal; O = oxygen) tend to form perovskite-type oxides, whereas the crystal structure can be approximated by using Goldschmidt's tolerance factor, t, which is defined as the sum of the A-site cation's and the oxygen ion's radii divided by the radii sum of the B-site cation's and the oxygen ion's radii multiplied by $\sqrt{2}$ (which follows from the Pythagorean Theorem as illustrated in Fig. 1.2).

$$2 \times (r_A + r_O) = 2 \times \sqrt{2}(r_B + r_O) \tag{1.1}$$

$$\Rightarrow t \equiv \frac{r_A + r_O}{\sqrt{2}(r_B + r_O)} \tag{1.2}$$

If $t = 1$, the ideal cubic perovskite will be achieved as shown in Fig. 1.2.
An ideal undistorted cubic perovskite structure is relatively rare and realized in $SrFeO_3$ and $SrTiO_3$. Several deviations from that are possible. For the case that

---

[5]The domain coloured in light blue represents experiments that have not been carried out during this work.
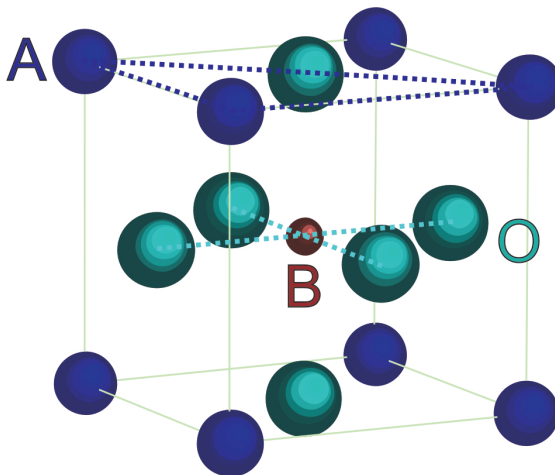
Figure 1.2: *Geometric construction of Goldschmidt's tolerance factor explained on the ideal cubic perovskite structure.*

the A-site cation has a small ionic radius, the tolerance factor decreases ($t < 1$), which results in rhombohedral or orthorhombic distortions of the formerly cubic structure. If the rare earth or alkaline earth is replaced by a transition metal and $t < 0.8$, the ilmenite structure will be realised in the ABO_3 compounds as is the case with the mineral ilmenite $FeTiO_3$. For $t > 1$, the hexagonal perovskite structure is found.

A convenient way to describe perovskite structures is to use the closest sphere packing. The cubic and the hexagonal perovskite structure can be regarded as hexagonally packed layers of A-site cations with oxygen ions (AO_3). While the stacking sequence of the (AO_3) layers is $ABCABCABC$ in cubic perovskites, the stacking sequence for hexagonal perovskites is $ABABABAB$. Consequently, the ideal cubic perovskite is based only on corner-sharing BO_6 octahedra, while the hexagonal perovskite is build from chains of face-sharing BO_6 octahedra. The ilmenite structure differs significantly from this building principle since only the oxygen ions form a hexagonally close-packed structure, in which two-thirds of the octahedral sites are occupied by both iron and titanium. Therefore, A-site and B-site are equivalent in the ilmenite structure, which directly reflects the similarity of A- and B-site cations in the ilmenite structure. Face- *and* edge-sharing $A(B)O_6$ octahedra result from this building principle [31–34].[6] Fig. 1.3 illustrates the three different perovskite structures, simplified as connected BO_6 octahedra in the cubic and the hexagonal perovskite structure and as connected $A(B)O_6$ octahedra in the ilmenite structure.

According to the ionic radii presented by Shannon, the tolerance factors are $t = 1.025$ for BSCF and $t = 1.002$ for BSFZ, where the weighted ionic radii from both cations of the B-site as well as for the A-site were calculated in order to determine the tolerance factor [35, 36].[7] Hence, cubic perovskite structures with $Pm\bar{3}m$ sym-

---

[6]The ilmenite structure can be also derived from the cubic perovskite structure in which the BO_6 are very strongly contorted in the direction of the room diagonale.

[7]Cobalt and iron were assumed to be in the $+3$ high spin state, and zinc was assumed to be in $+2$ oxidation state. For a detailed discussion, see sections 2.3 and 4.2.

ilmenite structure   **cubic perovskite structure**   **hexagonal perovskite structure**

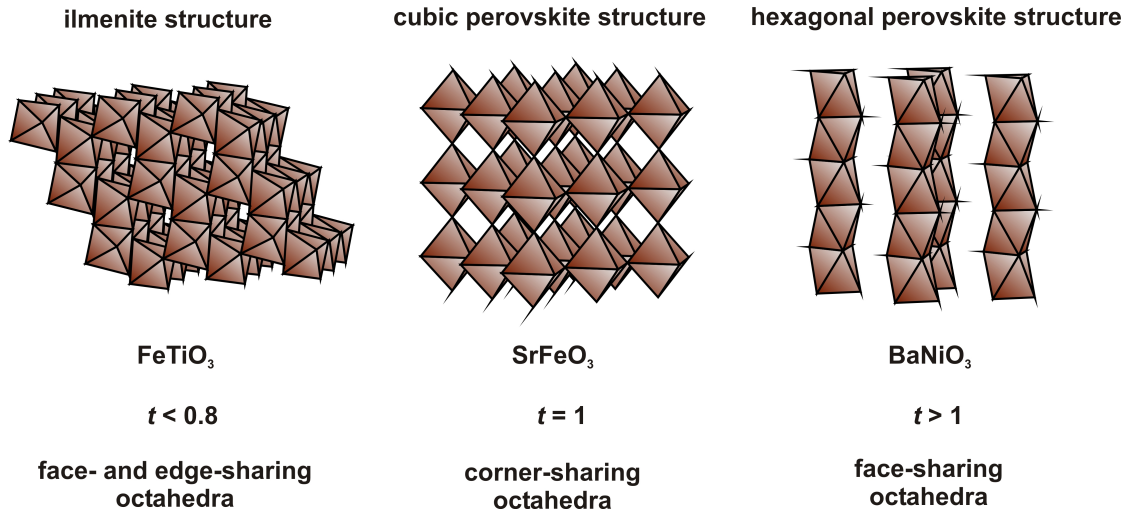| FeTiO$_3$	SrFeO$_3$	BaNiO$_3$
$t < 0.8$	$t = 1$	$t > 1$
face- and edge-sharing octahedra	corner-sharing octahedra	face-sharing octahedra

Figure 1.3: *Survey of different ABO$_3$ perovskite-type structures. Displayed are the BO$_6$ octahedra (in case of ilmenite: A(B)O$_6$). Among these three ideal approximations, several different distorted perovskite-type compounds have been reported.*

metry were found [37, 38]. However, this is only a simple approximation in order to provide an idea of which structure might be formed, and a very important issue has not been taken into account. By applying Goldschmidt's tolerance factor, only ionic bonding is consider important in these structures, which is generally not the case. Following Goodenough and co-workers [34], strong contributions of covalent bonding have to be considered, which will be discussed in the following section.

Another issue which has to be addressed in regards to deviations from the ideal perovskite structure is oxygen non-stoichiometry. It is well known that perovskite-type oxides tend to form oxygen vacancies in their crystal lattice. For example, the above mentioned ideal cubic perovskite structure SrFeO$_3$ should actually be written as SrFeO$_{3-\delta}$ with $3-\delta = 2.97$ in order to emphasise this non-stoichiometry. Depending on the synthetic conditions, the stoichiometry of oxygen can largely vary. For example, SrFeO$_{2.97}$ with a more or less stoichiometric amount of oxygen, can be successfully synthesised only under high oxygen pressures such as 500 atm [39, 40]. For BSCF, McIntosh et al. reported an oxygen stoichiometry of 2.48 at room temperature if the synthesis was carried out under ambient air conditions [37], where the oxygen non-stoichiometry is balanced through the valence of the B-site cation(s). In BSCF with stoichiometric oxygen, cobalt as well as iron should be in the +4 oxidation state. However, at room temperature the average B-site valence in BSCF is approximateley +2.7, according to McIntosh et al. [37], and, from work presented in section 4.2 of this thesis, cobalt and iron are in the +2.6 and the +3 oxidation states, respectively. The average valence on the B-site is therefore also +2.7. Under high temperature conditions (T $\approx$ 1200 K) and low oxygen partial pressures, the average valency of the B-site decreases actually down to +2.4 [37] and +2.3 (see section 4.2). Considering that at least 20 % of the oxygen positions remain vacant, the assumed octahedral coordination of the B-site cations by oxygen is only a rough approximation.

1.1.3 Electronical considerations

Basically, the complex bonding conditions and the electronic structure in solids can be described using two different concepts.

The first concept is based on the *molecular orbital theory* and is regarded as a chemical view of solids. In the molecular orbital theory, the isolated atoms are brought together to form a three dimensional array of atoms where, due to the strong overlap of the individual atomic orbitals, molecular orbitals are created. Within this atomic array, the molecular orbitals form bands, where the bandwidth is determined by the overlap integral (i.e. extent of the orbital overlap) of the molecular orbitals [31, 41, 42]. In metals where the coordination number is high, the overlap integral is large, thereby resulting in a large bandwidth. This results in a strong inter-band overlap, and hence, the electrons are mobile (also denoted as *delocalised or itinerant*) throughout the whole crystal, and large electronic conductivities are observed. Decrease in the overlap integral results in more separated bands, finally resulting in isolated atomic orbitals. It is obvious that smooth transitions between the two limits are possible; however, predictions of the electronic behaviour of solids are complex, particularly in case where several different kinds of atoms or ions are involved.

The second major concept is based on the *free electron gas theory* and provides a more physically motivated. In this approach, electrons are theoretically separated from the atomic nuclei and are treated as an electron gas described by the three dimensional Schrödinger equation for a free electron. Thus no interaction between the nucleus and the electron wave is considered. The effect of the atomic nuclei on the free electron waves can be included by introducing a potential term into the Schrödinger equation, which can be adjusted for a particular solid in order to describe the observed phenomena, for a detailed discussion see [43].

In the following discussion, the molecular orbital theory is used since it provides a more intuitive picture of the electronic structure in perovskites. According to Goodenough, the electronic structure of ABO_3 perovskites containing $3d$ block metals can be described in such a way that a bonding band with primarily oxygen $2p$ character is separated by a large energy gap of ≈ 6 eV from an antibonding band possessing cationic s and p character. These bands contribute very little to the physical properties of the solid. The antibonding $3d$ orbitals of the transition-metal parentage are located within the energy gap, and electrons within these orbitals can be either localised or delocalised [34, 44, 45]. It follows from crystal-field theory that under octahedral coordination, the five degenerated d-orbitals should split into three t_{2g}^*-orbitals and two e_g^*-orbitals that are separated by the crystal splitting energy. From symmetry considerations it follows further that the three t_{2g}^*-orbitals overlap with the nearest oxygen neighbours as well as with the nearest cation neighbours. The two e_g^*-orbitals overlap only with the neighbouring oxygen atoms. Depending on the overlap integrals, the t_{2g}^*- and e_g^*-orbitals might form bands, which can result in a narrow σ^*-band for the e_g^*-orbitals or in narrow σ^*- and π^*-bands for both kinds of orbitals. A scheme showing a simplified band structure as discussed above can be found in Fig. 1.4. It has to be emphasized at this point that the oxygen p-orbitals are hybridised with both the metal d- and the outer

metal s- and p-orbitals in the transition-metal oxides,[8] which has been extensively proven by electron energy-loss and X-ray absorption spectroscopy [46–55].
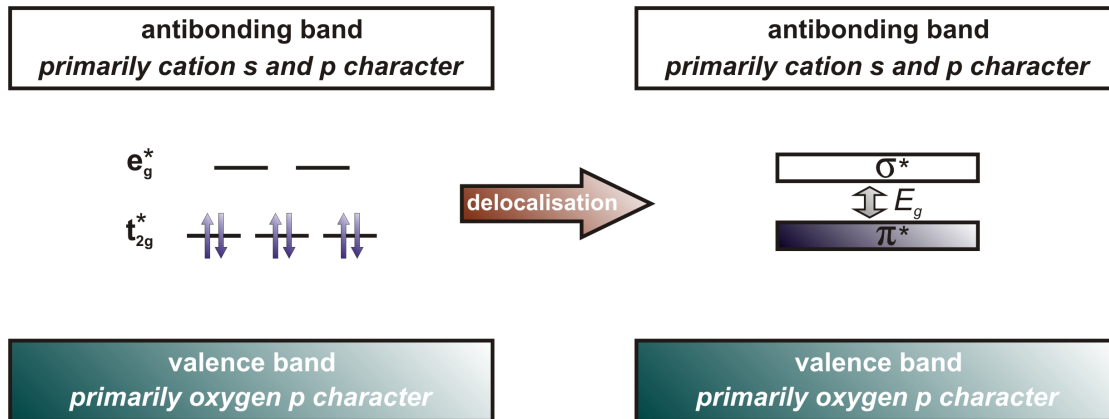
Figure 1.4: *The simplified band structure in perovskites with a B-site transition metal in d^6 (low-spin) configuration. The left part displays fully localised antibonding 3d-orbitals split by the octahedral ligand field, whereas the right part exhibits fully delocalised antibonding 3d-orbitals, i.e. σ^* and π^* bands. E_g is the energy band gap.*

This overlap also introduces an amount of covalency into this bonding, which reduces some charge from the metal cation and therefore leads to different ionic radii observed in these structures than reported by Shannon [35]. The transition *localised vs. itinerant* electrons is the key to understanding the electronic behaviour of perovskites and other transition metal oxides [34, 42, 44]. For BSCF, semiconductivity has been reported [18], which might be explained by the formation of a σ^*-band next to the t_{2g}^*-orbitals. Since the energy gap between the filled t_{2g}^*-orbitals and the σ^*-band is small ($\approx$ 1-2 eV), semiconductivity can be readily rationalised and is important, when discussing and observing mixed ionic-electronic conductivity in perovskite-type oxides.

1.2 Preparing perovskite-type membranes for oxygen separation

1.2.1 Raw perovskite powders

To prepare perovskite-type oxygen separating membranes, the desired perovskite-type oxides had to first be synthesised in a powder shape. Several methods are available for powder preparation, which can be classified into:

1. solid state reactions

2. liquid phase reactions

3. vapour phase reactions

---

[8]They also include the perovskite-type oxides.

In the particular case of BSCF and BSZF perovskite-type oxides, solid state reactions and liquid phase reactions are practical. In terms of the classical solid state method, powders from the educt phase(s) are first finely ground (or even ball milled) together and then heated to high temperatures for several hours or days. This method is also called the ceramic method and is widespread used in both industrial and laboratory settings [42, 56, 57]. Issues, which may arise by applying this method are discussed in the following. Basically, the formation of a product layer x in a solid state reaction between two ideally connected single crystals of A and B (as in Fig. 1.5) follows a parabolic growth law, where κ is the proportionality constant and t is the time [56, 58]:

$$x^2 = \kappa t \tag{1.3}$$

It has to be stressed that κ should not be confused with the Arrhenius rate constant of the homogeneous reactions, because κ includes not only kinetic parameters but also thermodynamic parameter relating to the driving force of the reaction. Eqn. 1.3 is only valid for the ideal case mentioned above and breaks down, if powder reactions, such as those used in the ceramic method, are applied. In order to describe powder reactions more exactly, eqn. 1.3 has to be adjusted. Jander [59] first derived an equation to take into account the spherical character of the reaction layer by simply converting the one-dimensional case of parabolic growth given in eqn. 1.3 to the three-dimensional case where α denotes the volume fraction which has already reacted, and r is the initial radius of the reacting particles:

$$\left[1 - (1 - \alpha)^{\frac{1}{3}}\right]^2 = \frac{\kappa t}{r^2} \tag{1.4}$$

This model can only provide a superficial estimation of the reaction kinetics due to the fact that the parabolic law for the thickness of the reaction product is only valid for the one-dimensional case and that any change of the molar volume between educt and product has been neglected [56]. These simplifications were later taken into account by Carter [60], who derived the Carter equation, where Z denotes the volume of the reaction product from the unit volume of the educt:

$$[1 + (Z - 1)\alpha]^{\frac{2}{3}} + (Z - 1)(1 - \alpha)^{\frac{2}{3}} = Z + (1 - Z)\frac{\kappa t}{r^2} \tag{1.5}$$

Despite the validity of eqn. 1.5 to describe the oxidation of nickel spheres, the creation of a more fundamental, analytical model to describe complex solid state reactions in such powders seems to be unrealistic because of both the complicated topological and inhomogeneous temperature distributions. However, even though a quantitative approach is difficult to develop, it follows from the above considerations that one very important parameter, the particle size, has to be decreased.[9] Short diffusion distances as well high concentrations of contact zones can be realized in that way.

Despite the common use of the ceramic method, two major disadvantages are obvious from the above discussion. First, particle sizes are comparably large (on

---

[9]Additionally, high temperatures and high defect concentrations promote the solid state reaction, but they will not be discussed here [57, 58].
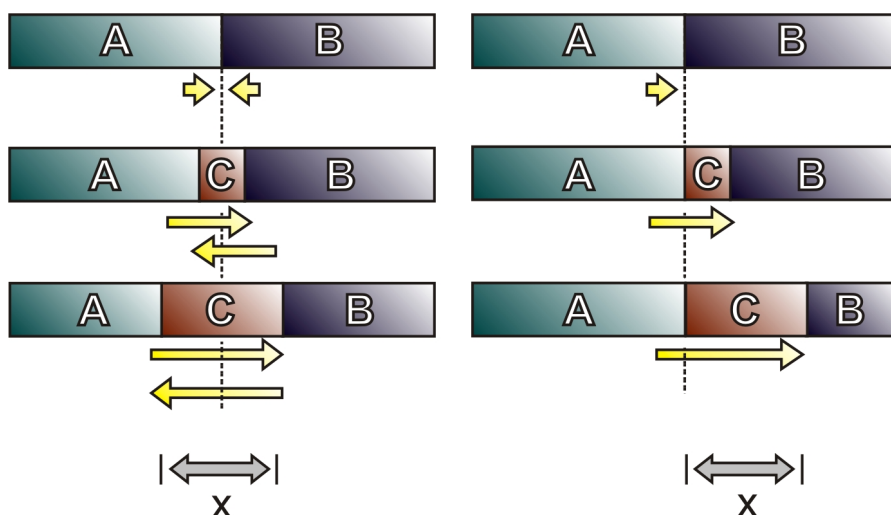
Figure 1.5: *Two possible mechanisms of solid state reactions. The reaction product can be either formed on the expense of both educts (left side), or on the expense of only one educt (right side). With increasing product concentration the diffusion pathway for the reactands increases in both cases.*

the micrometer scale) and therefore inappropriate under kinetic considerations. Second, local inhomogeneities of the educts might result in a stoichiometry of the product that varies across the sample.

In order to decrease the size of the reacting particles, liquid phase reactions, such as the sol-gel method, can be used. During these reactions, the educts (e.g. metal cations) are dissolved in a liquid (e.g., water), and then sol-forming additives (e.g., citric acid) are added to generate the sol. As the reaction progresses, the sol starts to gel, and finally the gel can be calcined (firing of the organics) to give the desired solid. Actually, during the calcination step also solid state reactions are involved, and the sizes of the reacting particles are commonly on the order of 30-50 nm. Fig. 1.6 shows both a high-angle annular dark-field micrograph of the gel obtained after stirring for 24 h at T = 423 K from the BSCF formation via the combined EDTA/citric acid sol-gel method and a Rietveld plot of the first crystalline products obtained after a calcination for 10 h at T = 923 K. The gel is characterized by a fine dispersion of metal complexes (high Z, bright contrast) in a polymerized organic network (low Z, grey contrast). The Rietveld analysis has proven, due to the determination of the crystallite sizes, the presence of the above mentioned nano-scaled solid state reactions. A mixed carbonate $(Ba_{0.5}Sr_{0.5})CO_3$ as well as a mixed spinel $(Fe_{0.6}Co_{0.4})Co_2O_4$ are the dominant phases present in this stage of the reaction. Thus, the sol-gel method provides an excellent method to produce finely dispersed powder particles, which can easily react to form the final solid [56, 61, 62]. Marcilly et al. first described the synthesis of perovskite-type oxides from stoichiometric metal nitrates using a citrate process [62]. Shao et al. further modified this method, by adding EDTA (*e*thylene-*d*iamine-*tetra*acetic acid) to the reaction in order to improve the dispersion of the metal cations [15]. This method was also applied during this work and extensively studied as presented in chapters 2 and 3. A flow chart representing the steps necessary to produce the
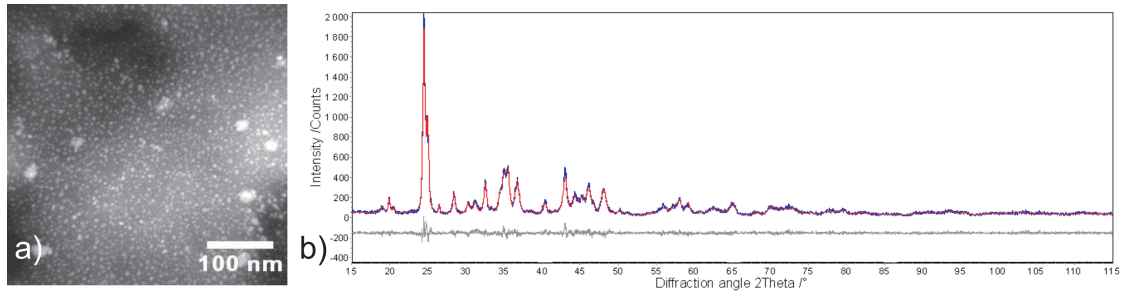
Figure 1.6: *Early stages of the BSCF formation via the combined EDTA/citric acid sol-gel method. a) High-angle annular dark-field micrograph of the gel obtained after stirring for 24 h at T = 423 K. b) Rietveld plot of the first crystalline products after calcination for 10 h at T = 923 K (The measured data (blue), together with the calculated data (red), and the difference between the observed and calculated data (grey) are given.*

products BSCF and BSFZ is shown in Fig. 1.7.

For the case where very small particles (on the nanometer scale) are used in the solid state reaction, the Carter-Equation (eqn. 1.5) for the formation of the product layer becomes even more unreliable since very thin product layers are formed during the reaction. A linear time law:

$$x \propto t \tag{1.6}$$

should be therefore applied, where t is the time and x is the product layer thickness [63–65]. It is clear from eqn. 1.6, that particles on the nanometer scale clearly promote the reaction rate, which now depends linearly on the time, compared to the parabolic growth law observed for large particles.
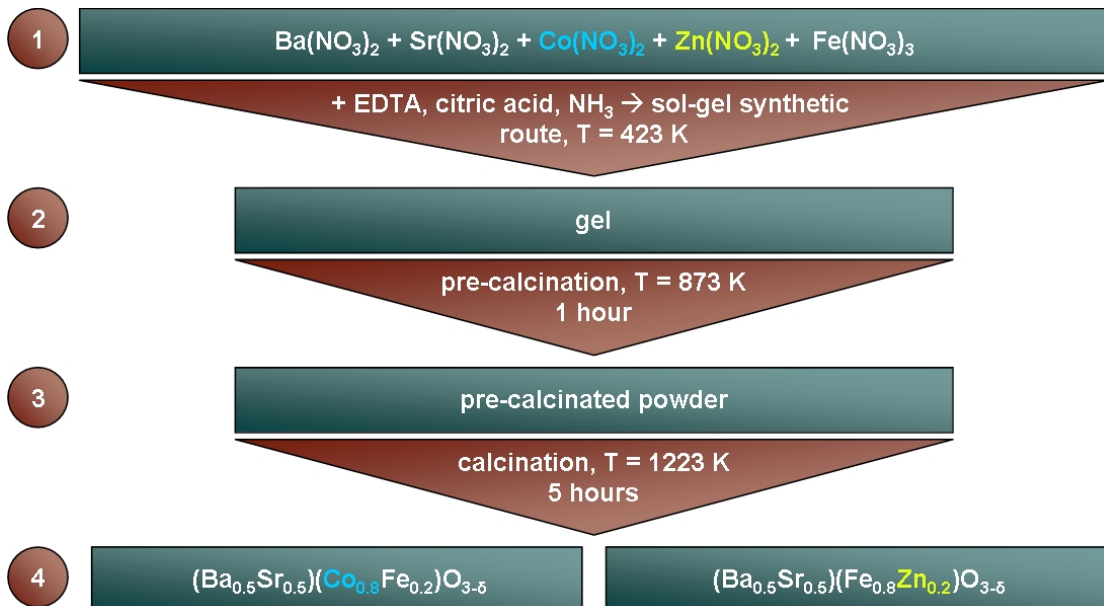
Figure 1.7: *The flow chart of the sol-gel synthetic route in order to the prepare the perovskite-type oxides BSCF and BSFZ.*

1.2.2 Perovskite ceramics – the sintering process

Once the raw perovskite powders have been synthesised, dense compacts (i.e. perovskite membranes) have to be prepared. First, the raw powders need to be consolidated (formed) into the desired shape. Several methods are available to prepare these green bodies [56], but in the present work, the BSCF and BSFZ powders were only uniaxially pressed to obtain green disc-shaped compacts. In order to obtain dense perovskite membranes, the green disc membranes were next pressurelessly sintered, e.g. T = 1423 K for 10 h.

Investigations into the sintering process are an important and even complex topic in material science, and only a short summary will be provided (for a more detailed discussion the reader is referred to common textbooks [56, 66]).

The driving force for the sintering process is the reduction of the free energy of the system, which can be accomplished by reducing the surface free energy of the consolidated particles and/or by applying pressure. Furthermore, a chemical reaction can also lead to sintering. In the following, only the effects of reducing the surface free energy will be discussed since the two other issues are not relevant to present work on the sintering of BSCF and BSFZ membranes.

Generally, the sintering process can be divided into three stages: initial, intermediate, and final stage.

Initial stage During the initial stage, particles can rearrange and the coordination number can increase. Grain boundaries are formed, and the large discrepancies between the surface curvatures are removed. Up to 65 % of the maximum density are achieved at this stage. The end of the initial stage is characterized by a pore equilibrium shape dictated by the surface and the grain boundary tension. Porosity is still continuous at this point of the sintering process. Reduction of the surface free energy can be accomplished by either *densification* (i.e., mass transport from the grain into the pore) or *coarsening* (i.e. rearrangement of matter, without transport from the grain into the pores). Densification and coarsening are often discussed in terms of competing mechanisms since coarsening reduces the driving force for the densification, which is the desired process. The theoretical steps that occur during the sintering process are illustrated in Fig. 1.8. Mechanism 1 (surface diffusion), mechanism 2 (lattice diffusion), and mechanism 3 (vapour transport) can only lead to coarsening and thereby decrease the driving force for densification. Mechanism 4 (grain boundary diffusion), mechanism 5 (lattice diffusion from the grain boundary), and mechanism 6 (plastic flow) can lead to densification.

Intermediate stage In the intermediate stage, a reduction in the pore cross-section is accomplished by steps 1, 4, 5 of Fig. 1.8, whereas only steps 4 and 5 can contribute to densification. Continuous porosity is replaced by isolated pores and the intermediate stage is taken to have ended when a density of 90 % is reached.

Final stage The final stage is characterised by the elimination of isolated pores and by the fact that grains start to grow at the expense of other grains. In the final stage, the density further increases up to 95 % - 98 % and coarse grains form.

Furthermore, pores potentially break from the grain boundaries into the grains, which is an undesired process since the pores are even more difficult to remove from the ceramic. In order to achieve high density ceramics, it is thus important to avoid the inclusion of pores into the grains. High density ceramics are therefore prepared starting with small particles and with relatively low heating rates during the sintering process in order to remove the pores from the solid before they are included into the grains [56, 66].

As will be discussed in section 1.3.3 and in chapter 6, oxygen transport through MIEC ceramic membranes is strongly affected by the ceramic's grain size distribution. In order to study whether the oxygen transport is affected by the microstructure, it is necessary to prepare ceramic membranes with different microstructures. For example, Wang et al. [17] and Diethelm et al. [67] reported that lowering the sintering time led to smaller grains, while longer sintering times led to relatively large grains.

Another way to influence the microstructure of the sintered ceramics is to use liquid phase sintering, which has been described in detail by Rahaman [56]. Liquid phase sintering is a widespread method which is used to achieve high density ceramics. Due to the introduction of a liquid phase during the sintering process, matter transport for densification as described above is facilitated. Two major liquid phase processes can be applied: *persistent liquid phase sintering* and *transient liquid phase sintering*. In persistent liquid phase sintering, the liquid additive remains in the ceramic, e.g. as a glassy solid, while in transient liquid phase sintering the liquid is completely removed. In chapter 6, the liquid phase sintering of BSCF and BSFZ ceramic membranes with boron nitride (BN) as a sintering aid is discussed with regards to controlling the grain size distribution of these ceramics with similar relative densities.
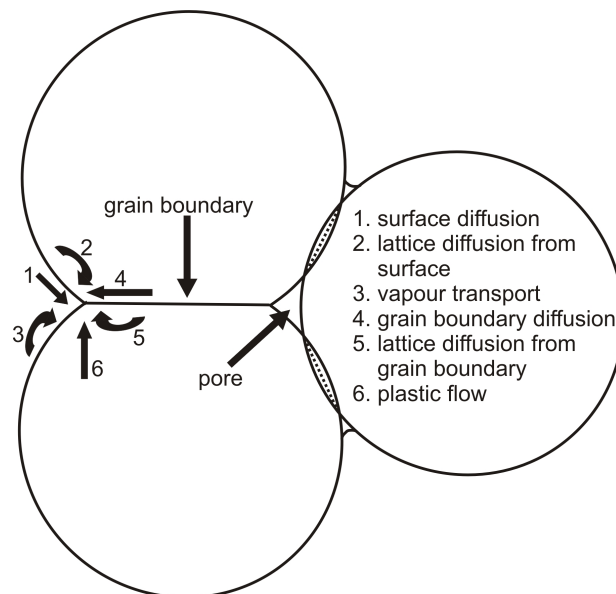

Figure 1.8: *Contributions to the sintering process. Mechanisms 1-3 lead to coarsening, mechanisms 4-6 lead to densification, while all influence the* **rate** *of densification. According to [56].*

1.3 Application of perovskite-type membranes

1.3.1 Oxygen permeation through MIEC membranes

1.3.1.1 Theoretical considerations

As described in section 1.1.1, membranes with a perovskite structure and MIEC are useful as oxygen separating membranes due to the high oxygen permeation fluxes accessible through these membranes as well as their infinite permselectivity. In order to achieve an oxygen permeation flux through the membrane, a gradient $\nabla\mu_{0_2}$ of the oxygen chemical potential has to be produced. Due to this gradient, oxygen is forced to travel from a higher oxygen chemical potential towards a lower oxygen chemical potential. The basic principle of this mechanism is described in Fig. 1.9.

The permeation process can be divided into three steps. First, an oxygen molecule is inserted into the perovskite lattice by reducing the oxygen molecules to form oxygen ions. Second, the oxygen ions move through perovskite membranes (by at least two distinct mechanisms as discussed in section 1.3.3 and chapter 6). Finally in the third step, the oxygen is removed from the perovskite membrane (the opposite of step 1). It follows from the presented scheme that two types of kinetics, bulk transport and surface exchange (assuming insertion and removal of oxygen are comparable) contribute to the whole process and have to be discussed separately.

Bulk Transport In order to describe the oxygen transport through the bulk of mixed conducting perovskites, a counteracting transport of oxygen ions and electrons due to charge compensation is assumed [9]. Following the idea of Wagner [68], the single particle flux of the charge carrier is proportional to the conductivity of each charge carrier as well as to the gradient of the electrochemical potential. Any formula for the oxygen flux through the membrane must include the electron flux, which is needed for charge balance. Strictly speaking, the oxygen flux through the membrane is dependent on both, the single particle flux of oxygen ions (ionic conductivity) and even on the single particle flux of the electrons (electronic conductivity). As derived by Wagner, eqn. 1.7 provides the dependence of the oxygen flux, j_{0_2}, upon on the electrical conductivity, σ_{el}, the ionic conductivity, σ_{ion}, and the oxygen chemical potential, $\nabla\mu_{O_2}$.

$$j_{0_2} \propto -\frac{\sigma_{el}\sigma_{ion}}{\sigma_{el} + \sigma_{ion}}\nabla\mu_{O_2} \tag{1.7}$$

For membrane applications, it is convenient to describe the oxygen chemical potential in terms of the oxygen partial pressure gradient across the membrane. Eqn. 1.7 then becomes the usual Wagner-Equation (1.8), where $p_{O_2}^p$ denotes the oxygen partial pressure of the low chemical potential side and $p_{O_2}^a$ denotes the oxygen partial pressure of the high chemical potential side, and L is the membrane thickness.

$$j_{0_2} \propto -\frac{1}{L}\int_{lnp_{O_2}^a}^{lnp_{O_2}^p}\frac{\sigma_{el}\sigma_{ion}}{\sigma_{el} + \sigma_{ion}}dlnp_{O_2} \tag{1.8}$$

According to Bouwmeester [69], the oxygen ionic conductivity is much lower compared to the electronic conductivity in perovskite-type oxides. Therefore, the oxygen ionic conduction is the rate limiting step, and eqn. 1.8 can be simplified as follows:

$$\dot{j}_{0_2} \propto -\frac{1}{L} \int_{lnp^a_{O_2}}^{lnp^p_{O_2}} \sigma_{ion} dlnp_{O_2} \qquad (1.9)$$

While discussing the influence of the ceramic membrane's microstructure on the oxygen permeability, it is therefore important to consider the influence of the microstructure on the oxygen ionic conductivity.
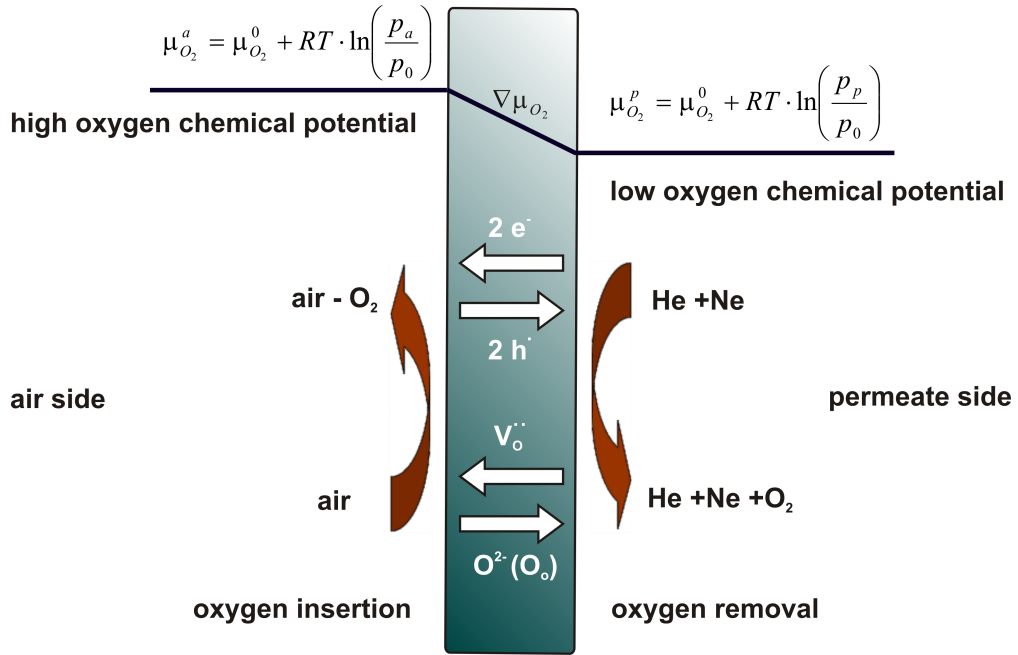
Figure 1.9: *The fundamental principle of oxygen permeation through dense perovskite membranes. Driving force is the gradient $\nabla\mu_{O_2}$ between the oxygen chemical potentials of the air side ($\mu^a_{O_2}$) and the permeate side ($\mu^p_{O_2}$), where $\mu^0_{O_2}$ denotes the standard potential, p_a the oxygen partial pressure on the air side, p_p the oxygen partial pressure on the permeate side, p_0 the standard pressure, $h^{'}$ the electron holes, and $V^{''}_O$ the oxygen ion vacancies.*

Surface Exchange   The oxygen surface exchange needs to be considered as a multi-step process which includes adsorption, oxygen reduction (charge transfer), surface diffusion of intermediate species, and the incorporation of oxygen into the perovskite lattice. Obviously, surface exchange is a complex process that includes several different parameters (for a detailed discussion the reader is referred to references [9, 58, 70] and the citations therein).
Therefore, two different processes, bulk transport and surface exchange, contribute to the oxygen permeation. Usually, the oxygen permeation flux is mainly dominated by the bulk transport, as long as the membrane thickness does not drop

below a critical value, which is referred to as the critical membrane thickness.
The above mentioned considerations are important in comparing permeation experiments. In order to be able to draw meaningful conclusions from experiments investigating the influence of the microstructure (such as those reported in chapter 6) the membrane thickness for each membrane studied needs to be of equal thickness for each membrane and to be higher than the critical membrane thickness in order to make the bulk transport the rate determining process.

1.3.1.2 Oxygen permeation experiments

As previously discussed, oxygen permeation across a perovskite membrane is realised by an ambipolar transport of oxygen ions and electrons through the perovskite lattice due to a gradient in the oxygen chemical potential (i.e. the oxygen partial pressure). Experimentally, oxygen permeation is commonly conducted using a setup as illustrated in Fig. 1.10 for the disc-shaped membranes used in the presented work.[10] The perovskite membrane was gas tight sealed (e.g., with gold paste) onto a hollow ceramic pipe, and synthetic air was flushed from the upper side (high oxygen chemical potential). A stream of noble gases was supplied from the lower membrane side (low oxygen chemical potential) in order to transport the permeated oxygen away from the membrane and thus to keep the gradient of the oxygen chemical potential across the membrane. Usually, permeation experiments are conducted in a temperature range from t= 1023 K to T = 1273 K. For a further description of such experiments, the reader is referred to reference [17] and chapters 5 and 6.

1.3.2 Membrane stability

1.3.2.1 Phase stability

When discussing the potential application of perovskite-type membranes in industrial processes, the long-time phase stability under different operating conditions must be considered. Under standard process conditions, membranes need to be stable under low oxygen partial pressures or even under reducing conditions as represented by the permeate side of the membrane (see Fig. 1.9). Additionally, the perovskite material must also be stable under relatively high oxygen partial pressures, which is the typical case on the air side of the membrane. Also, the temperature regime over which the perovskite material exhibits long-time phase stability must also be determined. For membrane reactor purposes, membranes should possess temperature stability between T = 1123 K and T = 1223 K [1, 13, 19, 21]. For applications of perovskites as a cathode material in intermediate temperature SOFCs (IT-SOFCs), the desired temperature regime is between T = 773 K and T = 873 K [4, 14].
For the BSCF perovskite-type oxide discussed in this work, excellent short-time phase stability under reducing and oxidising conditions has been reported accompanied by temperature stability over the whole temperature regime needed for use

---

[10]Other membrane geometries, such as hollow-fibre membranes are also frequently used.
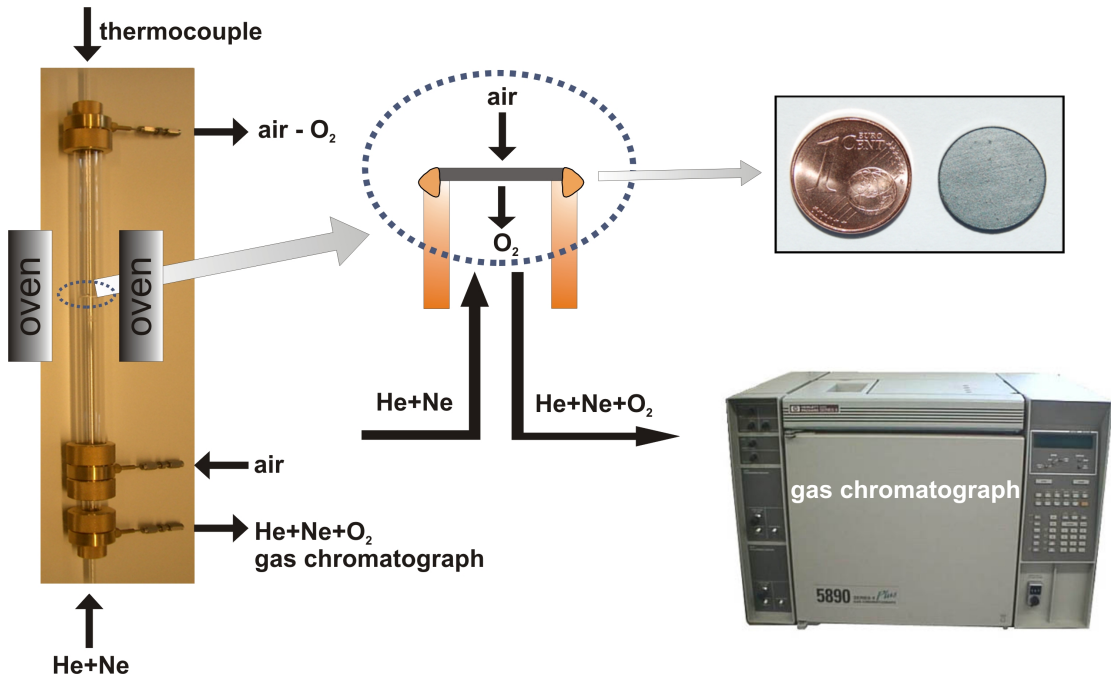
Figure 1.10: *Set up to measure the oxygen permeability of disc membranes with on-line gas chromatography. Left: Photograph of the high temperature oxygen permeation cell; middle: scheme of the membrane sealing and oxygen permeation through the membrane; right: photographs of disc membrane and gas chromatograph.*

in IT-SOFCs and for membrane reactor purposes [14, 37, 71]. However, it was also reported for BSCF, that long-time instability at temperatures below T = 1173 K is a serious issue. Shao et al. [15], Rebeilleau-Dassonneville et al. [23], and Švarcová et al. [72] described that if BSCF is kept either around or below 1123 K for several hours or days, a decomposition occurs which separates the former single cubic phase perovskite into a (at least) two phase mixture of a cubic and a hexagonal perovskite. Švarcová et al. proposed that the driving force for this phase decomposition was related to the pronounced oxidation of the B-site cations at intermediate temperatures, because oxidation of the perovskite at low temperatures led to a smaller effective ionic radius of the B-site cations. Therefore, the formation of the hexagonal perovskite structure is preferred, because of the smaller bonding distances between oxygen and the B-site cations in the hexagonal structure [32, 33, 72]. A detailed investigation of the driving force for this reaction and a differentiation between the cobalt and the iron site will be given in section 2.3.

1.3.2.2 Stability in harsh environments

Besides the intrinsic phase stability, the perovskite-type oxide's chemical stability against harsh environments must also be considered. For the case that the A-site cation of the perovskite-material is occupied by an alkaline earth, the chemical stability in a CO_2 atmosphere needs to be examined. During the partial oxidation, the produced CO further reacts to produce CO_2 according to the following the

scheme:

$$CH_4 + 1/2\, O_2 \rightarrow 2H_2 + CO \tag{1.10}$$

$$CO + 1/2\, O_2 \rightarrow CO_2 \tag{1.11}$$

Depending on the concentration, CO_2 can lead to membrane failures due to carbonate formation [13, 22]. Additionally, when applying ambient air in intermediate SOFCs, even very low CO_2 concentrations can negatively influence the cathode performance [26, 27] as carbonate formation of alkaline earth cations is pronounced at lower temperatures (see section 3.2). The oxygen separating membrane must withstand even higher CO_2 concentrations which are found during the Oxycoal-AC-process [11], which is basically a modified Oxyfuel-process as explained above [10]. The fundamental idea behind the Oxyfuel-process is the combustion of coal with a mixture of pure oxygen and CO_2. The exhaust gases consist then only of CO_2 and H_2O, which possess good properties in terms of easy precipitation. The Oxycoal-AC-process is different from the Oxyfuel-process in that the pure oxygen is delivered via MIECs membranes and not via the liquefaction of air. In this case, the MIEC membranes face very high CO_2 concentrations up to 80% [1]. Therefore, the effect of CO_2 on both the oxygen permeation performance and the microstructure of the perovskite-type membrane needs to be investigated, particularly if the perovskite contains alkaline earths cations. Several groups have already reported on the impact of CO_2 on alkaline earth containing perovskite membranes [73–77]. In this work, the impact of CO_2 on the oxygen permeability and the microstructure of BSCF membranes was systematically studied, and the results are presented in chapter 5.

1.3.3 Influence of the microstructure on the oxygen permeability

Perovskite-type membranes for oxygen separation are ceramics and therefore consist of a large number of single crystals connected by grain boundaries. Therefore, the oxygen transport through the bulk has to be separated into either lattice diffusion (i.e., diffusion of oxygen in the perovskite lattice) or as oxygen transport across the grain boundaries as sketched in Fig. 1.11. Whether the oxygen transport through the grain boundary affects the oxygen in a positive way (i.e., in terms of a higher oxygen flux) or negatively needs to be answered. Unfortunately, both scenarios have been reported in the literature. Materials exhibiting either a blocking effect [17, 78–85] or exhibiting a faster diffusion pathway [67, 86] for the ionic transport due to the grain boundaries have been reported and no general conclusion can be drawn for the effects of grain boundaries on the electrical conductivity in ceramics.[11]

The fundamental work of Maier and co-workers delivers a possible explanation for the blocking effect of the grain boundaries. Assuming an atomically thin grain boundary between two grains, i.e. no amorphous or other interfacial phase are present, a space-charge layer is produced on the grain boundary due to its structural singularity [58].

---

[11]The term *electrical* comprehends both the ionic and the electronic conductivity.
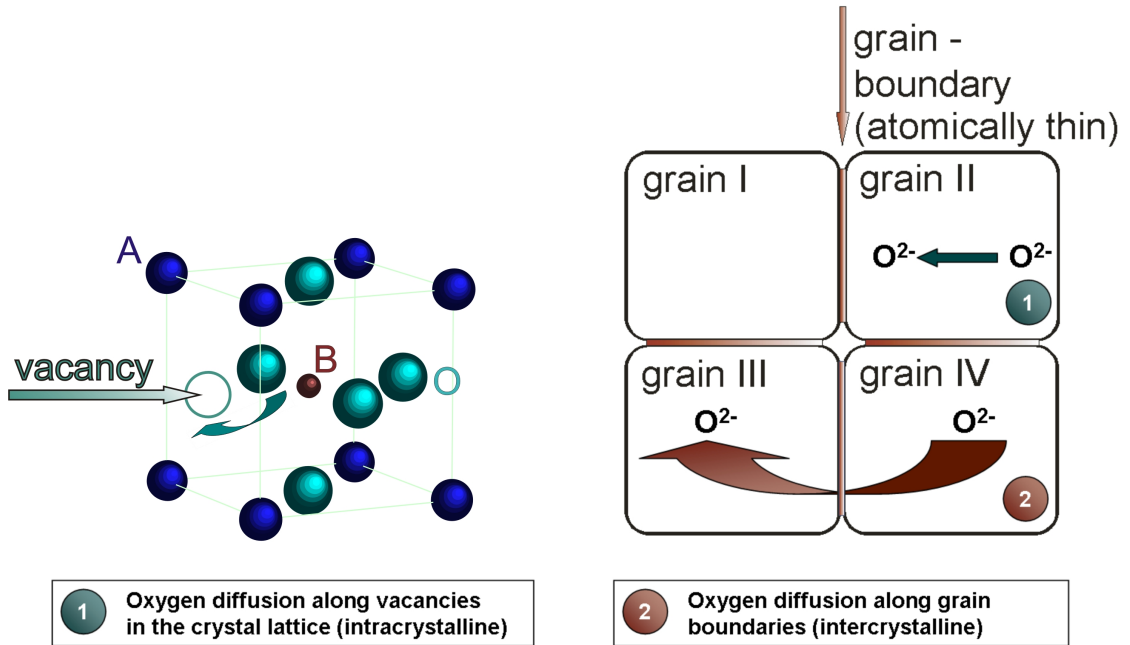
Figure 1.11: *Intracrystalline oxygen ion transport via the oxygen vacancies as well as intercrystalline oxygen ion transport via grain boundaries.*

The grain boundary displays a sink for charge carriers, which are therefore stuffed in front of the grain boundary. Hence, these space-charge layers display depletion layers of oxygen vacancies and electron holes, which results in lower transport coefficients at this particular site [79, 81, 87, 88]. In the case of an oxygen permeation experiment, the lower mobility of the oxygen ions (and the electrons) on the grain boundary leads to a further increase of the space-charge layer, and the grain boundary blocks the oxygen ion transport. If the space-charge layer influence significantly the charge carrier transport, a lower oxygen permeability through membranes containing small grains (i.e. higher concentration of grain boundaries) will be found, which is reported in chapter 6 for the materials under investigation.

2 Formation and phase stability of $(Ba_{0.5}Sr_{0.5})(Co_{0.8}Fe_{0.2})O_{3-\delta}$

2.1 Summary

This chapter comprehends two original research articles dealing with the formation of the $(Ba_{0.5}Sr_{0.5})(Co_{0.8}Fe_{0.2})O_{3-\delta}$ (BSCF) perovskite-type oxide. Intensive X-ray diffraction (XRD) investigations, including *in situ* experiments and Rietveld/Le Bail methods were applied to draw a detailed picture of the BSCF formation via the sol-gel synthetic route. Analytical transmission electron microscopy (ATEM) was further used to identify the stoichiometry of the reacting particles and to elucidate the solid state reactions on the nanometer scale. For that purpose, the reaction sequence was interrupted at different stages in order to obtain the individual reactants for XRD and ATEM. *In situ* X-ray diffraction was used to confirm that the intermediate products are indeed formed within the reaction sequence and that they are not simply due to quenching effects. First crystalline products are formed around 873 K and they were identified to be a mixed carbonate $(Ba_{0.5}Sr_{0.5})CO_{3-\delta}$ in aragonite modification as well as a mixed oxide $(Fe_{0.6}Co_{0.4})Co_2O_4$ in spinel modification.[1] No indication for additional phases is present, as verified by Rietveld analysis. Increasing the reaction temperature between T = 923 K and T = 973 K led to the formation of two different perovskite-type oxides. One was identified to be a $(Ba_{0.75}Sr_{0.25})CoO_{3-\delta}$ hexagonal perovskite and the second to be a $(Ba_{0.25}Sr_{0.75})(Co_{0.6}Fe_{0.4})O_{3-\delta}$ cubic perovskite with relatively small lattice constant. The reaction towards the final cubic perovskite $(Ba_{0.5}Sr_{0.5})(Co_{0.8}Fe_{0.2})O_{3-\delta}$ was found to occur at the expense of both the hexagonal and the small cubic perovskite. While the formation of BSCF at the expense of the small cubic perovskite is simply due to increasing of the lattice constant, the formation at the expense of the hexagonal occurs via the formation of a monoclinic superstructure.[2] This reaction sequence was attributed to the preferred electronic low-spin configuration of Co^{3+} ions in octahedral oxygen environments compared to Fe^{3+}, which is preferably in the high-spin state. Large differences in the effective ionic radii are the consequence. The phase pure, final perovskite structure was only obtained at temperatures as high as T = 1173 K. The last step of the synthetic process was found to be reversible and the presented results directly relate to the important issue of the BSCF's long-time instability at intermediate temperatures.

---

[1] The stoichiometry claims no site attribution of iron an cobalt.

[2] In the first article 2.2 the monoclinic cell was misleadingly determined as a tetragonal cell.

2.2 *In Situ* Study of the Reaction Sequence in the Sol-Gel Synthesis of a $(Ba_{0.5}Sr_{0.5})(Co_{0.8}Fe_{0.2})O_{3-\delta}$ Perovskite by X-Ray Diffraction and Transmission Electron Microscopy

Mirko Arnold, Haihui Wang, Julia Martynczuk, Armin Feldhoff

Journal

In Situ Study of the Reaction Sequence in the Sol–Gel Synthesis of a $(Ba_{0.5}Sr_{0.5})(Co_{0.8}Fe_{0.2})O_{3-\delta}$ Perovskite by X-Ray Diffraction and Transmission Electron Microscopy

Mirko Arnold,[†,‡] Haihui Wang,[‡,§] Julia Martynczuk,[‡] and Armin Feldhoff[‡]

[‡]Institute of Physical Chemistry and Electrochemistry, Leibniz Universität Hannover, D-30167 Hannover, Germany

[§]College of Chemical and Energy Engineering, South China University of Technology, Guangzhou 510640, China

Examination of the complexing citric acid/EDTA synthesis of $(Ba_{0.5}Sr_{0.5})(Co_{0.8}Fe_{0.2})O_{3-\delta}$ is presented by *in situ* X-ray diffraction and transmission electron microscopy, which elucidate all intermediate phases and the formation of the perovskite structure for the first time.

I. Introduction

MIXED ionic-electronic conductors (MIECs) with a perovskite structure are of considerable interest for many industrial processes because they allow the supply or removal of oxygen to or from reaction mixtures with infinite selectivity and high oxygen fluxes. Thus, many applications of MIECs have already been reported, e.g. as cathode material in solid-oxide fuel cells as well as in the production of oxygen-enriched air and in the conversion of hydrocarbons to synthesis gas.[1–3]

Particularly, membranes of the $(Ba_{0.5}Sr_{0.5})(Co_{0.8}Fe_{0.2})O_{3-\delta}$ (BSCF) type are regarded as state-of-the-art materials in view of their high oxygen permeation performance. Although many reports on this material are already available, a fundamental understanding of the synthesis process and thus the perovskite formation is still lacking. Additionally, investigation of this process is also believed to provide a clarification of the decomposition reaction that takes place in long-term oxygen permeation experiments in membranes of the BSCF material. Already in the year 2000, the decomposition of BSCF into $BaCoO_2$ and $Sr(Co_{0.6}Fe_{0.4})O_{3-\delta}$ was postulated but only due to X-ray diffraction (XRD) measurements of permeated membranes.[4] The appearance of similar additional reflections was described in 2005 in a temperature-programmed XRD pattern of BSCF particularly when the temperature was set below 700°C for 12 h. But no phase attribution was given there.[5]

Because a real understanding of the BSCF formation and decomposition does not exist, we present a detailed study of the synthesis process of BSCF by *in situ* XRD as well as by transmission electron microscopy (TEM) experiments.
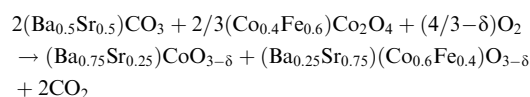
II. Experimental Procedures

The synthesis of BSCF was conducted via a sol–gel route as reported by Shao *et al.*[4] An aqueous solution containing stoichiometric amounts of the metal nitrates, citric acid, EDTA, and ammonia was stirred at 150°C until a purple-colored gel was obtained. The gel was precalcined at 600°C for 1 h in order to obtain the first crystalline products. XRD measurements were taken with steps of 20 and 25 K, respectively, in order to achieve a high resolution within the temperature dependence. Before each data acquisition, an equilibrium time of 1 h was set. Synthetic air was used as the atmosphere within the chamber. Moreover, an *ex situ* XRD study has been conducted in order to confirm *in situ* XRD measurements, to exclude changes in the unit cell dimensions simply due to heating, and as a reference to calculate unit cell parameters. TEM experiments were performed with a powder sample, which was preliminarily heated to 700°C for 1 h, quenched to room temperature, and then glued between silicon single crystals, polished, and finally Ar^+ sputtered to electron transparency.

III. Results and Discussion

Figure 1 shows the temperature-dependent XRD pattern of the reaction mixture between 400° and 950°C. Up to 600°C, the reaction mixture consists only of aragonite-type $(Ba_{0.5}Sr_{0.5})CO_3$ as well as $(Co_{0.4}Fe_{0.6})Co_2O_{3-\delta}$ with spinel modification.[6,7] At 600°C, two other phases start to form because additional reflections at 26.5°, 32.3°, and 42.5° emerge in the XRD pattern. These reflections are related to a cubic phase with a perovskite structure (perovskite I) and an additional second phase, which is attributed to $(Ba_{0.75}Sr_{0.25})CoO_{3-\delta}$ (hexagonal). In 1977, Taguchi *et al.* reported on a structure of $BaCoO_3$ that showed almost the same diffraction pattern as the hexagonal phase found here.[8] Therefore, the formation of a similar phase during the process reported here can be assumed. A detailed calculation of the cell dimensions shows a cell parameter for the initially formed cubic perovskite phase (perovskite I) that is smaller than that expected for BSCF.[9] Therefore, we postulate a strontium-enriched perovskite phase, namely $(Ba_{0.25}Sr_{0.75})(Co_{0.6}Fe_{0.4})O_3$. Further proof for this supposition lies in the systematic shift of the reflections that are related to the hexagonal phase (hexagonal) toward greater angles, indicating a smaller unit cell based on $(Ba_{0.75}Sr_{0.25})CoO_3$. This has been proved by the synthesis of several compositions within the system $(Ba_{1-x}Sr_x)CoO_{3-\delta}$.

Thus, the reaction of the first crystalline phases can be described as follows:

$$2(Ba_{0.5}Sr_{0.5})CO_3 + 2/3(Co_{0.4}Fe_{0.6})Co_2O_4 + (4/3-\delta)O_2$$
$$\rightarrow (Ba_{0.75}Sr_{0.25})CoO_{3-\delta} + (Ba_{0.25}Sr_{0.75})(Co_{0.6}Fe_{0.4})O_{3-\delta}$$
$$+ 2CO_2$$

On increasing the temperature, one observes a continuous increase of the cell parameter of the perovskite structure (perovskite I) until it reaches the maximum shift at 950°C. This can be concluded as the reflection related to the (110) plane that shifts toward lower angles (see Fig. 1). While the unit cell of the
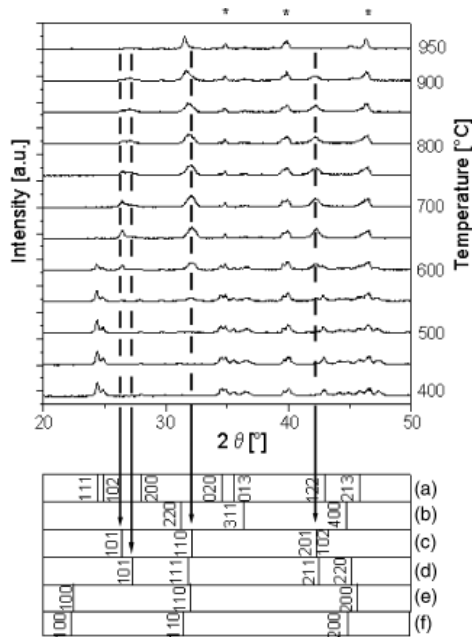
Fig. 1. *In situ* powder X-ray diffraction pattern at different temperatures of the synthesis process of $(Ba_{0.5}Sr_{0.5})(Co_{0.8}Fe_{0.2})O_{3-\delta}$. Reflections marked with an asterix are related to the sample holder (Pt–Rh alloy).
(a) $(Ba_{0.5}Sr_{0.5})CO_3$ (aragonite structure)
(b) $(Fe_{0.6}Co_{0.4})Co_2O_4$ (spinel structure)
(c) $(Ba_{0.75}Sr_{0.25})CoO_{3-\delta}$ (hexagonal) (*h*)
(d) $(Ba_{0.6}Sr_{0.4})(Co_{0.8}Fe_{0.2})O_{3-\delta}$ (tetragonal) (*t*)
(e) $(Ba_{0.25}Sr_{0.75})(Co_{0.6}Fe_{0.4})O_{3-\delta}$ (perovskite I) (*c*)
(f) $(Ba_{0.5}Sr_{0.5})(Co_{0.8}Fe_{0.2})O_{3-\delta}$ (perovskite II) (*c*).

perovskite structure increases, a systematic change in the hexagonal structure occurs. From the XRD pattern, it can be seen that the reflection related to the (101) plane of the hexagonal phase shifts toward higher angles. A detailed examination of

ex situ XRD measurements further indicates that this shift is not simply due to a further increase of the hexagonal unit cell as reflections related to planes (110) and (201) are shifted differently, which indicates the formation of a different structure. We believe that the change in the hexagonal phase (hexagonal) is due to the intake of strontium and iron ions caused by a gradient in the chemical potentials. This seems to be a logical step due to the incorporation of barium ions into the cubic phase and the cobalt-enriched hexagonal phase. *Ex situ* XRD patterns indicate a phase transformation toward a tetragonal unit cell (tetragonal), with cell parameters $a = 5.63$ Å and $c = 4.01$ Å, which is in good agreement with the findings of Yoshiya *et al.* in 2004.[9] They applied the first principles method to calculate the free energies within the system $Ba(Co_{1-y}Fe_y)O_{3-\delta}$. It has emerged that increasing the iron content lowers the transition temperature from the hexagonal to the above-mentioned tetragonal phase. This tetragonal phase can be regarded as a distorted cubic perovskite structure. The unit cell contains two formula units and reflects a nonideal arrangement of the BO_6 octahedra resulting in a tetragonal structure.

In order to support the XRD findings, TEM experiments were conducted to analyze the microstructural arrangement during the synthesis. Figure 2 shows an STEM bright-field micrograph and corresponding HRTEM micrographs of two grain contacts (Figs. 2(b) and (c)). Quantitative energy-dispersive X-ray analysis (EDXS) of the elemental distribution shows that the selected grain contacts are located between the cubic $(Ba_{0.25}Sr_{0.75})(Co_{0.6}Fe_{0.4})O_3$ and the hexagonal $(Ba_{0.75}Sr_{0.25})CoO_3$. The elemental distributions by EDXS of the cations are displayed in Fig. 3. Figures 4 and 5 present the grain contacts as in Figs. 2(b) and (c) but at higher magnifications. The related diffraction information was created via fast Fourier transformation of the HRTEM micrographs. The first grain contact (Fig. 4) is identified to be between a grain with a perovskite structure (perovskite I) and a grain with a hexagonal structure (hexagonal).

The combination of the diffraction information given by the HRTEM with the elemental distribution of these two grains underlines the XRD findings that indicated the coexistence of a perovskite phase with a comparable high strontium amount and a hexagonal structure with a high barium amount. The second
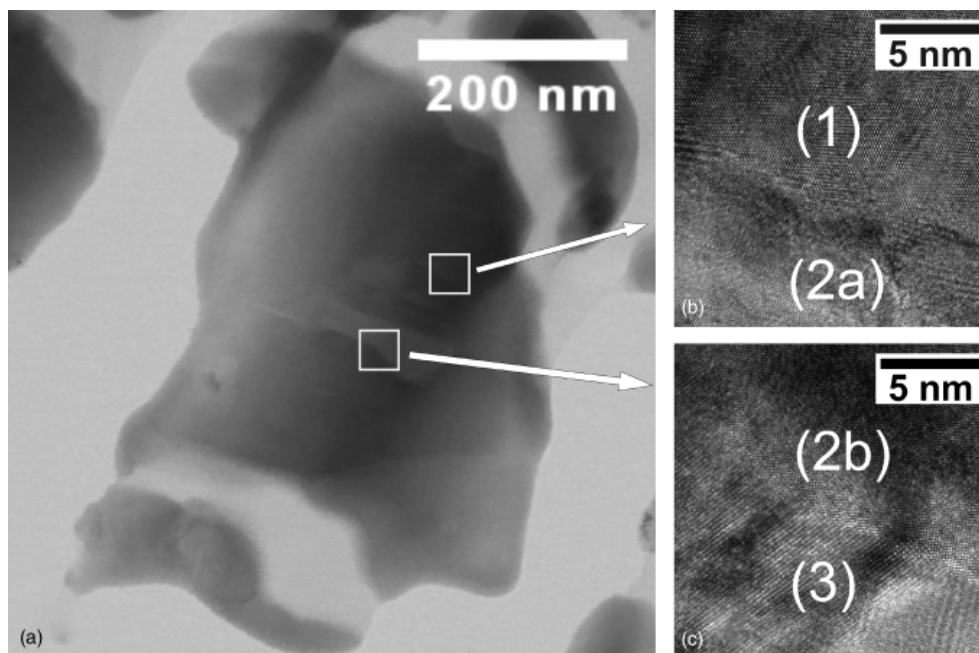

Fig. 2. STEM bright-field micrograph showing a particle containing the intermediate phases during the synthesis process (a). HRTEM micrograph of grain contact between hexagonal (1) and perovskite phases (2a) (b). HRTEM micrograph of grain contact between perovskite (2b) and tetragonal phase (3). The sample was heated for 1 h at 700°C, followed by quenching to room temperature.
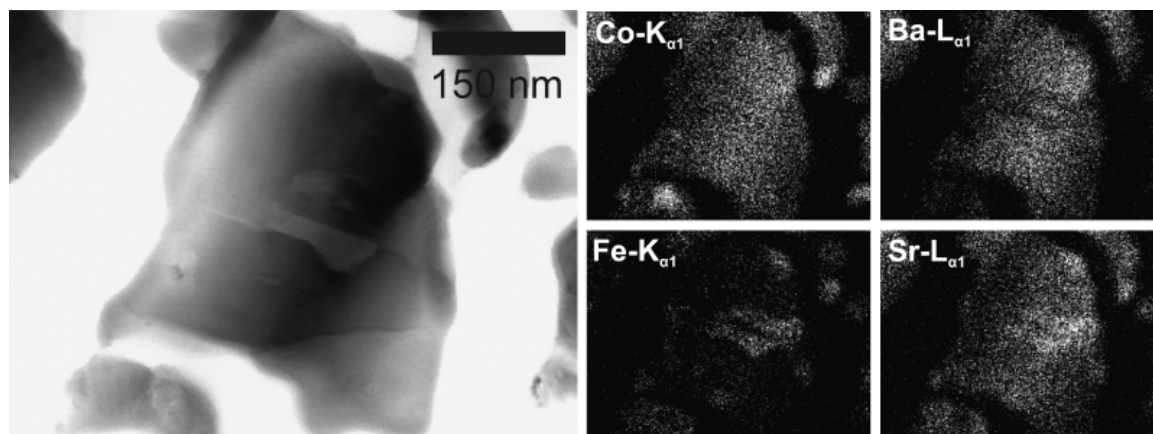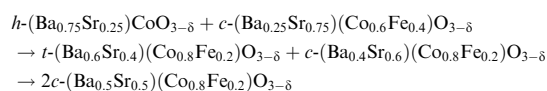
Fig. 3. STEM bright-field micrograph and elemental distributions by energy-dispersive X-ray analysis of the particle in Fig 2. The white contrast in the maps corresponds to high elemental concentrations. The sample was heated for 1 h at 700°C, followed by quenching to room temperature.

contact (Fig. 5) even exhibits the contact zone between two grains with the above-mentioned stoichiometries. Contrary to the above-described contact between the perovskite and hexagonal phases, the contact in Fig. 5 is identified to separate a grain with tetragonal modification and a second grain with perovskite. As mentioned above, a phase transition of the hexagonal to a tetragonal modification is observed. Thus, this particular grain contact exhibits a contact zone between a former hexagonal phase in which the postulated phase transition to the tetragonal modification has taken place. A closer look at the diffraction data shows that these grains are not randomly oriented but have parallel zone axes as $[1,0,0]_c \| [1,1,1]_t$ and parallel planes as $(-1,1,0)_c \| (0,1,0)_t$. This finding gives rise to the assumption that a reaction has occurred between these two grains and is underlining the fact that during uptake of strontium and iron ions into the hexagonal structure, a phase transition to a tetragonal structure occurs.

When the temperature was increased further, reflections for perovskite I shifted to lower angles (larger unit cell), which is due to the further uptake of barium ions. Additionally, the reflection for plane (101) of the tetragonal phase diminished, which was clearly due to an increase of symmetry, and ended up in a cubic perovskite structure. Thus, the first reaction is followed by transformation of the hexagonal into the tetragonal phase and the final formation of the perovskite; while the reaction process is a dynamic rather than a static process, the stoichiometry of the reactants vary within a certain tolerance.

$$h\text{-}(Ba_{0.75}Sr_{0.25})CoO_{3-\delta} + c\text{-}(Ba_{0.25}Sr_{0.75})(Co_{0.6}Fe_{0.4})O_{3-\delta}$$
$$\rightarrow t\text{-}(Ba_{0.6}Sr_{0.4})(Co_{0.8}Fe_{0.2})O_{3-\delta} + c\text{-}(Ba_{0.4}Sr_{0.6})(Co_{0.8}Fe_{0.2})O_{3-\delta}$$
$$\rightarrow 2c\text{-}(Ba_{0.5}Sr_{0.5})(Co_{0.8}Fe_{0.2})O_{3-\delta}$$

It has to be emphasized that the formation of the final cubic BSCF perovskite (perovskite II) takes place in both the tetragonal (former hexagonal) lattice and the cubic perovskite system (perovskite I) with a smaller unit cell. If the BSCF structure would only grow at the expense of the cubic phase by incorporation of barium ions, one would expect a simple diminution of the hexagonal barium-rich phase. As shown, in fact, a phase

Fig. 4. HRTEM micrograph of the grain contact shown in Fig. 2(b) (a). Diffraction data via fast Fourier-transformation from selected areas (b, c).
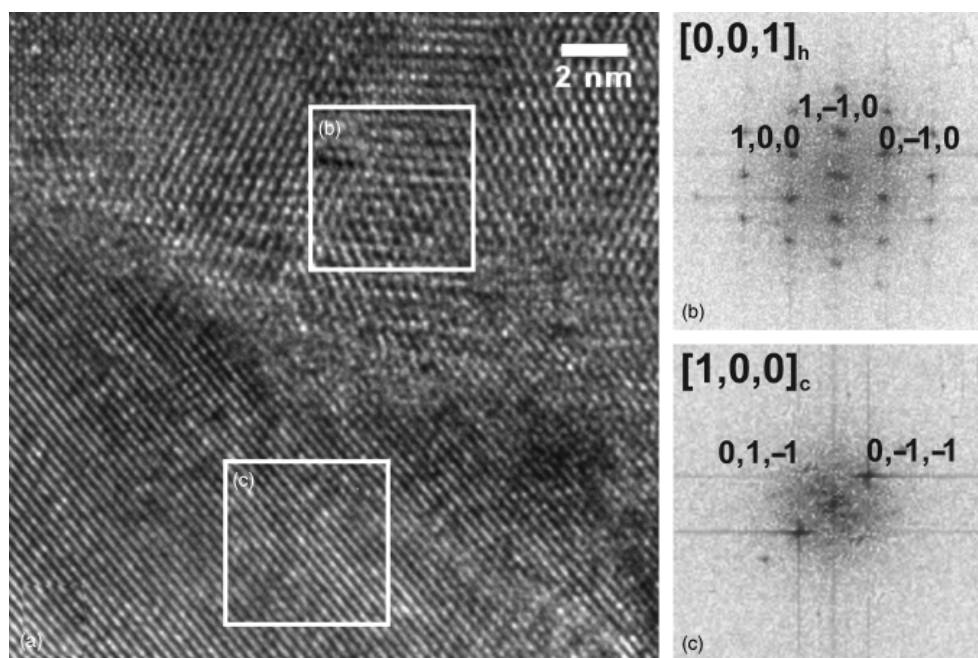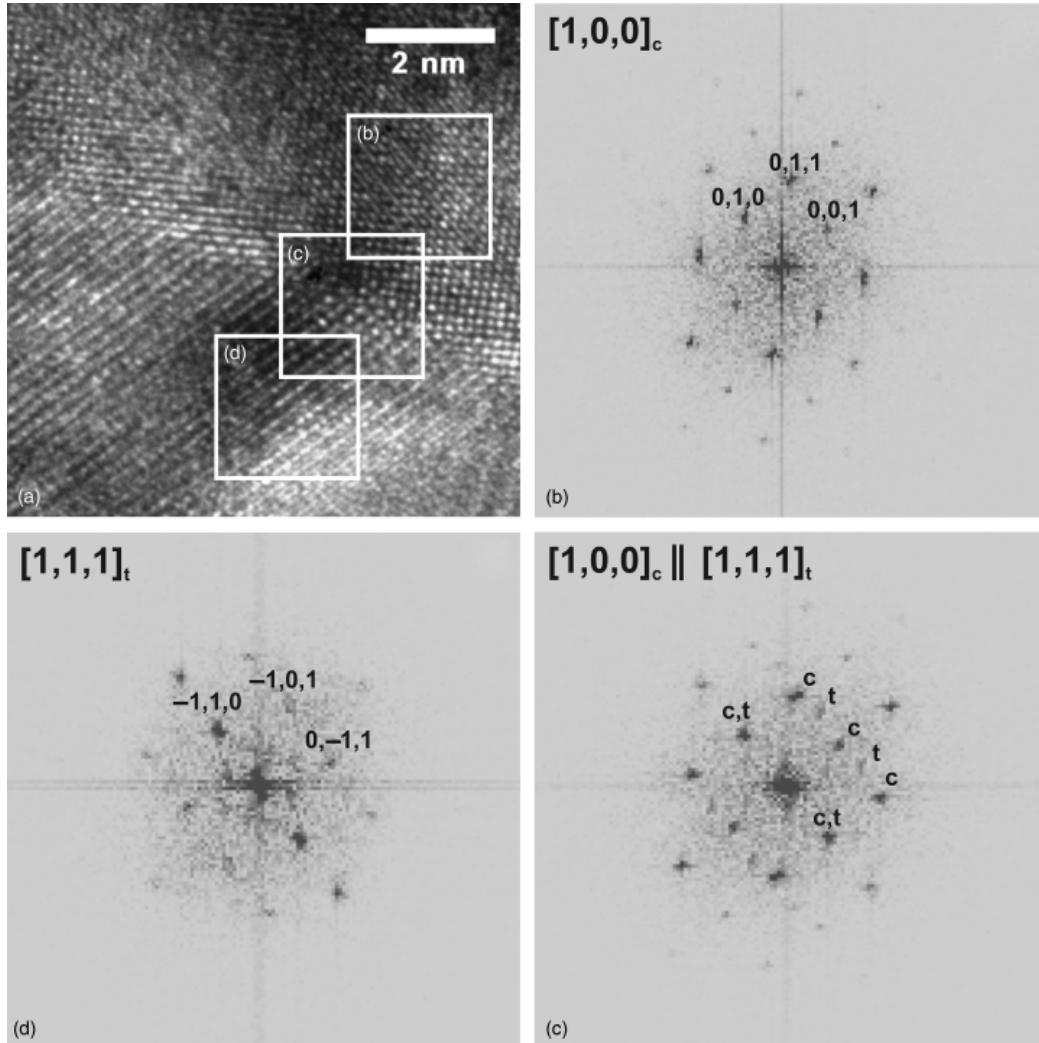
Fig. 5. HRTEM micrograph of grain contact shown in Fig. 2(c). Diffraction data taken via fast Fourier-transformation from selected areas (b–d).
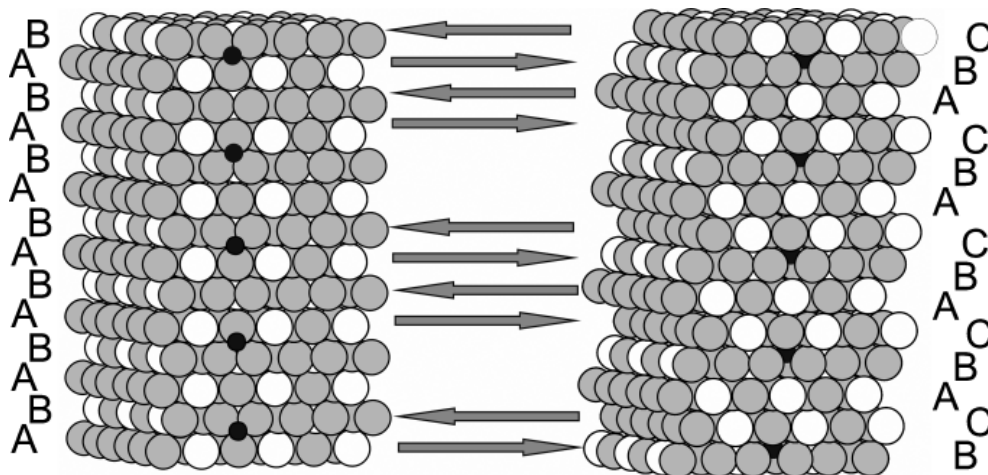

Fig. 6. Scheme of the relationship between hexagonal and cubic perovskite structures visualized by the stacking sequence of the hexagonal layers of barium and oxygen ions (gray ball, oxygen; white, barium; black, cobalt).

transition of the hexagonal to a tetragonal structure occurs. The oxide with a hexagonal structure is strongly related to the cubic perovskite structure. Both the cubic perovskite as well as the hexagonal oxide can be understood as close-packed hexagonal layers of barium (strontium) and oxide ions that are stacked in the hexagonal close packing in the first and in the cubic close packing in the second. While the CoO_6 octahedra share faces in the first place, only corner-sharing $(Co,Fe)O_6$ octahedra are eminent in the second place. Thus, it seems likely that the final perovskite is formed in both the hexagonal—via the formation of the tetragonal unit cell—and in the cubic system by a simple substitution of strontium by barium in the lattice, leading to a larger unit cell.

Figure 6 schematically displays the relation between the hexagonal and the cubic perovskite structure. The stacking sequence in the hexagonal cell is **ABABABAB**—containing just face-sharing octahedra—while the stacking sequence in the perovskite structure is **ABC**ABCAB—containing just corner-sharing octahedra. The existence of fairly distorted close-packed layers in the hexagonal structure is the reason for the occurrence of an intermediate tetragonal phase, which can be understood simply as a distorted perovskite structure explained above.

Obviously, the last reaction of the above-presented reaction sequence is a reversible process that becomes more favorable at temperatures significantly higher than 800°C. This explains the fast decomposition of BSCF below 800°C.

IV. Summary

The synthesis process of BSCF via the commonly applied sol–gel method has been studied in considerable detail. First crystalline intermediates have been identified as a mixed carbonate and a mixed spinel. Second, two mixed oxides are formed: one with a hexagonal structure and one with a cubic structure. Both structures are related to the structure of the cubic BSCF and it was shown that the cubic perovskite structure is finally formed at the expense of both the hexagonal phase—via a tetragonal phase—and the cubic structure.

References

[1] Z. Shao and S. Haile, "A High Performance Cathode for the Next Generation Solid-Oxide Fuel Cells," *Nature*, **431**, 170–3 (2004).

[2] H. Wang, S. Werth, T. Schiestel, and J. Caro, "Perovskite Hollow-Fiber Membranes for the Production of Oxygen-Enriched Air," *Angew. Chem. Int. Ed.*, **44**, 6906–8 (2005).

[3] C. S. Chen, S. J. Feng, S. Ran, D. C. Zhu, W. Liu, and H. J. M. Bouwmeester, "Conversion of Methane to Syngas by a Membrane-Based Oxidation-Reforming Process," *Angew. Chem. Int. Ed.*, **115**, 5196–8 (2003).

[4] Z. Shao, W. Yang, Y. Cong, H. Dong, J. Tong, and G. Xiong, "Investigation of the Permeation Behavior and Stability of a $Ba_{0.5}Sr_{0.5}Co_{0.8}Fe_{0.2}O_{3-\delta}$ Oxygen Membrane," *J. Membr. Sci.*, **172**, 177–88 (2000).

[5] M. Rebeilleau-Dassonneville, S. Rosini, A. C. van Veen, D. Farrusseng, and C. Mirodatos, "Oxidative Activation of Ethane on Catalytic Modified Dense Ionic Oxygen Conducting Membranes," *Catal. Today*, **104**, 131–7 (2005).

[6] A. Feldhoff, J. Martynczuk, and H. Wang, "Advanced $Ba_{0.5}Sr_{0.5}Zn_{0.2}Fe_{0.8}O_{3-\delta}$ Perovskite-Type Ceramics as Oxygen Selective Membranes: Evaluation of the Synthesis Process," *Prog. Solid St. Chem.*, **35**, 339 (2007).

[7] J. Martynczuk, M. Arnold, H. Wang, J. Caro, and A. Feldhoff, "How $(Ba_{0.5}Sr_{0.5})(Fe_{0.8}Zn_{0.2})O_{3-\delta}$ and $(Ba_{0.5}Sr_{0.5})(Co_{0.8}Fe_{0.2})O_{3-\delta}$ Perovskites form via an EDTA/citric acid complexing method," *Adv. Mater.*, in press, doi: 10.1002/adma.200700322.

[8] H. Taguchi, Y. Takeda, F. Kanamura, M. Shimada, and M. Koizumi, "Barium Cobalt Trioxide," *Acta Cryst.*, **B33**, 1299–301 (1977).

[9] M. Yoshiya, C. A. J. Fisher, Y. Iwamoto, M. Asanuma, J. Ishii, and K. Yabuta, "Phase Stability of $Ba(Co_{1-y}Fe_y)O_{3-\delta}$ by First Principles Calculations," *Solid State Ionics*, **172**, 159–63 (2004).   □

2.3 Correlation of the formation and the decomposition process of the BSCF perovskite at intermediate temperatures

Mirko Arnold, Thorsten M. Gesing, Julia Martynczuk, and Armin Feldhoff

Correlation of the formation and the decomposition process of the BSCF perovskite at intermediate temperatures

Mirko Arnold [a]*, Thorsten M. Gesing [b], Julia Martynczuk [a], and Armin Feldhoff [a]

[a] Leibniz Universität Hannover, Institut für Physikalische Chemie und Elektrochemie, Callinstraße 3-3A, D-30167 Hannover, Germany

[b] Leibniz Universität Hannover, Institut für Mineralogie, Callinstraße 3, D-30167 Hannover, Germany

Mirko.arnold@pci.uni-hannover.de

The mixed ionic-electronic conductor (MIEC) $(Ba_{0.5}Sr_{0.5})(Co_{0.8}Fe_{0.2})O_{3-\delta}$ (BSCF) is a renowned material with applications in membrane reactors and as cathodes in solid-oxide fuel cells. Despite BSCF's large oxygen permeabilities, long-time phase instability at intermediate temperatures has been reported. However, the mechanism of this decomposition is still unclear. Here, we present a study of the synthesis of BSCF and compare our results with those obtained from long-time decomposition. Rietveld and Le Bail analysis as well as transmission electron microscopy studies were applied to investigate the reaction sequence in BSCF formation. From our results, we are now able to draw the following conclusion about the reaction mechanism: the formation as well as decomposition is due to a reversible re-ordering of the hexagonal AO_3-layer stacking sequence in the cubic perovskite, which can occur if the cubic BSCF is kept at temperatures below T = 1173 K for long time periods, thereby leading to the decomposition of BSCF into a three phase mixture. The driving force for this reaction was identified to be at the cobalt site since cobalt prefers a low-spin configuration in the 3+ oxidation state. This reaction occurs only at temperatures below 1173 K due to the oxidation of cobalt at low temperatures.

Introduction

In the field of mixed ionic and electronic conductors (MIECs) with high oxygen conductivity, the $(Ba_{0.5}Sr_{0.5})(Co_{0.8}Fe_{0.2})O_{3-\delta}$ (denoted as BSCF) with cubic perovskite structure (ABO_3; A = alkaline earth, B = transition metal, O = oxygen) is regarded as one of the most promising materials.[1,2] MIECs with oxygen conductivity can be employed as membranes for oxygen separation[2,3-6] and as cathodes in solid-oxide fuel cells.[1,7,8] Exceptionally high concentrations of mobile oxygen vacancies accompanied by excellent phase stability are accountable for BSCF's large oxygen transport rates.[9] Despite its high oxygen permeability and short-term stability, other issues have to be examined in view of a BSCF's prospective industrial use.[10] Among others, the chemical long-term stability need to be discussed since membranes are usually set up for longer time periods. Chemical instability, i.e. the decomposition of the BSCF, could lead to membrane failures (cracking) as different unit cell volumes may occur in these phase mixtures at the same time. Secondly, decomposition is also expected to degrade the oxygen permeation fluxes which have to be avoided in industrial applications in order to ensure smooth processes.[10]

In the year 2000[3] and much more recently,[11,12] the long-term stability of BSCF has been investigated and discussed. Shao et al. reported that BSCF undergoes structural changes if the material is kept at T = 1023 K under air for time periods of 500 h. They attributed the observed additional peaks in the X-ray diffraction (XRD) pattern to $BaCoO_2$.[3] Further indications of the decomposition in BSCF were observed by Rebeilleau-Dassonneville et al. who observed additional intensities (25°-30° and 42.5° 2θ / Cu-$K_{\alpha1,2}$ radiation) in the XRD pattern, if the BSCF was kept below T = 1073 K, but no phase attribution

was provided in this study.[11] Švarcová stated that around and below a critical temperature of T = 1123 K, the former single cubic perovskite phase undergoes a decomposition into a hexagonal perovskite and a cubic perovskite, thus exhibiting a two phase region.[12] Švarcová has also shown that the decomposition process, which occurs from annealed BSCF samples, possess presumably the same phases as the raw powder re-annealed at T = 1023 K, thus claiming that the decomposition process is reversible.

We have already quoted that the synthetic process of BSCF may provide useful information about the decomposition as a reversible mechanism might be present.[13] We agree with Švarcová et al., that the decomposition of BSCF is characterized by the same reaction pathway as the synthetic process of BSCF because we found similar XRD patterns for the synthetic process as well as for the decomposing process. This presumption has been emphasized by comparing the XRD pattern of a re-annealed cubic perovskite powder with the XRD pattern of a BSCF powder that had been interrupted in the synthetic process. At this point we stress that Švarcová et al. obtained the same intermediate perovskites using the spray pyrolysis method as those reported using the sol-gel method. This places the presented findings about the sol-gel synthesis method in a more general context. As previously discussed, the reaction pathway of the BSCF formation via the sol-gel route can be divided into three parts.[13] The first part is the formation of a mixed barium-strontium carbonate $(Ba_{0.5}Sr_{0.5})CO_3$ and a mixed cobalt-iron spinel $(Fe_{0.6}Co_{0.4})Co_2O_4$ (the stoichiometry claims no site attribution of cobalt and iron and a real association to either tetrahedral/octahedral occupation could not be provided). The second part is the formation of an intermediate hexagonal perovskite (SG: *P6₃/mmc*)

and an intermediate cubic perovskite (SG: *Pm-3m*). Finally, the third part is the formation of the final cubic perovskite structure at the expense on both the hexagonal as well as the cubic perovskites. However, it has been postulated by Švarcová et al. that the decomposition of the BSCF at low temperatures is due to the oxidation of the B-site cations, which yields a hexagonal perovskite, due to the fact that the smaller ionic radii favour the formation of hexagonal perovskite structures. The compositions as well as the structures formed through this decomposition process remain unknown.

The present study focuses on the second and on the third part of the synthetic process. By applying Rietveld[14] and LeBail[15] refinement procedures to examine the final parts of the reaction sequence, we are able to draw an even more detailed picture of the reaction sequence from the picture presented in our previous report. This was accompanied by performing an intensive transmission electron microscopy study combined with quantitative energy dispersive X-ray spectroscopy (EDXS) of partly reacted powders in order to support the XRD findings.

Experimental Section

Powders of BSCF stoichiometry were synthesised by a sol-gel reaction procedure, as reported in detail elsewhere.[3,13,16,17] In order to obtain partly reacted powders and to avoid the complete reaction towards the BSCF, the final calcinations steps were conducted at temperatures below T = 1223 K. Detailed investigations of powders that had been prepared in ambient air with different dwell times in the temperature regime between T = 923 K and T = 1223 led us to the conclusion that five phases were involved during the

synthesis of the perovskite. This has also been confirmed by a previously reported *in situ* X-ray diffraction study.[13] Particular powders, which represent the final steps in the synthetic process, were selected in order to perform X-ray refinements as well as transmission electron microscopy (TEM) studies. In particular two powders, one at T = 973 K, 10 h (sample 1) and the other T = 1023 K, 10 h (sample 2), were investigated using the above techniques.

For structure refinements of the product phase, the X-ray powder diffraction data was collected on a Bruker AXS D8 Advance diffractometer using a flat sample geometry, a primary Göbel mirror and Cu-$K_{\alpha1,2}$ radiation. Additionally, a secondary graphite monochromator was used to suppress the fluorescence radiation of the sample. A total of 3750 data points were collected with a step width of 0.02° in the 2θ range from 10° to 85°. Rietveld refinements on the XRD powder data were carried out by using the TOPAS 3.0 (Bruker AXS) software. During refinements, general parameters, such as the scale factor, a maximum of three or four background parameters and the zero point of the counter, were optimized. Profile shape calculations were carried out on the basis of standard instrumental parameters using the fundamental parameter approach implemented in the program by varying also the average crystal size (integral breadth) and the strain parameter, ε_0. Additionally, the cell parameter and the displacement parameters were also refined. In the case of site occupation with mixed atoms, linear constraints were used for the occupancy (the occupancy of atom B is equivalent to 1.0 minus the occupancy of atom A) and the displacement parameters (atoms on the same position have the same displacement parameter).

TEM was performed at 200 kV on a field-emission instrument (JEOL JEM-2100F). The microscope was equipped with an ultra-high resolution pole piece that provides a point-resolution better than 0.19 nm (with a spherical aberration constant, C_S = 0.5 mm, and a chromatic aberration constant, C_C = 1.1 mm) and allowed us to perform high-resolution transmission electron microscopy (HRTEM) studies. The microscope was equipped with a 1k charge-coupled-device (CCD) camera. Diffraction data were obtained by fast Fourier transformation (FFT) of the HRTEM micrographs using the Gatan Digital Micrograph software (Version 1.70.16). Quantitative elemental analysis using energy-dispersive X-ray spectroscopy (EDXS) was performed on an Oxford Instruments INCA-200-TEM system with an ultra-thin window that was attached to the microscope. A detailed description of the TEM sample preparation can be found in our previous reports.[13,16,17]

Results

Figure 1 shows the Rietveld refinement of powder sample 1 that has been heated for 10 h at T = 973 K. Four phases were present, namely a mixed carbonate, a mixed spinel, a hexagonal, and a cubic perovskite. A detailed summary of the Rietveld analysis of the phase mixture can be found in Table 1. The carbonate and spinel phases were present to a minor extent (~ 8 %), whereas the hexagonal perovskite (~ 58 %) and the cubic perovskite (~ 25 %) were the major phases. Also, an unknown amount amorphous phase is present.
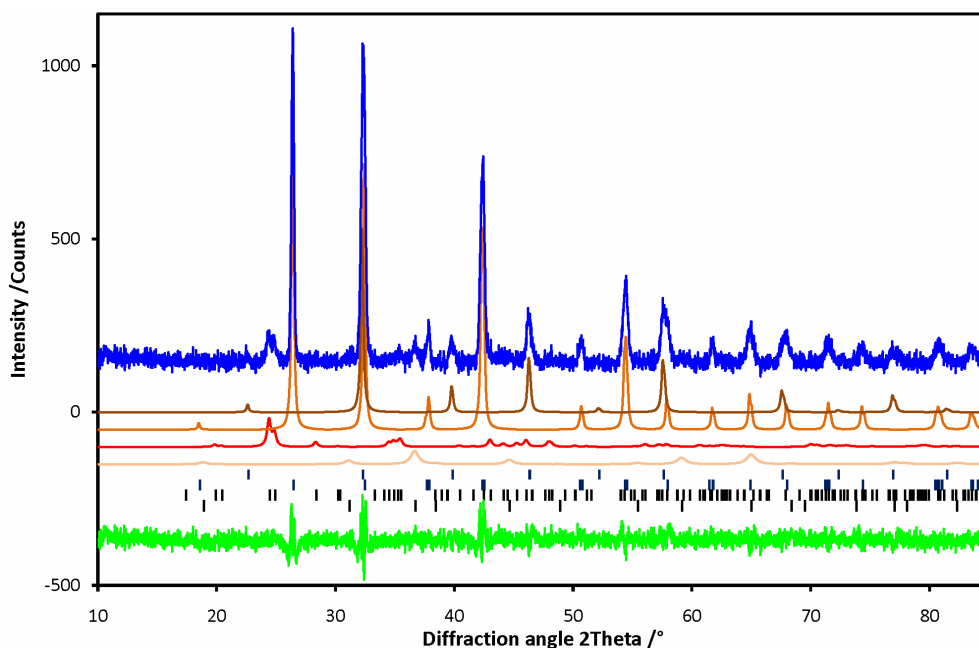
Figure 1. Rietveld plot of sample 1 (T = 973 K, 10 h). The observed (blue) and calculated intensities [brown, top: $(Ba_{0.25}Sr_{0.75})(Co_{0.6}Fe_{0.4})O_{3-\delta}$ (cubic-perovskite); light brown: $(Ba_{0.75}Sr_{0.25})CoO_{3-\delta}$ (hexagonal perovskite); red: $(Ba_{0.5}Sr_{0.5})CO_3$ (aragonite-modification); pink, bottom: $(Fe_{0.6}Co_{0.4})Co_2O_4$ (spinel-modification)] together with the difference (green) between the observed and calculated pattern as well as the possible reflex position (tick marks) are given.

The refinement converged to reliability factors of R_{WP} = 9.12 % and R_P = 7.52 % for the pattern with a goodness of fit = 1.17, and a Durban-Watson parameter of 1.47. We have assigned the following stoichiometries to the perovskite structures: $(Ba_{0.75}Sr_{0.25})CoO_{3-\delta}$ for the hexagonal perovskite and $(Ba_{0.25}Sr_{0.75})(Co_{0.6}Fe_{0.4})O_{3-\delta}$ for the cubic perovskite. This was in excellent agreement with the reported unit cell parameters for the cubic perovskite unit cell[9], and the hexagonal unit cell parameters were in excellent agreement with the findings by Gushee et al. and Taguchi et al.[21,22]. This is due to the fact that the unit cell of the observed hexagonal perovskite was smaller to that found in $BaCo_{2.83}$, and the unit cell parameters of the observed cubic perovskite was smaller than that reported for BSCF.

In order to determine the B-site stoichiometry, which is difficult to ascertain from the XRD data alone, and to confirm the A-site occupancy obtained from XRD analysis, we have conducted a quantitative EDXS study on a TEM for sample 1 (data not shown). Additionally, we successfully prepared samples of the hexagonal structure, within the series $(Ba_{1-x}Sr_x)CoO_{3-\delta}$, to prove the claimed the hexagonal phase present here. Together with the Rietveld analysis, we are able to provide a reasonable determination of these stoichiometries. However, since an amorphous part is still present, the mass balance of the overall stoichiometry was not only reflected by the crystalline part.
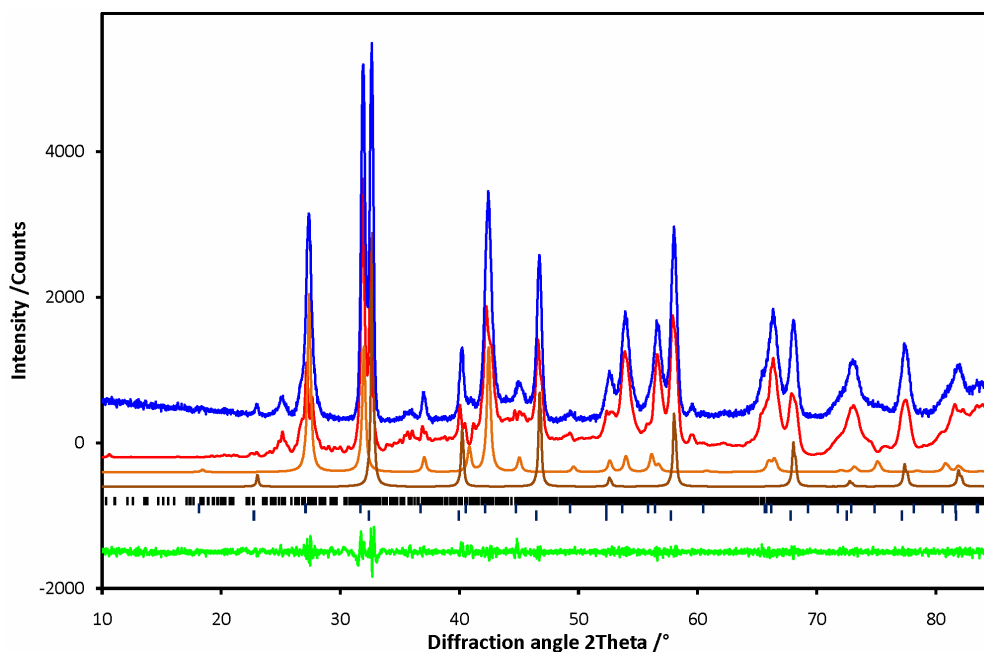
Figure 2. Rietveld / Le Bail plot of sample 2 (T = 1023 K, 10 h). The observed (blue) and calculated intensities [red, top: $(Ba_{0.6-x}Sr_{0.4+x})(Co_{1-y}Fe_y)O_{3-\delta}$ (monoclinic-perovskite); light brown: $(Ba_{0.6+x}Sr_{0.4-x})CoO_{3-\delta}$ (hexagonal-perovskite); brown, bottom: $(Ba_{0.25}Sr_{0.75})(Co_{0.6}Fe_{0.4})O_{3-\delta}$ (cubic-perovskite)] together with the difference (green) between the observed and calculated pattern as well as the possible reflex position (tick marks) are given.

2. Formation and phase stability of $(Ba_{0.5}Sr_{0.5})(Co_{0.8}Fe_{0.2})O_{3-\delta}$

A combined Rietveld/Le Bail analysis of the powder sample 2 is shown in Figure 2. The refinement converged to reliability factors of R_{WP} = 4.72 % and R_P = 3.45 % for the pattern with a goodness of fit = 1.25 and a Durban-Watson parameter of 1.41. The carbonate as well as spinel phases have completely vanished and have reacted towards the perovskite structures as they could not be detected by XRD in this sample.

Superficial investigation of the XRD pattern led to the conclusion that the hexagonal perovskite simply undergoes a change in the lattice parameters compared with the hexagonal perovskite observed in sample 1. Attempts to refine the pattern with *only* the hexagonal perovskite structure together with the cubic perovskite structure failed, as well as attempts using the tetragonal structure together with the cubic structure, which was suggested by us in an earlier report.[13] We finally arrived at the conclusion that a new structure (with lower symmetry) must be formed at the expense of the hexagonal perovskite. A Le Bail whole pattern decomposition method was applied to refine the unit cell and a monoclinic unit cell (SG: *P2/m*) with parameters obtained from the refinement in Figure 2 and shown in Table 1 was found to best fit the observed pattern. From our studies, three phases are present in powder sample 2: a cubic perovskite (~33 %), a hexagonal perovskite (~33 %), and a new monoclinic phase (~33 %).

Phase	Space goup	Space group ref.	Lattice parameter /nm
Sample 1			
$(Ba_{0.5}Sr_{0.5})CO_3$	*Pmcn*	De Villiers[18]	a = 0.51911(48)
		Kiseleva et al.[19]	b = 0.86708(91)
			c = 0.62752(67)
$(Fe_{0.6}Co_{0.4})Co_2O_4$	*Fd-3m*	Liu et al.[20]	a = 0.81073(42)
$(Ba_{0.75}Sr_{0.25})CoO_{3-\delta}$	*P6$_3$/mmc*	Gushee et al.[21]	a = 0.55076(4)
		Taguchi et al.[22]	c = 0.47409(5)
$(Ba_{0.25}Sr_{0.75})(Co_{0.6}Fe_{0.4})O_{3-\delta}$	*Pm-3m*	McIntosh et al.[9]	a = 0.39145(3)
Sample 2			
$(Ba_{0.6-x}Sr_{0.4+x})(Co_{1-y}Fe_y)O_{3-\delta}$	*P2/m*	this work	a = 1.10307(62)
			b = 0.97080(53)
			c = 1.40776(92)
			ß = 91.6526(45) °
$(Ba_{0.6+x}Sr_{0.4-x})CoO_{3-\delta}$	*P6$_3$/mmc*	Gushee et al.[21]	a = 0.56434(50)
		Taguchi et al.[22]	c = 0.44478(49)
$(Ba_{0.25}Sr_{0.75})(Co_{0.6}Fe_{0.4})O_{3-\delta}$	*Pm-3m*	McIntosh et al.[9]	a = 0.39063(17)

Table 1. Summary of the Rietveld refinement of sample 1 (T = 973 K, 10 h) and the Rietveld/Le Bail refinement of sample 2 (T = 1023 K, 10h).

The hexagonal perovskite undergoes a minor change in the lattice parameters compared to those observed in powder sample 1. It must be stressed that the unit cell of the cubic perovskite did not change significantly between sample 1 and sample 2, thus leading to the conclusion that no further uptake of barium had occurred (because this would have led to an increase in the unit cell parameters since the unit cell parameters of the perovskite structures strongly depend on the radii of the A-site cation. According to Shannon[23], Sr^{2+} = 0.144 nm, while Ba^{2+} = 0.161 nm, in the given twelve-fold cuboctahedral coordination.).[13] Quantitative EDXS on a TEM, indicated that during the reaction from sample 1 to sample 2, a slight change of the A-site cation occupancy at the hexagonal site had occurred (A-site$_{occupancy}$ = $(Ba_{0.75}Sr_{0.25})_{sample1}$ to $(Ba_{0.6+x}Sr_{0.4-x})_{sample2}$; a smooth transition between the hexagonal

and the monoclinic phase is indicated by the variable x). This is reflected in Table 1. Further on, minor extents of iron (indicated by the variable y in the stoichiometry) were found in the monoclinic phase.

Increasing the temperature leads then to a cubic perovskite structure with the reported unit cell parameter of ~ 0.4 nm (the data is not shown here but can be found elsewhere[13]). A summary of the reaction sequence is displayed in Figure 3. We emphasize that the presented stoichiometries of the intermediate crystalline phases are idealized and vary in certain tolerances since solid state reactions are not static but rather dynamic processes.

In order to deliver further proof for the proposed reaction mechanism, an HRTEM study was conducted, combined with the quantitative EDXS results mentioned previously.
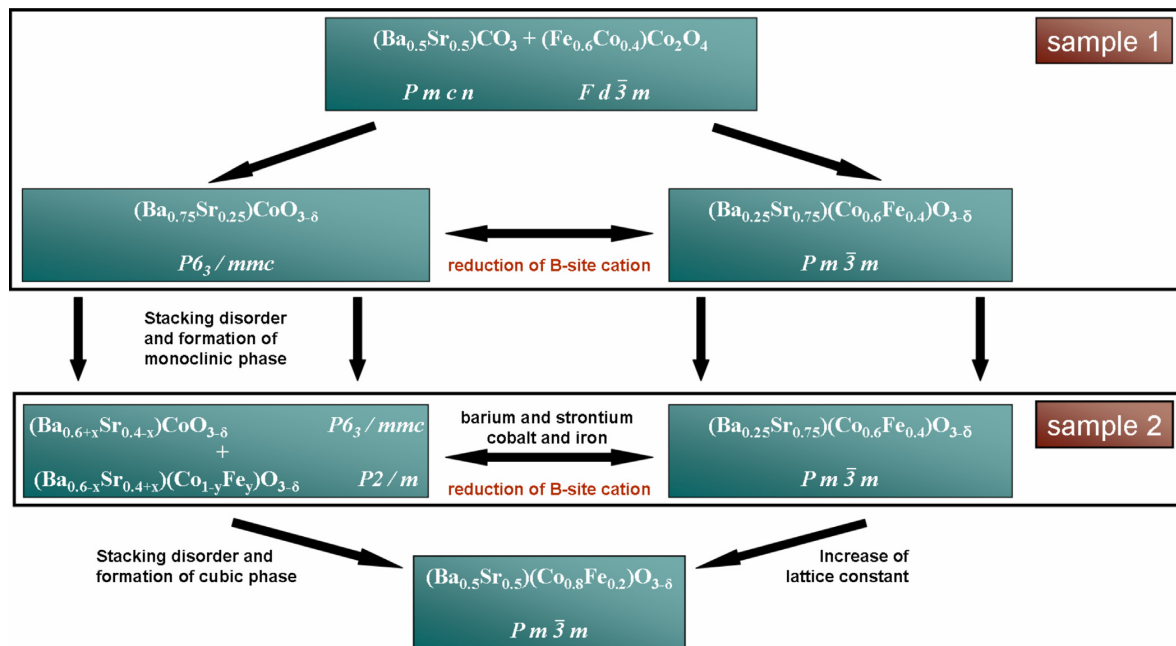

Figure 3.   Reaction scheme of the sol-gel synthetic route of BSCF.

In Figure 4a and 4b, a representative HRTEM micrograph acquired for sample 1 is displayed. It shows the contact zone between a grain with cubic perovskite symmetry (a = 0.39 nm) viewed along the [111] zone axis (Figure 4c) and a grain with hexagonal symmetry (a = 0.54 nm; c = 0.47 nm) viewed along the [122] zones axis (Figure 4d). The hexagonal structure exhibits a slightly smaller unit cell as that found for the hexagonal cell by Rietveld analysis, as well as superlattice reflections orientated along the [-210] direction, which indicates a cation ordering along this direction as illustrated by arrows. It has to be stressed that in nanosized powder reactions, slight deviations from the macroscopic observations (XRD) may occur as the cation distribution can vary from grain to grain. Figure 5 exhibits the coexistence of the cubic perovskite (a = 0.408 nm) viewed along the [01-1] zone axis (Figure 5b) as well as the monoclinic structure (derived from the Le Bail analysis) viewed along the [100] zone axis (Figure 5c) in sample 2. The diffraction data acquired directly from the contact zone (Figure 5d) clearly shows streaky intensities. This indicates the formation of stacking disordering with a vector **q** orientated along the $(111)_{cubic}$ direction, when viewed from the cubic phase and along the $(003)_{monoclinic}$ direction, when viewed from the monoclinic phase. Further on, the $(111)_{cubic}$ plane is parallel to $(006)_{monoclinic}$ plane and exhibits the same reciprocal length.
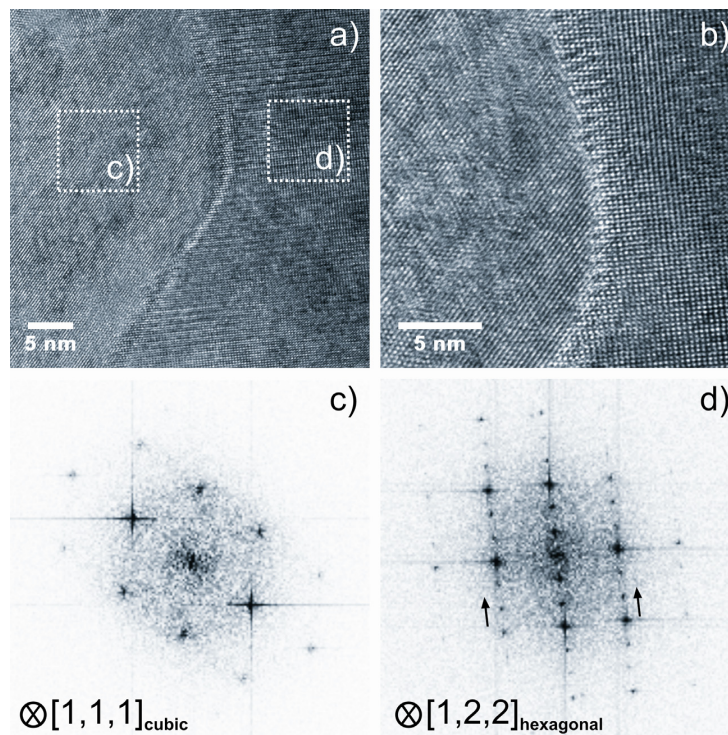
Figure 4. Transmission electron micrographs showing the contact zone between the cubic perovskite $(Ba_{0.25}Sr_{0.75})(Co_{0.6}Fe_{0.4})O_{3-\delta}$ (c) and the hexagonal perovskite $(Ba_{0.75}Sr_{0.25})CoO_{3-\delta}$ (d) in sample 1. a) and b) High-resolution TEM micrographs at different magnifications, c) and d) diffraction data acquired via FFT related to the marked positions in a). Arrows in d) indicate the direction of the cation ordering.
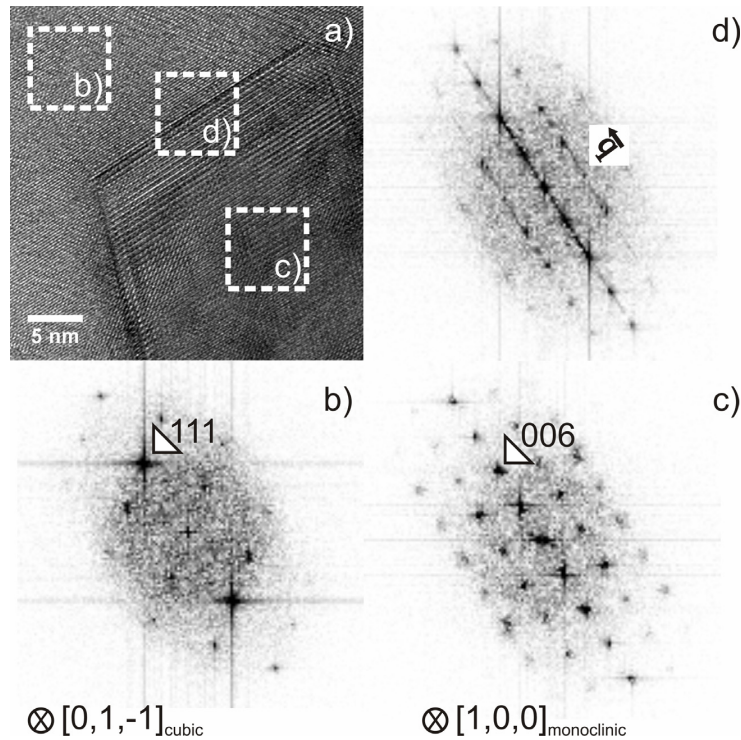
Figure 5. Transmission electron micrograph showing the contact zone between the cubic perovskite (b) and the monoclinic perovskite (c) in sample 2. a) High-resolution TEM micrograph, b), c) and d) diffraction data acquired via FFT related to the marked positions in a). The vector q (along $[003]_{monoclinic}$ and $[111]_{cubic}$) in d) indicates the direction of streaky intensities that are present in the vicinity of the phase boundary.

Discussion

The work of Shao et al., Rebeilleau-Dassonneville et al., and Švarcová et al. has shown that if BSCF is kept below 1123 K for a long time period, a decomposition occurs which separates the former single cubic perovskite phase into (at least) a two phase mixture.[3,11,12] The additional phase was referred by Shao et al. to be $BaCoO_2$. Švarcová et al. found a hexagonal structure but without space group determination. Rebeilleau-Dassonneville et al. also reported the decomposition into an additional phase, but here only the additional Bragg positions in the XRD pattern were given. The results of Švarcová et al. support the conclusion that a reversible process was present since they found the same phase separation in raw powders that had not been fully calcined towards the BSCF. In our work, we also found a clear evidence for the reversibility of this process. First, we prepared a cubic BSCF powder sample and verified the phase purity by XRD. Second, we annealed this sample for 20 h at 923 K in air and re-examined phase purity by XRD. This sample already demonstrated minor contributions of the hexagonal and the monoclinic phase found in sample 1 and sample 2 as previously discussed in this report.

The main goal of this study was to identify the way the cubic perovskite is formed at the expense of the hexagonal perovskite as well as to identify the driving force for this reaction. As previously mentioned, the first reaction products of the BSCF formation are the mixed spinel $(Fe_{0.6}Co_{0.4})Co_2O_4$ and the mixed carbonate $(Ba_{0.5}Sr_{0.5})CO_3$ followed by the formation of the cubic perovskite $(Ba_{0.25}Sr_{0.75})(Co_{0.6}Fe_{0.4})O_{3-\delta}$ and the hexagonal perovskite $(Ba_{0.75}Sr_{0.25})CoO_{3-\delta}$ (see Figure 3). Due to the fact that the reaction time was set to 10 hours for sample 1, it is unlikely that different diffusion kinetics yields the formation of the two different perovskites, and we assume a thermodynamic effect is responsible for this observation.
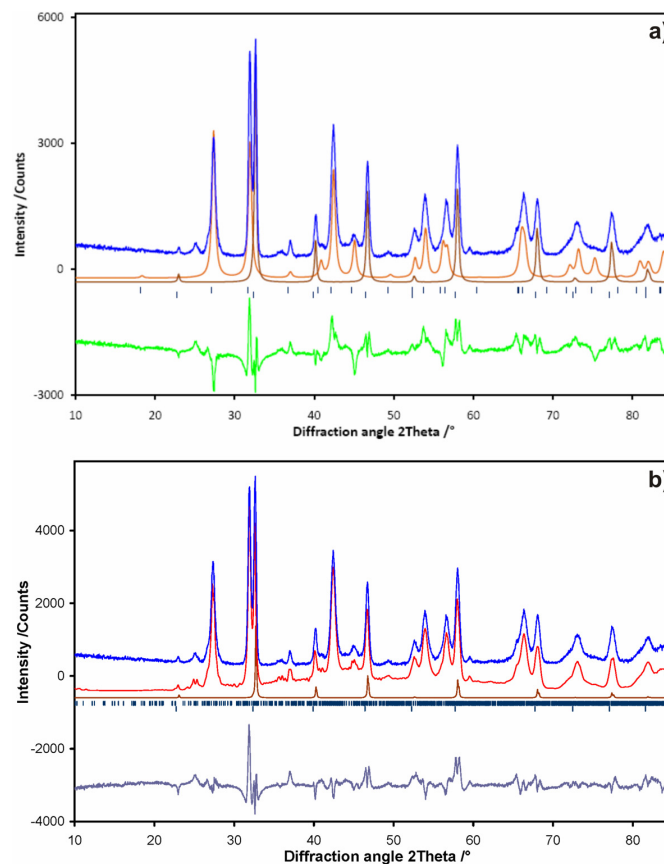
Figure 6. Refinement plots sample 2 (1023 K, 10 h) refined only with the hexagonal/cubic perovskite or the tetragonal/cubic perovskite. a) Rietveld refinement: The observed (blue) and calculated intensities [light brown, top: $(Ba_{0.6}Sr_{0.4})CoO_{3-\delta}$ (hexagonal-perovskite); brown, bottom: $(Ba_{0.25}Sr_{0.75})(Co_{0.6}Fe_{0.4})O_{3-\delta}$ (cubic-perovskite)] together with the difference (green) between the observed and calculated pattern as well as the possible reflex position (tick marks) are given.

b) Rietveld / Le Bail refinement: The observed (blue) and calculated intensities [red, top: tetragonal cell (*P4*, a= 0.563 nm, c = 0.401 nm; brown, bottom: $(Ba_{0.25}Sr_{0.75})(Co_{0.6}Fe_{0.4})O_{3-\delta}$ (cubic-perovskite) together with the difference (grey) between the observed and calculated pattern as well as the possible reflex position (tick marks) are given.

Particularly, the separation of cobalt and iron cannot be explained by diffusion kinetics. Furthermore, a successful preparation at temperatures of T = 1023 K under similar reaction conditions was previously reported for $(Ba_{0.5}Sr_{0.5})(Fe_{0.8}Zn_{0.2})O_{3-\delta}$, which displays a cobalt-free cubic perovskite.[16,17,24] That makes it even more plausible that the reactions presented here are thermodynamically controlled at this point of the formation on BSCF.

The first question which needs to be answered is why does the reaction follow this particular pathway? In a simplified model, both B-site cations are assumed to be initially in a +3 oxidation state. Though they have the same formal valence, a fundamental discrepancy between the preferred spin state of iron and cobalt has to be considered. While Fe^{3+} is mostly found in the high-spin state (octahedral oxygen environment), Co^{3+} occupies equivalent sites (octahedral oxygen environment) in the low-spin state.[25-27] This fact results in huge differences in the ionic radii: Fe^{3+} (HS) = 0.0645 nm and for Co^{3+} (LS) = 0.0545 nm.[23] The basic discrepancy between the cubic and hexagonal perovskite is the connection of the B-site octahedra. In case of the cubic structure, only corner-sharing octahedra are present with a B-O distances of ~ 0.195 nm, whereas in the hexagonal structure, face-sharing octahedral with B-O distances of ~ 0.184 nm are present. Considering the large difference between the ionic radius of cobalt and iron, it is clear why cobalt prefers to form the hexagonal perovskite structure. At this point it has to be stressed that the observed B-O bonding distance clearly deviates from sum the of the effective ionic radii[23], which can be attributed to a strong amount of covalent character in the B-O bond.[28]

The second question to be answered is why does the cubic perovskite BSCF form only above T = 1123 K and why does it exhibit a long time stability only above this temperature? As a matter of fact, the B-site cations of perovskite-type oxides possess higher oxidation states at lower temperatures, while increasing the temperature leads to a reduction of the B-site cations.[29] This has been previously suggested by Švarcová to be the reason for the stability of the cubic perovskite at temperatures above T = 1123 K.[12] In other words, the decrease of the ionic radii of the B-site cations was identified to be the driving force for the formation of the hexagonal perovskite. We partly agree with this argument, but we emphasize that this is due to cobalt which is occupying the hexagonal B-site. The redox behaviour of cubic BSCF is mainly due to cobalt.[28] Furthermore, the oxidation from Co^{2+} to Co^{3+} is accompanied by a change in the preferred spin state, which is the real driving force (Co^{2+} = 0.0745 nm (HS), Co^{3+} = 0.0545 nm (LS) compared to Fe^{2+} = 0.0780 nm (HS), Fe^{3+} = 0.0645 nm (HS)).[23]

The third question to be answered is how does the reaction proceed from the hexagonal perovskite structure towards the cubic perovskite structure, and are there any other structures involved that have been missed so far?

The structural relationships between the hexagonal and cubic structures were discussed already in our previous report.[13] As also described also by Negas et al.,[30] it is likely to assume that the transition from hexagonal to cubic perovskite occurs via a shear of the AO_3-hexagonal layers.

As mentioned above, we successfully refined the hexagonal perovskite together with the cubic perovskite structure on our powder sample 1.

According to Švarcová et al. our powder sample 2 should also exhibit only the hexagonal and the cubic perovskite.

Their results for a "raw"-powder synthesized at T = 1023 K were indexed with a hexagonal perovskite metric and showed a very similar diffraction pattern as the one reported here for our powder sample 2. However, all attempts to refine the pattern with the hexagonal perovskite structure failed.

Finally, a Le Bail refinement has provided evidence that sample 2 consisted of a *three phase* mixture containing a hexagonal, a cubic and a monoclinic phase with unit cell parameters shown in Table 1. To emphasize the *three phase* mixture including the monoclinic phase claimed above, a refinement of sample 2 with *two phase* mixtures is given in Figure 6, namely hexagonal/cubic (Figure 6a) as well as tetragonal/cubic (Figure 6b). The large discrepancies are immediately clear and are visible by the difference curves. Obviously, the so far unknown intermediate monoclinic structure must be

included in order to obtain probable refinement results. The creation of the monoclinic structure can be understood as described in Figure 7, where four unit cells of the hexagonal perovskite along the [001] zone axis are drawn. First, the hexagonal cell must be transformed into a pseudo-orthorhombic setting, which results in the following new unit cell parameters: $a_{hexagonal} \rightarrow a_{orthorhombic}$, $\sqrt{3} \times b_{hexagonal} \rightarrow b_{orthorhombic}$ and $c_{hexagonal} \rightarrow c_{orthorhombic}$. The monoclinic unit cell can then be approximated as a superstructure based on the pseudo-orthorhombic setting with $a_{monoclinic} = 2 \times a_{orthorhombic}$, $b_{monoclinic} = b_{orthorhombic}$, $c_{monoclinic} = 3 \times c_{orthorhombic}$. According to the assumed shearing of the hexagonal AO_3-layers, the superstructure is probable, particularly in the c-direction, which is the axis perpendicular to the stacking sequence. A scheme of the AO_3-layer stacking sequence of the hexagonal and cubic perovskite is shown in Figure 8.
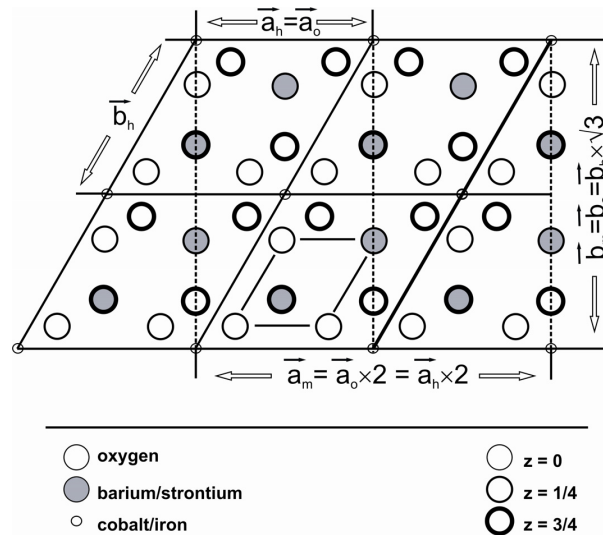
Figure 7. Transformation scheme of the hexagonal unit cell into the monoclinic unit cell via a pseudo-orthorhombic setting. The hexagonal unit cell is plotted along the [001] zone axis. Additionally, the AO_3-hexagonal layer stacking unit is highlighted.

The monoclinic stacking sequence displays an intermediate structure between these end members and a possible shift in the AO_3-layer stacking sequence from the hexagonal towards the cubic phase is indicated by arrows. The stacking sequence in the hexagonal perovskite is 2H, thus owing only face-sharing transition metal (TM) octahedra. Reactions toward the monoclinic cell is accompanied by a shift in some of the AO_3-layers, which results in a mixture of face-sharing as well as corner-sharing TM octahedra. Therefore, within the monoclinic unit cell, 3C as well as 2H stacking ordering can be observed. The final cubic BSCF perovskite is characterised by the normal 3C stacking ordering. Thus, the intermediate stacking sequence in the monoclinic cell directly reflects the intermediate valence state of the cobalt as the reaction temperature increased. As explained above,

the octahedral sites in the hexagonal stacking sequence are preferably occupied by Co^{3+}, and the octahedral sites in the cubic stacking are preferably occupied by Co^{2+}. (Actually, $Co^{2.2+}$ is present at 1223 K in BSCF according to *in situ* electron energy-loss spectroscopy.[29]) The development of the corner-sharing octahedral sites are also in good agreement with the fact, that iron was built into the lattice during the reaction hexagonal $\rightarrow$ monoclinic since iron preferably occupies corner-sharing octahedral sites. Prolonged heating above the critical temperature of T = 1173 K leads to a further reordering of the stacking sequence of the monoclinic cell, which ultimately results in the cubic perovskite accompanied with an exchange of cobalt and iron and barium strontium between these two phases, where the latter was clearly determined by *in-situ* XRD.[13]

Figure 8. Stacking sequence of the AO_3-hexagonal layers in the hexagonal, monoclinic and cubic perovskite structure. Indicated is one possible re-arrangement of the stacking sequence from the hexagonal towards the cubic perovskite structure.

Further evidence for the reaction of the monoclinic towards the cubic perovskite structure is shown Figure 5d. The plane $(111)_{cubic}$ is parallel to the $(006)_{monoclinic}$ plane of the monoc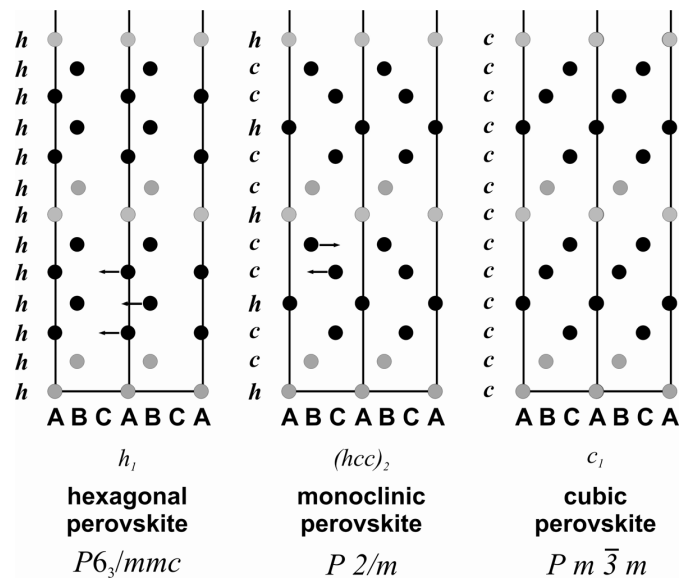linic grain with the same reciprocal length. Further on, a stacking disordering along a vector **q**, which is orientated along the $[111]_{cubic}$ direction of the cubic cell is indicated by stripes found in the diffraction data, which were acquired directly from the contact zone. This is in excellent agreement with the proposed mechanism since the stacking of the hexagonal AO_3-layers is perpendicular to the [111] room diagonal of the cubic perovskite. In view from the monoclinic unit cell, the stacking disordering occurs along the vector **q**, which is orientated along the $[003]_{monoclinic}$ direction. This is also in good agreement with the proposed reaction mechanism because the stacking of the hexagonal AO_3-layers is perpendicular to the [00l] direction of the monoclinic cell.

Conclusions

We have presented further evidence that the decomposition of the cubic $(Ba_{0.5}Sr_{0.5})(Co_{0.8}Fe_{0.2})O_{3-\delta}$ BSCF perovskite is a process that finally separates the former cubic single phase BSCF into a two phase mixture of hexagonal and cubic perovskites, which occurs via a new monoclinic perovskite. The hexagonal perovskite was found to be a barium-rich, iron-free cobalt perovskite while the cubic perovskite was identified to be a strontium-rich, iron-cobalt perovskite.

Furthermore, our results deliver arguments that the main driving force for this reaction is the oxidation of the B-site cobalt ion, which preferably occupies the low-spin state, if oxidised to states close to +3. This enforces the formation of a hexagonal perovskite with small B-O bonding distances. Additionally, we identified a reordering of the stacking sequence of the hexagonal perovskite that can lead to the cubic perovskite or backwards to the hexagonal perovskite. During this reaction, a so far unknown monoclinic phase was formed, which was found to be a superstructure based on the hexagonal perovskite. These results deliver the explanation as to why and how particularly cubic cobalt perovskites tend to segregate into hexagonally stacked perovskites at low temperatures.

References

(1)   Shao, Z.P.; Haile, S.M. *Nature*, **2004**, *431*, 170.

(2)   Chen, C.S.; Feng, S.J.; Ran, S.; Zhu, D.C.; Liu, W.; Bouwmeester, H.J.M. *Angew. Chemie Int. Ed.*, **2003,** *42*, 5354.

(3)   Shao, Z.P.; Yang, W.S.; Cong, Y.; Dong, H.; Tong, J.H.; Xiong, G.X. *J. Membr. Sci.*, **2000**, *172*, 177.

(4)   Caro, J.; Wang, H.H.; Tablet, C.; Kleinert, A.; Feldhoff, A.; Schiestel, T.; Kilgus, M.; Kölsch, P.; Werth, S. *Catal. Today*, **2006**, *118*, 128.

(5)   Ge, L.; Zhou, W.; Ran, R.; Liu, S.M.; Shao, Z.P.; Jin, W.; Xu, N.P. *J. Membr. Sci.*, **2007**, *306*, 318.

(6)   Zeng, P.Y.; Chen, Z.H.; Zhou, W.; Gu, H.X.; Shao, Z.P.; Liu, S.M. *J. Membr. Sci.*, **2007**, *291*, 148.

(7)   Lai, W.; Haile, S. *Phys. Chem. Chem. Phys.*, **2008**, *10*, 865.

(8)   Liu, Q.L.; Khor, K.A.; Chan, S.H. *J. Power Sources*, **2006**, *161*, 123.

(9)   McIntosh, S.; Vente, J.F.; Haije, W.G.; Blank, D.H.A.; Bouwmeester, H.J.M. *Chem. Mater.,* **2006**, *18*, 2187.

(10)   Vente, J.F.; McIntosh, S.; Haije, W.G.; Bouwmeester, H.J.M. *J. Solid State Electrochem.*, **2006,** *10*, 581.

(11)   Rebeilleau-Dassonneville, M.; Rosini, S.; van Veen, A.C.; Farrusseng, D.; Mirodatos, C. *Catal. Today*, **2005**, *104*, 131.

(12)   Švarcová S.; Wiik K.; Tolchard J.; Bouwmeester H.J.M.; Grande T.; *Solid State Ionics*, **2008**, *178*, 1787.

(13)   Arnold, M.; Wang, H.H.; Martynczuk, J.; Feldhoff, A. *J. Am. Ceram. Soc.*, **2007**, *90*, 3651.

(14)   Rietveld, H.M. *J. Appl. Cryst.* **1969**, *2*, 65.

(15)   Le Bail, A.; Duroy, H.; Fourquet, J.L. *Mat. Res. Bull.* **1988***, 23,* 447.

(16)   Feldhoff, A.; Arnold M.; Martynczuk J.; Gesing, Th.M.; Wang, H.H.; *Solid State Sci.*, doi:10.1016/j.solidstatesciences.2007.11.030.

(17)   Martynczuk, J.; Arnold, M.; Wang, H.H.; Caro, J.; Feldhoff A., *Adv. Mater.;* **2007**, *19*, 2134.

(18)   De Villiers, J.P.R. *Am. Miner.,* **1971**, *56*, 758.

(19)   Kiseleva, L.A.; Kotelnikov, A.R.; Martynov, K.V.; Ogorodova, L.P.; Kabalov, J.K. *Phys. Chem. Miner.*, **1994**, *21*, 392.

(20)   Liu, X.; Prewitt, C.T. *Phys. Chem. Miner.*, **1990**, *17*, 168.

(21)   Gushee, B.E.; Katz, L.; Ward, R. *J. Amer. Chem. Soc.*, **1957**, *79*, 5601.

(22)   Taguchi, H.; Takeda, Y.; Kanamaru, F.; Shimada, M.; Koizumi, M.; *Acta Cryst.,* **1977**, *B33*, 1299.

(23)   Shannon, R.D. *Acta Cryst.,* **1976,** *A32*, 751.

(24)   Feldhoff, A.; Martynczuk, J.; Wang, H.H. *Prog. Solid State Chem.*, **2007**, 35, 339.

(25)   Yoon, W.S.; Kim, K.B.; Kim, M.G.; Lee, M.K.; Shin, H.J.; Lee, J.M.; Lee, J.S.; *J. Phys. Chem. B*, **2002**, *106*, 2526.

(26)   de Groot, F.M.F.; Abbate, M.; van Elp, J.; Sawatzky, G.A.; Ma, Y.J.; Chen, C.T.; Sette, F. *J. Phys.: Condens. Matter* **1993**, *5,* 2277.

(27)   Abbate, M.; Fuggle, J.C.; Fujimori, A.; Tjeng, L.H.; Chen, C.T.; Potze, R.; Sawatsky, G.A.; Eisakia, H.; Uchida, S. *Phys. Rev.* **1993**, *B47,* 16124.

(28)   Goodenough, J.B.; Kafalas, J.A. *J. Solid State Chem.,* **1973**, *6*, 493.

(29)   Arnold, M.; Xu, Q.; Tichelaar, F.D.; Feldhoff, F. *Angewandte Chemie Int. Ed.,* **submitted**.

(30)   Negas, T.; Roth, R.S. *J. Solid State Chem.* **1970**, *1*, 409.

Acknowledgements

3 Formation of $(Ba_{0.5}Sr_{0.5})(Fe_{0.8}Zn_{0.2})O_{3-\delta}$

3.1 Summary

The results presented in the following two sections are about the formation of the $(Ba_{0.5}Sr_{0.5})(Fe_{0.8}Zn_{0.2})O_{3-\delta}$ (denoted as BSFZ) perovskite-type oxide as well as to compare the intial formation steps with those from the $(Ba_{0.5}Sr_{0.5})(Co_{0.8}Fe_{0.2})O_{3-\delta}$ (denoted as BSCF). An extensive ATEM study using electron energy-loss spectroscopy (EELS) and energy-filtered transmission electron microscopy (EFTEM) is given. Additionally, XRD and scanning electron microscopy (SEM) was applied to characterise the formation of the BSFZ perovskite in the first article. The second article emphasises the structural changes during the synthetic process by XRD and by high-resolution TEM (HRTEM). Also, thermodynamical considerations regarding the stability of the mixed carbonate were made.

As for the BSCF formation, reported in chapter 2, the first crystalline products are formed around T = 873 K and were also identified to be a mixed carbonate $(Ba_{0.5}Sr_{0.5})CO_{3-\delta}$ in aragonite modification and a mixed oxide $(Zn_{0.6}Fe_{0.4})Fe_2O_4$ in spinel modification, as found by XRD and EELS. Furthermore, it was proven by EFTEM and EELS that a nano-scaled solid state reaction between the spinel and the carbonate led to the perovskite structure. XRD studies have revealed that the phase pure perovskite BSFZ can be already obtained at temperatures of T = 1023 K.

A more detailed investigation regarding possible intermediate structures is outlined in the second article regarding this material. It was found that the reaction between the spinel and the carbonate does not lead *directly* towards the perovskite structure but a stuffed tridymite structure γ-$(Ba_{0.5}Sr_{0.5})Fe_2O_4$ was observed, which was accompanied by formation of the zinc enriched franklinite spinel.

Additionally, thermodynamic investigations revealed that the mixed carbonate remains theoretically stable up to T = 1063 K under ambient air conditions, which clearly delivers evidence that formation of BaO and SrO will not occur as the perovskite formation already takes place at temperatures of T = 1023 K. Hence the reaction takes place directly between the mixed spinel and the mixed carbonate.

3.2 How $(Ba_{0.5}Sr_{0.5})(Fe_{0.8}Zn_{0.2})O_{3-\delta}$ and $(Ba_{0.5}Sr_{0.5})(Co_{0.8}Fe_{0.2})O_{3-\delta}$ Perovskites Form via an EDTA/Citric Acid Complexing Method

Julia Martynczuk, Mirko Arnold, Haihui Wang, Jürgen Caro, and Armin Feldhoff

Advanced Materials, 19, 2134-2140 (**2007**)

COMMUNICATION

ADVANCED MATERIALS

How $(Ba_{0.5}Sr_{0.5})(Fe_{0.8}Zn_{0.2})O_{3-\delta}$ and $(Ba_{0.5}Sr_{0.5})(Co_{0.8}Fe_{0.2})O_{3-\delta}$ Perovskites Form via an EDTA/Citric Acid Complexing Method**

By *Julia Martynczuk*, *Mirko Arnold*, *Haihui Wang*, *Jürgen Caro*, and *Armin Feldhoff**

Nowadays, numerous perovskite materials with different elemental compositions are used in a range of applications. Perovskite-based ceramics are applied to the combustion of volatile organic compounds (VOCs), vehicular emission control, electrical pulse induced resistance-change and electric-field devices, high-frequency capacitors, the plasma activation of CO_2, electro- and thermochromic devices, and microwave applications such as mobile communication and satellite broadcast systems.[1] Furthermore, there is interest in perovskites for the chemical synthesis of ammonia at atmospheric pressure, ammonia oxidation, and application as nanoparticles.[2] The electrochemical importance of perovskite oxides is apparent in the case of solid oxide fuel cells (SOFCs).[3] After their first employment as cathode materials, perovskites are now used as electrolyte and anode materials, and full intermediate-temperature SOFCs are now being prepared.[4] Ceramics with both ionic and electronic conductivities are often of the perovskite type. Some basic work was carried out by Teraoka et al., who proposed $(La_{1-x}Sr_x)(Co_{1-y}Fe_y)O_{3-\delta}$ as a membrane material with a high oxygen permeability.[5] The oxygen permeation property[6] is used for the separation of oxygen from air, partial oxidation of methane, ethane, and propane, and oxygen enrichment in air.[7]

Instead of the classical solid-state synthesis route, that is, the blending and firing of powdered reactants, perovskite-type oxides of complex stoichiometries are now widely synthesized by wet-chemical methods, such as the combined citric acid and EDTA (ethylenediaminetetraacetic acid) complexing method,[8] which is investigated here, and which was first used by Shao et al.[9] The synthesis of mixed oxides by the decomposition of complex organic mixtures was introduced in the 1960s by Pâris et al.[10] Some years later Marcilly et al. described the first preparation of a perovskite-type oxide from the respective metal nitrates in a citrate process.[11] Up until now the single stages of the latter described synthesis route,

which maintains a fine-scale intermixing of the cations during all processing steps, have been investigated insufficiently even though this is essential for finding ways to utilize the full potential of the material and to optimize its functional properties.

In our group, the novel perovskite-type material $(Ba_{0.5}Sr_{0.5})(Fe_{0.8}Zn_{0.2})O_{3-\delta}$ has been developed.[12] It shows high oxygen permeation fluxes ($2.55 \text{ mL min}^{-1} \text{ cm}^{-2}$ in the partial catalytic oxidation of methane to syngas (POM) for 1.25 mm thick membrane disks) and an excellent phase stability under low oxygen partial pressures ($p_{O_2} < 1 \times 10^{-8}$ Pa in a 2 % H_2-Ar atmosphere).[13] The doping of the B site of the perovskite structure with a divalent metal like zinc, which exhibits a constant oxidation state, leads to the elimination of nonstoichiometric oxygen variations and lattice expansion caused by variations of the temperature or the chemical potential of oxygen. The procedure of the EDTA/citric acid complexing synthesis route is usually a low-temperature heating of the sol until gelation, followed by a heat treatment resulting in a pure perovskite powder. This workflow was interrupted by quenching samples for a stepwise structure analysis. The relevant stages from the gel to the pure perovskite powder are the crystallization of the amorphous gel at about 550–600 °C, the initiation of the perovskite structure formation at 600–650 °C, and the total disappearance of the intermediates at 750 °C. With this stepwise refinement it was possible to determine the crystalline intermediates formed during the preparation of a $(Ba_{0.5}Sr_{0.5})(Fe_{0.8}Zn_{0.2})O_{3-\delta}$ perovskite as a two-phase mixture of ultrafinely dispersed $(Zn_{0.6}Fe_{0.4})Fe_2O_4$ (spinel) and $(Ba_{0.5}Sr_{0.5})CO_3$ (carbonate in aragonite modification). It is interesting to note that there is obviously a prearrangement in groups of cations according to the later A (barium and strontium) and B (iron and zinc) sites in the perovskite on the nanometer scale.

This finding was verified by the following characterization methods. First, we proved the nanometer scale location of the perovskite formation between the intermediates by imaging using transmission electron microscopy (TEM) for ten different conglomerations, with homogeneous results. The specimen used was prepared, as described in the experimental part, from a quenched powder calcined at 750 °C for two hours. The exemplary TEM bright-field images the reaction pathway from spinel and carbonate to perovskite (Fig. 1a). The crystal sizes are of about 100 nm, as confirmed by TEM dark-field imaging. Having a particle with neighboring spinel and carbonate crystals, the perovskite is formed at their expense. The identification of the three phases was carried out by electron

[*] Dr. A. Feldhoff, J. Martynczuk, M. Arnold, Prof. J. Caro
Institute of Physical Chemistry and Electrochemistry
Leibniz Universität Hannover
Callinstr. 3-3a, 30167 Hannover (Germany)
E-mail: armin.feldhoff@pci.uni-hannover.de
Prof. H. Wang
College of Chemical and Energy Engineering
South China University of Technology
Guangzhou, 510640 (P.R. China)

WILEY InterScience®
DISCOVER SOMETHING GREAT
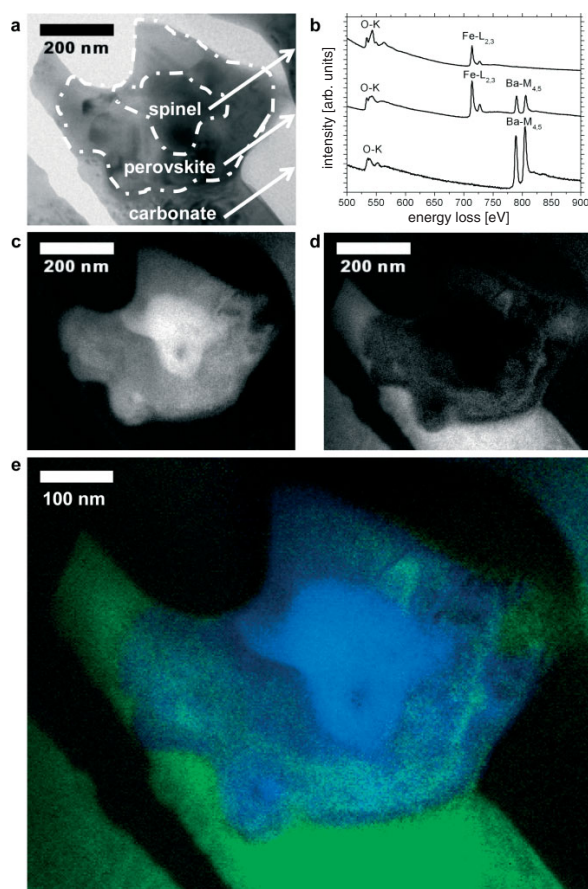
**ADVANCED
MATERIALS**

Figure 1. Transmission electron microscopy images showing the formation of the perovskite phase between the intermediates. a) Insight into the EDTA/citric acid complexing synthesis of the $(Ba_{0.5}Sr_{0.5})(Fe_{0.8}Zn_{0.2})O_{3-\delta}$ perovskite. Crystalline intermediates identified as $(Zn_{0.6}Fe_{0.4})Fe_2O_4$ spinel and $(Ba_{0.5}Sr_{0.5})CO_3$ carbonate in aragonite modification by transmission electron microscopy. b) Identification of these three phases by electron energy-loss spectroscopy (EELS) (top: spinel; middle: perovskite; bottom: carbonate). c–e) Accurate location of the different particles illustrated by energy-filtered TEM images, showing high elemental concentrations by bright contrast ((c) iron; (d) barium) or in different colours ((e) blue=iron; green=barium).

energy-loss spectroscopy (EELS), energy-filtered transmission electron microscopy (EFTEM) (Fig. 1b–1e) and selected-area electron diffraction (SAED). The presence of an Fe–$L_{2,3}$ edge and the characteristic energy-loss near-edge structure (ELNES) of the O–K ionization edge in the top spectrum identify the spinel (Fig. 1b). The carbonate structure is specified by the bottom spectrum using the Ba–$M_{4,5}$ white lines and the different characteristics of the O–K ELNES. In the middle, the O–K, the Fe–$L_{2,3}$, and the Ba–$M_{4,5}$ edges identify the perovskite structure. The accurate locations of the different particles are illustrated by Figure 1c–e, showing high elemental concentrations of iron and barium by bright contrast and different colors, respectively. The particle in the mid-

dle contains a high amount of iron (white in Fig. 1c, blue in Fig. 1e) but no barium, whereas the bottom particle comprises no iron but barium (white in Fig. 1d, green in Fig. 1e). The perovskite appears with moderate bright contrast in Figure 1c and d, and as a green/blue mixture in Figure 1e. For a more detailed specification, an investigation on the particular compounds was carried out by EELS in different energy ranges.

Electron energy-loss spectroscopy offers not only information about the elements contained in the compound, but also about their chemical environment. The inelastic scattered electrons can be resolved energy-dependently, and the resulting energy distribution with its characteristic ionization edges and energy-loss near-edge structures allows conclusions to be drawn about the element itself and, moreover, on its bonds to other elements.[14]

The specification of the carbonate structure comes to the fore in Figure 2b–2d, which shows three EEL spectra in different energy ranges. Two peaks in the C–K near-edge structure (290, 300 eV, Fig. 2b) originate from excitations of carbon 1s electrons into unoccupied non-bonding π^* and σ^* orbitals.[15] They reflect directly the presence of C=O double bonds and C–O single bonds in the carbonate ion (Fig. 2a). At 272 and 282 eV an Sr–$M_{2,3}$ ionization edge emerges. The low-loss spectrum in Figure 2c is characterized by Ba–$O_{2,3}$ and Sr–$N_{2,3}$ edges at 15–29 eV. A Ba–$N_{4,5}$ edge appears at 95 eV. O–K and Ba–$M_{4,5}$ edges are shown in Figure 2d. The fine structure of the O-K edge at 532 eV is in good agreement with that reported for $SrCO_3$.[15] Furthermore, neither an Fe-$M_{2,3}$ edge is present at 54 eV nor an Fe–$M_{2,3}$ edge at 708 eV.

The spinel is indicated by the two EEL spectra in Figure 2e and f: in the low loss region by the presence of an Fe–$M_{2,3}$ edge at 54 eV, and at higher energy losses by Fe–$L_{2,3}$ white lines (708 eV, 721 eV).[16] The characteristic ELNES of the O–K ionization edge is typical for spinels[17] and distinctly different from the one obtained for the carbonate in Figure 2c. Barium and strontium edges at 15–29 eV and 781 eV are not found.

The formation of the perovskite between the spinel and carbonate phases is shown by Figure 2g and h. The low-loss spectrum shows Ba–$O_{2,3}$ and Sr–$N_{2,3}$ edges at 15–29 eV. Additionally, an Fe–$M_{2,3}$ edge is found at 54 eV. At higher energies the Fe–$L_{2,3}$ (708 eV, 721 eV) and Ba–$M_{4,5}$ (781 eV, 796 eV) white lines appear. In addition, the characteristic O–K ELNES confirms the perovskite structure.[18]

Exemplary SAED patterns of the three phases involved in the formation of the perovskite are shown in Figure 3. For the carbonate in aragonite modification (Fig. 3a) along the [–1,7,–2] zone axis three different lattice plane distances (d = 1.77, 2.32, and 2.85 Å) are indicated. The spinel exhibits lattice plane distances of d = 4.22 and 2.98 Å along the [0,0,1] zone axis. The orientation of a perovskite particle along [1,–3,2] zone axis (Fig. 3b) resulted in lattice plane distances of d = 1.77, 1.61, 2.28, and 1.32 Å (Fig. 3c).

On the basis of these results we reason that the perovskite structure comprises the spinel and carbonate at their expense
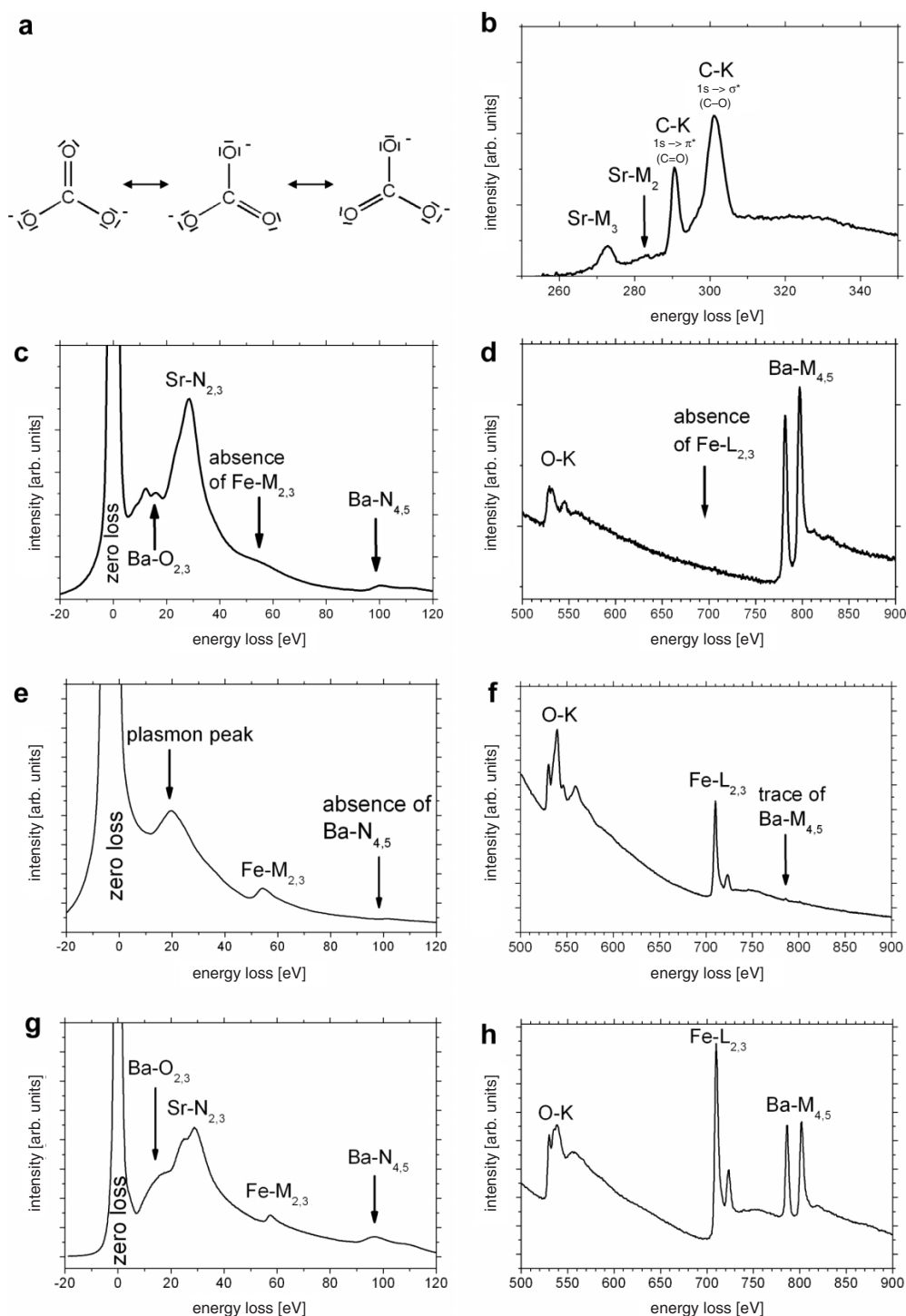
Figure 2. Identification of intermediates by elements and their chemical environment. a–d) Carbonate structure specified by three EEL spectra in different energy ranges by a closer look at the energy-loss near-edge structures (ELNES) at ionization edges for barium, strontium, carbon, and oxygen. e,f) Spinel indicated by two EEL spectra: in the low-loss region and at higher energy losses by Fe-edges and the characteristic ELNES of the O-K ionization edge. g,h) Formation of perovskite indicated by two EEL spectra. The low-loss spectrum shows Ba-O$_{2,3}$, Sr-N$_{2,3}$ and Fe-M$_{2,3}$ edges. At higher energies the characteristic O-K ELNES confirms the perovskite structure.

57
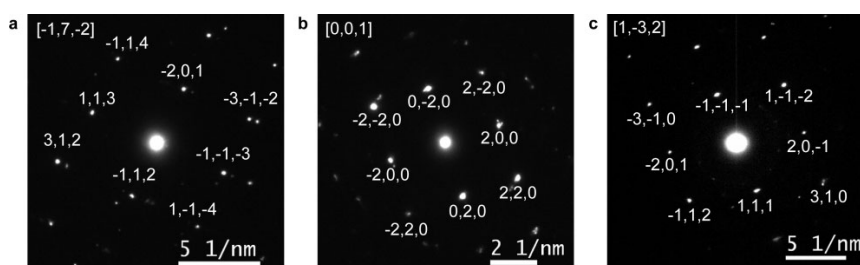
Figure 3. Selected-area electron diffraction (SAED) of the three phases: a) carbonate along the [–1,7,–2] zone axis and lattice plane distances of d = 1.77 Å (3,1,2; –1,1,4; –3,–1,–2; 1,–1,–4), d = 2.32 Å (1,1,3; –1,–1,–3), d = 2.85 Å (–2,0,1; –1,1,2). b) Spinel along [0,0,1] zone axis and lattice plane distances of d = 4.22 Å (0,–2,0; 2,0,0; 0,2,0; –2,0,0), d = 2.98 Å (2,–2,0; 2,2,0; –2,2,0; –2,–2,0). c) Perovskite along [1,–3,2] zone axis and lattice plane distances of d = 1.77 Å (2,0,–1; –2,0,1), d = 1.61 Å (–1,1,2; 1,–1,–2), d = 2.28 Å (1,1,1; –1,–1,–1), d = 1.32 Å (3,1,0; –3,–1,0).

in a solid state reaction. Further, we expect that the grain sizes of the primarily formed perovskite crystals are in the same range as those of the crystalline intermediates, and coarsen afterwards with time during temperature treatment.

The grain size distribution of the perovskite particles is of high importance for the subsequent properties of the synthesized ceramic. The smaller the grains of the powder underlying the green compact of the subsequent ceramic, the better is the sintering behavior, for example, lower sintering temperature and shorter time, giving less porosity and the possibility to obtain highly dense ceramics. Thus, it is essential to find the optimized calcination procedure to obtain a perovskite powder of high purity, but with the smallest possible grains.

Thermogravimetric analyses (TGA) pointed out that the organic compounds are burned step-by-step, and CO_3^{2-}, NO_3^-, and NH_4NO_3 are eliminated.[19] After crystallization of the amorphous gel at about 550–600 °C, no nitrogen-containing compounds are found, indicating the total release of NO_x. Figure 4a and b show scanning electron microscopy (SEM) images of a powder calcined at 650 °C for two hours, containing approximately equal amounts of int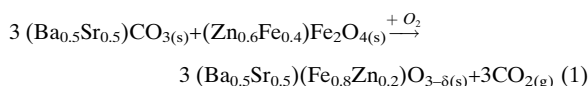ermediates and perovskite, as estimated by the XRD intensities. At the initiation of the perovskite structure formation at 600–650 °C, an evaporation of CO_2 caused by the decomposition of the carbonate is observed. Due to this evaporation the powder becomes porous, but the grain sizes remain in the range of 400 nm and smaller. The total disappearance of the intermediates is observable after calcination at 750 °C for ten hours (Fig. 4c, 4d). The grain coarsening has proceeded slightly to grain sizes of up to 700 nm. The calcination at 950 °C for 2 h produces a powder run through a coarsening of grains to sizes of around one micrometer. On account of the

grain growth at the expense of smaller grains the powder gets more and more porous. Figure 4f images the presintering in some parts of the powder. Based on these results a chemical equation for the solid-state reaction between the intermediates has been established:

$$3\ (Ba_{0.5}Sr_{0.5})CO_{3(s)}+(Zn_{0.6}Fe_{0.4})Fe_2O_{4(s)} \xrightarrow{+ O_2}$$
$$3\ (Ba_{0.5}Sr_{0.5})(Fe_{0.8}Zn_{0.2})O_{3-\delta(s)}+3CO_{2(g)} \quad (1)$$

This finding confirms that the primarily formed perovskite crystals possess grain sizes of the same range as those of the crystalline intermediates and that the usual calcination at higher temperatures is not required, and is even undesirable
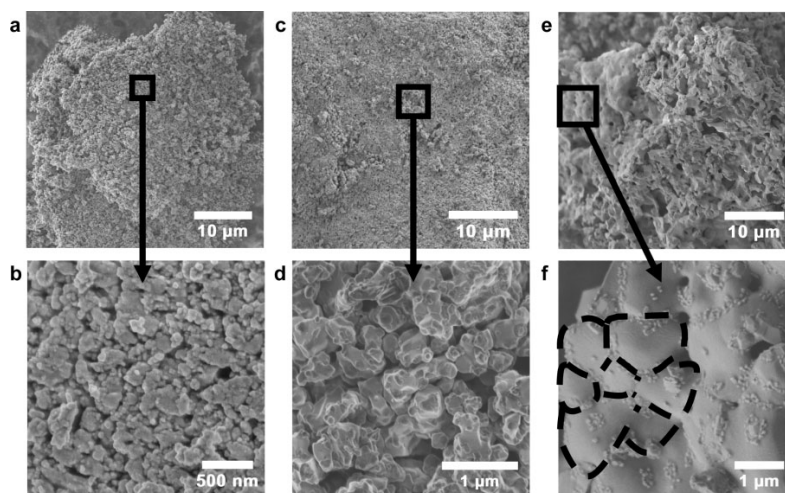
Figure 4. Grain coarsening and gaseous release during calcination at higher temperatures. a,b) Scanning electron microscopy (SEM) images of an approximately equal amount of intermediates and perovskite containing powder calcined at 650 °C for two hours. Grains are of size 400 nm and smaller. c,d) Pure perovskite powder in the SEM after calcination at 750 °C for ten hours. Sizes of the grains are up to 700 nm. The powder gets highly porous because of the release of gaseous CO_2 (Eq. (1)). e,f) Grain coarsening of perovskite powders to 1 μm after calcination at 950 °C for two hours.

**ADVANCED
MATERIALS**

due to grain coarsening during further heat treatment. Additionally, the presintering of the powder should be avoided in order to facilitate the pressing of the green compact for the ceramic production.

Why is the perovskite formed directly without the formation of barium strontium oxides? The decomposition of the carbonate can take place only if it forces a CO_2 potential that is higher than that in the surrounding atmosphere. The decomposition temperature for the $(Ba_{0.5}Sr_{0.5})CO_3$, which was calculated from the thermodynamic data for barium and strontium carbonate (see Supporting Information, Fig. S1), is 808 °C, higher than the temperature of the perovskite formation. Under the experimental conditions applied, zinc and iron do not form carbonates because, as calculated from thermodynamic data (Supporting Information Fig. S1), in ambient air, zinc carbonate and iron carbonate are not stable above 10 and 27 °C, respectively. Taking into account kinetic factors that inhibit the decomposition process, the measured temperature for zinc carbonate is in the range of 250–290 °C, and above 300 °C for iron carbonate.[20] Among the iron oxides, the spinel phase is the most stable phase in the relevant temperature range, as can be seen from ΔG curves.[21] In the pres-

ence of Zn, however, the incorporation of Zn^{2+} into the spinel is energetically favorable as ΔG_R lies in the range of –380 to –260 kJ mole^{-1} for 500–800 °C for the reaction:[22]

$$4FeFe_2O_{4(s)}+6ZnO_{(s)}+O_{2(g)}\rightarrow 6ZnFe_2O_{4(s)} \qquad (2)$$

The basis of the perovskite formation process of $(Ba_{0.5}Sr_{0.5})(Fe_{0.8}Zn_{0.2})O_{3-\delta}$ is now proved, and this knowledge provides new possibilities for optimization of the ceramic synthesis. But how general are these results? To verify the assumption that perovskite oxide formation in an EDTA/citric acid complexing synthesis route might proceed over through analogous crystalline intermediates, the $(Ba_{0.5}Sr_{0.5})(Co_{0.8}Fe_{0.2})O_{3-\delta}$ perovskite, which is a promising reduced-temperature cathode for SOFCs,[23] was also investigated. It was found that after gelation the first crystalline phases were a $(Ba_{0.5}Sr_{0.5})CO_3$ carbonate in the aragonite modification and an $(Fe_{0.6}Co_{0.4})Co_2O_4$ spinel documented by X-ray diffraction. The diffraction pattern in Figure 5a was measured for a $(Ba_{0.5}Sr_{0.5})(Co_{0.8}Fe_{0.2})O_{3-\delta}$ perovskite powder after calcination at 600 °C for two hours. In comparison to the diffraction pattern above (Fig. 5b) the pattern detected for a

Figure 5. Analogy with synthesis of another perovskite and development from intermediates to perovskite. X-ray diffraction pattern for $(Ba_{0.5}Sr_{0.5})(Co_{0.8}Fe_{0.2})O_{3-\delta}$ at 600 °C for two hours provides evidence that the perovskite formation proceeds through analogous intermediates (spinel and carbonate) as for the synthesis of $(Ba_{0.5}Sr_{0.5})(Fe_{0.8}Zn_{0.2})O_{3-\delta}$. The latter is formed by treatments from two hours at 600 °C to two hours at 750 °C to ten hours at 750 °C. The intermediates start to vanish due to the formation of the perovskite.

59

**ADVANCED
MATERIALS**

$(Ba_{0.5}Sr_{0.5})(Fe_{0.8}Zn_{0.2})O_{3-\delta}$ powder run through the same temperature treatment indicates that the identified phases coincide with a difference in the spinel lattice caused by the diverse cations. With this result we can expect that the perovskite oxide synthesis with EDTA/citric acid complexing methods can proceed with the formation of a spinel and carbonate after the gelation.

For the $(Ba_{0.5}Sr_{0.5})(Fe_{0.8}Zn_{0.2})O_{3-\delta}$ perovskite oxide the two diffraction patterns in Figure 5c and d exhibit the reaction pathway from the intermediates $(Ba_{0.5}Sr_{0.5})CO_3$ and $(Zn_{0.6}Fe_{0.4})Fe_2O_4$ towards the perovskite. Increasing the calcination temperature step by step no other phase transition is detected, and the perovskite formation at the expense of the carbonate and the spinel can be observed continuously. This was investigated in steps of 10 °C from 600–750 °C, and is shown for the heat treatment from two hours at 600 °C to two hours at 750 °C, to finally pure perovskite after ten hours at 750 °C. With increasing sizes of crystallites the perovskite reflexes narrow during calcinations, indicating a grain coarsening that was also observed by electron microscopy.

Advanced TEM methods together with SEM and XRD can give important new insights into the initial formation of a perovskite phase. A profound knowledge of the perovskite formation process opens new ways to engage the microstructure of the underlying ceramic material, for example, to fine-tune both grain stoichiometries and grain boundaries in the ceramic material and hence to optimize the sintering behavior (lower temperature and shorter time) in order to achieve fewer pores and highly dense ceramics.

We achieved a structural determination of the fine-scale intermixed intermediates formed during the perovskite preparation by employing an EDTA/citrate process as a spinel, and carbonate in the aragonite polymorph. Thus, prearrangement in groups of cations according to the later A and B sites in the perovskite structure is indicated. TEM and EFTEM as well as EELS provide evidence that the perovskite structure is formed in a nanometer-scale solid-state reaction between the above mentioned intermediates and at their expense. For this purpose not only the elemental composition of the three phases were determined, but also the near-edge structures were considered for chemical environment cognition and compared with current literature.

Grain sizes obtained in different perovskite synthesis steps show that the primarily formed perovskite crystals are of the same size as the intermediates and coarsen afterwards during temperature treatment. The common calcination temperature of 950 °C can be decreased to 750 °C to avoid presintering and therefore facilitate the pressing of the green compact for the ceramic production.

In the synthesis of two distinct perovskite oxides by an EDTA/citric acid complexing method it was shown that the perovskites form in nanometer-scale solid-state reactions between finely dispersed crystalline intermediates, and that the first crystalline intermediates are a complex spinel of the later B site ions and a complex carbonate of the later A site ions of the perovskite. Hence, it is expected that perovskite oxide

syntheses via EDTA/citric acid complexing methods will generally proceed with the formation of a spinel and a carbonate after gelation.

Experimental

A synthesis method with combined citric acid and EDTA acid as the complexing agents was applied. A given amount of $Ba(NO_3)_2$ powder was dissolved in an aqueous solution of $Zn(NO_3)_2$, $Fe(NO_3)_3$, and $Sr(NO_3)_2$, followed by the addition of EDTA acid. After agitation for a certain time, a proper amount of citric acid was introduced, with the molar ratio of EDTA acid : citric acid : total of metal cations controlled at around 1:1.5:1. After addition of $NH_3 \cdot H_2O$, the pH value of the solution was adjusted in the range of 6–9 by the addition of supplementary $NH_3 \cdot H_2O$. Water was evaporated with stirring in the temperature range of 120–150 °C. After evaporation for several hours, the transparent solution transformed into a dark purple gel. Further heat treatments were applied at temperatures up to 950 °C.

Transmission electron microscopy (TEM) was performed at 200 kV on a field-emission instrument of type JEOL JEM-2100F with an ultra-high resolution pole piece ($C_S = 0.5$ mm) that provides a point-resolution better than 0.19 nm. Moreover, the microscope was equipped with an energy filter (Gatan GIF 2001) with a 1k-CCD camera. The filter was employed to acquire energy-filtered transmission electron microscopy (EFTEM) images and electron energy-loss spectra (EELS), with a special emphasis on energy-loss near-edge structures (ELNES) at ionization edges. Powders were prepared for TEM investigation by crushing them by mortar and pestle and afterwards epoxy-gluing them between two silicon single crystals. 1×1.5×3 mm pieces were cut and polished on polymer embedded diamond lapping films to 0.01×1×2.5 mm, approximately. Finally, Ar^+ ion sputtering was employed at 3 kV (Gatan, model 691 PIPS, precision ion polishing system) under shallow incident angles of 4–8° until electron transparency was achieved.

Scanning electron microscopy (SEM) was employed on a field-emission instrument (JEOL JSM-6700F). Secondary electron (SE) microscopy images were taken at low excitation voltages in the range of 0.5–2 kV.

X-ray diffraction (XRD) was performed on a Philips X'pert-MPD instrument using monochromator-filtered Cu Kα radiation at 40 kV and 40 mA, receiving slit of 0.15 mm and count times of 3 s step^{-1}. Data were collected in a step-scan mode in the range of 20–50° with intervals of 0.03°. Data for interpretation were taken from the PDF-2 database with PDF numbers $FeFe_2O_4$ [19-629], $ZnFe_2O_4$ [22-1012], $CoFe_2O_4$ [3-864], $BaCO_3$ [45-1471], $SrCO_3$ [5-418], $SrFeO_{3-x}$ [34-641], $BaFeO_3$ [14-80]. Lattice parameters for the exact stoichiometries were calculated according to homogeneous solid solutions.

[1] a) S. Irusta, M. P. Pina, M. Menéndez, J. Santamaria, *Catal. Lett.* **1998**, *54*, 69. b) N. Labhsetwar, R. B. Biniwale, R. Kumar, S. Rayalu, S. Devotta, *Catal. Surv. Asia* **2006**, *10*, 55. c) X. Chen, J. Strozier, N. J. Wu, A. Ignatiev, Y. B. Nian, *New J. Phys.* **2006**, *8*, 229. d) C. H. Ahn, J.-M. Triscone, J. Mannhart, *Nature* **2003**, *424*, 1015. e) D. Dimos, C. H. Mueller, *Annu. Rev. Mater. Sci.* **1998**, *28*, 397. f) R. Li, Q. Tang, S. Yin, T. Sato, *Plasma Chem. Plasma Process.* **2006**, *28*, 267. g) V. Thangadurai, W. Weppner, *J. Electrochem. Soc.* **2004**, *151*, H1. h) P. Laffez, M. Zaghrioui, L. Reversat, P. Ruello, *Appl. Phys. Lett.* **2006**, *89*, 081 909. i) T. Liu, X.-Z. Zhao, W. Chen, *J. Am. Ceram. Soc.* **2006**, *89*, 1153.

[2] a) Z.-J. Li, R.-Q. Liu, J.-D. Wang, Y.-H. Xie, F. Yue, *J. Solid State Electrochem.* **2005**, *9*, 201. b) J. Pérez-Ramírez, B. Vigeland, *Angew.*

ADVANCED MATERIALS

Chem. Int. Ed. **2005**, *44*, 1112. c) Y. Mao, S. S. Wong, *Adv. Mater*. **2005**, *17*, 2194. d) A. Weidenkaff, *Adv. Eng. Mater*. **2004**, *6*, 709.

[3] H. Yokokawa, N. Sakai, T. Kawada, M. Dokiya, *Solid State Ionics* **1992**, *52*, 43.

[4] a) A. Esquirol, N. P. Brandon, J. A. Kilner, M. Mogensen, *J. Electrochem. Soc.* **2004**, *151*, A1847. b) S. Tao, J. T. S. Irvine, *Adv. Mater*. **2006**, *18*, 1581. c) T. Ishihara, *Bull. Chem. Soc. Jpn*. **2006**, *76*, 1155. d) Q. X. Fu, F. Tietz, D. Stöver, *J. Electrochem. Soc.* **2006**, *153*, D74. e) M.-F. Hsu, L.-J. Wu, J.-M. Wu, Y.-H. Shiu, K.-F. Lin, *Electrochem. Solid-State Lett*. **2006**, *9*, A193. f) S. Tao, J. T. S. Irvine, J. A. Kilner, *Adv. Mater*. **2005**, *17*, 1734.

[5] Y. Teraoka, H.-M. Zhang, S. Furukawa, N. Yamazoe, *Chem. Lett.* **1985**, *11*, 1743.

[6] R. Merkle, J. Maier, H. J. M. Bouwmeester, *Angew. Chem. Int. Ed.* **2004**, *43*, 5069.

[7] a) M. Liu, V. Joshi, Y. Shen, K. Krist, *US Patent 5 273 628*, **1993**. b) U. Balachandran, J. T. Dusek, R. L. Mieville, R. B. Poeppel, M. S. Kleefisch, S. Pei, T. P. Kobylinski, C. A. Udovich, A. C. Bose, *Appl. Catal., A* **1995**, *133*, 19. c) H. Wang, Y. Cong, W. Yang, *J. Membr. Sci.* **2002**, *209*, 143. d) H. Wang, Y. Cong, X. Zhu, W. Yang, *React. Kinet. Catal. Lett*. **2003**, *79*, 351. e) C. Hamel, A. Seidel-Morgenstern, T. Schiestel, S. Werth, H. Wang, C. Tablet, J. Caro, *AIChE J.* **2006**, *52*, 3118. f) H. Wang, S. Werth, T. Schiestel, J. Caro, *Angew. Chem. Int. Ed.* **2005**, *44*, 6906.

[8] H. J. M. Bouwmeester, A. J. Burggraaf, in *Fundamentals of Inorganic Membrane Science and Technology*, Vol. 4, (Eds: A. J. Burggraaf. L. Cot) Elsevier Science B. V., Amsterdam **1996**, Ch. 10.

[9] Z. Shao, W. Yang, Y. Cong, H. Dong, J. Tong, G. Xiong, *J. Membr. Sci.* **2000**, *172*, 177.

[10] J. Pâris, R. Pâris, *Bull. Soc. Chim. Fr.* **1965**, *4*, 1138.

[11] C. Marcilly, P. Courty, B. Delmon, *J. Am. Ceram. Soc.* **1970**, *53*, 56.

[12] H. Wang, G. Grubert, C. Tablet, J. Caro, *Patent EP 0 402 056*, **2005**.

[13] H. Wang, C. Tablet, A. Feldhoff, J. Caro, *Adv. Mater.* **2005**, *17*, 1785.

[14] *Electron Energy Loss Spectrometry in Materials Science*. 2nd ed. (Eds: M. M. Disko, C. C. Ahn, B. Fultz) TMS, Warrendale, Pennsylvania PA **2001**.

[15] J. L. Mansot, V. Golabkan, L. Romana, T. Césaire, *J. Microsc.* **2003**, *210*, 110.

[16] L. A. J. Garvie, P. R. Buseck, *Nature* **1998**, *396*, 667.

[17] a) C. C. Calvert, A. Brown, R. Brydson, *J. Electron Spectrosc. Rel. Phenom.* **2005**, *143*, 173. b) F. T. Docherty, A. J. Craven, D. W. McComb, J. Skakle, *Ultramicroscopy* **2001**, *86*, 273.

[18] A. S. Sefat, G. Amow, M.-Y. Wu, G. A. Botton, J. E. Greendan, *J. Solid State Chem.* **2005**, *178*, 1008.

[19] a) H. M. Zhang, T. Teraoka, N. Yamazoe, *Chem. Lett.* **1987**, *4*, 665. b) R. H. E. van Doorn, H. Kruidhof, A. Nijmeijer, L. Winnubst, A. J. Burggraaf, *J. Mater. Chem.* **1998**, *8*, 2109.

[20] a) A. M. Gadalla, *Int. J. Chem. Kinet.* **1984**, *16*, 1471. b) R. J. Meyer, *Gmelin Handbook of Inorganic Chemistry*, 8th ed., Chemie, Berlin **1932**, *59*, 508.

[21] R. A. Swalin, *Thermodynamics of Solids*, Wiley, New York, **1962**, p. 84.

[22] I. Barin, F. Sauert, G. Patzki, *Thermochemical Data of Pure Substances*, 3rd ed., Vol. 1 and 2, VCH, Weinheim, Germany **1995**.

[23] Z. Shao, S. M. Haile, *Nature* **2004**, *431*, 170.

3.3 The sol-gel synthesis of perovskites by an EDTA/citrate complexing method involves nanoscale solid state reactions

Armin Feldhoff, Mirko Arnold, Julia Martynczuk, Thorsten M. Gesing, Haihui Wang

ELSEVIER

The sol−gel synthesis of perovskites by an EDTA/citrate complexing method involves nanoscale solid state reactions

A. Feldhoff [a,*], M. Arnold [a], J. Martynczuk [a], Th.M. Gesing [b], H. Wang [a,c]

[a] *Institute of Physical Chemistry and Electrochemistry, Leibniz Universität Hannover, Callinstraße 3-3A, D-30167 Hannover, Germany*
[b] *Institute of Mineralogy, Leibniz Universität Hannover, Welfengarten 1, D-30167 Hannover, Germany*
[c] *College of Chemical and Energy Engineering, South China University of Technology, Guangzhou 510640, PR China*

On the occasion of the 75th birthday of Prof. Schmalzried.

Abstract

Nowadays, sol−gel procedures are well established in the synthesis of complex oxides as they allow to obtain phase pure products and to control precisely their stoichiometry. This quality makes them a tool of choice for the preparation of perovskite-type oxides. To optimize the functional properties of these materials, it is essential to set accurately their possible complex stoichiometries. However, details of the formation of the perovskite crystal remain obscure. Different stages of an ethylene-diamine-tetraacetic acid (EDTA)/citrate-gel based synthesis process for mixed conducting $(Ba_{0.5}Sr_{0.5})(Fe_{0.8}Zn_{0.2})O_{3-\delta}$ of cubic perovskite structure are elucidated. The combination of analytical transmission electron microscopy with X-ray diffraction reveals that the perovskite-type oxide is formed already at moderate temperatures at around 700 °C via nanoscale solid state reactions between finely-dispersed crystalline intermediates identified as a spinel and a carbonate. The reaction scheme, however, is intricate and includes stuffed tridymite structures as transient phases. The ultrafine intermixing of extremely small reactants makes EDTA/citrate-gel based procedures superior to classical solid state routes with respect to applications that demand phase purity and stoichiometry control.

1. Introduction

Conventionally, complex oxides are prepared by the solid state route that is the blending of powdered reactants, mostly oxides and carbonates, and their firing at temperatures as high as 1200 °C. At these high temperatures the loss of the most volatile component may easily occur leading to non-stoichiometric products with decreased functional properties.

Alternative chemical synthesis processes have been introduced in the 1960s by the thermal decomposition of stirred metal−organic complexes that employ distinctly lower temperatures in the range of 600−700 °C [1,2,3]. All these processes rely on the chemistry of gels that contain all the cations in the desired ratios [4,5]. Even though variants of these sol−gel procedures are widely used today, details of the formation of the final crystalline product are still little known. The combined ethylene-diamine-tetraacetic acid (EDTA)/citrate complexing method under investigation has been introduced some years ago [6]. It has been shown elsewhere [7−9] that complex oxides of cubic perovskite structure are formed in nanoscale solid state reactions between carbonate and spinel intermediates. The general reaction scheme has been outlined for the perovskite stoichiometries $(Ba_{0.5}Sr_{0.5})(Fe_{0.8}Zn_{0.2})O_{3-\delta}$ and

3. Formation of $(Ba_{0.5}Sr_{0.5})(Fe_{0.8}Zn_{0.2})O_{3-\delta}$

$(Ba_{0.5}Sr_{0.5})(Co_{0.8}Fe_{0.2})O_{3-\delta}$. The present study is devoted to details of the formation of the Zn-containing perovskite that turns out to be intricate on the atomic scale.

2. Materials and methods

The synthesis process is evaluated for a perovskite-type oxide that is a prospective membrane material for oxygen separation technologies [10−12] or electrode material for solid oxide fuel cells [13]. In the temperature range of 700−950 °C, $(Ba_{0.5}Sr_{0.5})(Fe_{0.8}Zn_{0.2})O_{3-\delta}$ [14,15] is a mixed electron and oxygen conductor that provides high oxygen fluxes and exhibits an excellent phase stability even under low oxygen partial pressures, superior to other compositions.

The processing route employs both citric acid and EDTA as the complexing and gelation agents [6] and has been adapted for the specific stoichiometry under investigation. Proper amounts of $Ba(NO_3)_2$, $Sr(NO_3)_2$, $Fe(NO_3)_3$, and $Zn(NO_3)_2$ were dissolved in water followed by the addition of citric acid, EDTA and NH_3. In the temperature range of 120−150 °C, the reaction mixture was then heated under constant stirring to obtain a purple-coloured gel. Afterwards, the gel was pre-calcined for 1 h at 700 °C. The pre-calcined powders were grounded and heated at temperatures up to 750 °C with a heating rate of 3 °C/min. Intermediates as well as final products were analyzed by several techniques that are described below.

X-ray diffraction (XRD) was conducted in a $\theta/2\theta$ geometry on a Philips X'pert-MPD instrument using monochromated Cu $K\alpha_{1,2}$ radiation at 40 kV and 40 mA, receiving slit of 0.15 mm and count times of 5 s/step. Data were collected in a step-scan mode in the 2θ range of 20−50° with intervals of 0.03°.

Data for interpretation were taken from the ICDD PDF-2 database with PDF numbers $FeFe_2O_4$ [19-629], $ZnFe_2O_4$ [22-1012], Fe_2O_3 [33-664], $SrFeO_{3-x}$ [34-641], and $BaFeO_{3-x}$ [147-180]. Lattice parameters for the exact stoichiometries have been calculated according to homogeneous solid solutions. To index experimental data related to $(Ba_{0.5}Sr_{0.5})CO_3$, the structure has been described with unit cell parameters according to Ref. [16]. To index data related to $(Ba_{1-x}Sr_x)Fe_2O_4$, the structure has been described in space group $Cmc2_1$ (No. 36) based on the structure given in Ref. [17].

For structure refinements of the product phase, X-ray powder diffraction data were collected on a Bruker AXS D8 Advance diffractometer using a transmission geometry, a Göbel mirror and Cu $K\alpha_{1,2}$ radiation. Six thousand data points were collected with a step width of 0.02° in the 2θ range from 20° to 140°. XRD powder data Rietveld refinements were carried out by using TOPAS 3.0 (Bruker AXS) software. During refinements, general parameters such as the scale factor, seven background parameters and the zero point of the counter were optimized. Profile shape calculations were carried out on the basis of standard instrumental parameters using the fundamental parameter method implemented in the program, varying also the average crystal size (integral breadth) and the strain parameter ε_0 (FWHM based strain calculation assuming intermediate strain broadening modelled by a Voigt function giving $\Delta d/2\theta$ with a 50% probability). Additionally, the cell parameter and the displacement parameters were refined. In the case of site occupation with mixed atoms, linear constraints were used for occupancy (occupancy of atom B is equivalent to 1.0 minus occupancy of atom A) and displacement parameters (atoms on the same position have the same displacement parameter).

Transmission electron microscopy (TEM) and scanning transmission electron microscopy (STEM) were performed at 200 kV on a field-emission instrument of the type JEOL JEM-2100F. The microscope was equipped with an ultra-high-resolution pole piece that provides a point-resolution better than 0.19 nm (spherical aberration constant $C_S = 0.5$ mm, chromatic aberration constant $C_C = 0.5$ mm) and allowed to make high-resolution transmission electron microscopy (HRTEM). STEM was conducted in high-angle annular dark-field (HAADF) contrast that allows to obtain mass-thickness information. The microscope was equipped with an energy filter of the type Gatan GIF 2001 with a 1k charge-coupled-device (CCD) camera. The filter was used to enhance the dynamics in selected area electron diffraction (SAED) pattern by elastic filtering with a bandwidth of 15 eV. The filter was employed as well to acquire electron energy-loss spectra (EELS) of core-loss energies with a special emphasis on energy-loss near-edge structures (ELNES) at ionization edges. To obtain elemental maps via energy-filtered transmission electron microscopy (EFTEM), the three-window technique was utilized with 40 eV energy slit and power law model [18]. For the Fe-L edge energy slits were centered at 643, 683 eV (pre-edge) and 728 eV (post-edge). To avoid any overlap with Fe-L signals, for the Ba-M edge energy slits were centered at 661, 751 eV (pre-edge) and 801 eV (post-edge). Individual exposure times were 30 s, respectively. Elemental analysis by energy-dispersive X-ray spectroscopy (EDXS) was made using an Oxford Instruments INCA-200-TEM system with an ultra-thin window that was attached to the microscope.

To obtain specimen for TEM, dried gel was crushed in ethanol by mortar and pestle. The suspension was dropped from a pipette to a 300-mesh copper-supported carbon foil (Quantifoil) that was placed on a piece of filter paper to wick away excess ethanol. Calcined powders were prepared for TEM investigations by epoxy gluing them between two pieces of silicon wafer. These sandwiches were cut into $1 \times 1.5 \times 3$ mm rectangular pieces and polished in cross-section on polymer embedded diamond lapping films down to $0.01 \times 1 \times 2.5$ mm, approximately (Allied High Tech, Multiprep). Thinned sandwiches were glued onto a copper slot grid, respectively, and Ar^+ ion sputtered at 3 kV under an incident angle of 6° (Gatan, model 691 PIPS, precision ion polishing system) until electron transparency was achieved.

A quantity of 2 g of pure $(Ba_{0.5}Sr_{0.5})CO_3$ powder and $(Zn_{0.6}Fe_{0.4})Fe_2O_4$ powder was synthesized by the EDTA/citrate method, and phase purity and crystal size were determined by SEM (JEOL JSM-6700F), respectively. Experimental determination of the CO_2 equilibrium pressure above the carbonate as a function of temperatures was performed in

3.3. The sol-gel synthesis of perovskites by an EDTA/citrate complexing method

a quartz glass equipment flanged to a turbo molecular pump. After sealing and evacuating the equipment from atmospheric pressure to 1 Pa and heating to 700 °C, the pressure was measured with a Pirani gage in steps of 50 °C up to 1000 °C after equilibration times of ca. 1/2 h, respectively.

3. Results and discussion

3.1. Early stages

Gelation takes place in the temperature range of 120–150 °C due to the release of water and is accompanied by the evaporation of ammonia. This leads to a decrease of the nitrogen and oxygen content as it is shown elsewhere [7]. Fig. 1 shows a magnification series of Z-contrast HAADF micrographs of the gel after 18 h at 150 °C. The gel is characterized by a fine dispersion of metal complexes (high Z) in a polymerized network (low Z). Individual metal atoms or clustered metal complexes give rise to strong electron scattering

and thus bright contrast in the micrographs. The polymeric matrix composed of atoms with much lower scattering cross-sections appears with grey contrast. Concerning the stability constants for the complex formation K given logarithmically in Table 1, the distinctly higher K-values for EDTA for all four cations make a total complexation with EDTA most likely. On the contrary, the citric acid contributes to the gelation, and formation of a polymeric network, by a condensation due to the esterification of the alcohol group of the citric acid molecule with the carboxyl group of another citric acid molecule or an EDTA molecule. In Fig. 1a and b some relatively large clusters of metal complexes with sizes of around 15 nm are present. Predominantly, cluster sizes are distinctly smaller as it can be seen in Fig. 1c and d. An eminent fraction of clusters is around 5 nm in size. Moreover, the close-up in Fig. 1d shows structural details with sizes of just 1 nm that hint to the presence of very small individual clusters of metal complexes. In conclusion, the sol−gel method prevails a very fine intermixing of metal cations on the nanometer scale.
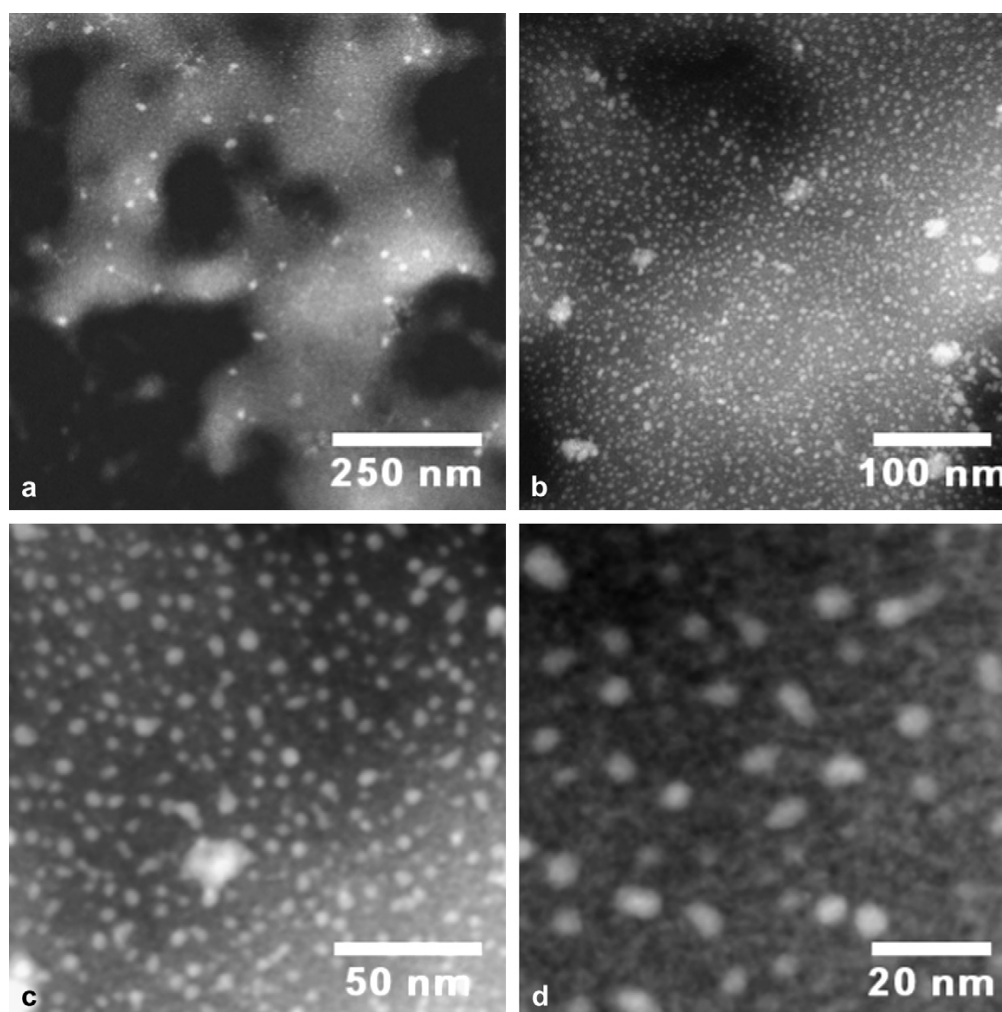

Fig. 1. Magnification series in high-angle annular dark-field contrast of the gel after 18 h at 150 °C.

3. Formation of $(Ba_{0.5}Sr_{0.5})(Fe_{0.8}Zn_{0.2})O_{3-\delta}$

Table 1
Complex forming constants of metal cations (from Refs. [19,20])

	EDTA, log K	Citric acid, log K
Ba^{2+}	7.86	2.73
Sr^{2+}	8.74	3.02
Fe^{3+}	25.1	11.2
Zn^{2+}	16.5	4.76

3.2. Crystalline intermediates and perovskite

During further heating the gel starts to crystallize at about 550–600 °C under the formation of intermediate phases that can be detected by XRD. Typical diffraction pattern after 1 h at 700 °C are given for three preparations in Fig. 2a–c showing reflections from an aragonite-type carbonate (Fig. 2a,c and f) and spinel-type $(Zn_{0.6}Fe_{0.4})Fe_2O_4$ oxide (Fig. 2b,c and g). During cumulated further heat treatments of the powder in
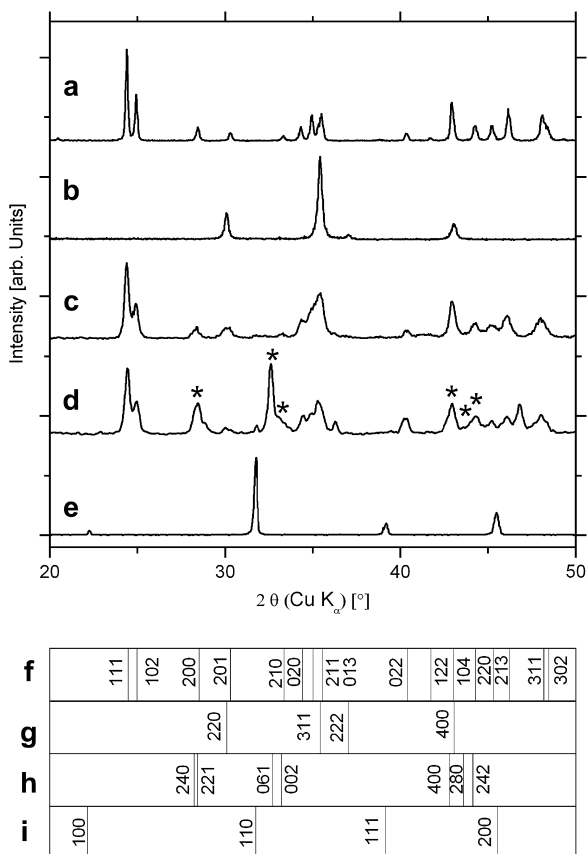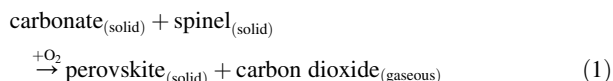

Fig. 2. X-ray powder diffraction of intermediates and perovskite. (a) Taken from the synthesis of $(Ba_{0.5}Sr_{0.5})CO_3$ after 10 h at 750 °C, (b) taken from the synthesis of $(Zn_{0.6}Fe_{0.4})Fe_2O_4$ after 1 h at 700 °C, (c–e) taken from the synthesis of $(Ba_{0.5}Sr_{0.5})(Fe_{0.8}Zn_{0.2})O_{3-\delta}$ after (c) 1 h at 700 °C, (d) additional 12 h at 700 °C, (e) additional 10 h at 750 °C. (f–i) Assignment of diffraction lines for different phases: (f) aragonite-type $(Ba_{0.5}Sr_{0.5})CO_3$ carbonate, (g) $(Zn_{0.6}Fe_{0.4})Fe_2O_4$ spinel, (h) γ-$(Ba_{0.5}Sr_{0.5})Fe_2O_4$, (i) perovskite-type $(Ba_{0.5}Sr_{0.5})(Fe_{0.8}Zn_{0.2})O_{3-\delta}$.

Fig. 2c, the reflections of the intermediate phases become smaller, reflections of a further transient phase of stuffed tridymite-type oxide arise (Fig. 2d), and finally the perovskite structure is formed (Fig. 2e).

Fig. 2d shows an XRD pattern after heating the powder additionally 12 h at 700 °C. The reflections of the intermediates are less pronounced and broad reflections of a Ba–Sr–Fe oxide dominate (marked by stars), which can be compared to a γ-$(Ba_{0.5}Sr_{0.5})Fe_2O_4$-type phase (Fig. 2h). More details concerning the transient phase are discussed below in context of Fig. 7. After additional heating for 10 h at 750 °C, the intermediate and transient phases are completely vanished and a pure perovskite powder is obtained (Fig. 2e and i).

The XRD analysis points to a solid state reaction in the nanoscale powder between the intermediates of the following simplified type:

$$\text{carbonate}_{(solid)} + \text{spinel}_{(solid)}$$

$$\xrightarrow{+O_2} \text{perovskite}_{(solid)} + \text{carbon dioxide}_{(gaseous)} \qquad (1)$$

The liberation of gaseous CO_2 is manifested in the evolution of a porous sponge-like solid that has been investigated by scanning electron microscopy [7,8]. Details of this reaction are, however, more intricate as it is manifested in additional transient phases. All involved phases are discussed in the following.

3.2.1. Rietveld refinement of the $(Ba_{0.5}Sr_{0.5})(Fe_{0.8}Zn_{0.2})O_{3-\delta}$ product

The stoichiometry of the product has been determined by EDXS during TEM experiments to be close to $(Ba_{0.5}Sr_{0.5})$ $(Fe_{0.8}Zn_{0.2})O_{3-\delta}$ as is described elsewhere [14]. By XRD (Fig. 3), the perovskite was found to crystallize in the cubic space group Pm-$3m$ (No. 221) with a lattice parameter of 0.39900(2) nm. Barium and strontium were refined on the same crystallographic position 1a (0,0,0) with 52(2)% occupation for the barium atoms corresponding to the chemical analysis and a displacement parameter of $B = 1.4(1)$. Iron (80%) and zinc (20%) were calculated on the 1b (1/2,1/2,1/2) position showing a high displacement of $B = 2.4(1)$. An individual refinement of the occupancy parameters for this position is not possible. An equivalent high displacement of $B = 3.1(5)$ was found for the oxygen atoms on the 3c (0,1/2,1/2) site. These higher displacement parameters correspond to a strain parameter of $\varepsilon_0 = 0.157(5)$ expressing the high distortion in the structure caused by the mixed occupancy of the anionic positions in combination with the oxygen deficit introduced by the lower 2+ charge of the zinc atoms in relation to the 2+/3+/4+ charge value of iron atoms. Refining the occupancy parameters of the oxygen atoms, only 81(2)% could be found. This could be a hint for a mainly 2+/3+ oxidation state for the iron atoms, but it has to be taken into account that the error for the occupancy parameter is difficult to calculate caused by the high scattering power of the cations in the structure. The refinement converged to reliability factors of $R_{WP} = 0.053$ and $P_P = 0.042$ for the pattern with a goodness of fit = 1.01, a Durban–Watson parameter of 1.92, and Bragg R-value of

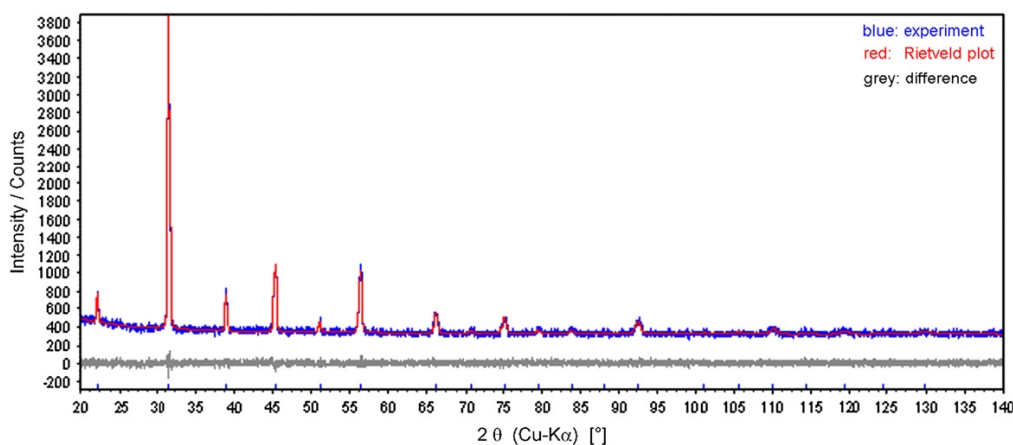Fig. 3. Rietveld plot of $(Ba_{0.5}Sr_{0.5})(Fe_{0.8}Zn_{0.2})O_{3-\delta}$. The observed (blue) and calculated (red) intensities together with the difference between the observed and calculated pattern (grey) as well as the possible reflex position (tick marks) are given.

0.007 for the perovskite structure. Further details could be taken from CSD-No. 418850 [40]. Additionally, the average crystal size was found to be 56(2) nm (L_{Vol}-IB).

3.2.2. The mixed carbonate $(Ba_{0.5}Sr_{0.5})CO_3$

Very detailed considerations on the structure of the aragonite-type $(Ba_{0.5}Sr_{0.5})CO_3$ carbonate are given elsewhere [7]. XRD pattern of the mixed carbonate indicates unit cell parameters $a = 0.62450$ nm, $b = 0.52020$ nm, and $c = 0.86420$ nm in space group *Pnma* (No. 62) which agrees well with data according to Ref. [16] but deviates slightly from values given by us elsewhere [7]. However, regarding the stability of the carbonate at the applied temperatures, an Ellingham diagram has been examined which is based on calculations that are valid for bulk phases [7]. For nanocrystalline powders, the influence of the surface cannot be neglected, and the Thomson–Freundlich equation [21] predicts a higher chemical potential of carbon dioxide, μ_{CO_2}, with respect to bulk phases. Consequently, the decarbonation temperature will decrease with decreasing particle size.

Thus, a pure $(Ba_{0.5}Sr_{0.5})CO_3$ powder with crystal sizes below 100 nm has been synthesized, and CO_2 equilibrium pressures have been measured. In the temperature range of 850–1000 °C, the CO_2 pressure above the nano-sized carbonate increases from about 100 Pa to 2.3 kPa. Data points have been connected with a spline function, and within the experimental error, the experimental curve lies slightly above the estimation from the Ellingham diagram (Fig. 4a). Considering the corresponding chemical potential, μ_{CO_2}, each experimental data point has been put into the Ellingham diagram in Fig. 4b by squared points. Their positions deviate slightly to higher values compared to the calculated mixed carbonate in bulk phase (dashed line) are interpolated by the respective solid line.

In contrast to the presentation in Ref. [7], the calculated Ellingham diagram in Fig. 4b gives directly the chemical potential of carbon dioxide, μ_{CO_2}, in dependence of the temperature.

Different partial pressures of CO_2 are considered as well as equilibrium values over mixtures of carbonates ($BaCO_3$, $SrCO_3$) and rocksalt-type oxides (BaO, SrO). The line that presents μ_{CO_2} above a mixture of $(Ba_{0.5}Sr_{0.5})CO_3$ and $(Ba_{0.5}Sr_{0.5})O$ is assumed to lie symmetrically between those of the simple carbonate/oxide mixtures, indicated by a dashed line.

As mentioned above, liberated CO_2 can easily evaporate through the porous sponge-like body of the reaction product. As all experiments were done under ambient atmospheres, it is assumed that isobaric conditions apply; with the partial pressure of CO_2 being that in air, $p_{CO_2} = 30$ Pa. The carbonate would thermally decompose if its oxidation forces a chemical potential of CO_2 that is higher than in the surrounding atmosphere. Considering bulk $(Ba_{0.5}Sr_{0.5})CO_3$, a decomposition temperature of 808 °C is read from Fig. 4b as the intersection point of the "p_{CO_2} in air" line with the respective carbonate line (dashed). Considering the experimental data points (square brackets), the line valid for the nano-sized carbonate is shifted up by approximately 4 kJ/mol (solid line) so that the decomposition temperature lies at about 790 °C. The analysis indicates that the decarbonation temperature of the nano-sized carbonate is decreased by ca. 20 °C with respect to bulk carbonate. But it is still approximately 40 °C higher than the highest applied temperature of 750 °C, and thus stability considerations support the solid state reaction pathway that is given in Eq. (1).

However, in powder reactions the reaction interface is large; especially if nanoscale powders are considered. This can lead to the liberation of large amounts of heat [23,24] and consequently to local overheating. Despite the moderate heating rate of 3 °C/min up to a nominal maximum temperature of just 750 °C makes it unlikely that in any of the experiments discussed here, the decomposition temperature of the carbonate (ca. 790 °C) has been exceeded. This is supported also by the fact that there have been observed in nanoscale reactions neither BaO nor SrO nor $(Ba_{0.5}Sr_{0.5})O$.
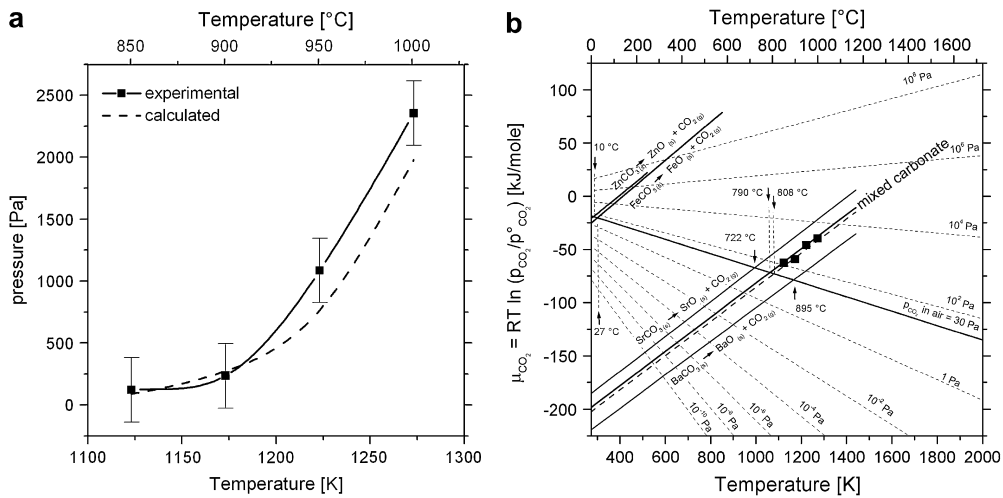
Fig. 4. (a) Experimental and calculated equilibrium CO_2 pressures above $(Ba_{0.5}Sr_{0.5})CO_3$ as a function of temperature, (b) chemical potential of CO_2 versus temperature plots for different partial pressures including equilibrium values above barium and strontium carbonates. Experimental data are added as squares. Calculations have been made after thermodynamic data [22] with reference to standard conditions ($p_{CO_2}^0 = 101.3$ kPa).

Fig. 4b contains also μ_{CO_2} plots for $ZnCO_3$ and $FeCO_3$ to illustrate that a formation of these carbonates do not play any role in the solid state reaction scheme.

3.2.3. The complex spinel $(Zn_{0.6}Fe_{0.4})Fe_2O_4$

To prove the formation of the $(Zn_{0.6}Fe_{0.4})Fe_2O_4$ spinel during the perovskite synthesis, the sol–gel method was
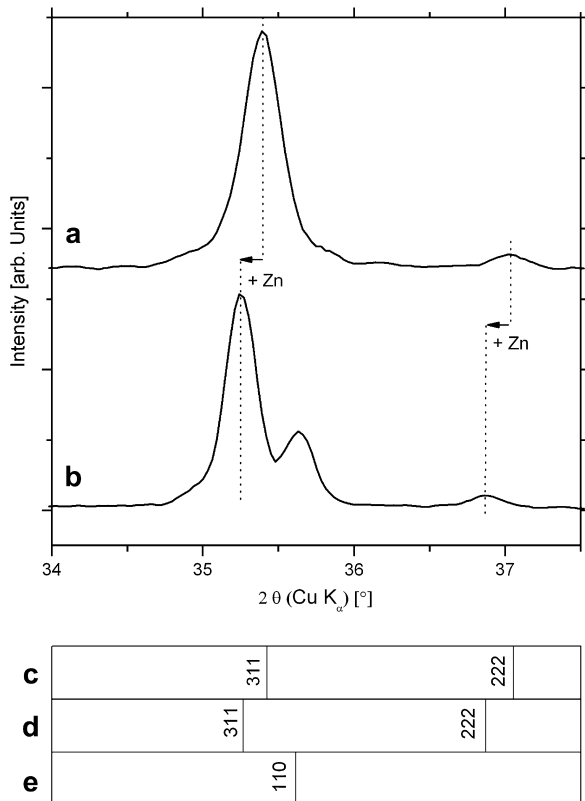

Fig. 5. X-ray powder diffraction: taken from the synthesis of $(Zn_{0.6}Fe_{0.4})Fe_2O_4$ (a) after 1 h at 700 °C, (b) after 10 h at 750 °C, (c) $FeFe_2O_4$ (magnetite), (d) $ZnFe_2O_4$ (franklinite), (e) α-Fe_2O_3 (hematite).
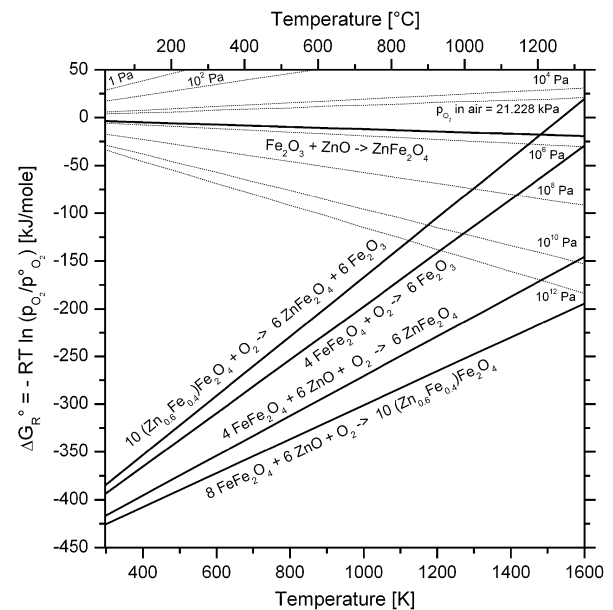

Fig. 6. Thermodynamic calculations for the system Zn–Fe–O under different O_2 partial pressures [22]. Free enthalpy of formation for the $(Zn_{0.6}Fe_{0.4})Fe_2O_4$ spinel has been calculated in consideration of the activities according to Ref. [26]. Standard free enthalpies of O_2 versus temperature plots for different partial pressures are shown with dashed lines in the range of 1–10^{12} Pa ($p_{O_2}^0 = 101.3$ kPa). All reactions illustrated proceed under atmosphere conditions (p_{O_2} in air = 21.3 kPa).
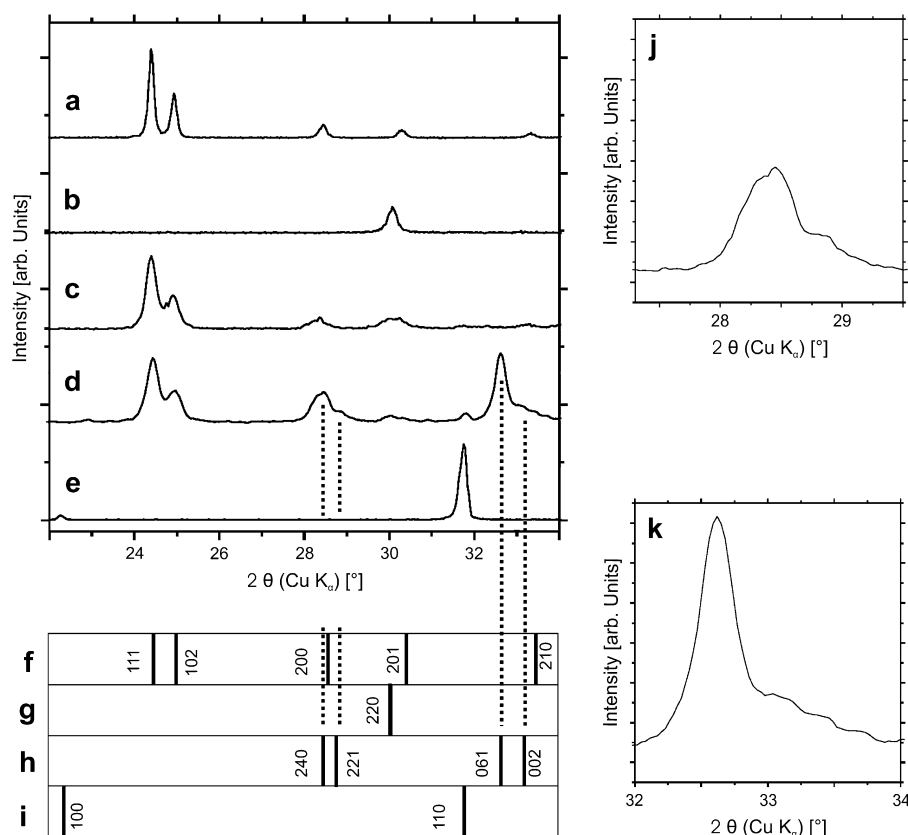
Fig. 7. Close-up X-ray powder diffraction of intermediates and perovskite in the 2θ range between 22° and 34°. (a) Taken from the synthesis of $(Ba_{0.5}Sr_{0.5})CO_3$ after 10 h at 750 °C, (b) taken from the synthesis of $(Zn_{0.6}Fe_{0.4})Fe_2O_4$ after 1 h at 700 °C, (c−e) taken from the synthesis of $(Ba_{0.5}Sr_{0.5})(Fe_{0.8}Zn_{0.2})O_{3-\delta}$ after (c) 1 h at 700 °C, (d) additional 12 h at 700 °C, (e) additional 10 h at 750 °C. (f−i) Assignment of diffraction lines for different phases: (f) aragonite-type $(Ba_{0.5}Sr_{0.5})CO_3$ carbonate, (g) $(Zn_{0.6}Fe_{0.4})Fe_2O_4$ spinel, (h) γ-$(Ba_{0.5}Sr_{0.5})Fe_2O_4$, (i) perovskite-type $(Ba_{0.5}Sr_{0.5})(Fe_{0.8}Zn_{0.2})O_{3-\delta}$, (j) close-up of peaks related to 240 and 221 of $(Ba_{1-x}Sr_x)Fe_2O_4$, (k) close-up of peaks 061 and 002 of $(Ba_{1-x}Sr_x)Fe_2O_4$.

performed without barium and strontium. After calcination for 1 h at 700 °C the formation of a $(Zn_{0.6}Fe_{0.4})Fe_2O_4$ spinel was confirmed by XRD measurements (Fig. 2b) and EDXS. Fig. 5a (1 h at 700 °C) shows details of the diffraction pattern in the 2θ range of 34−37.5°, in the vicinity of the most intense (311) spinel reflex. After heat treatment in air for additional 10 h

at 750 °C, the (311) and (222) spinel reflexes shift by about 0.14° to smaller diffraction angles 2θ. That indicates an incorporation of a larger ion like Zn^{2+} for Fe^{2+} (61 pm → 75 pm [25]) into the A site of the spinel structure. A slightly larger shift in the diffraction angle 2θ by about 0.16° is noticed between $FeFe_2O_4$ (Fig. 5c) and $ZnFe_2O_4$ (Fig. 5d) that corresponds to an increase of the unit cell dimension from 0.8394 to 0.8442 nm. Additionally, another reflection occurs at 35.6° (see Fig. 5b), which was identified with attention to complemental diffraction peaks in the 2θ range of 20−60° (Fig. 2b) as belonging to α-Fe_2O_3 (hematite, Fig. 5e). In conclusion, the $(Zn_{0.6}Fe_{0.4})Fe_2O_4$ spinel formed at 700 °C decomposes in the absence of $(Ba_{0.5}Sr_{0.5})CO_3$ carbonate at higher temperatures to a spinel with $ZnFe_2O_4$ stoichiometry and Fe_2O_3 as hematite.

To check whether this conclusion is in agreement with thermodynamics, calculations have been performed, the results of which are displayed in Fig. 6. Free enthalpy of formation for the $(Zn_{0.6}Fe_{0.4})Fe_2O_4$ spinel has been calculated considering the activities according to Ref. [26]. Because the graph for ΔG_R lies lower than that for O_2 partial pressure in air (p_{O_2} in air = 21.228 kPa), dashed line in Fig. 6, the oxidation

Table 2
Crystallographic data for γ-$(Ba_{0.5}Sr_{0.5})Fe_2O_4$

Atom	Site	x	y	z	Occ
Ba	4(a)	0	0.1307	0.2500	0.5
Sr	4(a)	0	0.1307	0.2500	0.5
Ba	4(a)	0	0.6173	0.2270	0.5
Sr	4(a)	0	0.6173	0.2270	0.5
Fe	8(b)	0.2776	0.0424	0.7320	1
Fe	8(b)	0.2913	0.2803	0.7740	1
O	8(b)	0.2430	0.0370	0.4030	1
O	8(b)	0.2250	0.1230	0.9170	1
O	8(b)	0.2913	0.2090	0.4170	1
O	4(a)	0	0.4530	0.2260	1
O	4(a)	0	0.2800	0.2260	1

Space group $Cmc2_1$ (No. 36) with $a = 0.8448$ nm, $b = 1.9050$ nm, $c = 0.5390$ nm (unit cell dimensions according to Ref. [17]).
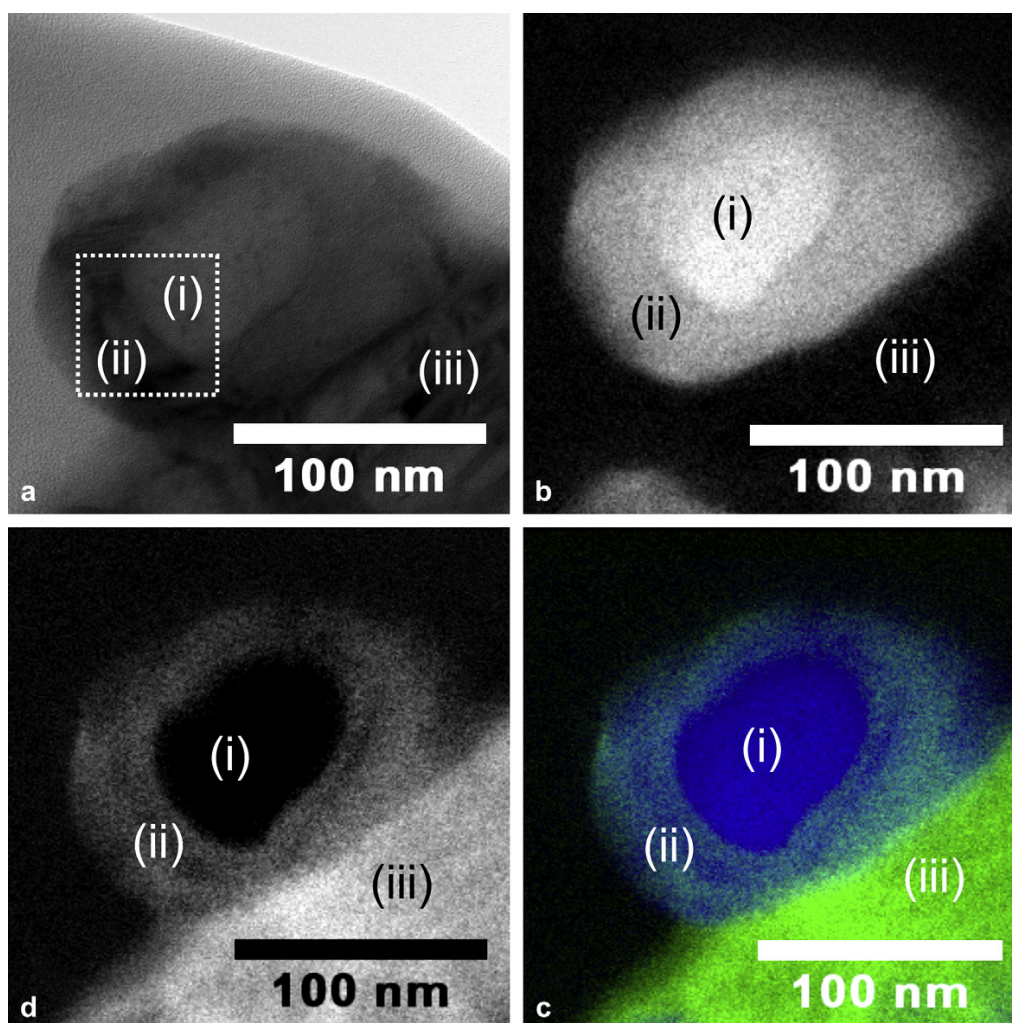
Fig. 8. Transmission electron micrographs showing the formation of the $(Ba_{1-x}Sr_x)Fe_2O_4$ phase between the $ZnFe_2O_4$ spinel and $(Ba_{0.5}Sr_{0.5})CO_3$ carbonate in the aragonite modification. (a) Bright-field micrograph with indicated area of high-resolution TEM, of Fig. 9, (b−c) location of the different particles illustrated by energy-filtered transmission electron micrographs showing high elemental concentrations by bright contrast: (b) iron, (c) barium, (d) location of the different particles illustrated by energy-filtered transmission electron micrographs showing high elemental concentrations by different colours (blue = iron, green = barium).

of the $(Zn_{0.6}Fe_{0.4})Fe_2O_4$ spinel to $ZnFe_2O_4$ and Fe_2O_3 takes place at atmospheric conditions in the whole temperature range of 20−1300 °C. Due to the fact that all graphs in Fig. 6 are below the "p_{O_2} in air" line, these reactions proceed regarding thermodynamics. In the presence of zinc oxide, the iron spinel favours to form the $(Zn_{0.6}Fe_{0.4})Fe_2O_4$ or $ZnFe_2O_4$ spinels, and in its absence hematite is formed. However, in presence of zinc oxide, the reaction of hematite to $ZnFe_2O_4$ spinel is thermodynamically advantageous, too. Strictly speaking, these thermodynamic considerations are valid for bulk phases only and not for nanoscale powders. But with the contemplations that have been made in context of Fig. 4, all ΔG_R curves in Fig. 6 would be shifted slightly down to represent the situation for nanopowders. Anyway, the relative stabilities of the different phases would not be affected.

Recapitulatory, the $(Zn_{0.6}Fe_{0.4})Fe_2O_4$ spinel is not the most stable spinel in the Zn−Fe−O system due to its decomposition at elevated temperatures. Thus, it is essential that the reaction towards the perovskite with the carbonate takes place immediately after the formation of the $(Zn_{0.6}Fe_{0.4})Fe_2O_4$ spinel.

3.2.4. Complex (Ba,Sr)-Fe oxide intermediates

As investigated by XRD pattern, crystalline intermediates that are formed during the synthesis process are $(Zn_{0.6}Fe_{0.4})Fe_2O_4$ spinel and $(Ba_{0.5}Sr_{0.5})CO_3$ carbonate in the aragonite modification. Against our previous assumption, the final perovskite might be formed directly between the spinel and the carbonate [7,8], we now deliver results that indicate a more complex reaction pathway. This is due to the consideration of quenched specimen that represents earlier intermediate stages in that
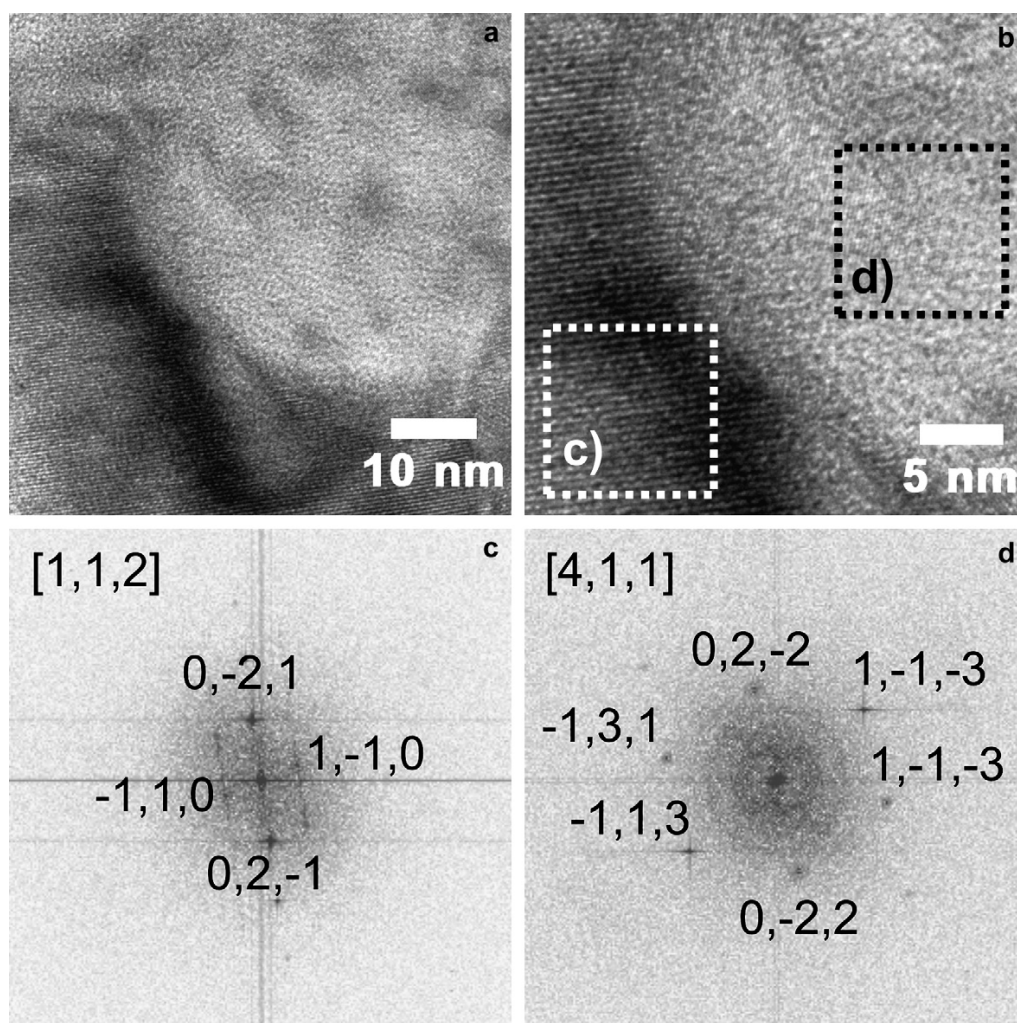
Fig. 9. (a and b) High-resolution transmission electron micrographs as indicated in Fig. 8a. (c) Diffraction data via FFT related to $ZnFe_2O_4$ spinel. (d) Diffraction data via FFT related to $(Ba_xSr_{1-x})Fe_2O_4$.

the perovskite structure is not yet clearly developed compared to Refs. [7,8]. Fig. 7 displays XRD patterns given in Fig. 2 with special emphasize on the 2θ range between $22°$ and $35°$. A first glance on the XRD pattern of Fig. 2d might lead to the conclusion the perovskite structure is already evident in the intermediate powder. Against this, a detailed examination of the XRD pattern in Fig. 7d indicates that a different phase is formed in the first place. The XRD pattern of Fig. 7d could be satisfactorily indexed by a mixed oxide, namely $(Ba_{1-x}Sr_x)Fe_2O_4$. Oxides of this kind have been intensively discussed by several authors in the past decades [17,27−31]. These oxides can be regarded as stuffed tridymite structures which are build of six-membered rings of corner-sharing FeO_4-tetrahedra while the arrangement of the tetrahedra corners within the rings determine the crystal structure [27]. Because of the particular arrangement of the FeO_4-tetrahedra within these structures, a channel-like network is evident

which can be occupied by the larger Ba^{2+} (160 pm [25]) and Sr^{2+} (144 pm [25]) ions, respectively. We found that the orthorhombic crystal structure of γ-$BaFe_2O_4$ fits best to the obtained XRD pattern [26].

In order to index XRD pattern as well as HRTEM micrographs, the structure has been described in space group $Cmc2_1$ (No. 36), see Table 2. It differs from $Bb2_1m$ given in Ref. [17] by a permutation of the crystal axes. At this point, it has to be stressed, that the investigated phases are determined within a mixture that contains at least three different phases. Additionally, it should be considered that the ideal stoichiometry of γ-$BaFe_2O_4$ should not be found in the reaction sequence, due to the cation ratio that has been applied in the reaction mixture. Thus, various stoichiometries like $(Ba_{1-x}Sr_x)Fe_2O_4$ should be evident. The existence of crystals with various, slightly different, lattice parameter can be concluded from Fig. 7j and k as many reflections for the same
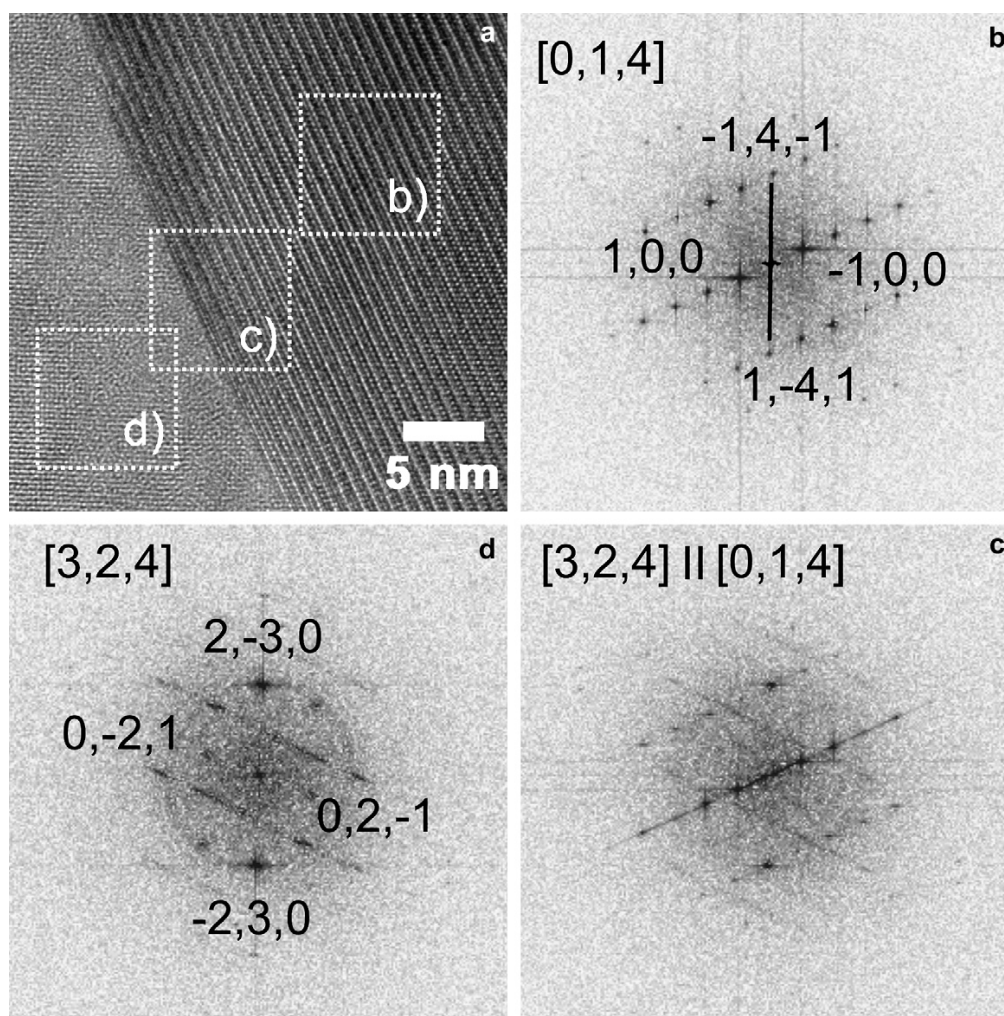
Fig. 10. (a) High-resolution transmission electron micrograph of contact zone of two $(Ba_xSr_{1-x})Fe_2O_4$ grains. (b–d) Diffraction data via FFT related to grains as indicated in (a).

plane are observed. This seems to be reasonable as similar structures like $(Ba_{0.5}Sr_{0.5})Fe_2O_4$ have been already described [28], and they show polymorphism [29]. In order to support XRD findings, TEM bright-field experiments have been conducted with powders as in the XRD pattern in Fig. 7d. Fig. 8 shows a TEM micrograph exhibiting the reaction zone between $ZnFe_2O_4$ spinel (i), the above mentioned $(Ba_{1-x}Sr_x)Fe_2O_4$ phase (ii) and $(Ba_{0.5}Sr_{0.5})CO_3$ carbonate (iii). Energy-filtered TEM (EFTEM) micrographs of this particle display the cation distributions by colours. Obviously, the inner core (i) contains no barium, whereas barium is evident in the border (ii) as well as in site (iii). Contrary to barium, iron can be found in the inner core as well in the border (ii) but not in site (iii). EFTEM investigations have been confirmed by quantitative EDXS of respective specimen areas. It has been found that the inner core (i) exhibits a stoichiometry like $ZnFe_2O_4$, whereas no zinc can be found in the border (ii)

and in site (iii). Further proof for this supposition can be found in Fig. 9a and b in which HRTEM micrographs of the contact zone between $ZnFe_2O_4$ and $(Ba_{1-x}Sr_x)Fe_2O_4$ are displayed. Structure determinations have been conducted via two-dimensional fast Fourier transformation (FFT) of the corresponding areas (Fig. 9c and d). The indexed pattern in Fig. 9c and d give hint to an orientation relationship between spinel (c) and stuffed tridymite (d) of the following type: $(0,2,-2)_c \parallel (0,-2,1)_d$ and $[4,1,1]_c \parallel [1,1,2]_d$. These findings agree well with the observations displayed in Figs. 5 and 6. Below 1400 °C, the $(Zn_{0.6}Fe_{0.4})Fe_2O_4$ spinel structure tends to separate into $ZnFe_2O_4$ and Fe_2O_3 with hematite structure (Fig. 6). Taken this into account, it can be concluded, that the $(Ba_{1-x}Sr_x)FeO_4$ phase has been grown at the expense of the Fe_2O_3 which is one reaction product of the spinel separation. In order to underline the assumption of the formation of a $(Ba_{1-x}Sr_x)Fe_2O_4$ phase, several other particles have been investigated with respect to

this phase. Fig. 10a displays an HRTEM micrograph exhibiting two grains of the $(Ba_{1-x}Sr_x)Fe_2O_4$ phase, but in different orientation. As it can be seen from FFTs in Fig. 10b−d, the grain related to (b) is viewed along the [0,1,4] zone axis, while grain related to (d) is viewed along [3,2,4]. Thus, $(-1,4,-1)_b \parallel (0,-2,3)_d$ and $[0,1,4]_b \parallel [3,2,4]_d$. Additionally, Fig. 10d shows an FFT of the contact zone as indicated in Fig 10c. Fig. 11 displays an HRTEM micrograph of the same grain as in Fig. 10d now viewed along the [2,1,2] zone axis instead of [3,2,4] (after tilting the sample holder). Summing up the above findings, we postulate a rather complicated reaction sequence. After formation of spinel and carbonate, the formation of a $(Ba_{1-x}Sr_x)Fe_2O_4$ phase is postulated. Considering that the spinel structure (B_3O_4) consists only of type-B cations (according to the perovskite terminology ABO_3) it is not surprising that structures like AB_2O_4 are evident which can be understood as intermediate compositions regarding the type-A cation concentration in the spinel and the perovskite. After prolonged reaction time, the diffusion processes, which have to be studied in more detail, between $ZnFe_2O_4$ spinel and the $(Ba_{1-x}Sr_x)Fe_2O_4$ phase might finally lead to the perovskite structure.

EEL spectra of the phases under consideration are given in Fig. 12a−d in the energy-loss range of 500−850 eV. These show up O-K, $Fe-L_{2,3}$, and $Ba-M_{4,5}$ ionization edges. The relative intensities of $Fe-L_{2,3}$ and $Ba-M_{4,5}$ white lines clearly show that the stuffed tridymite structure (Fig. 12b) contains more iron relative to barium compared to the perovskite structure (Fig. 12a). The oxygen K-edge reveals characteristic signatures of the different phases that are shown in more detail in Fig. 12e−h. The O-K ELNES of Fig. 12a,c,d,e,g, and h correspond to fingerprints given in the literature for spinel [32,33], carbonate [34], and perovskite [35], respectively. The stuffed tridymite structure shows after a pronounced leading peak a peak doublet (arrows in Figs. 12b and f) and is in good agreement with the spectral signature given in Ref. [36] for $CaAl_2O_4$ that is structurally related.

4. Conclusions

It is evidenced that in the sol−gel based synthesis route employed here, the cubic perovskite-type $(Ba_{0.5}Sr_{0.5})(Fe_{0.8}Zn_{0.2})O_{3-\delta}$ is formed in a nanoscale solid state reaction between finely-dispersed crystalline intermediates, i.e. a $(Ba_{0.5}Sr_{0.5})CO_3$ carbonate and a $(Zn_{0.6}Fe_{0.4})Fe_2O_4$ spinel. Obviously, the reaction pathway goes from cubic spinel over transient phases of orthorhombic stuffed tridymite-type finally to cubic perovskite-type. XRD and TEM snapshots on quenched samples reveal some details of the intricate reaction mechanism on the atomic scale, however, not all questions can be answered satisfactorily.

The technologically so important spinel/perovskite interfaces or superstructures [37,38] might suggest that a simple topotactic arrangement of both cubic structures, spinel and perovskite, with low lattice misfit could be expected in these nanoscale solid state reactions. Our investigations make clear that this is not the case. In the quenched specimens from different stages of the synthesis process, we may find even additional phases that could be different from the so far found ones. For instance in the analogous synthesis of a cobalt containing cubic perovskite-type oxide, $(Ba_{0.5}Sr_{0.5})(Co_{0.8}Fe_{0.2})O_{3-\delta}$, tetragonally distorted perovskite phases are involved [9].

From a general point of view it is nebulous how the spinel structure with FeO_4 and ZnO_4 tetrahedra and FeO_6 octahedra transforms to stuffed tridymite structures with FeO_4-tetrahedra and finally to a perovskite structure with FeO_6 and ZnO_6 octahedra. Zinc seems to be squeezed first into a $ZnFe_2O_4$ spinel and then probably into ZnO what was seen in some quenched specimen [7]. Incorporation of zinc into the perovskite structure occurs obviously late in the reaction sequence. At which stage, and how, this proceeds is not understood. In addition, the stuffed tridymite $(Ba,Sr)-Fe_2O_4$-type phases show polymorphism [29] so that in very detail everything is undoubtedly even more intricate. And, in these technologically so important
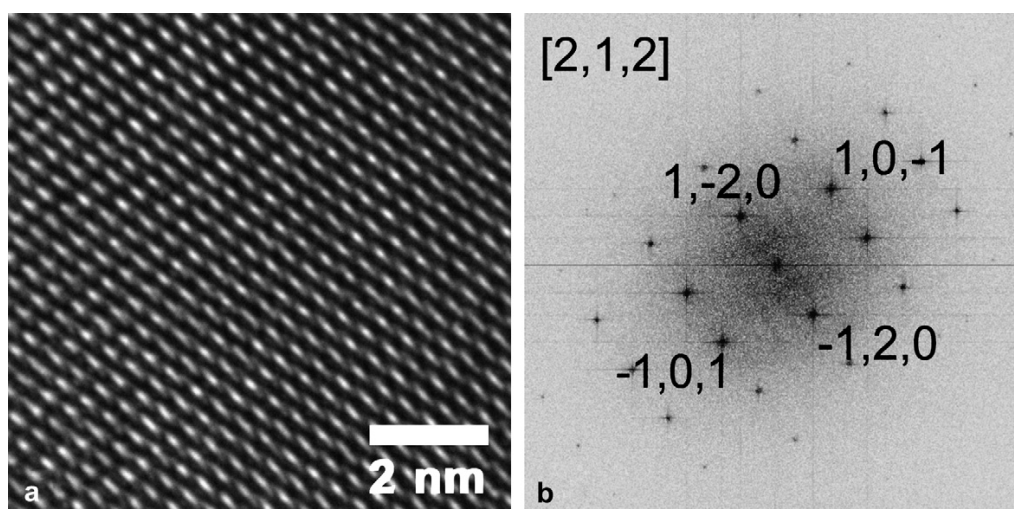

Fig. 11. (a) High-resolution transmission electron micrograph of $(Ba_xSr_{1-x})Fe_2O_4$ grain as in Fig. 9d viewed along different zone axis. (b) Diffraction data via FFT.
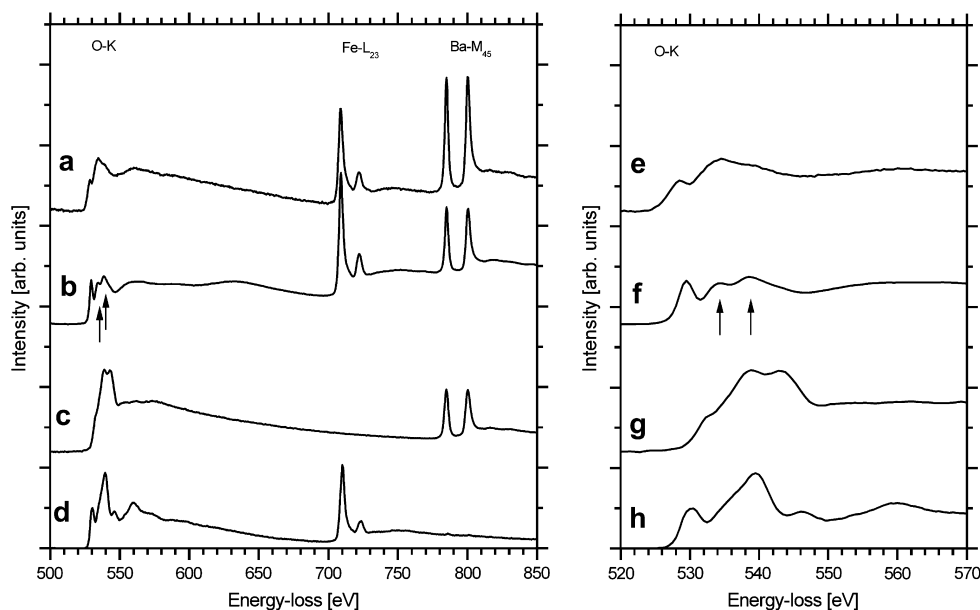
Fig. 12. Electron energy-loss spectra showing O-K, Fe-L$_{2,3}$ and Ba-M$_{4,5}$ ionization edges and O-K energy-loss near-edge structures of different phases. (a and e) Perovskite-type $(Ba_{0.5}Sr_{0.5})(Fe_{0.8}Zn_{0.2})O_{3-\delta}$, (b and f) stuffed tridymite-type $(Ba_xSr_{1-x})Fe_2O_4$, (c and g) $(Ba_{0.5}Sr_{0.5})CO_3$ carbonate, (d and h) $(Zn_{0.6}Fe_{0.4})Fe_2O_4$ spinel.

nanoscale powder reactions, mechanisms are more difficult to understand than in bulk solid state reactions by principle [39].

All in all it is somehow astonishing that the sol–gel procedure passes the same intermediate phases (carbonate and spinel) that are employed in classical solid state routes. However, several advantages of the sol–gel procedure are evident. Starting from the solution over the gel to the crystalline intermediates a nanoscale intermixing of cations is preserved that is the key to homogeneous products of complex stoichiometries.

Solid state reactions in minute reaction couples form tiny product layers and thus do not require the activation of long range diffusion processes. So, the reaction temperature can be kept below the decomposition temperature of the relevant carbonate. Conclusively, the reaction pathway is different from the classical solid route, even if the same type of reaction couples are employed. Reaction temperatures distinctly below 1000 °C diminish the risk of the evaporation of the most volatile constituents (in the systems under investigation Co or Zn) and are thus advantageous for the synthesis of homogeneous products of complex stochiometries. Moreover, low reaction temperatures lead to nanoscale grains that are favourable with respect to several demands.

Acknowledgements

References

[1] J. Pâris, R. Pâris, Bull. Soc. Chim. Fr. 4 (1965) 1795.
[2] M.P. Pechini, US Patent 3 330 697, 1967.
[3] C. Marcilly, P. Courty, B. Delmon, J. Am. Ceram. Soc. 53 (1970) 56.
[4] Y.G. Metlin, Y.D. Tretyakov, J. Mater. Chem. 4 (11) (1994) 1659.
[5] D. Segal, J. Mater. Chem. 7 (8) (1997) 1297.
[6] Z.P. Shao, W.S. Yang, Y. Cong, H. Dong, J.H. Tong, G.X. Xiong, J. Membr. Sci. 172 (2000) 177.
[7] A. Feldhoff, J. Martynczuk, H. Wang, Prog. Solid State Chem. 35 (2007) 339.
[8] J. Martynczuk, M. Arnold, H. Wang, J. Caro, A. Feldhoff, Adv. Mater. 19 (2007) 2134.
[9] M. Arnold, H. Wang, A. Feldhoff, J. Am. Ceram. Soc., doi:10.1111/j.1551-2916.2007.01932.x.
[10] J. Kilner, S. Benson, J. Lane, D. Waller, Chem. Ind. 17 (1997) 907.
[11] H. Wang, C. Tablet, A. Feldhoff, J. Caro, J. Membr. Sci. 262 (2005) 20.
[12] M. Arnold, H. Wang, A. Feldhoff, J. Membr. Sci. 293 (2007) 44.
[13] Z. Shao, S.M. Haile, Nature 431 (2004) 170.
[14] H. Wang, C. Tablet, A. Feldhoff, J. Caro, Adv. Mater. 17 (2005) 1785.
[15] H. Wang, G. Grubert, C. Tablet, J. Caro, EU Patent EP 1 630 148, 2006.
[16] I.A. Kiselva, A.R. Kotelnikov, K.V. Martyniov, L.P. Ogordova, Ju.K Kabalov, Phys. Chem. Miner. 21 (1994) 392.
[17] H. Mitsuda, S. Mori, C. Okazaki, Acta Crystallogr. B 27 (1971) 1263.
[18] R.F. Egerton, Electron Energy-Loss Spectroscopy in the Electron Microscope, Plenum Press, New York, 1986.
[19] R.M. Smith, A.E. Martell, Critical Stability Constants, vol. 6, Plenum Press, New York, 1989, pp. 96–99, 356–358.
[20] A.E. Martell, R.M. Smith, Critical Stability Constants, vol. 5, Plenum Press, New York, 1982, 330.
[21] R.A. Swalin, Thermodynamics of Solids, John Wiley & Sons, New York, 1962.
[22] I. Barin, F. Sauert, G. Patzki, Thermochemical Data of Pure Substances, third ed., vols. I and II, VCH, Weinheim, 1995.
[23] H. Schmalzried, Solid State Reactions. In: Monographs in Modern Chemistry, vol. 12, Verlag Chemie, Weinheim, 1981.

[24] M.N. Rahaman, Ceramic Processing and Sintering, second ed. Marcel Dekker, New York, 2003.

[25] R.D. Shannon, Acta Crystallogr. A 32 (1976) 751.

[26] A.A. Lykasov, V.V. D'yachuk, Inorg. Mater. 29 (1993) 786.

[27] W. Leib, H.K. Müller-Buschbaum, Z. Anorg. Allg. Chem. 538 (1986) 71.

[28] S. Meriani, G. Sloccari, Acta Crystallogr. B 26 (1970) 1184.

[29] S. Meriani, Acta Crystallogr. B 28 (1972) 1241.

[30] E. Lucchini, D. Minichelli, S. Meriani, Acta Crystallogr. B 29 (1973) 919.

[31] W. Hörkner, H.K. Müller-Buschbaum, J. Inorg. Nucl. Chem. 38 (1976) 983.

[32] F.T. Docherty, A.J. Craven, D.W. McComb, J. Skakle, Ultramicroscopy 86 (2001) 273.

[33] C.C. Calvert, A. Brown, R. Brydson, J. Electron Spectrosc. Relat. Phenom. 143 (2005) 173.

[34] J.L. Mansot, V. Golabkan, L. Romana, T. Césaire, J. Microsc. 210 (2003) 110.

[35] A.S. Sefat, G. Amow, M.Y. Wu, G.A. Botton, J.E. Greendan, J. Solid State Chem. 178 (2005) 1008.

[36] N. Jiang, J. Appl. Phys. 100 (2006) 13703.

[37] G. Chern, C. Cheng, J. Vac. Sci. Technol. A 17 (1999) 1097.

[38] H. Zheng, J. Wang, S.E. Lofland, Z. Ma, L. Mohaddes-Ardabili, T. Zhao, L. Salamanca-Riba, S.R. Shinde, S.B. Ogale, F. Bai, D. Viehland, Y. Jia, D.G. Schlom, M. Wuttig, A. Roytburd, R. Ramesh, Science 3003 (2004) 661.

[39] H. Schmalzried, Angew. Chem. 8 (1963) 353.

[40] Additional material to this paper can be ordered to the CSD-No. 418850, names of the authors, and citations of the paper at the Fachinformationszentrum Karlsruhe, Gesellschaft für wissenschaftlich-technische Information mbH, D-76344 Eggenstein-Leopoldshafen, Germany.

4 Local charge disproportion in BSCF

4.1 Summary

In order to probe the local charge disproportion in the BSCF perovskite-type oxide, an *in situ* electron energy-loss spectroscopy study of the cobalt, iron, and oxygen sites was conducted. This was accomplished by using monochromised electrons from a dedicated TEM combined with a heatable sample holder at the *National Centre for High Resolution Electron Microscopy* at the Technical University of Delft, the Netherlands. This TEM is able to deliver an energy resolution better than 0.15 eV with an excellent energy stability, which is essential to draw meaningful conclusions in this particular experiment.

In order to determine the temperature dependent oxidation states of cobalt and iron, the absolute peak positions of the cobalt-$L_{2,3}$ and the iron $L_{2,3}$-edge were measured and compard with absolute peak positions of the edges derived from known standard materials. The absolute peak position of these edges is sensitive to the oxidation state of the investigated element. Additionally, the oxygen K-edge was examined, since the transition-metal d-orbital occupancy is also reflected in the oxygen edge due to hybridization effects. Therefore, the relative excitation probability of the oxygen $1s$ electrons into the hybridised metal-d oxygen-p orbitals compared to the excitation probability into metal-sp oxygen-d orbitals changes with the d-orbital electron occupancy.

The key findings are the following: at room temperature, the average B-site cation valence was determined to be $+2.7$, and the cobalt and the iron were found to be in the high-spin state. The average B-site valence decreases down to $+2.3$ between T = 773 K and T = 1223 K, where the major effect was found to be at the cobalt site.

The reduction of cobalt from $Co^{2.6+}$ down to $Co^{2.2+}$ at high temperatures is an important finding, because it provides the explaination why the BSCF is stabilized for long times only at high temperatures: oxidation of cobalt in BSCF at intermediate temperatures enables the formation of hexagonally stacked cobalt-perovskites, and thus leading to the decomposition of BSCF.

The experimental findings on the transition metal site were in excellent agreement with observations on the oxygen site.

4.2 Local Charge Disproportion in a High Performance Perovskite

Mirko Arnold, Qiang Xu, Frans D. Tichelaar, and Armin Feld-hoff

Local Charge Disproportion in a High Performance Perovskite

Mirko Arnold*, Qiang Xu, Frans D. Tichelaar, and Armin Feldhoff

With the invention of mixed ionic and electronic conductive (MIEC) ceramics, a fast growing new branch in materials science has been established. Besides possessing a variety of fascinating properties, they are widely used as oxygen semi-permeable membranes.[1] Due to their unique mixed conductivity properties, these materials are nowadays applied to two major processes. One application of MIECs is in solid-oxide fuel cells (SOFCs) where MIECs can be installed as cathode materials.[2] The second important application of MIECs is found in membrane reactors, where catalytic processes are combined with oxygen separation.[3,4]

The fundamental principle behind oxygen separation from gaseous mixtures via MIEC membranes is the ambipolar transport of oxygen ions and electrons through the MIEC crystal lattice. By applying a gradient in the oxygen chemical potential between two half spaces separated by the MIEC membrane, oxygen ions move through the MIEC membrane from the higher to the lower chemical potential.[1,3,4,5] Permeation fluxes are significantly enhanced by the amount of mobile oxygen vacancies[1,5] in the crystal lattice because of the Nernst-Einstein equation, which gives a linear relationship between the ionic conductivity and the concentration of the oxygen vacancies. Removal of oxygen is accompanied by the reduction of the B-site transition-metal (TM), which are therefore found in variety of different valences.

It has been already proven by neutron diffraction[6] and thermal gravimetry[7] that oxygen stoichiometry ranges from ~2.5 (at T = 298 K) down to ~2.2 (at T = 1173 K) in $(Ba_{0.5}Sr_{0.5})(Co_{0.8}Fe_{0.2})O_{3-\delta}$ (denoted BSCF) without collapsing into a brownmillerite phase, thereby making BSCF an excellent oxygen conductor in the high temperature regime. However, the element specific reduction is still unknown. In other words, it is not known to what extent cobalt or iron is reduced, but the local charge disproportion of MIECs at elevated temperatures is an important key in the understanding the

phase stability and the electrical conductivity.[8,9] Švarcová et al. pointed out that the oxidation of the B-site cations leads to the phase instability of the BSCF at lower temperatures, because of the change in the effective ionic radii.[8]

In order to address the question of phase stability, the valence and spin state of the B-site cations must be determined, and such information cannot be provided from neutron or X-ray diffraction. The valence and spin state is strongly connected with the metal-oxygen distance and thus with the phase stability.[10] Particularly, if two different B-site cations are employed, a clear valence association is necessary in order to develop sophisticated explanations. For example, $Sr(Co_{0.8}Fe_{0.2})O_{3-\delta}$ (denoted as SCF) which is the endmember within the system $(Ba_xSr_{1-x})(Co_{0.8}Fe_{0.2})O_{3-\delta}$, exhibits a phase transition from cubic perovskite to brownmillerite at elevated temperatures, and oxygen vacancies become immobile resulting in a reduced oxygen conductivity.[11] Differences in the local charge distribution between BSCF and SCF might be useful to explain the difference in this behaviour.

In this work, we present an *in situ* high-resolution electron energy-loss (HR-EELS) study in order to probe the local charge distribution and oxygen non-stoichiometry in BSCF. EELS is used to measure the energy-loss of electrons which interact with the sample and is a valuable tool to investigate the local environment of probe atoms. Sharp ionization edges occur if the core level electrons are excited to unoccupied electronic states by high energy electrons from a transmission electron microscope. Information obtained by EELS is almost identical to X-ray absorption spectroscopy (denoted as XAS) and are therefore used equivalently in this study. By analysing the electron energy-loss near-edge structure (ELNES), it is possible to obtain detailed structural and charge information of the investigated element.[12-14] Since the electronic structure of unoccupied states is influenced by the chemical environment, ELNES can provide the coordination, spin states, and valence of a particular element.[12-14] Another benefit of EELS is the high spatial resolution compared to other methods which are also used to probe the electronic environment in solids, such as XAS and X-ray photoelectron spectroscopy (XPS). This is an important issue with regard to local inhomogeneities which are inherent in these materials. Here we present HR-EELS data from a BSCF sample acquired by monochromised electrons operated in a transmission electron microscope. Monochromised electrons combine the advantages of high spatial resolution with high energy resolution (better than 0.15 eV), which enables the local charge distribution to be probed in very fine detail.[15] Additionally, transmission electron microscopes equipped with monochromators were specially designed for high energy stability, thus strongly reducing the shift of the peak positions.[15,16] In order to investigate the electronic structure in BSCF, the cobalt-$L_{2,3}$, iron-$L_{2,3}$, and the oxygen K-edge were examined. The $L_{2,3}$-edges of cobalt and iron display an electronic transition from the transition metal's (TM) $2p$ core orbitals (split into $2p_{1/2}$ and $2p_{3/2}$ by spin-orbit coupling[14]) to the partly unoccupied $3d$ orbitals ($2p^6 + 3d^n \rightarrow 2p^5 + 3d^{n+1}$), which are hybridized with oxygen $2p$ orbitals. Figure 1 displays a simplified energy diagram in BSCF and qualitatively shows the important

[*] Mirko Arnold, Dr. Armin Feldhoff
Institute of Physical Chemistry and Electrochemistry
Leibniz Universität Hannover
Callinstraße 3-3A, D-30167 Hannover, Germany
Fax: (+49 511-762-19121)
E-mail: mirko.arnold@pci.uni-hannover.de
homepage: http://www.unics.uni-hannover.de/nhcfarmi/akfeldhoff.htm

Dr. Qiang Xu, Dr. Frans D. Tichelaar
National Centre for High Resolution Electron Microscopy
Technical University Delft, Lorentzweg 1, 2628 CJ Delft, the Netherlands

electronic transitions present in the discussed EELS experiment and reflects the fundamental idea of Goodenough. Basically, a valence band (VB) of mostly oxygen $2p$ character and an empty antibonding band of mostly the TM $4s$ and $4p$ character are formed due to a strong overlap of these orbitals.[9] The VB and the antibonding band are separated by a large band gap in which the hybridised TM $3d$ orbitals as well as the oxygen $2p$ fraction of this hybridization are located. Due to excitation into the $3d$ orbitals, it is possible to obtain information about the chemical environment since the $3d$ orbitals mainly contribute to the bonding of the $3d$ TM. However, the $L_{2,3}$-edges of TMs exhibit complex patterns due to the strong overlap of the core wave function with valence wave functions (strong $3d$-$2p$ interactions) as well as the $3d$-$3d$ interactions. Therefore, a huge splitting of the electronic states and thus a complex spectrum were found.[12-15,17-19] The spectral features of the $L_{2,3}$-edges, and the absolute peak positions provide information about the chemical environment. This is the valence state of the TM, unless the local symmetry, covalence, and spin state remain constant.[14,20] Due to an increase of the net formal charge of the TM, a shift in the $L_{2,3}$-edges towards higher energy was observed since a the positively charged nucleus is less screened and higher energy is required to excite the core electrons to the outer electron orbitals.[21]
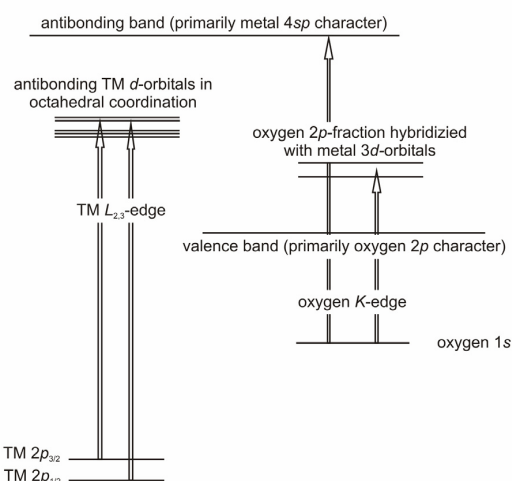
not affected. Additional information can be obtained from the energy difference between "parts A and B". A larger energy difference between "parts A and B" with increasing iron valence has already been reported.[24,25] Colliex et al. found an energy difference of 9.0 eV (Fe^{2+}) and 10.9 eV (Fe^{3+}), respectively.[24] This finding can be explained by the fact the nucleus is more screened due to the higher occupation of the hybridized metal $3d$ orbitals which in turn lowers the energy necessary to excite electrons into the hybridized $4sp$ band.

Following these arguments, a shift of the absolute peak positions of the $L_{2,3}$-edges for cobalt and iron as well as the change of the ratio of relative intensities and the energy difference within the oxygen K-edge were analysed. Because reduction of the B-site TM was noticed at elevated temperatures and the fact that BSCF membranes are commonly operated between T = 973 K and T = 1223 K, the HR-EELS experiments were performed using a heatable sample holder at temperatures up to T = 1223 K.

It should be noted that other methods, which can be used to determine the formal valence of TM in oxides or other compounds from EELS data, are not suitable in the present study. One method is based on the idea that any sample under investigation is a mixture of TMs with different distinct valences,[26] thus, the acquired spectra are simply the overlaid spectra from known compounds. The formal intermediate valence is therefore calculated by the fraction of each species in the sample. Methods to deconvolute these spectra are discussed in detail by Calvert et al.[27] This method is not applicable to the present study since the valence of the TM in BSCF is not an average of isolated distinct valences but rather each TM ion displays an intermediate valence. Therefore the acquired spectra for the TM in BSCF are not simply overlaid spectra of known standards.

Another method requires determining the TM L_3/L_2 intensity ratio,[28,29] which is also sensitive to the TM valence. The L_3/L_2 intensity ratio method is not applicable to the current study since the cobalt $L_{2,3}$-edges overlap with the barium $M_{4,5}$-edge, making it very difficult to accurately determine the whole peak area and therefore to determine the intensity ratio.

Figure 1. Qualitative energy diagram in BSCF. Electron transition of the TM $L_{2,3}$-edges and the oxygen K-edge are indicated by arrows.

As a consequence of the hybridization of the TM orbitals with the oxygen $2p$ ligand orbitals, the $3d$ orbitals occupation is also reflected in the oxygen K-edge, which displays the $1s^2 + 2p^4 \rightarrow 1s^1 + 2p^5$ transition. Strictly speaking, the local charge disproportion between oxygen and the TM is reflected in both the metal $L_{2,3}$-edge as well as in the oxygen K-edge.[22] The oxygen K-edge, when hybridized with a lighter TM, is roughly separated into two parts. The low energy part (denoted as part A) reflects the hybridization with the partly occupied TM $3d$ orbitals and a high energy part (part B) reflecting the hybridization with the empty metal $4sp$ band. As the formal valence of the TM decreases, occupation of the hybridizised TM $3d$ orbitals with the oxygen $2p$ ligand is diminished. Therefore, the probability to excite a core electron into these orbitals is lower, which is reflected in the peak area.[23,24] Thus the intensity ratio B/A should also increase as "part B" of the oxygen K edge is

Figure 2. a. Temperature dependent evaluation of the cobalt-L_3 and the barium M_5-edge in BSCF compared to the cobalt L_3-edge in Co_3O_4 and CoO. The error of the absolute energy position was determined to be ±0.1eV. b. Plot of the cobalt L_3 centroid's abscissa and relative intensity of the low energy shoulder (as indicated by the arrow) compared to the main peak versus temperature.

Figure 2 presents the temperature development of the cobalt L_3-edge compared with the well known materials, Co_3O_4 and CoO (Fig. 2a) as well as a plot of its absolute energy position and its symmetry

(Fig. 2b). The spectra can be evaluated with regard to the peak shape and the absolute peak position. The peak shape will be discussed only qualitatively since many components contribute to the spectral shape, and a quantitative discussion might be rather speculative, particularly if the temperature is raised. The absolute peak position can be more reliable addressed due to the low energy drift of the electron microscope used in the experiment[15]. Additionally, the shift of the cobalt L_3-edge can be related to the position of the barium M_5-edge, because the energy difference between these two lines is not larger than 5 eV. Thus it is possible to use the inert barium M_5-edge as an internal standard since the electronic structure of barium in BSCF does not change with increasing temperature.

At room temperature the peak shape was consistent with a Co^{3+} in a high spin configuration simulated and measured by Hu et al.[19] (pyramidal coordination) and Lozano-Gorrin et al.[30] (octahedral coordination). Comparing the absolute energy value of the cobalt in BSCF with the absolute energy values of CoO (Co^{2+}) and Co_3O_4 ($Co^{2.67+}$), we concluded that the cobalt in BSCF has a formal charge of +2.60 with a high spin configuration in BSCF. We used the centroid's absolute energy position of the Co L_3-edge in CoO and Co_3O_4 (Co^{2+}: 782.80 eV, $Co^{2.67+}$: 783.63 eV) and, by assuming a linear function between these two valence states, we identified the cobalt valence in BSCF. It is clear from Figure 2 that increasing the temperature caused a shift of the absolute peak position of the cobalt L_3-edge as well as a vanishing of the low energy shoulder (higher symmetry of the peak). Figure 2b displays the absolute peak position and the intensity of the low energy shoulder (A_2) compared with the main peak (A_1). We can rationalise the absolute energy shift as resulting from a decrease in the net formal valence of the cobalt (as is explained above). The cobalt valence decreased to +2.3 at T = 523 K and reached the minimum valence of +2.2 at T = 773 K. Further increases in temperature did not change the valence of the cobalt, but symmetry and the broadening of the L_3-edge resulted in a pure Gaussian shape of the edge, which meant that no low energy shoulder could be observed at high temperatures. Several effects contributed to the pronounced symmetry of the L_3-edge and it was difficult to distinguish between these effects.

For example excitation of lattice vibration (phonon broadening) or reduction of symmetry due to mobile oxygen vacancies may led to the vanishing of the low energy shoulder.

The second B-site TM in BSCF is iron, and the temperature dependence of its L_3-edge is plotted in Fig. 3 along with two standards, α-Fe_2O_3 (octahedral Fe^{3+}) and $FeTiO_3$ (octahedral Fe^{2+}). At room temperature, we found that the iron was in a 3+ high spin valence state, which was in good agreement with the findings of Paterson et al.,[20] who had compared the $L_{3,2}$-edge of α-Fe_2O_3 and γ-Fe_2O_3 and had reported not only a remarkable difference in the absolute energy position, but more importantly, a different splitting of the edges, which is independent from energy drifts of the instrument. By comparing the energy position as well as the splitting of the iron L_3-edge in BSCF with α-Fe_2O_3 and the results of Paterson et al. we come to the conclusion that the iron is indeed in the +3 valence state, though it differs from the measured α-Fe_2O_3. Increases in temperature led to a decrease of the iron's valence of +2.7 at T = 523 K. An equilibrium valence state of +2.8 was reached after further temperature increases. As described for the case of cobalt, a linear fit between Fe^{3+} and Fe^{2+} was applied in order to determine the valence of iron at elevated temperatures.

Figure 4 shows a plot of the oxygen K-edge with increasing temperature. We found a significant increase of the intensity ratio, B/A, as well as a decrease of the energy difference between the B and A peaks. "Part A" and "Part B" were fitted using several Gaussian functions from which we determined the absolute peak positions and areas. For both parameters, drastic changes occured between T = 298 K and T = 773 K. Changes in the peak areas can be clearly attributed to the loss of oxygen, which causes a reduction of the cobalt and the iron, resulting in a formal valence of the B-site of +2.3. This implies a higher occupation of the hybridevised TM d - oxygen p orbitals and thus a reduction in probability for excitation into these orbitals. Besides changes in intensity, a decrease in the energy difference can rationalised since the nucleus is more screened by the increased electron population in the hybridized TM d - oxygen p orbitals,[21,24] which in turn lowers the energy necessary to excite core electrons into the hybridized TM sp - oxygen p band.

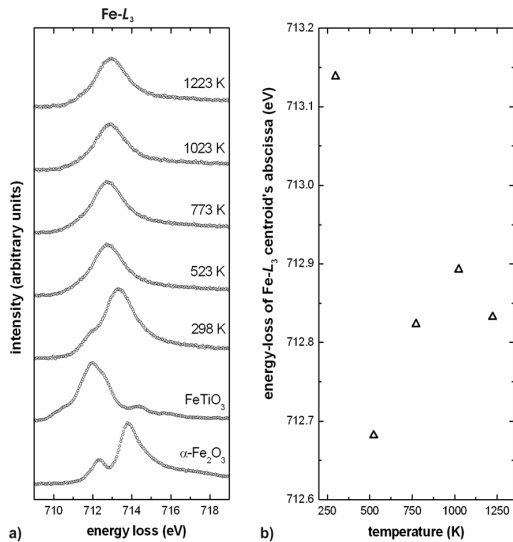**Figure 3.** a. Temperature dependent evaluation of the iron L_3-edge in BSCF compared to the iron L_3-edge in α-Fe_2O_3 and $FeTiO_3$. The error of the absolute energy position was ±0.1eV. b. Plot of the iron L_3 centroid's abscissa versus temperature.
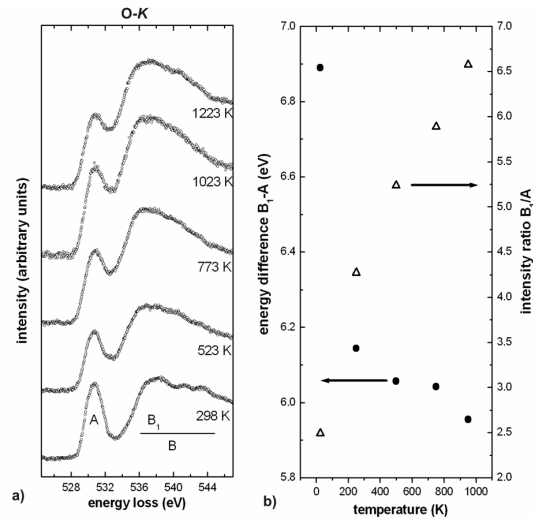
Figure 4. a. Temperature dependent evaluation of the oxygen K-edge in BSCF. b. Plot of the energy difference and intensity ratio of feature A and B in the oxygen K-edge.

Further increases of temperature (> 773 K) left the summed valence of the B-site constant, and both the intensity ratio as well as the energy difference changed little within the oxygen K-edge (Fig. 4b). These minor changes might be either due to a pronounced charge transfer towards the oxygen site at elevated temperatures or the lower sensitivity of the TM $L_{2,3}$-edge with regard to the reduction.

A summary of the key findings can be found in Table 1. The overall B-site valence decreased from +2.7 at T= 298 K to +2.3 between T = 773 and T = 1223 K, and cobalt was more strongly reduced relative to iron. Reduction on the B-site TM associated by the absolute peak position was in excellent agreement with findings at the oxygen K-edge. The intensity ratio of the peaks B/A as well as the energy difference between peaks B and A exhibited similar changes in the same temperature regime.

We have presented unambiguous evidence that oxygen removal in the mixed conductor BSCF is due to a reduction of the B-site TM, namely cobalt and iron, with the cobalt more strongly reduced. Though the conditions in a TEM are not comparable to those in ambient air, the experiment provides the information that mainly cobalt is reduced in BSCF when increasing the temperature. From the fact that $Co^{+2.2}$ is stable at high temperatures, BSCF's stability only at high temperatures is plausible. At lower temperatures BSCF (and hence cobalt) is oxidised in air atmospheres and it is proposed that this yields the formation of hexagonal perovskites containing Co^{3+} in the low spin state. Thus, the information reflecting the redox behaviour of perovskites under ambient atmospheres, derived from neutron diffraction as well as thermal gravimetric measurements together with the site specific charge distribution obtained from *in situ* HR-EELS, provide the explanation of BSCF's stability at high temperatures.

Table 1. Summary of the temperature dependant evaluation of the B-site valence and difference and intensity ratio of feature A and B in the oxygen K ELNES.

temperature (K)	valence of B-site cation			oxygen site	
	cobalt	iron	sum	peak ratio B_1/A	peak difference B_1-A / eV
298	2.6	3.0	2.7	2.49	6.89
523	2.3	2.7	2.4	4.26	6.14
773	2.2	2.8	2.3	5.24	6.06
1023	2.2	2.8	2.3	5.89	6.04
1223	2.2	2.8	2.3	6.57	5.96

Experimental Section

Thermal treatment and *in situ* EELS were performed on a FEI Tecnai-200FEG monochromator, equipped with a pre-specimen monochromator and a high-resolution Gatan Imaging Filter (GIF) for EELS and single tilt heating holder (model 628, Gatan Inc., Pleasanton, CA). The specimen holder was water cooled to allow operation at high temperatures (up to 1573 K) and to prevent specimen drift. All parts of the hot stage were made of tantalum. The furnace temperature was controlled using a miniature encapsulated 10 W heater. During heat treatment, the temperature was adjusted with a potentiometer controller by setting the heater current to the desired values. For HR-EELS acquiring, the high tension was set to 200 kV. The probe size was around 50-100nm. All spectra were recorded in diffraction mode with entrance aperture 0.65mm and camera length 200mm. The energy resolution was measured in each experiment as the full-width half-maximum (FWHM) of the zero loss peak (ZLP), as acquired on the specimen. In order to maintain optimal energy resolution, a series of spectra, each acquired with short acquisition time (typically 15~20s for one spectra for the cobalt-L or the iron L-edge) were recorded

Data processing was conducted as following. First, all spectra were background subtracted using the power law model implemented in the Gatan Digital Micrograph software (Version 1.70.16). Each spectrum was then adjusted by the ZLP and following, several spectra for each edge and temperature were summed to improve the signal-to-noise ratio. In order to determine the absolute peak position, the edges were fitted using several Gaussian functions. The weighted medium of the Gaussian functions was then taken as the absolute peak position of the edges. In the case of the oxygen K-edge, the area below the pre-edge peak (part A) as well the area below the first energy range (4 eV window) of part B (denoted as B_1 in Figure 4) were also determined by Gaussian fits in order to estimate the intensity ratio.

BSCF samples were prepared by the commonly applied sol-gel synthetic route. Proper amounts of the metal nitrates were dissolved in water and e*thylene-d*iamine-*t*etra*a*cetic acid (EDTA), citric acid and ammonia were added. The mixture was then heated to obtain dark-purple coloured gel, which was then calcined for 5 hours at T = 1223 K. Phase purity was determined by X-ray diffraction. The calcined powders were uniaxially cold pressed (at 140 kN) to get "green" bodies which were then sintered at T = 1423 K for 10 hours.

The sintered membranes were polished down a thickness of approximately 80 µm with on polymer embedded diamond lapping films (Allied High Tech, Multiprep). Polished samples were dimpled reaching a maximum thickness of 10 µm at the center of the membrane. Finally, the dimpled membranes were Ar^+ sputtered to achieve electron transparency (Gatan, model 691 PIPS, precision ion polishing system).

[1] H.J.M Bouwmeester, A.J. Burggraaf, in *Fundamentals of inorganic membrane science and technology*, (Eds. A.J. Burggraaf, L. Cot), Elsevier, Amsterdam, **1996**, pp. 435-528.
[2] Z.P. Shao, S.M. Haile, *Nature*, **2004**, *431*, 170-173.
[3] C.S. Chen, S.J. Feng, S. Ran, D.C. Zhu, W. Liu, H.J.M. Bouwmeester, *Angew. Chemie*, **2003**, *115*, 5354-5356; *Angew. Chemie Int. Ed.*, **2003**, *42*, 5196-5198.
[4] J. Caro, H.H. Wang, C. Tablet, A. Kleinert, A. Feldhoff, T. Schiestel, M. Kilgus, P. Kölsch, S. Werth, *Catal. Today*, **2006**, *118*, 128-135.
[5] P.Y. Zeng, Z.H. Chen, W. Zhou, H.X. Gu, Z.P. Shao, S.M. Liu, *J. Membr. Sci.*, **2007**, *291*, 148-156.
[6] S. McIntosh, J.F. Vente, W.G. Haije, D.H.A. Blank, H.J.M. Bouwmeester, *Chem. Mater.*, **2006**, *18*, 2187-2193.
[7] J.F. Vente, S. McIntosh, W.G. Haije & H.J.M. Bouwmeester, *J. Solid State Electrochem.*, **2006**, *10*, 581-588.
[8] S. Švarcová, K. Wiik, J. Tolchard, H.J.M. Bouwmeester, T. Grande, *Solid State Ionics*, **2008**, *178*, 1787-1791.
[9] J.B. Goodenough, in *Structure and Bonding,* Vol. 98(Ed. D.M.P. Mingos) Springer, Berlin **2000**, pp 1-15.
[10] R.D. Shannon, *Acta Cryst.*, **1976**, *A32*, 751-767.
[11] S. McIntosh, J.F. Vente, W.G. Haije, D.H.A. Blank & H.J.M. Bouwmeester, *Solid State Ionics*, 2006, *177*, 833-842.
[12] R.F. Egerton, A. Malac, *J. Electron Spectrosc. Relat. Phenom.*, **2005**, *143*, 43-50.
[13] R.F. Egerton, *Electron energy-loss spectroscopy in the transmission electron microscope*, Plenum Press, New York & London **1986**.
[14] F.M.F. de Groot, *Coord. Chem. Rev.*, **2005**, *249*, 31-63.
[15] C. Mitterbauer, G. Kothleitner, W. Grogger, H. Zandbergen, B. Freitag, P. Tiemeijer, F. Hofer, *Ultramicrosc.*, **2003**, *96*, 469-480.

[16]   P.L. Potapov, D. Schryvers, *Ultramicrosc.*, **2004**, *99*, 73-85.

[17]   J. Zaanen, G.A. Sawatzky, J. Fink, W. Speier, J.C. Fuggle, *Phys. Rev. B*, **1985**, *32*, 4905-4913.

[18]   M. Abbate, J.C. Fuggle, A. Fujimori, L.H. Tjeng, C.H. Chen, R. Potze, G.A. Sawatzky, H. Eisaki, S. Uchida, *Phys. Rev. B*, **1993**, *47*, 16124-16130.

[19]   Z. Hu, H. Wu, M.W. Haverkort, H.H. Hsieh, H.J. Lin, T. Lorenz, J. Baier, A. Reichl, I. Bonn, C. Felser, A. Tanaka, C.T. Chen, L.H. Tjeng, Phys. Rev. Lett., 2004, 92, 207402-1-207402-4.

[20]   J.H. Paterson, O.L. Krivanek, *Ultramicrosc.*, **1990**, *32*, 319-325.

[21]   W.S. Yoon, K.B. Kim, M.G. Kim, M.K. Lee, H.J. Shin, J.M. Lee, J.S. Lee, *J. Phys. Chem. B*, **2002**, *106*, 2526-2532.

[22]   F.M.F de Groot, M. Grioni, J.C. Fuggle, J. Ghijsen, G.A. Sawatzky, H. Petersen, *Phys. Rev. B*, **1989,** *40*, 5715-5723.

[23]   A. Gloter, J. Ingrin, D. Bouchet, C. Colliex, *Phys. Rev. B*, **2000**, *61*, 2587-2594.

[24]   C. Colliex, T. Manoubi, C. Ortiz, *Phys. Rev. B*, **1991,** *44*, 11402-11411.

[25]   J.G. Chen, B. Frühberger, M.L. Colaianni, *J. Vac. Sci. Technol. A*, **1995***, 14*, 1668-1673.

[26]   L.A.J. Garvie, P.R. Buseck, *Nature*, **1998**, *396*, 667-670.

[27]   C.C. Calvert, A. Brown, R. Brydson*, J. Electron Spectrosc. Relat. Phenoma*, **2005,** *143*, 173-187.

[28]   D.H. Pearson, C.C. Ahn, B. Fultz, *Phys. Rev. B*, **1993**, *47*, 8471-8478.

[29]   Z.L. Wang, J.S. Yin, W.D. Mo, Z.J Zhang, *J. Phys. Chem. B*, **1977**, *101*, 6793-6798.

[30]   A.D. Lozano-Gorrin, J.E. Greedana, P. Nunez, C. Gonzalez-Silgo, G.A. Botton, G. Radtke, *J. Solid State Chem.*, **2007,** *180***,** 1209-1217.

5 Effect of CO_2 on the $(Ba_{0.5}Sr_{0.5})(Co_{0.8}Fe_{0.2})O_{3-\delta}$ perovskite-type oxide

5.1 Summary

This chapter presents investigations made regarding the poisoning effect of CO_2 on BSCF perovskite-type membranes under different experimental conditions. In the investigations, different concentrations of CO_2 were added to the supplied feed air as well as to the sweep gas (permeate side). The reversibility as well as long-time effects of the CO_2 treatment were examined. Quantitative on-line gas chromatography was used to investigate the influence of CO_2 on the oxygen permeability. Analytical electron microscopy (AEM) as well as X-ray diffraction (XRD) measurements were conducted to examine the microstructure of the membranes after permeation experiments in CO_2 atmospheres.

Application of pure CO_2 as a sweep gas has yielded an immediate cessation of the oxygen permeation, while subsequent sweeping with helium recovered the oxygen permeation as well as microstructure of the membrane. Long time treatment for 72 h with pure CO_2 on the permeate side has showed that the perovskite structure was impaired only up to a depth of 50 μm. Concentration dependent experiments have further shown that BSCF membranes are capable of sustaining CO_2 for 120 min at T = 1148 K, if the O_2:CO_2 ratio does not fall significantly below 2:1 in the feed air, where 5% in the sweep gas already caused a decrease in the oxygen permeation flux of 50%.

Investigations on the microstructure by AEM and XRD revealed that treatment with CO_2 results in the formation of a mixed carbonate (with an excess of strontium compared to barium) and a needle-like, grown mixed oxide $(Ba,Sr)_x(Co,Fe)_yO_z$ with an unknown structure. The carbonate layer was found to be tarnishing since it does not penetrate the membrane deeper than 50 μm, even if the exposition to CO_2 was conducted for up to three days.

5.2 Influence of CO_2 on the oxygen permeation performance and the microstructure of perovskite-type $(Ba_{0.5}Sr_{0.5})(Co_{0.8}Fe_{0.2})O_{3-\delta}$ membranes

Mirko Arnold, Haihui Wang, and Armin Feldhoff

ELSEVIER

Influence of CO_2 on the oxygen permeation performance and the microstructure of perovskite-type $(Ba_{0.5}Sr_{0.5})(Co_{0.8}Fe_{0.2})O_{3-\delta}$ membranes

Mirko Arnold [a,*], Haihui Wang [a,b], Armin Feldhoff [a]

[a] *Institute of Physical Chemistry and Electrochemistry, Leibniz Universität Hannover, Callinstr. 3-3 A, D-30179 Hannover, Germany*
[b] *College of Chemical and Energy Engineering, South China University of Technology, Guangzhou 510640, PR China*

Abstract

The influence of CO_2 on the oxygen permeation performance of perovskite-type $(Ba_{0.5}Sr_{0.5})(Co_{0.8}Fe_{0.2})O_{3-\delta}$ (BSCF) membranes under different experimental conditions is presented. First, pure CO_2 was applied as the sweep gas at 875 °C yielding an immediate cessation of the oxygen permeation. In order to probe the reversibility of this stagnancy, several cycles of changing the sweep gas between helium and CO_2 were conducted. The analysis of the microstructure after permeation experiments were carried out by transmission electron microscopy (TEM), X-ray diffraction (XRD) as well as by scanning electron microscopy (SEM). It was found that both microstructure as well as oxygen permeation are recovered in a helium atmosphere. Additionally, long-time treatment with pure CO_2 for 72 h on the permeate side and the concentration effect of CO_2 in the sweep gas were accomplished showing that the perovskite structure is impaired only up to a depth of 50 μm. Further on, the impact of CO_2 on the feed side was examined by adding certain amounts of CO_2 to the feed air. It was found that the impact of CO_2 on the oxygen permeation applied in the sweep gas is superior to that applied on the feed gas.
© 2007 Elsevier B.V. All rights reserved.

Keywords: BSCF; Oxygen permeation; CO_2; Carbonate; Perovskite

1. Introduction

Much importance has been attached in the past years to solid oxide membranes regarding their property to separate oxygen from air with infinite selectivity. Especially mixed ionic–electronic conductors (MIECs) with perovskite structure are of great interest for many industrial processes in which a constant supply or removal of oxygen to or from reaction mixtures is required [1]. Many promising applications of MIECs as cathode material in solid-oxide fuel cells as well as in the production of oxygen-enriched air and in the conversion of hydrocarbons to synthesis gas have been reported [2–5]. Major advantages of these membranes are unreached permselectivity and remarkable high oxygen fluxes in the range observed on microporous materials [1].

In the area of MIECs with perovskite structure, compositions of $(Ba_xSr_{1-x})(Co_{0.8}Fe_{0.2})O_{3-\delta}$ are regarded as state-of-the-art materials in view of their high oxygen permeation fluxes. For prospective industrial applications not only high permeability but also sufficient phase stability is essential. This includes reasonable thermal next to chemical stability particularly in reducing gas atmospheres or atmospheres containing CO_2. The poisoning effect of CO_2 is related to the fact that earth alkali metals – included in the perovskite structure – tend to form carbonates. Wang et al. and McIntosh et al. found that BSCF exhibits good phase stability down to a pO_2 of 2×10^{-5} atm [6,7]. Recently, Yan et al. have published results dealing with the effect of CO_2 between 450 and 750 °C on the cell performance of solid oxide fuel cells (SOFCs) having electrodes of the same material [8]. They found a negative but reversible effect on the cell performance even if relatively low CO_2 partial pressures were supplied to the cathode side. Generally, the effect of CO_2 on the membrane performance needs to be examined since CO_2 is contained in natural air as well it is a by-product of the synthesis gas production. Especially with

5. Effect of CO_2 on the BSCF perovskite-type oxide

the advent of zero emissions plants in which oxygen permeating membranes are flushed with CO_2-containing exhaust gases, the demand for CO_2 capable membranes becomes more significant [9]. It has to be stressed that – depending on the potential application of perovskite membranes – either the feed side or the permeate side needs to be examined regarding the CO_2 stability. Therefore, several investigations concerning – inter alias – the effect of CO_2 on different materials with the perovskite-type structure have been published in recent years [10–16].

Already in 1995 Pei et al. described the chemical decomposition of $Sr(Co_{1-x}Fe_x)O_{3-\delta}$ (SCF) hollow fibre membranes after partial oxidation of methane to synthesis gas. It was found that on the reaction side of the membrane the SCF tend to form strontium carbonate as well as a mixture of iron and cobalt oxides leading to membrane failures [10]. Tong et al. discovered the effect of CO_2 on the permeation performance of $Ba(Co_{0.4}Fe_{0.6-x}Zr_x)O_{3-\delta}$ (BCFZ) disc membranes when applied in the feed gas as well as in the sweep gas. Strong decrease of oxygen permeation flux was noticed for the case if the sweep gas contains CO_2. Otherwise no significant attenuation was found, if CO_2 was delivered on the feed side [11]. Similar results were found by Yi et al. after treatment of $Sr_{0.95}(Co_{0.8}Fe_{0.2})O_{3-\delta}$ with CO_2 and or H_2O containing atmospheres [12]. Homonnay et al. described the adsorption of CO_2 in the lattice of $(Sr_{0.95}Ca_{0.05})(Co_{0.5}Fe_{0.5})O_{3-\delta}$ by Mössbauer spectroscopy. They found that CO_2 adsorption of about 4% occurs preferentially in Co-rich regions attributed to a lower coordination number of cobalt in the pristine material resulting in a separation of cobalt and iron pockets [13]. High-temperature in situ neutron powder diffraction on SCF ceramics in CO/CO_2 atmospheres were carried out by different groups while diffraction pattern of whole membrane profiles show no or even low contents of earth alkali carbonates but the formation of various oxides [14,15]. Very recently Yang et al. proposed the application of $(La_{0.1}Sr_{0.9})(Co_{0.5}Fe_{0.5})O_{3-\delta}$ (LSCF) to produce oxygen-enriched CO_2 via adsorption/desorption processes as it might be implemented in the oxyfuel process. High desorption efficiency and good reversibility of the sorption process was found if LSCF powder were treated by turns with O_2 and CO_2 [16].

Despite a few information is already available, a detailed examination of BSCF regarding CO_2-containing atmospheres is still lacking. Especially a profound investigation of the microstructure of BSCF membranes after poisoning with CO_2 has not been reported yet. Here, we present investigations concerning the influence of CO_2 on the oxygen permeation flux of BSCF disc membranes when applied in both the sweep as well as in the feed gas. Additionally, investigations of the microstructure after treatment with these atmospheres were carried out by (scanning) transmission electron microscopy (STEM, TEM) combined with electron energy-loss spectroscopy (EELS) involving electron-loss near-edge structures (ELNES), selected area electron diffraction (SAED) and energy-dispersive X-ray spectroscopy (EDXS). Furthermore scanning electron microscopy (SEM) and X-ray diffraction (XRD) experiments were applied for analytical purposes.

2. Experimental

BSCF powders were synthesized via a combined citrate and EDTA complexing method according to Shao et al. Proper amounts of $Ba(NO_3)_2$, $Sr(NO_3)_2$, $Co(NO_3)_2$ and $Fe(NO_3)_3$ were dissolved in water and followed by the addition of citric acid, EDTA and NH_3 [17]. The reaction mixture was then heated under constant stirring to obtain a purple-coloured gel. Afterwards the gel was pre-calcined for 10 h at 350 °C. The pre-calcined powders were grounded and finally fired for 10 h at 950 °C to get the pure perovskite phase. The powders were then coldly pressed under 13 atm to prepare "green" membranes which were sintered at 1150 °C with a dwelling time of 5 h.

To study the effect of CO_2 on the oxygen permeation, several permeation experiments were carried out on a self-made high-temperature permeation cell which is described in detail elsewhere [18]. Discs of BSCF (Ø = 16 mm, thickness = 1 mm) were sealed onto a ceramic tube with gold-paste (conducting paste, C5754, Heraeus) at 950 °C for 2 h. After sealing, gas flow rates were delivered to the reactor by mass flow controllers (Bronckhorst Hi-Tech) and continuously read by an on-line gas chromatograph (Agilent Technologies, HP 6890, equipped with a Carboxen 1000 column). The feed side of the membrane was flushed either with pure air or with selected amounts of CO_2 (>99.95% purity) in air. On the permeate side pure helium or mixtures of helium with CO_2 were applied. The total flow rate on the feed side of the membrane was set to be 150 ml/min, the total flow rate on the permeate side to 30 ml/min or 140 ml/min, respectively. The absolute flow of the effluents rate was determined by using neon as an internal standardization. For that purpose the concentration of neon in effluents was measured. Since the flow rate of neon is known, it is thus possible to calculate the total effluents flow rate. The permeation flux through the membrane could then be calculated by the fraction O_2 in the effluents and the determination of the effective permeation area of the membrane which was 0.75 cm^2. The leakage was evaluated by measuring the amount N_2 in the effluents stream. After permeation experiments, the membranes were quenched to room temperature under indicated atmospheres.

In order to analyze the microstructure of membranes after permeation experiments, TEM was conducted at 200 kV with a JEOL JEM-2100F-UHR field-emission instrument equipped with a Gatan GIF 2001 energy filter and a 1k-CCD camera in order to obtain EEL spectra. EDXS was carried out by a light-element detector using the Cliff–Lorimer quantification technique (INCA 200 TEM, Oxford Instruments). Specimens for TEM investigations were prepared as follows. First, pieces of 1 mm × 1 mm × 2 mm were cut out of the membrane followed by covering of the permeate side with a silicon single crystal using epoxy. Accordingly, the protected membrane pieces were polished on polymer embedded diamond lapping films down to 0.02 mm × 1 mm × 2 mm and glued onto a copper slot grid. Electron transparency was achieved by Ar^+ ion sputtering at 3 kV under incident angles of 6° and 4° (Gatan, model 691 PIPS).

Additionally, SEM combined with EDXS as well as XRD were conducted on both surfaces and on fracture surfaces. SEM

studies were carried out on a JEOL JSM-6700F field-emission instrument using a secondary electron detector (SE) at an accelerating voltage of 2 kV. EDX spectra were obtained at an accelerating voltage of 15 kV using a light-element detector (INCA 300, Oxford Instruments). To determine the crystal structure of membrane surfaces, XRD were conducted with monochromated Cu Kα_1 radiation in the range of 20–90° 2θ at room temperature (Philips X'Pert-PW1710). Light reflection microscopy was made on polished cross-sections of specimen prepared for TEM (Leitz Orthoplan equipped with a phototube and a Nikon D50 digital camera).

3. Results and discussion

Fig. 1 shows the oxygen permeation of a BSCF membrane while swept in periodic cycles by helium and CO_2 at 875 °C. If helium is used as the sweep gas, permeation fluxes of 1.9 ml/min cm^2 are obtained which are in the same order of magnitude as reported earlier, e.g. by Shao et al. [17]. Changing the sweep gas to CO_2 causes an immediate stagnancy of the oxygen permeation. However, if the sweep gas is shifted back to pure helium the virgin oxygen permeation flux or even higher values are be obtained. This reversibility is in good agreement with data published for BCFZ by Tong et al. [11]. Fig. 2a shows a sketch of the chemical potential gradient of oxygen across the perovskite membrane. The marked area indicates the particular area of investigation by secondary electron SEM micrographs of membrane fracture surfaces as displayed in Fig. 2b–d.

In Fig. 2b the fracture surface of a membrane when stopped in a CO_2 atmosphere (after a treatment time for 100 min) is displayed. Three areas with different chemical compositions (cf. Table 1) and morphologies have been assigned. Decomposition of the perovskite structure (i) occurs up to a depth of 40 μm, as indicated by the morphology as well as by EDXS because the pure perovskite stoichiometry is found so far. The decomposed layer itself is separated into two basically distinct areas assigned with (ii) and (iii). Layer (ii), which abuts on the pure perovskite phase, exhibits a plate-like morphology as well as a different stoichiometry (cf. Table 1) and is restricted to a thickness of approximately 25 μm. EDXS analysis give raise to the
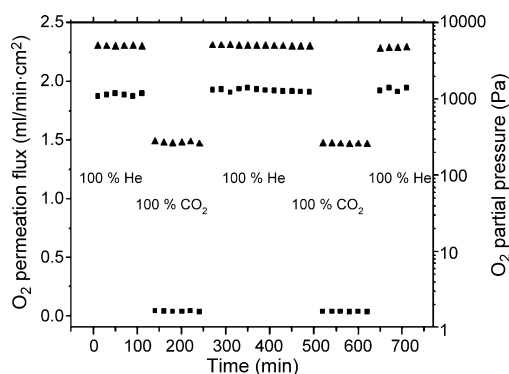
assumption that a mixture of carbonates as well mixed-oxides are present in this layer. Also, a gradient of the carbonate formation can be concluded because a diminution of the carbon content in this layer from 21 at.% (close to the surface film (iii)) down to 15 at.% (close to the bulk (i)) is observed. At the very edge of the permeate side, a film exhibiting a thickness of 5 μm is labelled as layer (iii). Since this film contains almost no iron and cobalt it is assumed that only a mixed strontium-enriched carbonate $(Ba_xSr_{1-x})CO_3$ is present. The particular enrichment of strontium can be attributed to the fact that the mixing enthalpy of $(Ba_xSr_{1-x})CO_3$ solid solutions reaches a maximum if $x = 0.35$ as described by Kiselva et al. [20].

Further on, the elemental distribution at the permeate side of the membrane is visualised by EDXS in Fig. 3a, emphasizing the above-explained phase formations. In order to confirm the formation of a carbonate top layer, XRD measurements of the permeate surface were conducted. XRD pattern clearly indicate the formation of the mixed carbonate with an excess of strontium as mentioned above. Kiselva et al. examined the variation in lattice constants of various $(Ba,Sr)CO_3$ stoichiometries. Using these parameters, it is found that applying an orthorhombic cell ($a = 6.2262$; $b = 5.1957$; $c = 8.6190$) which is related to $(Ba_{0.4}Sr_{0.6})CO_3$ fits very well to the XRD pattern in Fig. 4c and d. This finding underlines the enrichment of strontium in the carbonate, as indicated by EDXS. XRD pattern show several additional reflections, which are not identified but further discussed below.

As already noted, the oxygen permeation flux is totally recovered, when the sweep gas is shifted to helium. It might be assumed, that the recovering of the oxygen permeation flux is accompanied by a reconstruction of the perovskite phase. This presumption was proven by SEM, EDXS and XRD on a membrane that has been treated first for 100 min with pure CO_2 as sweep gas followed by a substitution with helium for 100 min like the alternating cycle displayed in Fig. 1. Fig. 2c shows that the plate-like morphology of the intermediate layer (ii) in Fig. 2b is completely vanished, whereas the very edge of the membrane exhibits a slight deviation from the dense structure of layer (i). Additionally, a minor enrichment of carbon – compared to the pure perovskite – is present (cf. Table 1). This circumstance gives raise to the assumption that a little amount of carbonate remains in this layer, which is therefore labelled as (i*).

The elemental distribution by EDXS in Fig. 3b shows an homogenous distribution off all four cations underlying the fact, that only a poor amount of the carbonates resides in layer (i*). XRD pattern of the recovered membrane in Fig. 4b emphasizes the assertion that only small amounts of the carbonate phase exist since only reflections that are related to the perovskite structure in Fig. 4a can be found.

In order to study the mechanism of decomposition of the perovskite phase, a long-time permeation experiment was conducted in which the permeate side had been exposed to CO_2 for 4320 min. No visible increase of the surface film (iii) could be observed (cf. Fig. 2d) and no significant change in its chemical composition is found for the long-time treatment. Only a more accented separation of layers (ii) and (iii) is observed as displayed by Fig. 3c. It shows a well-defined boundary between

Fig. 1. Oxygen permeation flux (■) while changing the sweep gas. Conditions: feed airflow rate 150 ml/min, sweep flow rate helium or CO_2 30 ml/min. (▲) Oxygen partial pressure. Equilibrium time between concentrations: 30 min.

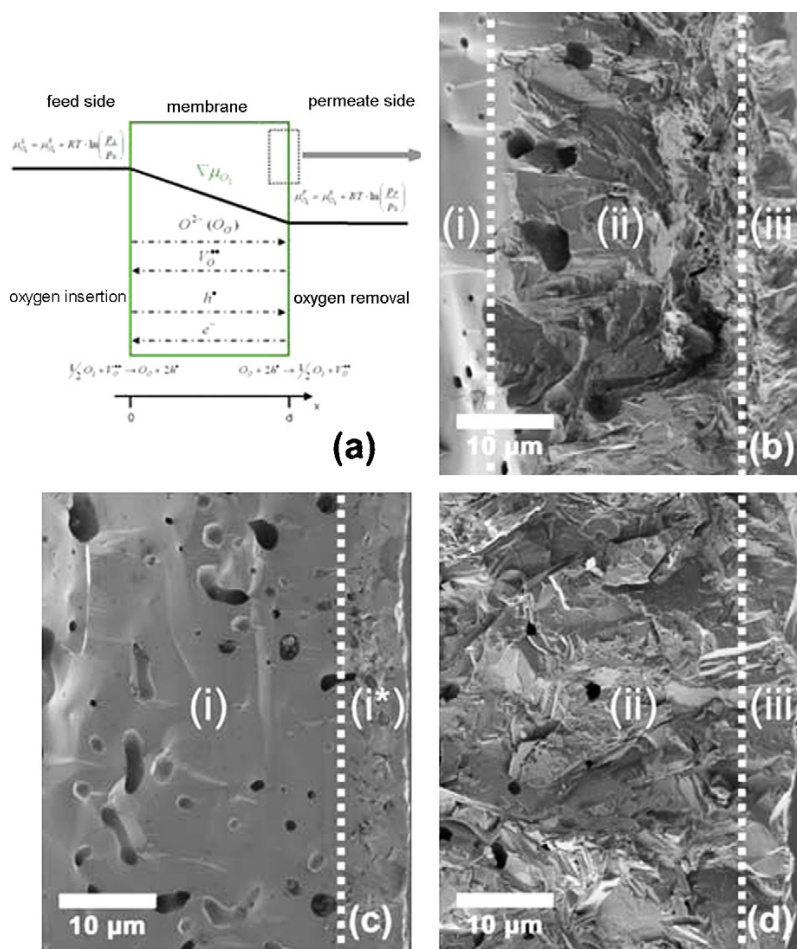# 5. Effect of CO_2 on the BSCF perovskite-type oxide

Fig. 2. (a) Sketch clarifying the mechanism of oxygen permeation through the membrane. (b–d) SEM micrographs showing the permeate side of the membrane when permeation was stopped after a treatment (b) for 100 min with pure CO_2 as sweep gas, (c) after recovering for 100 min with pure helium as sweep gas and (d) for 4320 min with CO_2 as sweep gas.

layers (ii) and (iii) as indicated by the distribution of iron and cobalt. The intermediate layer (ii) shows a slight expansion (app. 10 μm) as shown in Fig. 2d. Quantitative analysis of the chemical composition inside this layer is found to follow the same trend as the intermediate layer obtained in the short-time CO_2

treatment, exhibiting a monotonic diminution of the carbonate content. XRD pattern of long-time CO_2 treated membranes indicate a similar XRD pattern as for the short-time treated (cf. Fig. 4c and d). Obviously, a decrease of the carbonate reflections is found while the reflections for the unknown phase

Table 1
Summary of the elemental distribution of Ba, Sr, Co, Fe, O and C obtained by EDXS at fracture surfaces of membranes after treatment with CO_2 (100 min), CO_2 (4320 min) and recovering with helium (100 min)

	Stopped in CO_2, after 100 min				Stopped in CO_2, after 4320 min				Stopped in helium, after 100 min			
	0 μm[a]	5 μm[a]	20 μm[a]	500 μm[a]	0 μm[a]	5 μm[a]	20 μm[a]	500 μm[a]	0 μm[a]	5 μm[a]	20 μm[a]	500 μm[a]
Ba (at.%)	5.9	4.5	7.0	8.8	6.7	8.7	7.0	9.2	5.9	7.5	7.2	9.3
Sr (at.%)	7.8	4.9	6.9	9.3	8.8	7.0	6.0	9.5	6.9	8.0	8.0	9.4
Co (at.%)	0.6	5.7	10.9	12.5	0.3	8.9	11.8	12.3	7.9	10.2	9.7	11.9
Fe (at.%)	0.6	1.2	2.9	3.1	0.0	2.2	2.8	3.2	2.0	2.5	2.3	3.5
O (at.%)	58.1	62.5	58.2	61.1	57.2	54.4	57.8	60.0	62.2	60.9	65.2	59.9
C (at.%)	26.8	21.2	14.1	5.2	27.0	18.9	14.7	5.9	14.9	10.9	7.6	5.8

The standard deviation for quantification data of Ba, Sr, Co, Fe is assumed to be $\pm 12\%$, according to [19]. Quantifications for carbon demonstrate only trends.
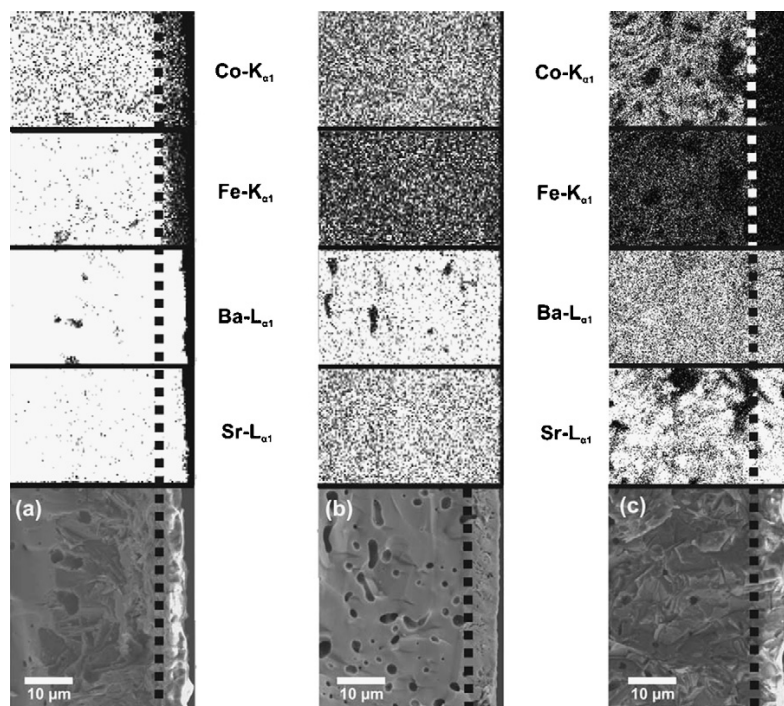[a] Distance to edge of permeate side.

Fig. 3. Elemental distributions by EDXS at the permeate side when permeation was stopped after a treatment (a) for 100 min with pure CO_2 as sweep gas, (b) after recovering for 100 min with pure helium as sweep gas and (c) for 4320 min with CO_2 as sweep gas.

increase. Considering that the carbonate layer thickness does not change significantly, the increase of the reflections related to the unknown phase might be due to proceeding crystallisation of this phase. Hence, the formation of the unknown phase in layer (ii) occurs slower than the formation of the carbonate. This phenomenon can be explained as follows: first, strontium and barium form the carbonate, when CO_2 is applied. The moi-

ety of the cations forms a second crystalline phase, with slower kinetics. Due to that reason the crystallinity of this phase can then be detected by XRD with higher intensity, if a longer reaction period is applied.

As already mentioned, no significant increase in the thickness of the decomposed layer is observed. This fact can be attributed to the above assumed mechanism of the
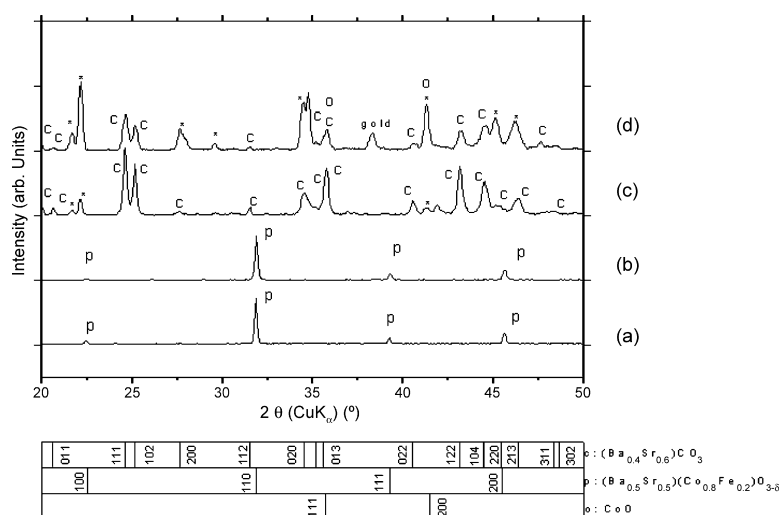

Fig. 4. (a) Powder XRD pattern of BSCF as synthesized. (b–d) XRD pattern of the permeate side after a treatment (b) after recovering for 100 min with pure helium as sweep gas, (c) for 100 min with pure CO_2 as sweep gas and (d) for 4320 min with CO_2 as sweep gas. Peaks labeled with an asterix do not belong to the carbonate, but are retrieved in SAED of single crystals in Fig. 5. The gold peak belongs to the membrane sealing material.
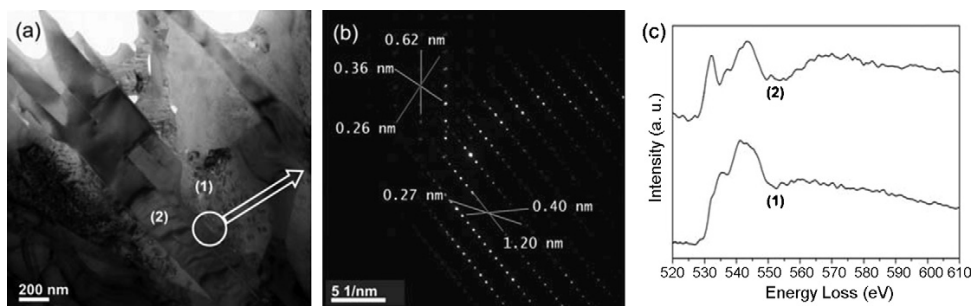
5. Effect of CO_2 on the BSCF perovskite-type oxide

Fig. 5. TEM micrographs of the intermediate layer at the permeate side after a treatment time with CO_2 for 4320 min. (a) Bright-field, (b) SAED and (c) O-K ELNES (numbers are related to bright-field micrograph).

decomposition, regarding a fast formation of the carbonate top layer. This layer can be appreciated as a protective layer regarding the carbonate formation. Gomes and Dekeyser refer this case, if the reaction product builds up a layer between the reactants, to tarnishing reactions [21]. If the reaction product forms a compact, non-porous layer, the reaction rate is limited by transport phenomena through the product layer. Since the thickness of the carbonate is restricted to 5 μm even after long-time treatment, it can be therefore concluded that a dense carbonate layer is formed. This layer causes an immense decrease of the CO_2 transport to the buried perovskite surface resulting in a stagnancy of the carbonate formation.

In order to get a more detailed understanding of the microstructure of layer (ii), TEM investigations were conducted at the boundary to layer (iii). Fig. 5a shows a bright-field micrograph of layer (ii). The plate-like morphology found by SEM and light microscopy (cf. Fig. 6) in this layer can be confirmed even by TEM. Elemental distributions acquired by EDXS, clearly
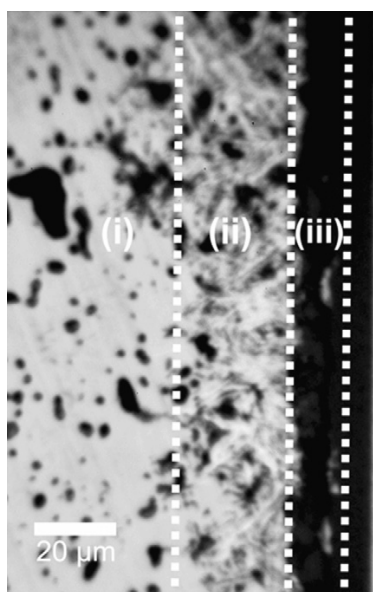

Fig. 6. Light microscope photograph showing the permeate side of the membrane when permeation was stopped after a treatment with CO_2 for 4320 min.

indicate the presence of two distinct phases (cf. Fig. 7). The first can be attributed to the plate-like morphology being a mixed oxide $(Ba,Sr)_x(Co,Fe)_yO_z$ – thus containing all four cations – with complex structure. The second occurs complementary between the plate-like parts and can be related to the above-mentioned strontium-enriched carbonate. SAED of the marked circular area indicates the occurrence of carbonate single crystals next to single crystals of the mixed oxide (cf. Fig. 5a and b).

As already mentioned, several non-carbonate reflections were investigated in the XRD pattern in Fig. 4c and d which cannot be explained by already known phases. Despite the fact a phase attribution is lacking, unindexed d-values in the XRD pattern can be found in SAED of Fig. 5b, by converting them according to the Bragg equation ($d = 0.4095, 0.4014, 0.3202, 0.3017, 0.2601, 0.2580, 0.2181, 0.2008$ nm). Furthermore, a large unit cell is assumed as because of d-values found in the SAED. This can be concluded since at least one cell parameter has a minimum size of 1.2 nm.

Additionally, O-K ELNES were used to confirm the local chemical environment around oxygen atoms. The spectra have been acquired with a small spectrometer entrance aperture to obtain solely information from forwarded scattered electrons that suffered just small transversal momentum transfers. Thus, primarily dipole selection rules apply, and the O-K ELNES probes transitions from O 1s core levels into unoccupied final states of p character that are centered on the oxygen atom. Therefore, the spectra of Fig. 5c reflect on O 2p bands that may hybridize with the metal 3d and higher energy orbitals. In Fig. 5c, the O-K near-edge fine-structure of area 1 clearly indicates the presence of a carbonate bonding [22] with two pronounced peaks, whereas a first small peak at ∼535 eV is followed by an intensive peak at ∼541 eV exhibiting a shoulder-like structure towards higher energies. The spectrum of the complex oxide, $(Ba,Sr)_x(Co,Fe)_yO_z$, from area 2 shows a leading, relatively narrow peak at ∼532 eV. This leading peak reflects that the t_{2g} states (d_{xy}, d_{xz}, and d_{yz} orbitals) of cobalt and iron are hybridized with the unoccupied oxygen 2p states via 2p–3d interactions, as it is often observed in complex oxides [23]. Further on, a broad peak has a maximum at ∼543 eV with two clearly resolved peaks in the left shoulder: at ∼537 and ∼541 eV, respectively. The peak at ∼543 eV refers to excitations of O 2p electrons into unoccupied (Co,Fe) e_g states (d_{z^2}, $d_{x^2-y^2}$ orbitals). The extra features at
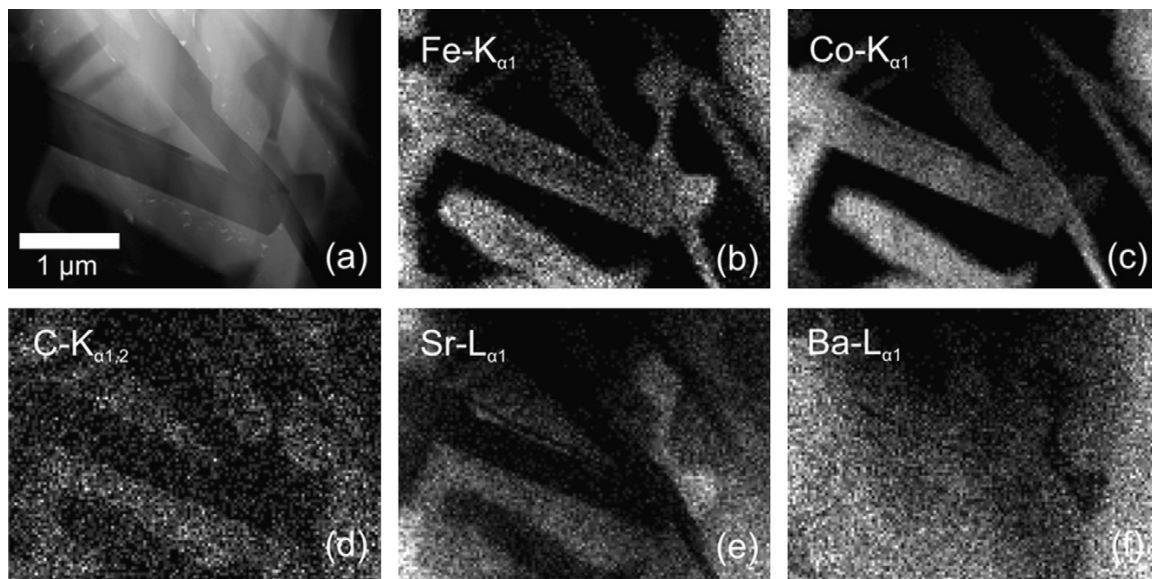
Fig. 7. (a) STEM bright-field micrograph of the intermediate layer at the permeate side of the membrane after a treatment with CO_2 for 4320 min. (b–f) Elemental distributions by EDXS.

$\sim$537 and $\sim$541 eV can be attributed to additional interactions of the oxygen ligand with ns and np states of barium and strontium cations [22]. All these characteristics of the O-K ELNES show some structural relationship to perovskites (ABO_3) with octahedral coordination of the B-site cation (here cobalt and iron) to oxygen.

To a minor extent, cobalt oxide with rocksalt structure is eminent in the intermediate layer. Fig. 8 shows a TEM bright-field micrograph accompanied with an SAED of this oxide. Additionally, the presence of pure cobalt oxide was proven by EDXS.

Summarizing the above-presented results, the following circumstance can be concluded. If CO_2 is applied as the sweep gas, first a strontium-enriched carbonate is formed along a fast reaction pathway, resulting in an immediate stop of the oxy-

gen permeation due the protective character of the carbonate. Second, the remaining cations form a new complex oxide, with large unit cell, in which the crystallisation increases with reaction time accompanied with the formation of cobalt oxide in rocksalt structure.

As discussed above, a complete vanishing of the oxygen permeation flux can be found, if helium is substituted by CO_2. Following, the concentration and time effect of CO_2 when applied either in the feed or in the sweep gas will be discussed. Fig. 9 shows the CO_2 concentration depending diminution of the oxygen permeation flux if supplied in the sweep gas and the associated oxygen partial pressure. Introducing 5% CO_2 in the sweep gas causes an attenuation of 17% after 2 min of CO_2 addition. This fact fits the assumption of fast kinetics regarding
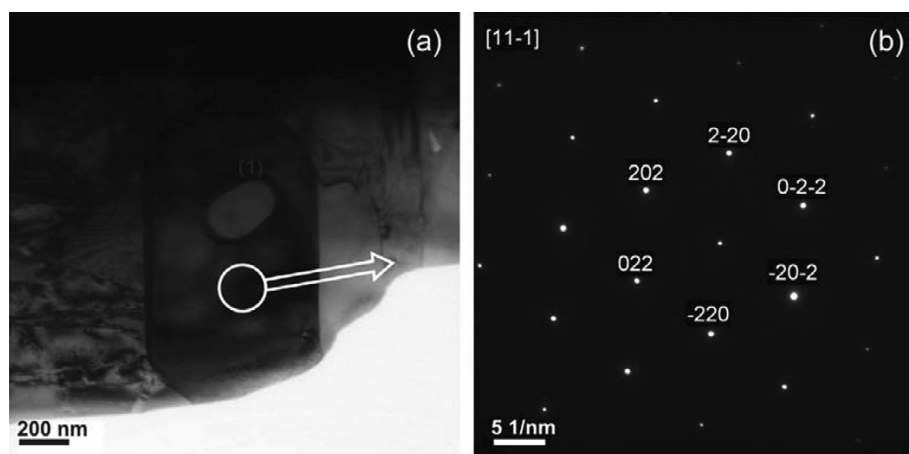

Fig. 8. (a) TEM micrographs of a cobalt oxide with rocksalt structure in the intermediate layer at the permeate side of the membrane after a treatment time with CO_2 of 4320 min and (b) SAED of the circularly marked area in (a).
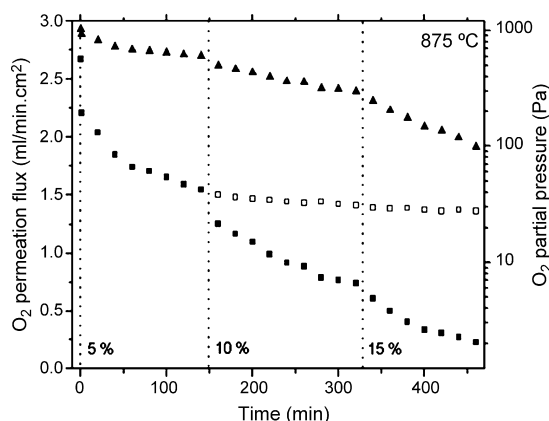
Fig. 9. Effect of the CO_2 concentration in a mixture with helium in the sweep gas on the oxygen flux. Conditions: feed flow rate air 150 ml/min, total sweep flow rate 140 ml/min. Helium $140 - x$ ml/min, $CO_2 x$ ml/min. (■) Oxygen permeation flux in dependence of time and concentration; (□) oxygen flux while kept at 5% CO_2; (▲) oxygen partial pressure associated to (■) data points. Time point 0 min corresponds to CO_2 delivery.

Fig. 10. Effect of the CO_2 concentration in the feed air on the oxygen permeation flux (■). (▲) Oxygen partial pressure on the feed side. Conditions: total feed flow rate 150 ml/min. Air $150 - x$ ml/min, CO_2 flow rate x ml/min. Sweep flow rate helium 140 ml/min. Time point 0 min corresponds to CO_2 delivery.

the formation of the carbonate top layer. Following, the oxygen permeation flux declines down to 60% of the virgin flux already after a reaction time of 120 min and down to 50% after 460 min of CO_2 supply. A this point a steady-state is reached since even an exposure time for more than 20 h did not cause a significant further decrease of the oxygen permeation flux.

A second experiment was conducted in which the CO_2 concentration was set to 10% and 15% after a certain reaction time in order to examine whether the decrease of the oxygen permeation performance is simply due to time. Obviously, a strong acceleration of the descent emerges if the CO_2 concentration is increased. Comparing the oxygen permeation under the influence of 5% CO_2 with 10% CO_2 in the sweep gas flux after 320 min one can see that a doubling of the CO_2 content halves the oxygen permeation flux.

From the long-term experiment in which 5% CO_2 was applied it can be concluded that the carbonate layer reaches an equilibrium thickness that still allows oxygen permeation even though with a reduced performance. That indicates a competition between two reactions. The first reaction, that stabilizes the perovskite phase, is supported by oxygen, as commonly known in literature [24]. The second reaction leading to the formation of the carbonate and the above mentioned oxides. Implying that no competition would take place the oxygen permeation flux would stop after a certain time in each applied CO_2 concentration since a continuously increase of the carbonate would occur. Therefore, the relation between the amounts of oxygen compared to the amount of CO_2 contained in the gas atmosphere seems to be the important factor that causes diminishing of oxygen permeation across the BSCF membrane.

Further proof for this supposition is shown in Fig. 10, in which the oxygen permeation flux is plotted versus the CO_2 content in the feed air. Up to 10% CO_2, the oxygen permeation flux decreases only down to 90%, whereas the oxygen permeation flux decreased down to 50%, if only 5% of CO_2
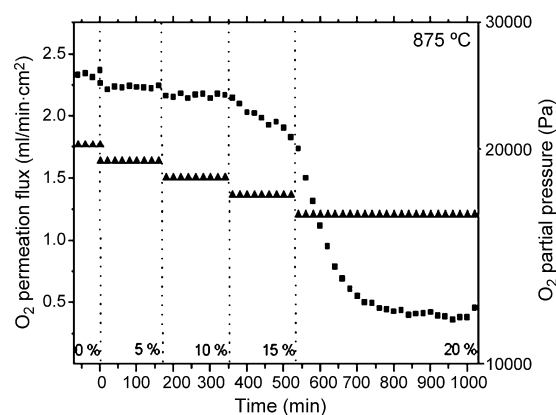
was applied in the sweep gas. If the oxygen content on the feed side was increased to 15%, a relatively fast decrease of the oxygen permeation performance down to 78% within 120 min was observed. The concentration step from 10% to 15% CO_2 can therefore be assumed to be the threshold at which the decomposition of the perovskite becomes significant. Further increase to 20% resulted in a fast reduction to 22% in the space of time of 120 min.

The effect of the temperature on the carbonate formation and hence the impact of the temperature on the oxygen permeation flux can be found elsewhere [25]. Feldhoff et al. reported the free enthalpy in dependence of the temperature. It can be seen that raising the temperature avails the formation of the mixed carbonate. Hence, one can conclude that lowering the temperature during would even lower the oxygen permeation because of the advanced carbonate formation.

4. Conclusion

The poisoning effect of CO_2 on the oxygen permeation flux as well as on changes in the microstructure of BSCF membranes has been investigated. It has been shown, that using pure CO_2 as sweep gas causes an immediate stop of the oxygen permeation flux but can be easily recovered by sweeping with pure helium. Examinations of the microstructure clearly indicate the decomposition of the perovskite structure up to a maximum depth of 40–50 μm, even when exposed to CO_2 for more than 4300 min. The decomposed layer was found to be separated into two different phases, whereas the intermediate layer contains mainly a strontium-enriched mixed carbonate next to a novel mixed oxide, as indicated by SEM, XRD and TEM observations. Further, the concentration effect of CO_2 in the gas exposed to the membrane was examined regarding their influence on the oxygen permeation. It was found that BSCF membranes are capable to sustain up to 10% CO_2, if applied in the feed air. That leads to the assumption that if the O_2:CO_2 ratio falls not significantly below 2:1, BSCF membranes can be

operated in these environments without significant decrease in their performance at least for 120 min.

References

[1] H.J.M. Bouwmeester, A.J. Burggraaf, Dense ceramic membranes for oxygen separation, in: A.J. Burggraaf, L. Cot (Eds.), Fundamentals of Inorganic Membrane Science and Technology, Elsevier, Amsterdam, 1996, p. 435.

[2] Z. Shao, S. Haile, A high-performance cathode for the next generation of solid-oxide fuel cells, Nature 431 (2004) 170.

[3] H. Wang, S. Werth, T. Schiestel, J. Caro, Perovskite hollow-fibre membranes for the production of oxygen-enriched air, Angew. Chem. Int. Ed. 44 (2005) 6906.

[4] C.S. Cheng, S.J. Feng, S. Ran, D.C. Zhu, W. Liu, H.J.M. Bouwmeester, Conversion of methane to syngas by a membrane-based oxidation-reforming process, Angew. Chem. Int. Ed. 115 (2003) 5354.

[5] W. Zhu, W. Han, G. Xiong, W. Yang, Mixed reforming of heptane to syngas in the Ba$_{0.5}$Sr$_{0.5}$Co$_{0.8}$Fe$_{0.2}$O$_{3-\delta}$ membrane reactor, Catal. Today 104 (2005) 149.

[6] H. Wang, C. Tablet, W. Yang, J. Caro, In situ high temperature X-ray diffraction studies of mixed ionic and electronic conducting perovskite-type membranes, Mater. Lett. 59 (2005) 3750.

[7] S. McIntosh, J.F. Vente, W.G. Haije, D.H.A. Blank, H.J.M. Bouwmeester, Oxygen stoichiometry and chemical expansion of Ba$_{0.5}$Sr$_{0.5}$Co$_{0.8}$Fe$_{0.2}$O$_{3-\delta}$ measured by in situ neutron diffraction, Chem. Mater. 18 (2006) 2187.

[8] A. Yan, M. Cheng, Y. Dong, W. Yang, V. Maragou, S. Song, P. Tsiakaras, Investigation of Ba$_{0.5}$Sr$_{0.5}$Co$_{0.8}$Fe$_{0.2}$O$_{3-\delta}$ based cathode IT-SOFC. Part I. The effect of CO$_2$ on the cell performance, Appl. Catal. B 66 (2006) 64.

[9] J.H. Horlock, Advanced Gas Turbine Cycles, Pergamon, Oxford, 2003.

[10] S. Pei, M.S. Kleefisch, T.P. Kobylinski, J. Faber, C.A. Udovich, V. Zhang-McCoy, B. Dabrowski, U. Balachandran, R.L. Mieville, R.B. Poeppel, Failure mechanism of ceramic membrane reactors in partial oxidation of methane to synthesis gas, Catal. Lett. 30 (1995) 201.

[11] J. Tong, W. Yang, B. Zhu, R. Cai, Investigation of ideal zirconium-doped perovskite-type ceramic membrane materials for oxygen separation, J. Membr. Sci. 203 (2002) 175.

[12] J. Yi, S. Feng, Y. Zuo, W. Liu, C. Chen, Oxygen permeability and stability of Sr$_{0.95}$Co$_{0.8}$Fe$_{0.2}$O$_{3-\delta}$ in a CO$_2$- and H$_2$O-containing atmosphere, Chem. Mater. 17 (2005) 5856.

[13] Z. Homonnay, K. Nomura, G. Juhász, M. Gál, K. Sólymos, S. Hamakawa, T. Hayakawa, A. Vértes, Simultaneous probing of the Fe and Co sites in the CO$_2$-absorber perovskite Sr$_{0.95}$Co$_{0.8}$Fe$_{0.2}$O$_{3-\delta}$: a Mössbauer study, Chem. Mater. 14 (2002) 1127.

[14] B.J. Mitchell, R.C. Rogan, J.W. Richardson Jr., B. Ma, U. Balachandran, Stability of the cubic perovskite SrFe$_{0.8}$Co$_{0.5}$O$_{3-\delta}$, Solid State Ionics 146 (2002) 313.

[15] Y. Li, E.R. Maxey, J.W. Richardson Jr., Structural behaviour of oxygen permeable SrFe$_{0.2}$Co$_{0.8}$O$_x$ ceramic membranes with and without pO$_2$ gradients, J. Am. Ceram. Soc. 88 (2005) 1244.

[16] Q. Yang, Y.S. Lin, M. Bülow, High temperature sorption separation of air for producing oxygen-enriched CO$_2$ stream, AIChE J. 52 (2006) 574.

[17] Z.P. Shao, W.S. Yang, Y. Cong, H. Dong, J.H. Tong, G.X. Xiong, Investigation on the permeation behaviour and stability of a Ba$_{0.5}$Sr$_{0.5}$Co$_{0.8}$Fe$_{0.2}$O$_{3-\delta}$ oxygen membrane, J. Membr. Sci. 172 (2000) 177.

[18] H. Wang, C. Tablet, A. Feldhoff, J. Caro, Investigation of phase structure, sintering, and permeability of perovskite-type Ba$_{0.5}$Sr$_{0.5}$Co$_{0.8}$Fe$_{0.2}$O$_{3-\delta}$ membranes, J. Membr. Sci. 262 (2005) 20.

[19] P.J. Statham, Limitations to accuracy in extracting characteristic line intensities from X-ray spectra, J. Res. Natl. Inst. Stand. Technol. 107 (2002) 531.

[20] L.A. Kiseleva, A.R. Kotelnikov, K.V. Martynov, L.P. Ogorodova, J.K. Kabalov, Thermodynamic properties of strontianite–witherite solid solution (Sr,Ba)CO$_3$, Phys. Chem. Miner. 21 (1994) 392.

[21] W.P. Gomes, W. Dekeyser, Factors influencing the reactivity of solids, in: N.B. Hannay (Ed.), Treatise on Solid State Chemistry, vol. 4, Plenum Press, New York, 1976, p. 61.

[22] J.L. Mansot, V. Golabkan, L. Romana, T. Césaire, Chemical and physical characterization by EELS of strontium hexanoate reverse micells and strontium carbonate nanophase produced during tribological experiments, J. Microsc. 210 (2003) 110.

[23] A.S. Sefat, G. Amow, M.Y. Wu, G. Botton, J.E. Greedan, High-resolution EELS study of the vacany-doped metal/insulator system, Nd$_{1-x}$TiO$_3$, $x = 0$–0.33, J. Solid State Chem. 178 (2005) 1008.

[24] J.F. Vente, S. McIntosh, W.G. Haije, H.J.M. Bouwmeester, Properties and performance of Ba$_{0.5}$Sr$_{0.5}$Co$_{0.8}$Fe$_{0.2}$O$_{3-\delta}$ materials for oxygen transport membranes, J. Solid State Electrochem. 10 (2006) 581.

[25] A. Feldhoff, J. Martynczuk, H. Wang, Advanced Ba$_{0.5}$Sr$_{0.5}$Co$_{0.8}$Fe$_{0.2}$O$_{3-\delta}$ perovskite ceramics as oxygen selective membranes: evaluation of the synthesis process, Prog. Solid State Chem., (2007), (doi:10.1016/j.progsolidstchem.2007.01.007).

6 Influence of the microstructure on the oxygen permeability of perovskite-type membranes

6.1 Summary

Results presented in the following chapter describe the effects of the microstructure on the oxygen permeation performance of BSCF and BSFZ perovskite-type membranes. Dense ceramic membranes of BSCF and BSFZ were successfully prepared via liquid phase sintering with BN as sintering aid. Different concentrations with up to 10 mol-% BN were added to the membranes prior to sintering. Scanning electron microscopy revealed that the concentration of BN significantly changes the microstructure of the prepared membranes where large amounts of BN lower the average grain size in these membranes. It has been further shown by XRD and AEM (including energy dispersive X-ray spectroscopy and electron energy-loss spectroscopy) that BN has been completely removed from the membranes and that the grain boundaries are atomically thin and exhibit no amorphous layer or other interfacial phase.

For both the BSCF and BSFZ membrane materials, a decrease in the average grain size (introduced by BN) reduced the oxygen permeability. This effect was especially pronounced in the case of BSCF membranes where the oxygen permeation flux decreased proportionally with decreasing average grain size.

6.2 Grain boundaries as barrier for oxygen transport in perovskite-type membranes

Mirko Arnold, Julia Martynczuk, Konstantin Efimov, Haihui Wang, and Armin Feldhoff

Journal of Membrane of Science, 317, 137-144 (**2008**)

Grain boundaries as barrier for oxygen transport in perovskite-type membranes

Mirko Arnold [a,*], Julia Martynczuk [a], Konstantin Efimov [a], Haihui Wang [b], Armin Feldhoff [a]

[a] Institute of Physical Chemistry and Electrochemistry, Leibniz Universität Hannover, Callinstr. 3-3A, D-30167 Hannover, Germany
[b] College of Chemical and Energy Engineering, South China University of Technology, Guangzhou 510640, PR China

Abstract

Perovskite-type membranes of $(Ba_{0.5}Sr_{0.5})(Co_{0.8}Fe_{0.2})O_{3-\delta}$ (BSCF) and $(Ba_{0.5}Sr_{0.5})(Fe_{0.8}Zn_{0.2})O_{3-\delta}$ (BSFZ) were successfully prepared via liquid-phase sintering using BN as sintering aid. The obtained membranes were examined via powder X-ray diffraction pattern (XRD), differential scanning calorimetry (DSC), scanning electron microscopy (SEM), transmission electron microscopy (TEM) and oxygen permeation experiments. It has emerged that the use of BN as sintering aid lowers sintering temperatures in order to obtain dense membranes with relative densities in the range of 93–96% as proven by the Archimedes method. It was further shown that the perovskite structure could be maintained after sintering with BN. Additionally, BN was completely removed from the sintered membranes. Investigation of the microstructure revealed that the average grain size of the membranes was influenced by the amount of BN added prior the sintering process. It was found that large amounts of BN effectively lower the average grain size. Oxygen permeation experiments have shown that the lower the average grain size the lower the oxygen permeation performance, particularly in the case of BSCF. Transmission electron microscopy revealed that no evidence for an amorphous layer or any other interfacial phase in the grain boundary is present.
© 2007 Elsevier B.V. All rights reserved.

Keywords: BSCF; BSFZ; Oxygen permeation; Grain boundaries; Transmission electron microscopy; Perovskite; Liquid-phase sintering; BN; Grain size distribution

1. Introduction

Nowadays, mixed ionic–electronic conductors (MIECs) with perovskite structure are applied in many different processes as they allow to selectively separate oxygen from gaseous mixtures. Due to their intrinsic mixed conductivity, they are of great interest for many industrial processes in which a constant supply or removal of oxygen to or from reaction mixtures is required [1]. Applications such as the usage of MIEC as cathode material in solid-oxide fuel cells as well as in the production of oxygen enriched air and in the conversion of hydrocarbons to synthesis gas have been reported [2–6]. Major advantages of these membranes are their almost infinite permselectivity and remarkable high oxygen fluxes in the range observed on microporous materials [1].

Within the MIECs, $(Ba_{0.5}Sr_{0.5})(Co_{0.8}Fe_{0.2})O_{3-\delta}$ (BSCF) is regarded to be one of the most promising materials as mem-

branes made of it show high oxygen permeation fluxes and excellent phase stability even under low oxygen partial pressures and reducing gas atmospheres [7–9]. Recently, a new perovskite system $(Ba_{0.5}Sr_{0.5})(Fe_{0.8}Zn_{0.2})O_{3-\delta}$ (BSFZ) was invented which also exhibits excellent phase stability and remarkably high oxygen fluxes [10–12]. As these perovskite systems display two of the state-of-the-art materials, they are of special interest and thus investigated regarding their microstructure and oxygen permeation performance in the presented study.

Several groups have reported that the microstructure and thus the relation between bulk and grain boundary oxygen ion diffusivity within dense ceramic membranes significantly influences the oxygen permeation performance [13-19]. Different perovskite systems were studied in these reports and no clear trend is visible whether the transport along grain boundaries displays a barrier or acts as a pathway for fast oxygen transport. Diethelm et al. found for $(La_{0.5}Sr_{0.5})FeO_{3-\delta}$ that the larger the obtained grains – and thus the fewer the grain boundaries – the smaller the observed oxygen permeation performance [13–14]. Similar findings were reported for $LaCoO_{3-\delta}$ by Kharton and Marques [15]. Contrary to that, in ceramics

* Corresponding author. Tel.: +49 511 762 4896; fax: +49 511 762 19121.
E-mail address: mirko.arnold@pci.uni-hannover.de (M. Arnold).

of $Ca(Ti_{0.8}Fe_{0.2})O_{3-\delta}$ – prepared by mechanical activation – grain boundaries are suggested to act as a barrier for oxygen permeation [16]. Most remarkably, opposite results were found within the system $(Ba_{1-x}Sr_x)(Co_{0.8}Fe_{0.2})O_{3-\delta}$. The end member $Sr(Co_{0.8}Fe_{0.2})O_{3-\delta}$ provides improved oxygen permeation performance by decreasing the average grain size, whereas for $(Ba_{0.5}Sr_{0.5})(Co_{0.8}Fe_{0.2})O_{3-\delta}$ opposite observations have been obtained [17–19]. As several parameters during the preparation influence the properties of the membrane, the effect of the microstructure on the oxygen permeation has to be studied more systematically. This could be done by varying the microstructure in different perovskite systems via the same way, i.e. the sintering temperature and dwelling time. Additionally, care has to be taken by comparing results, if the raw perovskite powder has been prepared in different ways, which might also influence the properties of the final membrane.

In this study, we have applied a liquid-phase sintering to obtain BSCF and BSFZ membranes using BN as sintering aid. The method was described by Ho on the $BaTiO_3$ perovskite system [20]. It was shown that the application of BN as sintering aid allows to lowering the sintering temperature, and no incorporation of boron into the perovskite lattice was observed. Due to the fact that during the sintering process a liquid-phase is eminent in the membrane, a lowering of the average grain size is expected [21]. In order to study the changes in microstructure and its influence on the oxygen permeation performance, membranes of BSCF and BSFZ with varying BN content during sintering were prepared. Investigations of the microstructure were carried out by scanning electron microscopy (SEM) combined with energy-dispersive X-ray spectroscopy (EDXS). Transmission electron microscopy (TEM) along with EDXS and electron energy-loss spectroscopy (EELS) was conducted to examine the microstructure and elemental composition of grain boundaries. Additionally, differential scanning calorimetry (DSC), X-ray diffraction (XRD) and oxygen permeation experiments as well as relative density measurements were applied for characterization purposes.

2. Experimental

BSCF and BSFZ powders were synthesized via a combined citrate and ethylene-diamine-tetraacetic acid (EDTA) complexing method according to Shao et al. [9]. Proper amounts of $Ba(NO_3)_2$, $Sr(NO_3)_2$, $Co(NO_3)_2 \cdot 6(H_2O)$, $Fe(NO_3)_3 \cdot 9(H_2O)$, and $Zn(NO_3)_2 \cdot 2(H_2O)$ were dissolved in water, followed by the addition of citric acid, EDTA and $NH_3 \cdot (H_2O)$. The reaction mixtures were then heated under constant stirring to obtain a purple-coloured gel. Afterwards the gels were pre-calcined for 2 h at 700 °C. The pre-calcined powders were grounded and finally fired for 10 h at 950 °C to get the pure perovskite phases. The pure perovskite powders were then carefully grounded together with certain amounts of hexagonal-BN (space group: $P6_3/mmc$ (194), $a = 2.5044$ Å, $c = 6.6562$ Å; Powder Diffraction File: 34–421, average particle size of $\emptyset = 1$ μm): 2.5, 5, 7.5, and 10 mol%. The grounded powders were then coldly pressed under 140–150 kN for 20 min to prepare "green" membranes which were finally sintered at 1050 °C (BSCF) and 1100 °C (BSFZ)

with a dwelling time of 10 h in an ambient air atmosphere. In order to estimate the optimal sintering temperature, the melting point of each membrane was measured via (DSC) on a SETSYS TGA-DSC instrument. Relative densities of the sintered membranes were acquired via the Archimedes method on a Sartorius balance model BP 211D with a resolution of 0.01 mg equipped with compatible attachment.

To study the oxygen permeation performance of the sintered membranes, several permeation experiments were carried out on a self-made high temperature permeation cell which is described in detail elsewhere [18]. Discs of BSCF and BSFZ ($\emptyset = 14$ mm, thickness = 1.15 mm) were sealed onto a ceramic tube with gold-paste (conducting paste, C5754, Heraeus) at 950 °C for 2 h. After sealing, gas flow rates were delivered to the reactor by mass flow controllers (Bronkhorst Hi-Tech) and continuously read by an on-line gas chromatograph (Agilent Technologies, HP 6890, equipped with a Carboxen 1000 column). The feed side (outer site of the ceramic tube onto the membrane was sealed) of the membrane was flushed with synthetic air. On the sweep side (inner site of the ceramic tube onto the membrane was sealed) pure helium and neon were applied. The total flow rate on the feed side of the membrane was set to be 150 ml/min, and the total flow rate on the sweep side to 30 ml/min. The absolute flow rate of the permeate stream (sweep plus permeated oxygen plus leakage) was determined by using neon as an internal standardization. The permeate stream (consisting of helium, oxygen, nitrogen, and neon) was examined by gas chromatography. For each component a quantitative calibration with known standards was conducted. Thus, the area of each component chromatogram was directly related to a certain percentage of this component. As the supplied sweep flow rate (i.e. helium and neon with no permeated oxygen) was known, it was thus possible to determine the total permeate flow rate from the concentration of neon in the permeate stream. The total leakage (<5%) was calculated by the amount of nitrogen, i.e. the percentage nitrogen found in the permeate stream was treated as the leakage. The related amount of oxygen was then subtracted from the total oxygen in the chromatogram leading to the net permeated oxygen. The permeation flux through the membrane could then be calculated by the fraction O_2 in the effluents and the determination of the effective permeation area of the membranes. Permeation experiments were conducted in the temperature range from 800 to 925 °C with steps of 25 °C. For each temperature step, an equilibrium time of 60 min was set. The actual temperature was measured slightly above the membranes.

In order to analyze the microstructure of the sintered membranes, SEM combined with EDXS as well as XRD were conducted on both surfaces and on fracture surfaces. Grain size distributions were evaluated by SEM on a JEOL JSM-6700F field-emission instrument using a secondary electron detector (SE) at an accelerating voltage of 2 kV. Fracture surfaces were etched with aqueous HCl (2 M) for 2–5 s in order to visualize grain boundaries. EDX spectra were obtained at an accelerating voltage of 15 kV using a light-element detector (INCA 300, Oxford Instruments). To determine the crystal structure of sintered membranes, XRD were conducted with monochromated Cu $K_{\alpha 1}$ radiation in the range of 20–50° 2θ at room temperature
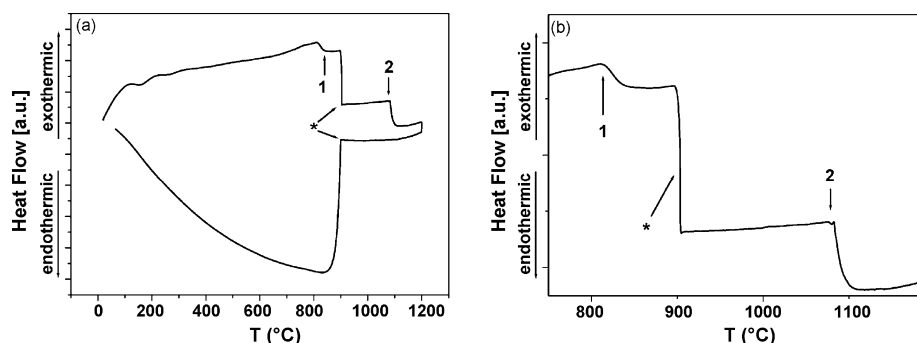
Fig. 1. DSC data obtained from a "green" BSCF membrane containing 10 mol% BN in a synthetic air atmosphere. The asterisk indicate a sensitivity switch of the instrument.

(Philips X′Pert-PW1710) on surfaces and grounded membranes. Powder XRD data for interpretation were taken from literature, ZnO: ICDD database PDF number [36–1451], BSCF [22], BSFZ [23].

Additionally, TEM was conducted at 200 kV with a JEOL JEM-2100F-UHR field-emission instrument equipped with a Gatan GIF 2001 energy filter and a 1k-CCD camera in order to obtain EEL spectra. EDXS was carried out by a light-element detector using the Cliff–Lorimer quantification technique (INCA 200 TEM, Oxford Instruments). Furthermore, the specimen for TEM investigations was prepared as follows. First, pieces of 1 mm × 1 mm × 2 mm were cut out of the membrane followed by covering of both sides with silicon single crystal using epoxy. Accordingly, the protected membrane pieces were polished on polymer embedded diamond lapping films down to 0.02 mm × 1 mm × 2 mm and glued onto a copper slot grid. Electron transparency was achieved by Ar$^+$ ion sputtering at 3 kV under incident angles of 6° and 4° (Gatan, model 691 PIPS).

3. Results and discussion

Fig. 1a and b shows DSC data obtained from a "green" BSCF membrane containing 10 mol% BN in a synthetic air atmosphere. Around 800 °C (point 1), BN starts to oxidise yielding in B_2O_3 as indicated by an endothermic process. As B_2O_3 starts to melt immediately after oxidisation, we postulate that the endothermic process of oxidisation covers the endothermic melting process. Thus, the heat flow of this melting process is not directly visible. At 1078 °C (point 2), an endothermic heat flow is observed, which is clearly related to the melting process of the membrane followed by the decomposition of the melt.

For both materials, BSCF and BSFZ, respectively, excellent phase maintenance after sintering with BN has been observed as it can be concluded by comparing the obtained XRD pattern with those obtained from pure BSCF and BSFZ powders [22,23] as visible in Fig. 2a and b. Despite the fact the perovskite structure could be maintained even after sintering with BN, small amounts of CoO have been found in the BSCF membrane that was sintered with 10 mol% (not visible in XRD pattern but confirmed by EDXS of the fracture surface). In the case of BSZF membranes that were sintered with 7.5 and 10 mol% small amounts of ZnO
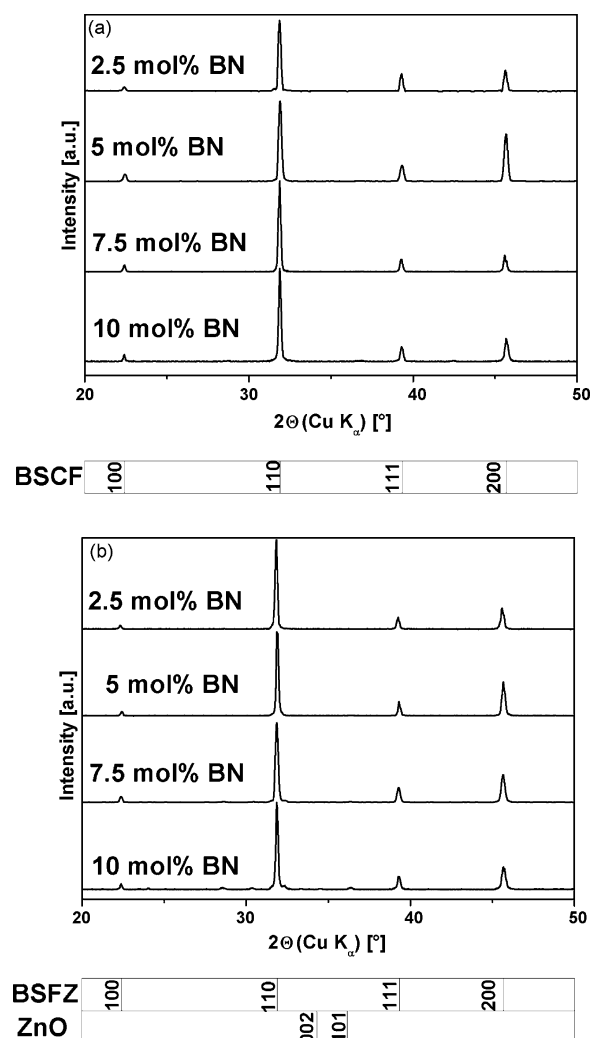

Fig. 2. XRD pattern taken of sintered membranes (surfaces) as synthesized: (a) BSCF, (b) BSFZ. XRD data obtained of pure BSCF and BSFZ and ZnO are displayed for comparison.
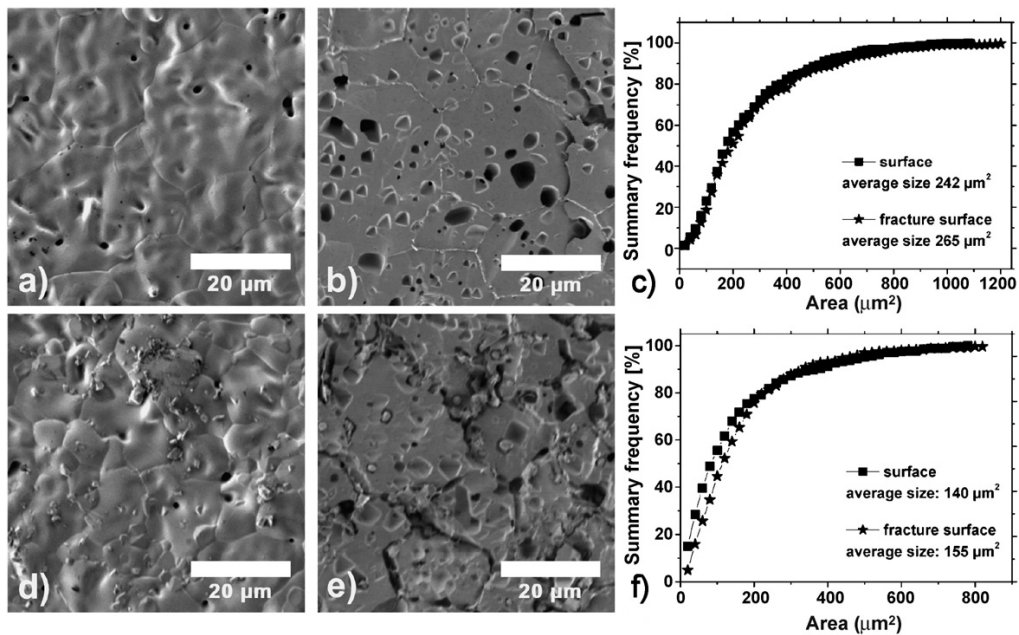
Fig. 3. SEM micrographs showing surfaces and fracture surfaces of sintered BSCF membranes (a–f). (a) Surface, (b) fracture surface, and (c) grain size distribution of a BSCF membrane containing 2.5 mol% BN. (d) Surface, (e) fracture surface, and (f) grain size distribution of a BSCF membrane containing 10 mol% BN.

have been detected on the surface as shown in Fig. 2b. Additionally, two unidentified reflections with very low intensities at 28.6° 2θ and 30.4° 2θ were found in these membranes.

In order to examine the microstructure of the sintered membranes, SEM was conducted on both surfaces and fracture surfaces on each membrane (Figs. 3 and 4). Fig. 3 displays SEM

micrographs and corresponding grain size distributions of BSCF membranes after sintering with 2.5 mol% BN (a–c) and with 10 mol% BN (d–f) for 10 h at 1050 °C, respectively. As it can be seen in Fig. 3, dense membranes of BSCF sintered with BN have been achieved with low level of porosity even if the sintering temperature was decreased to 1050 °C. Wang et al. found
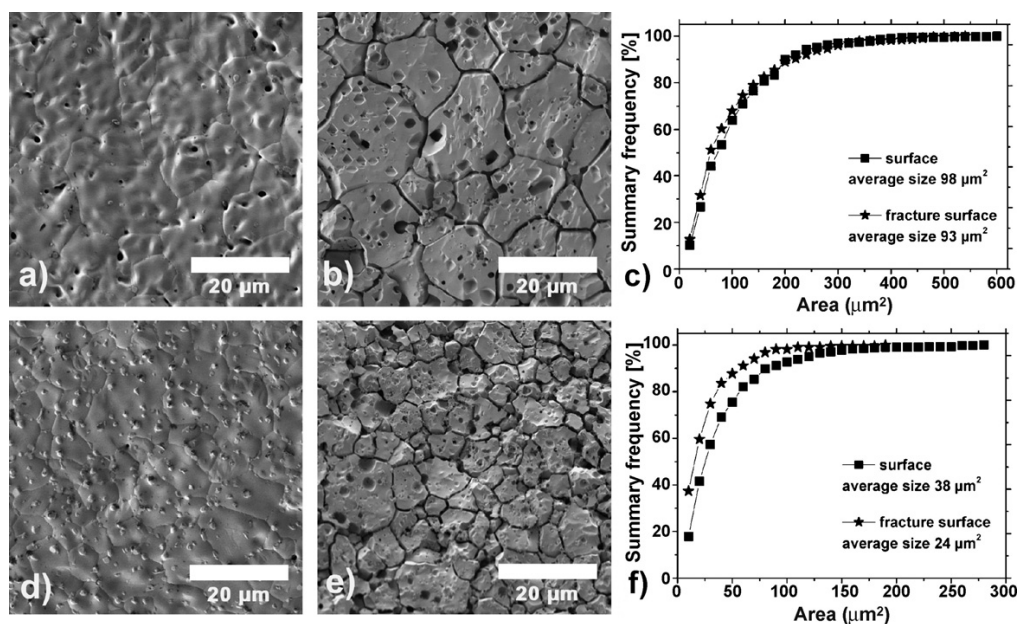

Fig. 4. SEM micrographs showing surfaces and fracture surfaces of sintered BSFZ membranes (a–f). (a) Surface, (b) fracture surface, and (c) grain size distribution of a BSFZ membrane containing 2.5 mol% BN. (d) Surface, (e) fracture surface, and (f) grain size distribution of a BSFZ membrane containing 10 mol% BN.

6.2. Microstructure and oxygen permeation in BSCF and BSFZ

Table 1
Summary of melting points of membranes after sintering with indicated mol% BN obtained via DSC

BSCF (mol% BN)	T_{melt} (°C)	BSFZ (mol% BN)	T_{melt} (°C)
2.5	1131	2.5	1218
5	1102	5	1161
7.5	1088	7.5	1142
10	1078	10	1117

Table 3
Relative densities of BSCF and BSFZ membranes after sintering obtained by the Archimedes method

mol% BN	BSCF (%)	BSFZ (%)
10	94	92
7.5	96	94
5	96	95
2.5	93	93

that sintering temperatures of at least 1150 °C were needed to obtain dense BSCF membranes with negligible porosity [18]. Obviously, the sintering aid BN helped to lower the sintering temperature of the prepared dense membranes. This was confirmed by DSC, as the melting point of the membranes was decreased using BN as sintering aid. A summary of the melting temperatures of the sintered BSCF and BSFZ membranes is given in Table 1.

Quantitative evaluation of the grain size distribution via SEM have shown that the addition of large amounts of BN lead to a decrease of the average grain size (Fig. 3c and f). The average grain size of BSCF-membranes sintered with 2.5 mol% BN has been determined to be 242 μm^2 at the surface and 265 μm^2 at the fracture surface, respectively. Contrary, membranes sintered with 10 mol% exhibit average grain sizes of 140 μm^2 (surface) and 155 μm^2 (fracture surface). In the case of 10 mol% BN, small particles of CoO ($\sim$1 μm^2) have been found on the fracture surface as confirmed by EDXS.

Similar experiments were conducted for membranes of BSFZ. It has emerged, that melting temperatures of BSFZ membranes with BN as sintering lie generally up to 70 °C higher than that for the BSCF membranes (Table 1). In Fig. 4, SEM micrographs and grain size distributions of membranes after sintering with 2.5 mol% BN (a–c) and membranes sintered with 10 mol% BN are displayed (d–f). As for the case of BSCF, BSFZ membranes sintered with BN exhibit a low level of porosity and the same trend for the average grain size was found as for the BSCF membranes: The higher the amount of added BN the lower the average grain size. The average grain size of membranes sintered with 2.5 mol% has been determined to be 98 μm^2 (surface) and 93 μm^2 (fracture surface) compared to 38 μm^2 (surface) and 24 μm^2 (fracture surface) if 10 mol% BN was added (Fig. 4c and f). It has to be noted that small particles ($\sim$1 μm^2) of ZnO (Fig. 4d) were found on the membrane surface after sintering with 7.5 and 10 mol% BN, respectively. Table 2 summarizes average grain sizes found in each membrane and it clearly demonstrates that increasing the amount of BN as

sintering aid leads to a decrease in the average grain size. Additionally, it has to be emphasized that no boron has been found by EDXS in the surface or in the fracture surface in membranes of BSCF and BSFZ, respectively. Relative densities, displayed in Table 3, of the sintered membranes by the Archimedes method are estimated to vary randomly from 93 to 96% which display reasonable values as reported elsewhere [18].

As already found by Wang et al. [18], grain boundaries may affect the oxygen permeation in BSCF membranes in a negative manner. Therefore, oxygen permeation experiments were conducted in order to determine the influence of the average grain size (and thus the impact of grain boundaries) on the oxygen transport through the perovskite membranes. Fig. 5a and b displays the temperature-dependent oxygen permeation flux of BSCF and BSFZ membranes sintered with varying BN content. For all membranes, an almost linear slope for the oxygen permeation is observed in the temperature regime studied here. BSCF membranes sintered with 2.5 mol% BN exhibit an oxygen permeation performance that varies from 1.50 ml/min cm^2 at 850 °C to 2.60 ml/min cm^2 at 925 °C. As the amount of BN was increased during sintering, a diminution of the oxygen permeation flux has been observed (0.80 ml/min cm^2 at 850 °C to 1.60 ml/min cm^2 at 925 °C for 10 mol% BN added). In the case of BSFZ membranes sintered with BN, the oxygen permeation performance is not as strongly affected by the addition of BN as in the case of BSCF. Up to 7.5 mol% BN added as sintering aid no change in the oxygen permeation performance could be found and its ranges from 0.40 ml/min cm^2 (850 °C) to 0.85 ml/min cm^2 (925 °C) which is in the same order of magnitude as reported for membranes without sintering aid [10]. Only if the BN addition was set to 10 mol%, a distinct diminution in the oxygen permeation performance has been observed, as the oxygen permeation flux is found to range between 0.37 ml/min cm^2 (850 °C) and 0.80 ml/min cm^2 (925 °C) in this case.

In order to better visualize the dependence of oxygen permeation performance on the amount BN added to the membranes

Table 2
Summary of average grain sizes in sintered membranes with varying BN content

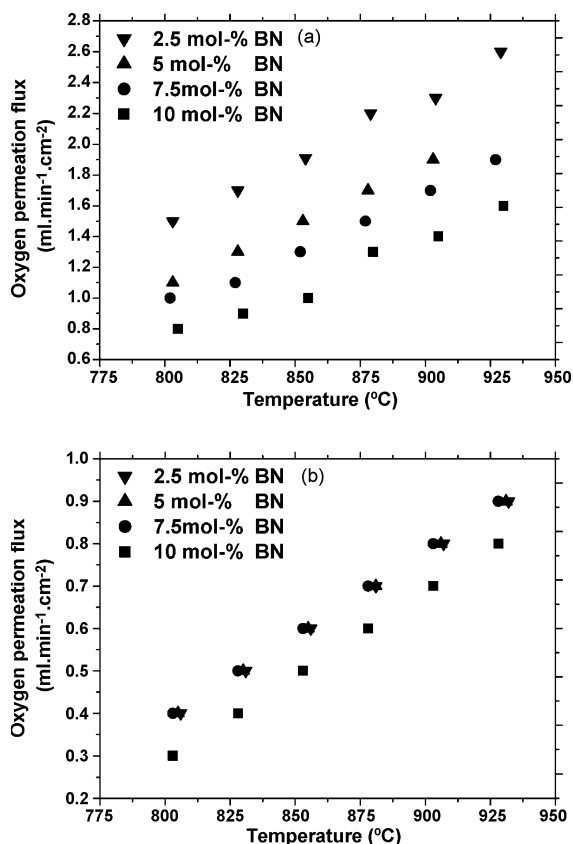| BSCF			BSFZ		
mol% BN	Area (μm^2) (surface)	Area (μm^2) (fracture surface)	mol% BN	Area (μm^2) (surface)	Area (μm^2) (fracture surface)
2.5	242	265	2.5	98	93
5	250	218	5	68	69
7.5	216	199	7.5	46	33
10	140	155	10	38	24

Fig. 5. Temperature-dependent oxygen permeation flux of sintered membranes with different BN content: (a) BSCF, (b) BSFZ. Conditions: feed synthetic air flow rate 150 ml/min, sweep flow rate 30 ml (helium 29 ml/min, neon 1 ml/min).
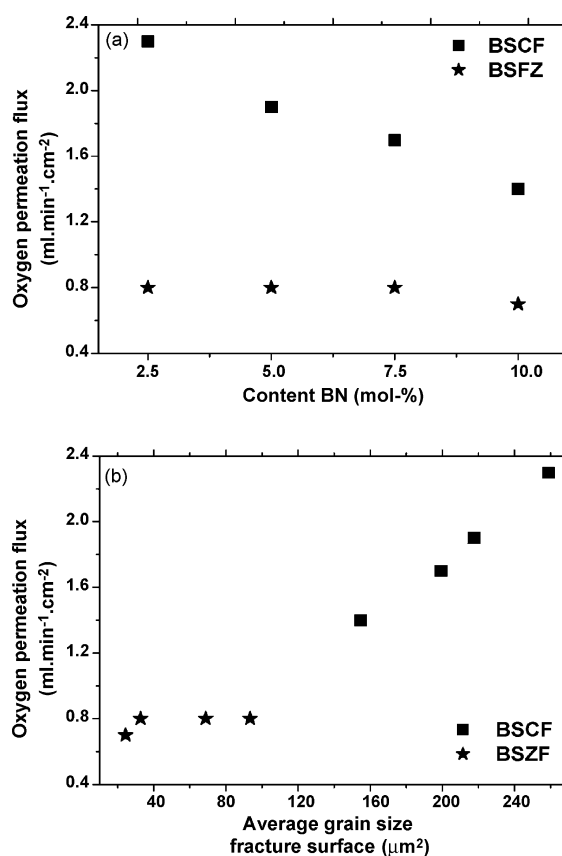

Fig. 6. Oxygen permeation flux of sintered membranes with different BN content at 900 °C. (a) Oxygen permeation flux in dependence of BN content and (b) oxygen permeation flux in dependence of average grain size at fracture surface. Conditions: feed synthetic air flow rate 150 ml/min, sweep flow rate 30 ml (helium 29 ml/min, neon 1 ml/min).

before sintering, oxygen permeation fluxes are plotted against the BN content and the average grain size on the surface at fixed temperature (Fig. 6a and b). At a temperature of 900 °C the oxygen permeation decreases from 2.30 ml/min cm^2 (2.5 mol% BN) down to 1.40 ml/min cm^2 (10 mol% BN) for BSCF membranes, whereas the oxygen permeation flux of BSFZ membranes range from 0.80 down to 0.70 ml/min cm^2 at 900 °C (Fig. 6a). The influence of the average grain size of the membranes on the oxygen permeation performance is displayed in Fig. 6b. For the case of BSCF membranes a decrease of the oxygen permeation flux from 2.30 down to 1.40 ml/min cm^2 is observed whereas the corresponding average grain size ranges from 265 to 155 μm^2 at the fracture surface. It should be stressed that the oxygen permeation performance decreases proportionally to the average grain size. In order to draw a general conclusion, membranes that have been sintered without boron nitride were also studied. Permeation experiments show that membranes consisting of an average grain size of 468 μm^2 (surface) and 430 μm^2 (fracture surface) exhibit an oxygen flux of 2.70 ml/min cm^2 at 900 °C, which is in excellent agreement with results discussed above.

In the case of BSFZ, the oxygen permeation flux varies from 0.77 to 0.72 ml/min cm^2 at 900 °C whereas the average grain size at the fracture surface ranges from 93 to 24 μm^2.

Again, membranes without BN addition were prepared. It was found that a membrane with an average grain size of 435 μm^2 (surface) and 317 μm^2 (fracture surface) show an oxygen permeation flux of 0.80 ml/min cm^2 at 900 °C, which is higher than in the case of the membrane sintered with 2.5 mol% BN (oxygen permeation flux for this membrane: 0.77 ml/min cm^2).

In the case of BSCF, it is obvious that the larger the grain sizes the greater the oxygen permeation flux. This is in good agreement with findings of Wang et al. who also found a positive correlation between larger grains and higher oxygen permeation flux [18]. BSFZ membranes do not exhibit an influence of the average grain size that is as strong as for BSCF membranes.

In order to achieve a better understanding of the microstructure at the grain boundaries, an HRTEM study was conducted on a BSCF membrane which was sintered with 10 mol% BN as it is shown in Fig. 7. A TEM micrograph of two BSCF grains which can be discriminated by bright contrast is displayed in Fig. 7a. BSCF stoichiometry of these two grains has been confirmed by an EDXS analysis. For that purpose an ovally shaped convergent electron beam was used. The convergent beam mode allows to acquire as much signal as possible from the grain boundary.
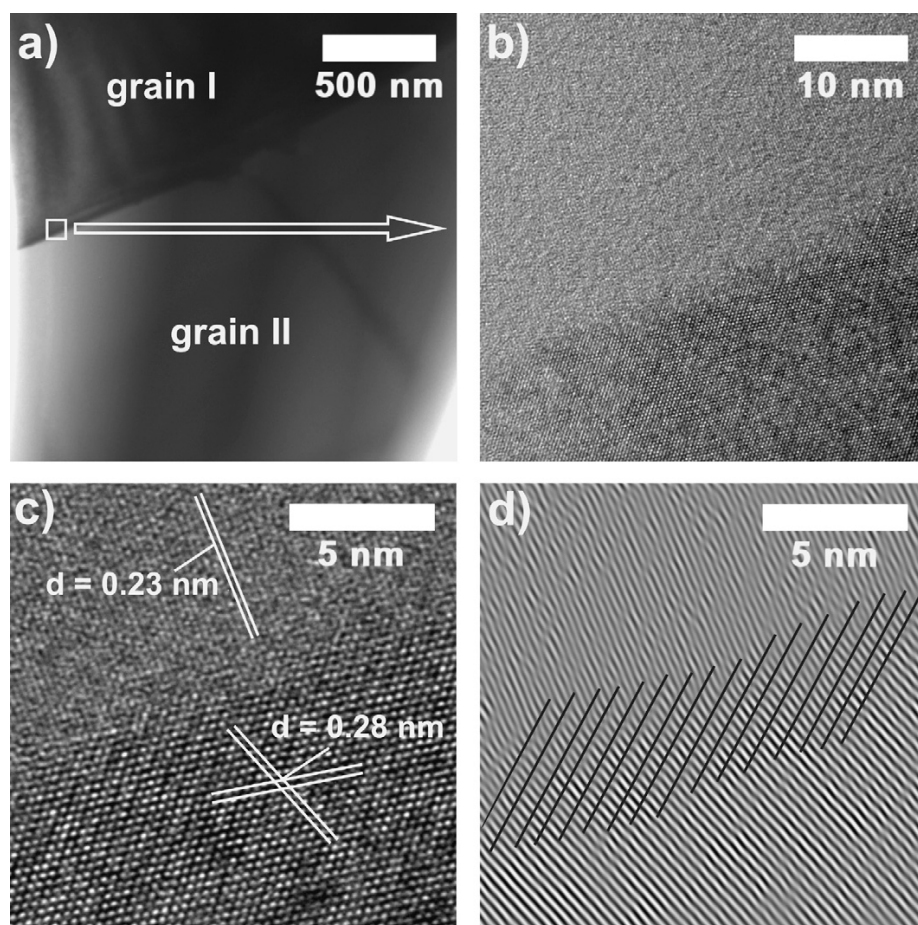
Fig. 7. TEM micrographs obtained from a BSCF membrane containing 10 mol% BN showing two different grains (a–d). (a) TEM bright-field micrograph, (b and c) HRTEM micrographs, and (d) inverse FFT of HRTEM micrograph as shown in (c). Black lines indicate direction of Moiré pattern.

From the EDXS analysis no difference in the elemental composition of grain I, grain II, and the grain boundary have been found as it can be seen in Table 4. As EDXS might not be the most sophisticated method to elucidate light elements like boron, electron-energy loss spectroscopy (EELS) was also conducted. Even via EELS, no boron could be found. Fig. 7b and c show HRTEM micrographs of a selected part of this grain boundary. Neither an interfacial phase nor an amorphous layer has been found to be located between the two grains as it can be seen in Fig. 7c. No zone axis could be determined for grain I but the observed plane spacing was determined to be 0.23 nm which is related to the (1,1,1)-plane of BSCF. The zone axis of grain

II was found to be [1,1,1]. Thus, the grain boundary displays the contact zone between (1,1,1)-planes of grain I and (1,1,0)-planes of grain II whereas the angle between these planes is determined to be 21°. An inverse fast-Fourier transformation (based on (1,1,1) of grain I and (1,1,0) of grain II) was conducted which is shown in Fig. 7d. As indicated by black lines, Moiré pattern has been observed indicating an overlap of approximately 6 nm of grain I and grain II. As the contrast of the lattice planes do not abate towards the contact zone, no indication for an amorphous layer is given. Diethelm et al. suggested that in the case of $(La_{0.5}Sr_{0.5})FeO_{3-\delta}$ an amorphous layer at the most of 0.5 nm may be prominent [13,14]. As reported for this material, smaller average grain sizes promote the oxygen permeation flux. Thus, the amorphous layer may act as fast diffusion pathway. This finding could further deliver an explanation for the blocking effect of the grain boundaries in the study presented here, as we believe no amorphous or interfacial layer is eminent in the grain boundaries of BSCF. Feldhoff et al. [11] reported even in BSFZ the grain boundaries are atomically thin containing no second phase, which underlines the findings presented here.

Table 4
Quantitive analysis of elemental composition by EDXS of grain I, grain II and grain boundary as shown in Fig. 7

Element	Grain I (atom%)	Grain II (atom%)	Grain boundary (atom%)
Ba	28	29	28
Sr	24	23	25
Co	37	37	36
Fe	11	11	11

4. Conclusion

Dense ceramic membranes of BSCF and BSFZ with BN as sintering aid were successfully prepared via liquid-phase sintering. It has emerged that using BN as sintering aid the sintering temperature could be lowered down to $1050\,°C$ in the case of BSCF membranes and down to $1100\,°C$ in the case of the BSFZ membranes. It is also shown that the obtained membranes exhibit excellent phase stability after sintering with only very few impurities and no boron remained in the membranes after the sinter process. For both membrane materials BSCF and BSFZ, an increase of the added amount BN lead to a decrease of the average grain size. Oxygen permeation experiments delivered evidence that membranes containing particularly larger grains exhibit a better oxygen permeation performance. This effect is especially pronounced in the case of BSCF membranes in which the oxygen permeation flux is lowered proportionally to the abatement of the average grain size. A TEM study gives first indication that no amorphous material or interfacial phase is incorporated at the grain boundaries. That leads to the assumption that a lattice misfit between the grains and associated straining of grain boundary near regions could have negative impact on the oxygen ion transport. Considering former reports on the correlation of microstructure and oxygen permeation, future investigations should focus on the microstructure of the grain boundaries as their nature may give a better understanding of the oxygen permeation through dense ceramic membranes.

Acknowledgements

References

[1] H.J.M. Bouwmeester, A.J. Burggraaf, Dense ceramic membranes for oxygen separation, in: A.J. Burggraaf, L. Cot (Eds.), Fundamentals of Inorganic Membrane Science and Technology, Elsevier, Amsterdam, 1996, p. 435.

[2] Z.P. Shao, S. Haile, A high-performance cathode for the next generation of solid-oxide fuel cells, Nature 431 (2004) 170.

[3] H. Wang, S. Werth, T. Schiestel, J. Caro, Perovskite hollow-fibre membranes for the production of oxygen-enriched air, Angew. Chem. Int. 44 (2005) 6906.

[4] C.S. Cheng, S.J. Feng, S. Ran, D.C. Zhu, W. Liu, H.J.M. Bouwmeester, Conversion of methane to syngas by a membrane-based oxidation-reforming process, Angew. Chem. Int. Ed. 115 (2003) 5354.

[5] W. Zhu, W. Han, G. Xiong, W. Yang, Mixed reforming of heptane to syngas in the $Ba_{0.5}Sr_{0.5}Co_{0.8}Fe_{0.2}O_{3-\delta}$ membrane reactor, Catal. Today 104 (2005) 149.

[6] B. Wei, Z. Lü, X. Huang, Z. Liu, J. Miao, N. Li, W. Su, $Ba_{0.5}Sr_{0.5}Zn_{0.2}Fe_{0.8}O_{3-\delta}$ Perovskite oxide as novel cathode for intermediate-temperature solid-oxide fuel cells, J. Am. Ceram. Soc. 90 (2007)3364.

[7] H. Wang, C. Tablet, W. Yang, J. Caro, In situ high temperature X-ray diffraction studies of mixed ionic and electronic conducting perovskite-type membranes, Mater. Lett. 59 (2005) 3750.

[8] S. McIntosh, J.F. Vente, W.G. Haije, D.H.A. Blank, H.J.M. Bouwmeester, Oxygen stoichiometry and chemical expansion of $Ba_{0.5}Sr_{0.5}Co_{0.8}Fe_{0.2}O_{3-\delta}$ measured by in situ neutron diffraction, Chem. Mater. 18 (2006) 2187.

[9] Z.P. Shao, W.S. Yang, Y. Cong, H. Dong, J.H. Tong, G.X. Xiong, Investigation on the permeation behaviour and stability of a $Ba_{0.5}Sr_{0.5}Co_{0.8}Fe_{0.2}O_{3-\delta}$ oxygen membrane, J. Membr. Sci. 172 (2000) 177.

[10] H. Wang, C. Tablet, A. Feldhoff, J. Caro, A cobalt-free oxygen-permeable membrane based on the perovskite-type oxide $Ba_{0.5}Sr_{0.5}Zn_{0.2}Fe_{0.8}O_{3-\delta}$, Adv. Mater. 17 (2005) 1785.

[11] A. Feldhoff, J. Martynczuk, H. Wang, Advanced $Ba_{0.5}Sr_{0.5}Zn_{0.2}Fe_{0.8}O_{3-\delta}$ perovskite-type ceramics as oxygen selective membranes: evaluation of the synthetic process, Prog. Solid State Chem. 35 (2007) 339.

[12] J. Martynczuk, M. Arnold, H. Wang, J. Caro, A. Feldhoff, How $(Ba_{0.5}Sr_{0.5})(Fe_{0.8}Zn_{0.2})O_{3-\delta}$ and $(Ba_{0.5}Sr_{0.5})(Co_{0.8}Fe_{0.2})O_{3-\delta}$ perovskites form via an EDTA/citric acid complexing method, Adv. Mater. 19 (2007) 2134.

[13] S. Diethelm, J. Van herle, J. Sfeir, P. Buffat, Correlation between oxygen transport properties and microstructure in $La_{0.5}Sr_{0.5}FeO_{3-\delta}$, J. Eur. Ceram. Soc. 25 (2005) 2191.

[14] S. Diethelm, J. Van herle, J. Sfeir, P. Buffat, Influence of microstructure on oxygen transport in perovskite type membranes, Br. Ceram. Trans. 103 (2004) 147.

[15] V.V. Kharton, F.M.B. Marques, Mixed ionic–electronic conductors: effect of ceramic microstructure on transport properties, Curr. Opin. Solid State Mater. Sci. 6 (2002) 261.

[16] A.L. Shaula, R.O. Fuentes, F.M. Figueiredo, V.V. Kharton, F.M.B. Marques, J.R. Frade, Grain size effects on oxygen permeation in submicrometric $CaTi_{0.8}Fe_{0.2}O_{3-\delta}$ ceramics obtained by mechanical activation, J. Eur. Ceram. Soc. 25 (2005) 2613.

[17] K. Zhang, Y.L. Yang, D. Ponnusamy, A.J. Jacobson, K. Salama, Effect of microstructure on oxygen permeation in $SrCo_{0.8}Fe_{0.2}O_{3-\delta}$, J. Mater. Sci. 34 (1999) 1367.

[18] H. Wang, C. Tablet, A. Feldhoff, J. Caro, Investigation of phase structure, sintering, and permeability of perovskite-type $Ba_{0.5}Sr_{0.5}Co_{0.8}Fe_{0.2}O_{3-\delta}$ membranes, J. Membr. Sci. 262 (2005) 20.

[19] J.F. Vente, S. McIntosh, W.G. Haije, H.J.M. Bouwmeester, Properties and performance of $Ba_{0.5}Sr_{0.5}Co_{0.8}Fe_{0.2}O_{3-\delta}$ materials for oxygen transport membranes, J. Solid State Electrochem. 10 (2006) 581.

[20] I.C. Ho, Semiconducting barium titanate ceramics prepared by boron-containing liquid-phase sintering, J. Am. Ceram. Soc. 77 (1994) 829.

[21] M.N. Rahaman, Ceramic Processing and Sintering, second ed., Marcel Dekker Inc, New York, Basel, 2004.

[22] H. Koster, F.H.B. Mertins, Powder diffraction of the cubic $(Ba_{0.5}Sr_{0.5})(Co_{0.8}Fe_{0.2})O_{3-\delta}$, Powder Diffr. 18 (2003) 56.

[23] A. Feldhoff, M. Arnold, J. Martynczuk, T. Gesing, H. Wang, The sol–gel synthesis of perovskites by an EDTA/citrate complexing method involves nanoscale solid state reactions, Solid State Sci., submitted for publication.

Bibliography

[1] J. Caro. Membranreaktoren für die katalytische Oxidation. *Chemie Ingenieur Technik*, 78:899–912, **2006**.

[2] J.H. Gary and G.E. Handwerk. *Petroleum Refining Technology and Economics*. Marcel Dekker, New York, 2nd edition, **1984**.

[3] D.P. Bhasin, M.S. Liebeison, and G.J. Chapman. Oxygen increases FCC throughput. *Hydrocarbon Process*, 62:85–88, **1983**.

[4] B.C.H. Steele and A. Heinzel. Materials for fuel-cell technologies. *Nature*, 414:345–352, **2001**.

[5] N.P. Brandon, S. Skinner, and B.C.H. Steele. Recent advances in materials for fuel cells. *Annual Review of Materials Research*, 33:183–213, **2003**.

[6] R. Baker. *Membrane Technology in the Chemical Industry: Further Directions: R. Baker in Membrane Technology in the Chemical Industry, Part II*. Wiley-VCH, Weinheim, 1st edition, **2001**.

[7] A.F. Holleman and E. Wiberg. *Lehrbuch der anorganischen Chemie*. de Gruyter, Berlin, New York, 101st edition, **1995**.

[8] R.V. Jasra, N.V. Choudary, and S.G.T. Bhat. Separation of gases by pressure swing adsorption. *Separation Science and Technology*, 26:885–930, **2001**.

[9] H.J.M. Bouwmeester and A.J. Burggraaf. *Dense ceramic membranes for oxygen separation, in: A.J. Burggraaf and L. Cot (Eds.), Fundamentals of inorganic membrane science and technology*. Elsevier, Amsterdam, 1st edition, **1996**.

[10] A. Rodewald and A. Kather. Thermodynamische und wirtschaftliche Machbarkeitsstudie zum Steinkohle befeuerten Oxyfuel-Dampfkraftprozess. *Chemie Ingenieur Technik*, 76:1320–1321, **2004**.

[11] M. Modigell, R. Kneer, H. Maier, N. Peters, D. Abel, and R. Niehuis. Oxycoal AC — Entwicklung eines CO_2 emissionsfreien thermischen Kraftwerkprozesses. *Chemie Ingenieur Technik*, 77:1147–1148, **2005**.

[12] P.J. Gellings and H.J.M. Bouwmeester. Solid state aspects of oxidation catalysis. *Catalysis Today*, 58:1–53, **2000**.

[13] C.S. Chen, S.J. Feng, S. Ran, D.C. Zhu, W. Liu, and H.J.M. Bouwmeester. Conversion of methane to syngas by a membrane-based oxidation-reforming process. *Angewandte Chemie International Edition*, 42:5196–5198, **2003**.

[14] Z.P. Shao and S.M. Haile. A high-performance cathode for the next generation of solid-oxide fuel cells. *Nature*, 431:170–173, **2004**.

[15] Z.P. Shao, W.S. Yang, Y. Cong, H. Dong, J.H. Tong, and G.X. Xiong. Investigation of the permeation behavior and stability of a $(Ba_{0.5}Sr_{0.5})(Co_{0.8}Fe_{0.2})O_{3-\delta}$ oxygen membrane. *Journal of Membrane Science*, 172:177–188, **2000**.

[16] A.C. van Veen, M. Rebeilleau, D. Farrusseng, and C. Mirodatos. Studies on the performance stability of mixed conducting BSCFO membranes in medium temperature oxygen permeation. *Chemical Communications*, 2003:32–33, **2003**.

[17] H.H. Wang, C. Tablet, A. Feldhoff, and J. Caro. Investigation of phase structure, sintering, and permeability of perovskite-type $(Ba_{0.5}Sr_{0.5})(Co_{0.8}Fe_{0.2})O_{3-\delta}$ membranes. *Journal of Membrane Science*, 262:20–26, **2005**.

[18] P.Y. Zeng, Z.H. Chen, W. Zhou, H.X. Gu, Z.P. Shao, and S.M. Liu. Re-evaluation of $(Ba_{0.5}Sr_{0.5})(Co_{0.8}Fe_{0.2})O_{3-\delta}$ perovskite as oxygen semi-permeable membrane. *Journal of Membrane Science*, 291:148–156, **2007**.

[19] Z.P. Shao, G.X. Xiong, H. Dong, W.S. Yang, and L.W. Lin. Synthesis, oxygen permeation study and membrane performance of a $(Ba_{0.5}Sr_{0.5})(Co_{0.8}Fe_{0.2})O_{3-\delta}$ oxygen-permeable dense ceramic reactor for partial oxidation of methane to syngas. *Separation and Purification Technology*, 25:97–116, **2001**.

[20] H.H. Wang, Y. Cong, and W.S. Yang. High selectivity of oxidative dehydrogenation of ethane to ethylene in an oxygen permeable membrane reactor. *Chemical Communications*, 2002:1468–1469, **2002**.

[21] H.H. Wang, Y. Cong, and W.S. Yang. Partial oxidation of ethane to syngas in an oxygen-permeable membrane reactor. *Journal of Membrane Science*, 209:143–152, **2002**.

[22] W.L. Zhu, W. Han, G.X. Xiong, and W.S. Yang. Mixed reforming of heptane to syngas in the $(Ba_{0.5}Sr_{0.5})(Co_{0.8}Fe_{0.2})O_{3-\delta}$ membrane reactor. *Catalysis Today*, 104:149–153, **2005**.

[23] M. Rebeilleau-Dassonneville, S. Rosini, A.C. van Veen, D. Farrusseng, and C. Mirodatos. Oxidative activation of ethane on catalytic modified dense ionic oxygen conducting membranes. *Catalysis Today*, 104:131–137, **2005**.

[24] S.M. Liu and G.R. Gavalas. Oxygen selective ceramic hollow fiber membranes. *Journal of Membrane Science*, 246:103–108, **2005**.

[25] J. Caro, H.H. Wang, C. Tablet, A. Kleinert, A. Feldhoff, T. Schiestel, M. Kilgus, P. Kölsch, and S. Werth. Evaluation of perovskites in hollow fibre and disk geometry in catalytic membrane reactors and in oxygen separators. *Catalysis Today*, 118:128–135, **2006**.

[26] A. Yan, M. Cheng, Y.L. Dong, W.S. Yang, V. Maragou, S.Q. Song, and P. Tsiakaras. Investigation of a $(Ba_{0.5}Sr_{0.5})(Co_{0.8}Fe_{0.2})O_{3-\delta}$ based cathode IT-SOFC I. The effect of CO_2 on the cell performance. *Applied Catalysis B: Environmental*, 66:64–71, **2006**.

[27] A. Yan, M. Cheng, Y.L. Dong, W.S. Yang, V. Maragou, S.Q. Song, and P. Tsiakaras. Investigation of a $(Ba_{0.5}Sr_{0.5})(Co_{0.8}Fe_{0.2})O_{3-\delta}$ based cathode SOFC II. The effect of CO_2 on the chemical stability. *Applied Catalysis B: Environmental*, 76:320–327, **2007**.

[28] W. Lei and S.M. Haile. Electrochemical impedance spectroscopy of mixed conductors under a chemical potential gradient: a case study of $Pt\,|SDC|\,BSCF$. *Physical Chemistry Chemical Physics*, 10:865–883, **2008**.

[29] H.H. Wang, C. Tablet, A. Feldhoff, and J. Caro. A cobalt-free oxygen-permeable membrane based on the perovskite-type oxide $(Ba_{0.5}Sr_{0.5})(Fe_{0.8}Zn_{0.2})O_{3-\delta}$. *Advanced Materials*, 17:1785–1788, **2005**.

[30] J. Martynczuk, M. Arnold, H.H. Wang, J. Caro, and A. Feldhoff. How $(Ba_{0.5}Sr_{0.5})(Fe_{0.8}Zn_{0.2})O_{3-\delta}$ and $(Ba_{0.5}Sr_{0.5})(Co_{0.8}Fe_{0.2})O_{3-\delta}$ Perovskites Form via an EDTA/Citric Acid Complexing Method. *Advanced Materials*, 19:2134–2140, **2007**.

[31] U. Müller. *Anorganische Strukturchemie, in: C. Elschenbroich, F. Hensel, H. Hopf (Eds.), Teubner Studienbücher Chemie*. Teubner, Stuttgart, 3rd edition, **1996**.

[32] B.E. Gushee, L. Katz, and R. J. Ward. The preparation of a barium cobalt oxide and other phases with similar structures. *Journal of the American Chemical Society*, 79:5601–5603, **1957**.

[33] Y. Takeda, F. Kanamaru, M. Shimada, and M. Koizumi. The crystal structure of $BaNiO_3$. *Acta Crystallographica*, B32:2464–2466, **1976**.

[34] J.B. Goodenough. *Localized to Itinerant Electronic Transition in Perovskite Oxides, in: D.M.P. Mingos, Structure and Bonding*. Springer, Berlin, 1st edition, **2000**.

[35] R.D. Shannon. Revised effective ionic radii and systematic studies of interatomic distances in halides and chalcogenides. *Acta Crystallographica*, A32:751–767, **1976**.

[36] A. Feldhoff, J. Martynczuk, and H.H. Wang. Advanced $Ba_{0.5}Sr_{0.5}Zn_{0.2}Fe_{0.8}O_{3-\delta}$ perovskite-type ceramics as oxygen selective membranes: Evaluation of the synthetic process. *Progress in Solid State Chemistry*, 35:339–353, **2007**.

[37] S. McIntosh, J.F. Vente, W.G. Haije, D.H.A. Blank, and H.J.M. Bouwmeester. Oxygen stoichiometry and chemical expansion of $(Ba_{0.5}Sr_{0.5})(Co_{0.8}Fe_{0.2})O_{3-\delta}$ measured by in situ neutron diffraction. *Chemistry of Materials*, 18:2187–2193, **2006**.

[38] A. Feldhoff, M. Arnold, J. Martynczuk, Th.M. Gesing, and H.H. Wang. The sol-gel synthesis of perovskites by an EDTA/citrate complexing method involves nanoscale solid state reactions. *Solid State Sciences*, doi:10.1016/j.solidstatesciences.2007.11.030:./., **2007**.

[39] Y. Takeda, K. Kanno, T. Takada, O. Yamamoto, M. Takano, N. Nakayama, and Y. Bando. Phase relation in the oxygen nonstoichiometric system, $SrFeO_x$, $(2.5 \le x \le 3.0)$. *Solid State Sciences*, 63:237–249, **1986**.

[40] P. Adler and S. Eriksson. Structural Properties, Mössbauer Spectra, and Magnetism of Perovskite-Type Oxides $SrFe_{1-x}Ti_xO_{3-y}$. *Zeitschrift für Anorganische und Allgemeine Chemie*, 626:118–124, **2000**.

[41] R. Hoffmann. *Solids und Surfaces. A Chemist's View of Bonding in Extended Structures.* Wiley-VCH, Weinheim, 1st edition, **1988**.

[42] L. Smart and E. Moore. *Einführung in die Festkörperchemie.* Vieweg, Braunschweig/Wiesbaden, 2nd edition, **1997**.

[43] Ch. Kittel. *Einführung in die Festkörperphysik.* Oldenbourg, München, 3rd edition, **1968**.

[44] J.B. Goodenough. Covalence criterion for localized vs. collective electrons in oxides with perovskite structure. *Journal of Applied Physics*, 37:1415–1422, **1966**.

[45] J.B. Goodenough. Metallic oxides. *Progress in Solid State Chemistry*, 5:145–399, **1976**.

[46] C. Mitterbauer, G. Kothleitner, W. Grogger, H. Zandbergen, B. Freitag, P. Tiemeijer, and F. Hofer. Electron energy-loss near-edge structures of $3d$ transition metal oxides recorded at high-energy resolution. *Ultramicroscopy*, 96:469–480, **2003**.

[47] M. Abbate, J.C. Fuggle, A. Fujimori, L.H. Tjeng, C.H. Chen, R. Potze, G.A. Sawatzky, H. Eisaki, and S. Uchida. Electronic structure and spin state of $LaCoO_3$. *Physical Review B*, 47:16124–16130, **1993**.

[48] Z. Hu, H. Wu, M.W. Haverkort, H.H. Hsieh, H.J. Lin, T. Lorenz, J. Baier, A. Reichl, I. Bonn, C. Felser, A. Tanaka, C.T. Chen, and L.H. Tjeng. Different look at the spin state of Co^{3+} ions in a CoO_5 pyramidal coordination. *Physical Review Letters*, 92:207402–4, **2004**.

[49] J.H. Paterson and O.L. Krivanek. ELNES of transition metal oxides II. Variations with oxidation state and crystal structure. *Ultramicroscopy*, 32:319–325, **1990**.

[50] W.S. Yoon, K.B. Kim, M.G. Kim, M.K. Lee, H.J. Shin, J.M. Lee, and J.S. Lee. Oxygen contribution on Li-Ion intercalation-deintercalation in $LiCoO_2$ investigated by O K-edge and Co L-edge X-ray absorption spectroscopy. *Journal of Physical Chemistry B*, 106:2526–2532, **2002**.

[51] F.M.F de Groot, M. Grioni, J.C. Fuggle, J. Ghijsen, G.A. Sawatzky, and H. Petersen. Oxygen 1s X-ray-absorption edges of transition-metals oxides. *Physical Review B*, 40:5715–5723, **1989**.

[52] A. Gloter, J. Ingrin, D. Bouchet, and C. Colliex. Composition and orientation dependence of the O-K and Fe-$L_{2,3}$ EELS fine structures in $Ca_2(Al_xFe_{1-x})_2O_5$. *Physical Review B*, 61:2587–2594, **2000**.

[53] C. Colliex, T. Manoubi, and C. Ortiz. Electron energy-loss spectroscopy near edge fine structures in the iron oxygen system. *Physical Review B*, 44:11402–11411, **1991**.

[54] J.G. Chen, B. Frühberger, and M.L. Colaianni. Near-edge X-ray absorption fine structure characterization of compositions and reactivities of transition metal oxides. *Journal of Vacuum Science and Technology A*, 14:1668–1673, **1995**.

[55] A.D. Lozano-Gorrin, J.E. Greedana, P. Nunez, C. Gonzalez-Silgo, G.A. Botton, and G. Radtke. Structural characterization, magnetic behavior and high-resolution EELS study of new perovskites $Sr_2Ru_{2-x}Co_xO_{6-\delta}$ (0.5 = x = 1.5). *Journal of Solid State Chemistry*, 180:1209–1217, **2007**.

[56] M.N. Rahaman. *Ceramic Processing and Sintering*. CRC Press/Taylor and Francis Group, Boca Raton, 2nd edition, **2003**.

[57] H. Schmalzried. *Solid State Reactions*. Verlag Chemie, Weinheim, 1st edition, **1981**.

[58] J. Maier. *Festkörper — Fehler und Funktion, Prinzipien der Physikalischen Festkörperchemie*. Teubner, Stuttgart-Leipzig, 1st edition, **2000**.

[59] W. Jander. Reaktionen im festen Zustande bei höheren Temperaturen. *Zeitschrift für Anorganische und Allgemeine Chemie*, 163:1–30, **1927**.

[60] R.E. Carter. Kinetic model for solid-state reactions. *Journal of Chemical Physics*, 34:2010–2015, **1961**.

[61] J. Pâris and R. Pâris. Obtention doxydes mixtes et de solutions solides doxydes par decomposition de complexes organiques mixtes. *Bulletin Société Chimique de France*, 4:1138–1141, **1965**.

[62] C. Marcilly, P. Courty, and B. Delmon. Preparation of highly dispersed mixed oxides and oxide solid solutions by pyrolysis of amorphous organic precursors. *Journal of the American Ceramic Society*, 53:56–57, **1970**.

[63] A. Vantomme R. Pretorius, C.C. Theron and J.W. Mayer. Compound phase formation in thin film structures. *Critical Reviews in Solid State and Materials Sciences*, 24:1–62, **1999**.

[64] U. Gösele and K.N. Tu. Growth kinetics of planar binary diffusion couples: Thin-film case versus bulk case. *Journal of Applied Physics*, 53:3252–3560, **1982**.

[65] F.M. d'Heuerle. Nucleation of a new phase from the interaction of two adjacent phases: Some silicides. *Journal of Materials Research*, 3:167–195, **1988**.

[66] R.W. Cahn and P. Haasen. *Physical Metallurgy.* Elsevier Science BV, North Holland, 4th edition, **1996**.

[67] S. Diethelm, J. Van herle, J. Sfeir, and P. Buffat. Correlation between oxygen transport properties and microstructure in $La_{0.5}Sr_{0.5}FeO_{3-\delta}$. *Journal of the European Ceramic Society*, 25:2191–2196, **2005**.

[68] C. Wagner. Equations for transport in solid oxides and sulfides of transition metals. *Progress in Solid State Chemistry*, 10:3–16, **1975**.

[69] H.J.M Bouwmeester. Dense ceramic membranes for methane conversion. *Catalysis Today*, 82:141–150, **2003**.

[70] M. Liu. *Theoretical assessment of oxygen separation rates of mixed conductors, in T.A. Ramanarayanan and H.L. Tuller (Eds.), Ionic and Mixed Conducting Oxide Ceramics.* Electrochemical Society, New York, 1 edition, **1991**.

[71] H.H. Wang, C. Tablet, W.S. Yang, and J. Caro. In situ high temperature X-ray diffraction studies of mixed ionic and electronic conducting perovskite-type membranes. *Materials Letters*, 59:3750–3755, **2005**.

[72] S. Švarcová, K. Wiik, J. Tolchard, H.J.M. Bouwmeester, and T. Grande. Structural instability of cubic perovskite $Ba_xSr_{1-x}Co_{0.8}Fe_{0.2}O_{3-\delta}$. *Solid State Ionics*, 178:1787–1781, **2008**.

[73] S. Pei, M.S. Kleefisch, T.P. Kobylinski, J. Faber, C.A. Udovich, V. Zhang-McCoy, B. Dabrowski, U. Balachandran, R.L. Mieville, and R.B. Poeppel. Failure mechanism of ceramic membrane reactors in partial oxidation of methane to synthesis gas. *Catalysis Letters*, 30:201–212, **1995**.

[74] J. Tong, W.S. Yang, B. Zhu, and R. Cai. Investigation of ideal zirconium-doped perovskite-type ceramic membrane materials for oxygen separation. *Journal of Membrane Science*, 203:175–189, **2002**.

[75] J. Yi, S. Feng, Y. Zuo, W. Liu, and C. Chen. Oxygen permeability and stability of $Sr_{0.95}Co_{0.8}Fe_{0.2}O_{3-\delta}$ in a CO_2-and H_2O-containing atmosphere. *Chemistry of Materials*, 17:5856–5861, **2005**.

[76] Z. Homonnay, K. Nomura, G. Juhasz, M. Gal, K. Solymos, S. Hamakawa, T. Hayakawa, and A. Vertes. Simultaneous probing of the Fe and Co sites in the CO_2-adsorber perovskite $Sr_{0.95}Ca_{0.05}Co_{0.5}Fe_{0.5}O_{3-\delta}$: a Mössbauer study. *Chemistry of Materials*, 14:1127–1135, **2002**.

[77] Q. Yang, Y.S. Lin, and M. Bülow. High temperature sorption separation of air for producing oxygen-enriched CO_2 stream. *AIChE Journal*, 52:574–581, **2006**.

[78] R. Waser. Bulk conductivity, defect chemistry of acceptor-doped strontium titanate in the quenched state. *Journal of the American Ceramic Society*, 74:1934–1940, **1991**.

[79] X. Guo, J. Fleig, and J. Maier. Separation of electronic and ionic contributions to the grain boundary conductivity in acceptor-doped $SrTiO_3$. *Journal of the Electrochemical Society*, 148:J50–J53, **2001**.

[80] G.E. Pike and C.H. Seager. DC voltage dependence of semiconductor grain-boundary resistance. *Journal of Applied Physics*, 50:3414–3422, **1979**.

[81] X. Guo and J. Maier. Grain boundary blocking effect in zirconia: A schottky barrier analysis. *Journal of the Electrochemical Society*, 148:E121–E126, **2001**.

[82] V.V. Kharton and F.M.B. Marques. Mixed ionicelectronic conductors: effect of ceramic microstructure on transport properties. *Current Opinion in Solid State and Materials Science*, 6:261–269, **2002**.

[83] A.L. Shaula, R.O. Fuentes, F.M. Figueiredo, V.V. Kharton, F.M.B. Marquesa, and J.R. Frade. Grain size effects on oxygen permeation in submicrometric $CaTi_{0.8}Fe_{0.2}O_{3-\delta}$ ceramics obtained by mechanical activation. *Journal of the European Ceramic Society*, 25:2613–2616, **2005**.

[84] K. Zhang, Y.L. Yang, D. Ponnusamy, A.J. Jacobson, and K. Salama. Effect of microstructure on oxygen permeation in $SrCo_{0.8}Fe_{0.2}O_{3-\delta}$. *Journal of Materials Science*, 34:1367–1372, **1999**.

[85] J.F. Vente, S. McIntosh, W.G. Haije, and H.J.M. Bouwmeester. Properties and performance of $Ba_{0.5}Sr_{0.5}Co_{0.8}Fe_{0.2}O_{3-\delta}$ materials for oxygen transport membranes. *Journal of Solid State Electrochemistry*, 10:581–588, **2006**.

[86] S. Diethelm, J. Van herle, J. Sfeir, and P. Buffat. Influence of microstructure on oxygen transport in perovskite type membranes. *British Ceramic Transactions*, 103:147–152, **2005**.

[87] J. Maier. Transport in electroceramics: micro- and nano-structural aspects. *Journal of the European Ceramic Society*, 24:1251–1257, **2004**.

[88] J. Jamnik and J. Maier. Chemical diffusion through grain boundaries in mixed conductors. *Journal of the Electrochemical Society*, 145:1762–1767, **2001**.

List of Figures

Publications and contributions to conferences

Publications included in this work (in chronological order)

(1) Influence of CO_2 on the oxygen permeation performance and the microstructure of perovskite-type $(Ba_{0.5}Sr_{0.5})(Co_{0.8}Fe_{0.2})O_{3-\delta}$ membranes

<u>Mirko Arnold</u>*, Haihui Wang, and Armin Feldhoff
Journal of Membrane Science, **293**, 44-52 (**2007**).

(2) *In situ* Study of the Reaction Sequence in the Sol-Gel Synthesis of a $(Ba_{0.5}Sr_{0.5})(Co_{0.8}Fe_{0.2})O_{3-\delta}$ Perovskite by X-Ray Diffraction and Transmission Electron Microscopy

<u>Mirko Arnold</u>*, Haihui Wang, Julia Martynczuk, and Armin Feldhoff
Journal of the American Ceramic Society, **90**, 3651-3655 (**2007**).

(3) How $(Ba_{0.5}Sr_{0.5})(Fe_{0.8}Zn_{0.2})O_{3-\delta}$ and $(Ba_{0.5}Sr_{0.5})(Co_{0.8}Fe_{0.2})O_{3-\delta}$ Perovskites Form via an EDTA/Citric Acid Complexing Method

Julia Martynczuk, <u>Mirko Arnold</u>, Haihui Wang, Jürgen Caro, and Armin Feldhoff*
Advanced Materials, **19**, 2134-2140 (**2007**).

(4) Grain boundaries as barrier for oxygen transport in perovskite-type membranes

<u>Mirko Arnold</u>*, Julia Martynczuk, Konstantin Efimov, Haihui Wang, and Armin Feldhoff
Journal of Membrane Science, **316**, 137-144 (**2008**).

(5) The sol-gel synthesis of perovskites by an EDTA/citrate complexing method involves nanoscale solid state reactions

Armin Feldhoff*, <u>Mirko Arnold</u>, Julia Martynczuk, Thorsten M. Gesing, and Haihui Wang
Solid State Sciences, doi:10.1016/j.solidstatesciences.2007.11.030 (**2008**).

(6) Correlation of the formation and the decomposition process of the BSCF perovskite at intermediate temperatures

Mirko Arnold*, Thorsten M. Gesing, Julia Martynczuk, Armin Feldhoff
Chemistry of Materials, submitted.

(7) Local Charge Disproportion in a High Performance Perovskite

Mirko Arnold*, Qiang Xu, Frans D. Tichelaar, and Armin Feldhoff
Angewandte Chemie International Edition, submitted.

Publications not included in this work

(8) First Approaches to prepare supported metal-organic framework (MOF) membranes

Mirko Arnold*, Pavel Kortunov, Jörg Kärger, and Jürgen Caro
Proceedings of the 9th International Conference on Inorganic Membranes (ICIM9), Lillehammer, 25-29th July 2006, (ed. by R. Bredesen, H. Raeder), pp. 461-464, ISBN 978-82-14-04026-5, SINTEF, Blindern, Norway (**2006**).

(9) Oriented Crystallisation on Supports and Anisotropic Mass Transport of the Metal-Organic Framework Manganese Formate

Mirko Arnold*, Pavel Kortunov, Deborah J. Jones, Yannig Nedellec, Jörg Kärger, and Jürgen Caro
European Journal of Inorganic Chemistry, **1**, 60-64 (**2007**).

(10) Intracrystalline Diffusivities and Surface Permeabilities
Deduced from Transient Concentration Profiles: Methanol in MOF Manganese Formate

Pavel V. Kortunov, Lars Heinke, Mirko Arnold, Yannic Nedellec, Deborah J. Jones, Jürgen Caro, and Jörg Kärger*
Journal of the American Chemical Society, **129**, 8041-8047 (**2007**).

(11) Influence of grain size on the oxygen permeation performance of perovskite-type $(Ba_{0.5}Sr_{0.5})(Fe_{0.8}Zn_{0.2})O_{3-\delta}$ membranes

Julia Martynczuk*, Mirko Arnold, Ulrich Vogt, and Armin Feldhoff
Journal of Membrane Science, submitted.

Contributions to Conferences

(1) Perovskite-Membranes on the way to industry, Structure-Applications-Challenges

Mirko Arnold*,
ZFM Festkörpernachmittag, Salzgitter, 5th July (**2006**) (Talk).

(2) First approaches to prepare supported Metal-Organic Framework (MOF) Membranes

Mirko Arnold*, Pavel V. Kortunov, Jörg Kärger, and Jürgen Caro
9th International Conference on Inorganic Membranes (ICIM9), Lillehammer, 25th - 29th July (**2006**) (Poster).

(3) Influence of processing conditions on the microstructure and function of $(Ba_{0.5}Sr_{0.5})(Fe_{0.8}Zn_{0.2})O_{3-\delta}$ - membranes

Julia Martynczuk*, Haihui Wang, Mirko Arnold, and Armin Feldhoff
9th International Conference on Inorganic Membranes (ICIM9), Lillehammer, 25th - 29th July (**2006**) (Poster).

(4) The soft chemical formation of $(Ba_{0.5}Sr_{0.5})(Fe_{0.8}Zn_{0.2})O_{3-\delta}$ perovskite studied by analytical TEM

Julia Martynczuk*, Mirko Arnold, Haihui Wang, and Armin Feldhoff
5. Workshop für EELS/EFTEM 2006, EF-EELS Arbeitskreistreffen der Deutschen Gesellschaft für Elektronenmikroskopie (DGE), Vienna, 27th - 29th September (**2006**) (Poster).

(5) In situ study of the reaction sequence in the sol-gel synthesis of the $(Ba_{0.5}Sr_{0.5})(Co_{0.8}Fe_{0.2})O_{3-\delta}$ perovskite

Mirko Arnold*, Julia Martynczuk, Haihui Wang, and Armin Feldhoff
10th International Conference and Exhibition of the European Ceramic Society (ECerS), Berlin, 17th - 21st June (**2007**) (Talk).

(6) Local in situ study of charge disproportion in mixed-conducting perovskite ceramics

Armin Feldhoff*, Ingo Bergmann, Vladimir Šepelàk, Julia Martynczuk, Mirko Arnold, and Haihui Wang
10th International Conference and Exhibition of the European Ceramic Society (ECerS), Berlin, 17th - 21st June (**2007**) (Talk).

(7) Tuning the functional properties of perovskite-type oxygen permeation membranes by advanced powder processing

Julia Martynczuk*, <u>Mirko Arnold</u>, Haihui Wang, and Armin Feldhoff
Euromat 2007, Nuremberg, 9th - 14th September (**2007**) (Oral Poster).

(8) Analytical TEM study of the formation of perovskite-type oxides by the EDTA/citrate complexing method

Armin Feldhoff*, <u>Mirko Arnold</u>, and Julia Martynczuk
2007 E-MRS Fall Meeting, Warsaw, 17th - 21st September (**2007**) (Talk).

(9) A new monoclinic phase within the formation of the $(Ba_{0.5}Sr_{0.5})(Co_{0.8}Fe_{0.2})O_{3-\delta}$ perovskite via the sol-gel synthesis route

<u>Mirko Arnold</u>, Thorsten Gesing* and Armin Feldhoff
16. Jahrestagung der Deutschen Gesellschaft für Kristallographie, Erlangen, 3rd - 6th March (**2008**) (Poster).

(10) Reaction pathways in the sol-gel based formation of the perovskite $(Ba_{0.5}Sr_{0.5})(Co_{0.8}Fe_{0.2})O_{3-\delta}$ and their impact on the high-temperature application of membranes for oxygen separation

Armin Feldhoff*, <u>Mirko Arnold</u>
Electroceramics XI, Manchester, 31st August - 3rd September (**2007**) (accepted as Talk).

(11) Crystalline intermediate phases in the sol-gel synthesis of the mixed ionic-electronic conductor $La_2NiO_{4+\delta}$ studied by transmission electron microscopy and X-ray diffraction

Konstantin Efimov*, <u>Mirko Arnold</u>, Julia Martynczuk, and Armin Feldhoff
Electroceramics XI, Manchester, 31st August - 3rd September (**2007**) (accepted as Poster).

Erklärung zu dieser Dissertation

Hiermit erkläre ich, dass ich die vorliegende Dissertationsschrift selbstständig verfasst und alle benutzten Hilfsmittel sowie zur Hilfeleistung herangezogene Institutionen vollständig angegeben habe.
Diese Dissertation wurde nicht schon als Diplom- oder ähnliche Prüfungsarbeit verwendet.

Hannover, 25. Mai 2008

Curriculum Vitae

Personal data

Date of birth:	3rd / January / 1980
Place of birth:	Hannover, Germany
Nationality:	german
Marital status:	unmarried, no children

Higher Education

05/2008	**Leibniz Universität Hannover**, Naturwissenschaftliche Fakultät, **Submission of the doctoral thesis:** „Studies on the Solid State Chemistry of Perovskite-Type Oxides for Oxygen Separating Membranes"
02/2006 - 07/2008	**Leibniz Universität Hannover**, Institut für Physikalische Chemie und Elektrochemie **Scientific co-worker**, Prof. Dr. Caro's group
08/2004 - 03/2005	**University of Cambridge**, UK **Intern**, Prof. Dr. Elliott's group, Physical Chemistry „Photo-Induced Softening in Chalcogenide Glasses"
10/2000 - 01/2006	**Leibniz Universität Hannover**, Chemistry Degree: Diplom-Chemiker **Diploma thesis** together with Prof. Dr. Caro: „Präparation und Ausprüfung neuer H_2-selektiver Membranen"

Education

07/1998	**Trifels-Gymnasium**, Annweiler Participant, Deutsche Schülerakademie Topic: „Mechanismen des Erkennens"
08/1990 - 06/1999	**Albert-Einstein-Schule**, Laatzen Degree: Abitur Intensive courses: Chemistry und Biology
08/1986 - 07/1990	**Grundschule Grasdorf**, Laatzen

Civilian Service

07/1999 - 07/2000	**Johanniter-Unfall-Hilfe e.V.**, Hannover